

Institute of Physical Engineering, Faculty of Mechanical Engineering,
Brno University of Technology

Surface Physics from SPM to Graphene

Habilitation Thesis

Ing. Miroslav Bartošík, Ph.D.
Brno 2018

Dedication

I dedicate this work to my father and to my brother, who in my childhood answered my first inquisitive questions like how aircraft can fly, ships float and nuclear reactors produce an immense amount of energy. While doing so, they used the language of physics. Therefore, when I had my first class of physics in sixth grade of elementary school, my mind had been already set so that an amazing meaningful adventure able to answer my questions just started.

Acknowledgment

At this point, I would like to thank many people who contributed in any way to this work, supported me and inspired my interest in solving surface physics problems. I would like to mention primarily prof. RNDr. Tomáš Šikola, CSc. for creation of an amazing and supportive background at the Institute of Physical Engineering that allows us to freely research. Furthermore, my colleague and friend Ing. Jindřich Mach, Ph.D. for stimulating and passionate discussions about the physical essence of experimental problems. My thanks also include prof. RNDr. Jiří Spousta, Ph.D. and doc. Ing. Radek Kalousek, Ph.D. for reading and commenting on this text, however, any errors found in the text can be attributed to the author, since I have not in all cases obeyed the advice of these wise men. My thanks go to all members of the graphene group because we would like never get further if we did not work as a team and in the same spirit I would also like to thank all the other members of the Institute of Physical Engineering, Brno University of Technology.

Abstract

This thesis deals with scanning probe microscopy (SPM) and two-dimensional material graphene and their impact on the modern physics of surfaces. The brief introductions of the field are extended about the comments of author's contributions represented by seven selected papers. The contributions are of a theoretical and experimental character touching on the issues of atomic force microscopy water-bridge, Kelvin probe force microscopy mapping of charge transport on graphene/SiO₂ nanostructures, local anodic oxidation fundamentals and applications in selective growth, graphene fabrication and doping of graphene by gallium.

Key words

SPM, graphene, water, LAO, selective growth, KPFM, charge transport, diffusion equation, BET theory, electron hopping theory, gallium, DFT

Content

1	Introduction.....	1
2	A brief overview of SPM.....	3
2.1	Ambient SFM and water-bridge.....	5
2.2	EFM and KPFM.....	7
2.3	LAO and Mechanical nanolithography.....	11
3	A brief overview of graphene.....	17
3.1	Graphene CVD fabrication on copper foil.....	21
3.2	Graphene and gallium.....	23
4	Great unification – graphene, biosensors, sensors and SPM.....	27
5	Conclusion.....	29
	References.....	33
	Commented paper 1.....	43
	Commented paper 2.....	55
	Commented paper 3.....	65
	Commented paper 4.....	73
	Commented paper 5.....	81
	Commented paper 6.....	87
	Commented paper 7.....	99

1 Introduction

The main and linking topic of this habilitation thesis is physics of surfaces seen from the perspective of scanning probe microscopy (SPM) and graphene. Despite being different, SPM is a **microscopy technique** and graphene is a **two-dimensional material**, both together caused a real revolution in our understanding of surface physics. Though almost nobody had heard of SPM before 1981, and even graphene before 2004, since then a huge volume of scientific articles has been published and numerous patent applications dealing with these topics have been filed. In today's scientific world, special conferences are held and special journals are printed, dealing only with SPM or graphene and both of them have become a common part of scientific dictionaries in various fields. Here, we have to ask: *“What is behind this hint? Why have these two discoveries been so influential in modern surface physics, in addition to other fields?”* To answer these questions, let us have a look at things in a wider context.

In general, physics of surfaces is a difficult discipline, since the presence of surface boundaries disturbs the periodicity and symmetry of atom arrangement in bulk solids, making their mathematical description more difficult. This fact was nicely expressed by Wolfgang Pauli in his famous statement: *“God made bulk; surfaces were invented by devil.”* Unfortunately, the harder it is to understand the surfaces, the more fruitful they are; since nowadays, in the era of nanotechnology, we more often meet and will meet objects defined predominantly by their surface. Therefore, any discovery that brings the slightest light into the *“dark devil”* area of surface physics is of significant importance not only in theory but also in applications. In this sense, we can say about SPM and graphene without exaggeration that they really are the huge lights and as the gospel of John said with relief: *“... the light shines in the darkness...”* (*“... lux in tenebris lucet ...”*). This is mainly caused by the following facts. SPM includes a family of tools that first enabled us to observe the surface and its properties down to the atomic level. Graphene is then a direct embodiment of the first isolated two-dimensional one-atom-thick material consisting only of its surface. These facts were known or at least expected in 1986 when Gerd Binnig and Heinrich Rohrer were awarded the Nobel Prize *“for their design of the scanning tunneling microscope”* first one in the SPM family and in the year 2010 when Andre Geim and Konstantin Novoselov received the Nobel Prize *“for groundbreaking experiments regarding the two-dimensional material graphene”*. Although these discoveries contribute to surface physics in slightly different ways, what they have in common is a relative simplicity, wide versatility, easy accessibility, potential for solving fundamental questions and a broad range of possible applications. It all caused their popularity across the scientific community shortly after their invention and led to their *“massive”* utilization.

The path that author of this thesis took from SPM to graphene is far less *“groundbreaking”* but undoubtedly also filled with a lot of very interesting physics and has its own story. At the end of 2002, I first learned about SPM techniques while working on my diploma thesis at the Institute of Physical Engineering at Brno University of Technology (IPE BUT). At that time, I was testing the possibilities of atomic force microscopy (AFM) for the study of self-assembled monolayers (SAM) and modification of surface by local anodic oxidation (LAO) using the AFM tip. The second topic attracted most of my attention, since LAO represents a quite simple and easily applicable method for local surface modification, however, behind it is hidden a lot of nice, fundamental and not very well-understood physics (e.g. charge diffusion across oxide barrier, the influence of extreme electric fields and the strange behavior of water at the nanometer scale).

Therefore, during my Ph.D. study in 2003-2009, I focused on the understanding of the basic processes governing the LAO, however, I was also fascinated by its applications for the selective growth

of metals, and mainly by its utilization in the fabrication of real quantum-mechanical nanodevices where phenomena like quantum transport in point contact, the Coulomb blockage or the Aharonov-Bohm effect could be studied. In nanostructures exhibiting such a behavior it is necessary to confine the charge carrier motion to a small area without a significant disturbance of their crystallinity to fulfill the strict conditions of ballistic transport. The usual way of limiting the carrier motion in 2 dimensions at high mobility is by use of two-dimensional electron/hole gases (2DE/HG) fabricated at the interface of heterostructures (e.g. AlGaAs/GaAs) with the use of a relatively expensive and demanding molecular-beam epitaxy (MBE). Thanks to my part-time job at the Institute of Physics at the Academy of Sciences (IP AS) in Prague I had access to an apparatus producing these “perfect” 2DE/HG that could be used as a basic substrate for further patterning towards the mentioned quantum devices. Optical lithography or electron beam lithography (EBL) is often used to pattern 2DE/HG into a required lateral shape, however, we decided to test the possibilities of LAO in such patterning since it appeared to be much finer, especially with regard to the creation of edges that are a critical issue. Although during my doctoral study LAO proved to be a useful technique for patterning 2DEG and confining the lateral motion of electrons, it proved to be very difficult to fabricate shallow 2DEG with sufficiently high electron density to observe all those “nice” quantum effects in transport experiments. It was not difficult to fabricate a heterostructure quantum-well deep beneath the surface (> 50 nm), however, the obstacles of this task grow as the quantum-well approaches the surface (< 30 nm). The closer the surface, the more electrons are trapped by unpredictable “devil” surface states, however, to reach the 2DEG by low penetrating LAO, it is necessary to have the quantum well close to the surface. This was a problem that could not be easily solved by heterostructures of AlGaAs/GaAs and MBE.

Moreover, this was the year 2009 when I finished my Ph.D., moved completely to Brno (IPE BUT), left my part-time job in Prague (IP AS), and also lost easy access to an expensive MBE apparatus so necessary for studying 2DE/HG. It looked like the end of my work with two-dimensional gases of charge carriers. However, during the years of my cooperation with IP AS, I found pleasure in the physics of 2DE/HG and I did not want to leave this field completely even though I was still keen on SPM technologies. During this time, graphene appeared like “a bolt from the blue”. Apart from its other extraordinary and interesting physical features, it seemed to me like a “dream” – an almost ideal material to replace the 2DE/HG GaAs/AlGaAs heterostructures and continue my work. Graphene could be placed directly on a surface, it had charge carriers with a high mobility even at room temperature (RT), it was incredibly stable, yet, thinnest possible, and, finally best of all, it was available to anyone without any extra budget. Mechanical exfoliation of graphene using Scotch-tape that we first decided to use in Brno cost almost nothing but effort. And later when we started to use our home-built chemical-vapor deposition (CVD) furnace, everything was much cheaper in comparison with MBE technology, and the physics behind it was just as fascinating.

This was the main story, how the author of this thesis could move from SPM technologies to graphene, however, he remained faithful to both. Further in this work, the most important results achieved by the author and his colleagues in these fields (SPM, graphene) will be described and, primarily, included into the overall scientific framework of surface physics.

2 A brief overview of SPM

Nowadays, scanning probe microscopy (SPM) includes more than 30 techniques [1] that have in common scanning of a sample surface using a sharp probe (tip) to gain information about its local physical properties down to atomic resolution. It does not make sense to list all the SPM branches here and instead let us focus on those ones that have been used or are important to present the results of this work (Figure 2.1).

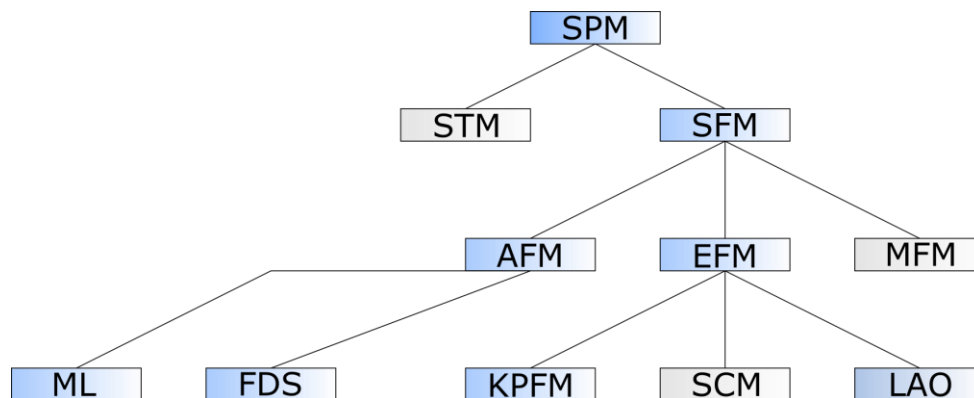


Figure 2.1: A brief overview of SPM used (blue shaded) and mentioned (grey shaded) in this work and their relationship. (ML – mechanical lithography, FDS – force distance spectroscopy)

The first of the SPM techniques is scanning tunneling microscopy (STM) born in 1981. STM utilizes an exponential decay of a tunneling current with a tip-sample separation to image a sample topography (more accurately, local density of states). Although the physical principles of quantum tunneling have been known since the beginning of the 19th century, the inventors of STM Gerd Binnig and Heinrich Rohrer were able to solve plenty of practical problems leading to a truly usable apparatus and thus opened the door to all other SPM's. These most basic problems were (1) motion of tip/sample in a distance of less than one atom, (2) tip sharpening into an almost single atom, and (3) damping of ubiquitous vibrations. For this purpose, the inventors used all the possible and “impossible” means like (1) piezoelectric materials, (2) high electric fields in vacuum, “tip-touching” the surface, and (3) double-stage spring-system with eddy-current damping [2]. Moreover, they showed a benefit of STM by imaging the challenging 7x7 reconstruction of Si(111) [3]. In an incredibly short time of 5 years (until winning the Nobel Prize in 1986), the set of technical solutions inspiring all the SPM industry were performed. Among others, the STM was moved from vacuum into the air [4], incorporated into a scanning electron microscope (SEM)[5], used to determine energy gaps using tunneling spectroscopy [6], and to gain local surface potential [7].

Since STM is primarily designed to measure conductive samples, Gerd Binnig patented the atomic force microscopy (AFM) technique [8] in 1986 applicable also on non-conductive samples [9]. AFM uses a dependency of atomic forces down to 10^{-18} N on a tip-sample separation to image a sample topography (more accurately, local tip-sample force). AFM laid foundations of a large scanning force microscopy (SFM) family utilizing a detection of different forces, e.g. short-range Pauli repulsion, van der Waals, capillary and electromagnetic forces. In all SFM, the tip-sample force is usually detected by a bending (static mode) or by a resonance frequency change (dynamic mode) of a cantilever where the tip is placed on. Recently, a subatomic resolution corresponding the inner-atomic charge density can be achieved by a dynamic AFM mode using a q-plus sensor based on a watchmaking tuning fork [10-11].

SFM techniques can be divided according to the kind of a prevalent force in a certain tip-sample distance. The short-range Pauli repulsion ($\approx d^{-13}$) and van der Waals attraction ($\approx d^{-7}$) is used in AFM. On the other hand, the long-range magnetostatic ($\approx d^{-4}$) and electrostatic interaction ($\approx d^{-2}$)* is used in electrostatic force microscopy (EFM) and magnetic force microscopy (MFM), respectively. As stated by Richard Feynman in his famous lectures [12] the force versus the distance between two interacting atoms is of the most important in science being at the basis of our understanding of interaction between two objects. Therefore, all SFM's are extremely important apparatus allowing us to perform a force-distance spectroscopy (FDS) in a single point often at the atomic level.

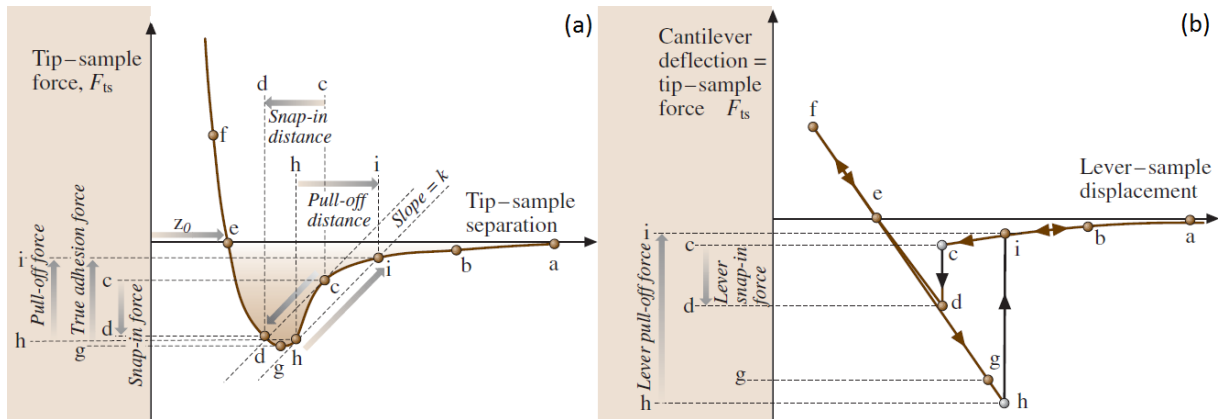


Figure 2.2: Tip-sample force as a function of tip-sample separation (a) and a corresponding force-distance curve measured in real AFM experiment during approaching/retracting of the tip, respectively [1].

Figure 2.2 (a) depicts the ideal dependency of the tip-sample force on the distance and Figure 2.2 (b) the usual real force-distance curve measured by approaching/retracting of the AFM tip in static mode. While in the ideal curve (a) a nice smooth transition from repulsive to attractive forces can be observed, the real measurement is often characterized by an approaching snap-in (Figure 2.2 c-d) and a retracting pull-off (Figure 2.2 h-i) force as a consequence of a sudden cantilever deflection. The approaching snap-in of the tip towards the surface can be explained by a sudden predominance of the attractive tip-sample force over the repulsive force caused by the cantilever deflection (Figure 2.2 a-c). The cantilever deflection force is depicted as a line (Figure 2.2 dashed line crossing the c), since it can be approximated by a linear Hooke's law $F = k\Delta d$, where k is the force constant of cantilever and Δd is the bending of the cantilever. On the other hand, the retracting pull-off is caused by a sudden predominance of the repulsive cantilever deflection force over the attractive tip-sample force (Figure 2.2 h). Consequently, the pull-off force (Figure 2.2 h-i on force axis) is proportional, but not exactly equal to the maximum attractive tip sample force. This problem is solved by utilization of the cantilever with a suitable stiffness or by combination of a static and dynamic mode [13] when the real curve (Figure 2.2 b) is more like the ideal curve (Figure 2.2 a). In ambient condition, the pull-off force is mainly determined by a force resulting from the condensation of water between the tip and the surface[†] which is the topic we dealt with in the commented paper 1 and which is briefly described in the following chapter.

* The dependences of force on distance d are valid for two atoms, magnetic dipoles or ions.

[†] The same capillary and tension forces held together the grains of wet sand when we built castles as children.

2.1 Ambient SFM and water-bridge

In general, the best resolution using SFM is achieved in vacuum conditions, however, with increasing utilization in chemistry, biology and technologies the SFM techniques are widely applied in atmospheric conditions with a hydrophilic tip or on a hydrophilic surface. Here, a condensation of water molecules between the tip and the surface into a water bridge occurs (Figure 2.3) and is stable even at relative humidity less than 100% (saturated vapors). This is described by the equilibrium thermodynamic Kelvin-Young-Laplace equation [14]

$$r_K = \left(\frac{1}{r_1} + \frac{1}{r_2} \right)^{-1} = \frac{\gamma_{LV} V_m}{RT \ln \left(\frac{p_v}{p_v^*} \right)}, \quad (2.1)$$

where r_K is Kelvin radius characterizing the mean curvature of water – water vapor interface determined by the main radii of curvature r_1, r_2 ; γ_{LV} is the interfacial energy of the liquid and water vapor, V_m is the molar volume of water, R is the molar gas constant, T is the thermodynamic temperature, and the ratio of partial water vapor pressure p_v and saturated water vapor pressure p_v^* corresponds to the relative humidity RH. Since most of the SFM measurements are carried out at $RH < 100\%$, the water-bridge is stable when $r_K < 0$ which is achieved in an SFM water bridge by a low negative radius r_1 . Therefore, the bridge is more like a cavity, not a drop. The Kelvin-Young-Laplace equation also predicts an increase of the water-bridge dimensions with relative humidity. Strongly dipolar water molecules and highly curved surface of this water bridge results in a reduction of van der Waals and electrostatic forces, respectively. Consequently, the water-bridge capillary and tension forces have a crucial impact on AFM and EFM in ambient conditions.

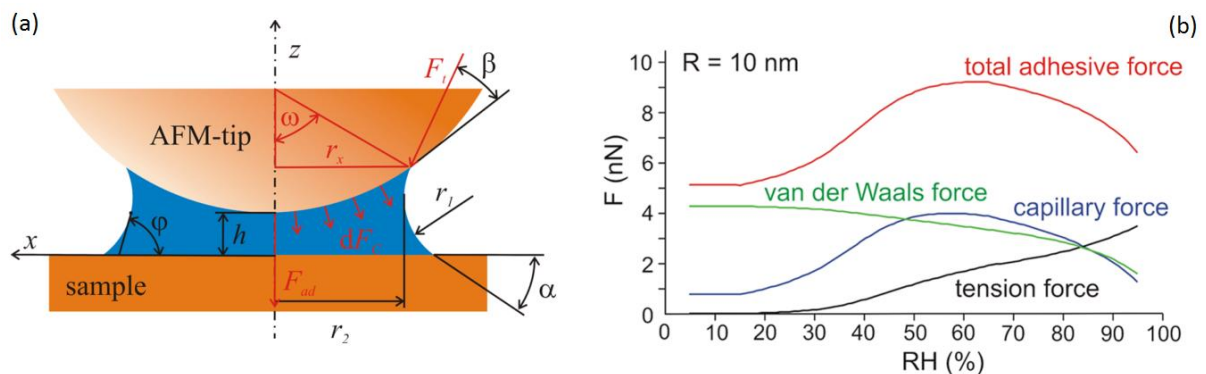


Figure 2.3: (a) Geometry of water-bridge (meniscus) between the AFM tip and the surface. (b) Calculated forces as a function of relative humidity for AFM-tip with radius $R = 10$ nm [15].

The water-bridge between the SFM tip and surface influences not only forces but also has a strong impact on SPM nanolithography techniques, e. g. local anodic oxidation (LAO) and dip-pen nanolithography (DPN) (see below Chapter 2.3). Moreover, the water-bridge exhibits extreme fundamental physical properties of nano-volume water governed mainly by their “devil” surface.

For example, the Laplace pressure difference [14]

$$\Delta P = \frac{\gamma_{LV}}{r_K} \quad (2.2)$$

between the inside and outside of the meniscus at RT and RH of 30 % is recordable negative [16] -160 MPa* [17,18,19]. At such a strong negative pressure the water vapor cavities should start nucleating or, easily said, the water should start boiling even at room temperature. That is not the case of nano-volume AFM water-bridge, since any cavity needs to achieve a certain critical value to continue growing, unless it disappears. This can be explained if we calculate a change in Gibbs free energy ΔG when a cavity of radius R forms [19]

$$\Delta G = G_V - G_{LV} = -\frac{4}{3}\pi R^3 n_V \Delta\mu + 4\pi R^2 \gamma_{LV}, \quad (2.3)$$

where G_V and G_{LV} are Gibbs energies inside a spherical vapor cavity and its liquid-vapor surface, respectively. The $-\Delta\mu$ corresponds to a decrease of a chemical potential of a single molecule of liquid water transforming into a single molecule of vapor water which is more stable at conditions of cavitation. The cavity can grow independently if it reaches the critical radius [19]

$$R_c = \frac{2\gamma_{LV}}{n_V \Delta\mu} \quad (2.4)$$

above which the Gibbs free energy decreases. In a nano-volume water bridge, the cavities cannot achieve the critical size, cannot grow and the bridge is stable at this extremely negative pressure[†]. The liquid water at a negative pressure at RT belongs to metastable liquids which can be evaporated by a sudden stimulus since they are not thermodynamically stable[‡]. The concept of negative pressure is related to the fact that the interatomic forces of water can be both repulsive and attractive, similarly to tip-sample force depicted in Figure 2.2 (a), however, at a pressure less than zero the attractive forces between water molecules prevail. Such water will tend to collapse and act on the outside with the opposite (negative) pressure. The water-bridge formation itself is very fast. The time necessary to form the bridge is 5 ms at RT and approximately 1 ms at higher temperature of 60 °C [19].

Based on the above, no wonder the SPM water bridge attracts such attention. The direct experimental observation of bridge was performed by high-pressure environmental scanning electron microscope (SEM). The bridge appeared to be larger than the thermodynamic prediction. This was concluded by the failure of the classical thermodynamic model [20]. Later, van Honschoten *et al.* [21] calculated the charging of the water-bridge by SEM electrons reducing the interfacial energy of liquid leading to unpredictable increase of water-bridge dimensions. The indirect experimental observation of the bridge was done by the measurement of its print in the salt crystal. Here, the properties of water are strongly distorted by the presence of dissolved salt again [22].

In commented paper 1, we used the force distance spectroscopy (FDS) measurement of the pull-off force to estimate the dimensions of water as a function of relative humidity. For this purpose, the theoretical model was suggested. The shape and dimensions of the water-bridge were predicted

* That is value beyond the theoretical limit predicted by homogeneous nucleation theory (-140 MPa at 25 °C) and below the theoretical limit predicted by spinodal breakdown theory (-200 MPa at 35 °C). The experimentally most negative pressure -25 MPa was achieved by an acoustic method in macro-volumes of water, and -140 MPa achieved by an aqueous inclusions using quartz crystals in micro-volumes of water [17-19].

[†] The similar negative pressure is achieved in water filling the pores of tree leaves (cell wall pores) having diameters of 2 – 5 nm. Therefore, the trees are able to pull water up to the heights above 100 m even though the standard atmospheric pressure (10^5 Pa) would enable to get water up to a maximum of 10 m. Moreover, above the height of 10 m, the pressure inside the tree xyleme tubes is less than zero and water should boil at room temperature. The boiling or the cavity creation cannot occur due to a small diameter of xyleme 20 - 200 μ m and pores at which the critical radius of cavity cannot be achieved.

[‡] It is similar to a situation when the undercooled water can freeze after a first nucleation center is induced by shaking or stroke.

using the differential form of the thermodynamic Kelvin-Young-Laplace equation. Based on this, the total adhesive force consisted from capillary, tension and van der Waals contribution was calculated (Figure 2.3 b). The dependence of capillary force on RH increases up to 60 % due to the increase of the water-bridge dimension and tip-area dipped into the water. However, above 60 % the capillary force goes down, since the Kelvin radius increases reducing the Laplace pressure difference. In the suggested model, the van der Waals contribution is reduced by strongly polar water molecules at higher relative humidity.

In commented paper 1, a lot of attention was paid to the pull-off force measurement reproducibility that proved to be crucial for the measurement of a nano-size water bridge. The problem of reproducibility was nicely addressed by Don Eigler, the father of SPM manipulations of individual atoms, who said [23]: *“For us, that’s a sort of sacred thing. The key thing and more important thing about science is reproducibility. If you cannot reproduce your own results, you might as well forget it. It’s as if you’d never done it”*. Thanks to the careful consideration of reproducibility and measurement errors, it was able to find up the accurate pull-off force vs RH dependence with the convex-concave like initial increase of the total adhesive force (Figure 2.3 b RH from 20 to 60 %). Based on this, we suggested a reduction of water surface tension from bulk value 72 mN/m to curved surface value of 9 mN/m. Such a reduction of a macroscopic surface tension for small or highly curved surfaces is in qualitative agreement with the conclusion made by Josiah Willard Gibbs early in the 19th century transformed in 1949 by Richard Tolman into a relation [24] between the surface γ_{LV} and bulk tension γ_{LVbulk}

$$\frac{\gamma_{LV}}{\gamma_{LVbulk}} = \frac{1}{1 + 2\delta_{\infty}/R}, \quad (2.5)$$

where δ_{∞} is the Tolman length which is an empirical constant for a droplet of infinite radius and R is the real finite radius.

However, the future will probably belong to the bottom-up approach by molecular calculations of water-bridge on the basis of molecular dynamics (MD), Monte Carlo (MC) or density functional theory (DFT). They still have problems to explain the whole adhesive (pull-off) force curve (Figure 2.3 b) in its decreasing part [25], or even its whole character [26] (permits only a fall or growth, not both as can be seen in Figure 2.3 b). From this point of view, the correction of surface tension term in macroscopic thermodynamic Kelvin-Young-Laplace equation can help us with a top-down approach to the experimental reality.

2.2 EFM and KPFM

In 1898 William Thomson, later knighted “lord Kelvin of Largs”, was first to measure the contact potential difference (CPD) of copper and zinc plate in an arrangement similar to today’s plate capacitor [27]. The CPD between the conductive tip and surface is a voltage V_{CPD} proportional to the difference of their work functions Φ_{Tip} and Φ_S defined as [28]

$$V_{CPD} = \frac{1}{e}(\Phi_{Tip} - \Phi_S), \quad (2.6)$$

where e is the elementary charge. Generally, when the plate capacitor is in an electric circuit equalizing the Fermi levels, the CPD corresponds to the charge trapped in surface states which was the case measured by Kelvin using an old-time gold-leaf electroscope. A more precise measurement of CPD can be achieved by mapping the current flowing across the circuit while the distance between the plates of capacitor oscillate (changes capacity in the circuit) as was firstly performed [29] by William Albert Zisman in 1932. The method based on this current mapping is called Kelvin Probe (KP) and measures

average macroscopic CPD of the whole sample with an energy resolution of 1 meV. On the other hand, the Kelvin probe force microscopy (KPFM) which was first introduced by Nonnemacher [30] et al. and Weaver [31] et al. in 1991 measures local CPD with a spatial resolution better than 10 nm and energy resolution 5 – 20 meV. Since then, the KPFM has experienced a huge expansion and shifted its resolution to measuring the potential distribution of individual molecules.

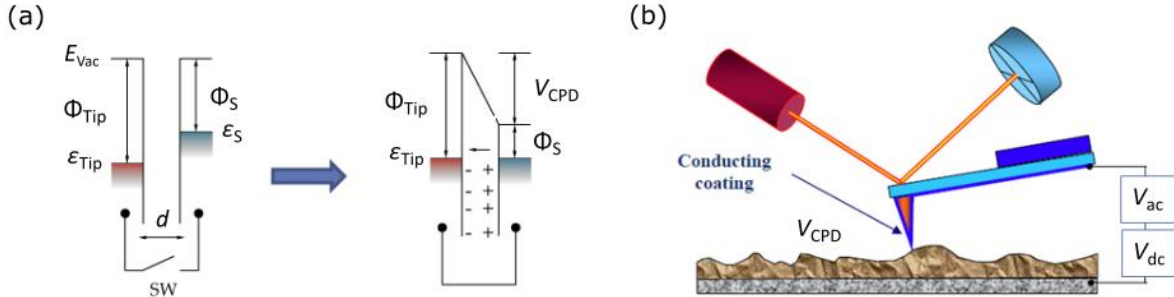


Figure 2.4: (a) The creation of contact potential difference in case of two different metals as a consequence of their different Fermi levels. (b) The scheme of Kelvin probe force microscopy (KPFM) [32].

KPFM is based on the measurement of electric force which is very similar to the original Kelvin's approach, however, between the tip and the surface is applied oscillating alternating voltage V_{ac} (Figure 2.4 b) which is the advantage of Zisman's approach. Then, the tip-surface voltage can be expressed as [28]

$$V = V_{dc} - V_{CPD} + V_{ac}\sin(\omega t), \quad (2.7)$$

where V_{dc} is a direct voltage component. A consequent vertical component of the electrostatic force acting on the tip can be derived using a classical relationship between force and energy of a plane capacitor U_{el} with capacity C as follows [28]

$$F_{el_z} = -\frac{\partial U_{el}}{\partial z} = -\frac{1}{2} \frac{\partial C}{\partial z} V^2 - CV \frac{\partial V}{\partial z} \quad (2.8)$$

Neglecting the second term on the right side of the previous equation in case of conductive tip/sample and substituting the expression (2.7) results in [28]

$$F_{el_z} = F_{dc} + F_{\omega} + F_{2\omega}, \quad (2.9)$$

where F_{dc} , F_{ω} , $F_{2\omega}$ are the constant and oscillating components of the electrostatic force, respectively. The force component oscillating at frequency ω [28]

$$F_{\omega} = -\frac{\partial C}{\partial z} (V_{dc} - V_{CPD}) V_{ac} \sin(\omega t) \quad (2.10)$$

is the force used in electrostatic force microscopy (EFM). Assuming the capacity of plane condenser we can simplified (2.10) as $F_{\omega} \approx \epsilon(V_{dc} - V_{CPD})$, where ϵ is the dielectric function. Therefore, the EFM measurement is a mixture of indistinguishable information about local dielectric properties and CPD. However, by setting the V_{dc} so that the F_{ω} is nullified which is practically realized by a feedback loop, the net value of CPD can be found by KPFM.

Why are the equations in the previous paragraph necessary? Since there is a cliché in literature that "KPFM measures the difference of tip/sample work functions" corresponding to the relationship (2.6) which is true in case of a conductive/semiconductive sample (and tip). However, the

understanding of the previous relationship can offer us a wider picture. For example, we can realize that in case of a non-conductive sample, KPFM provides information about the local surface potential U_{sp} , induced by all surface charge/dipoles produced by different processes. Moreover, we can see that KPFM gives much cleaner information about the surface potential than the mentioned EFM whose signal is a mixture of surface potential and dielectric properties of the sample. This property was used in commented paper 2 where we were studying the charge transport by KPFM between graphene flakes placed on SiO_2 .

The study of charge propagation across graphene/ SiO_2 interface and its further propagation on SiO_2 is important due to the basic function of electronics, since it can lead to negative short circuits between isolated graphene parts and also to hysteresis caused by an accumulation of charge on the SiO_2 surface close to the graphene limiting the electronic width of graphene conductive parts. In commented paper 2, we showed the charge propagation exponentially grows with relative humidity, which is especially important for the design of the graphene-biosensors operating in humid air or even more often in water solutions! Since the rapid increase of isolating SiO_2 conductivity with RH can gradually destroy their function completely. On the other hand, the SiO_2 surface conductivity dependence on RH can be used to build the most sensitive sensors that have ever been built based just on the rapid exponential increase of SiO_2 conductivity with RH [33].

In commented paper 2, we introduced for the first time how to obtain the surface resistivity of “isolating” SiO_2 from the KPFM measurement of local surface potential distribution in time. As it has been mentioned, KPFM can provide information about the charge propagation on the surface, however, sometimes it is necessary to get more physically comparable (tableted) quantity such as surface resistivity. For this purpose, the following model and experimental procedure was suggested. The model is based on the solution of the diffusion equation for charge in two dimensions [33]

$$\frac{\partial \rho_{2D}}{\partial t} = \vec{\nabla}(\rho_s^{-1} \vec{\nabla} U_{sp}) \quad (2.11)$$

where ρ_{2D} is a two-dimensional surface charge density, and ρ_s is the surface resistivity. The equation (2.11) is a combination of differential Ohm’s law and continuity equation for charge conservation. Ohm’s law behaves here similarly to 1st Fick’s law and has a form of

$$\vec{J}_s = \rho_s^{-1} \vec{E} = -\rho_s^{-1} \vec{\nabla} U_{sp}, \quad (2.12)$$

where \vec{J}_s is the surface current density and \vec{E} is the electrical intensity. The two-dimensional continuity equation is

$$\frac{\partial \rho_{2D}}{\partial t} = -\vec{\nabla} \cdot \vec{J}_s. \quad (2.13)$$

Generally, surface resistivity is a function of surface coordinates $\rho = \rho(x, y)$. Therefore, the equation (2.11) has the potential to find out the local resistivity, however, the mathematical solution is then quite complicated and time-consuming. Therefore, surface resistivity was assumed to be constant on graphene, and especially on SiO_2 . Then the equation (2.11) can be simplified as

$$\frac{\partial \rho_{2D}}{\partial t} = \rho_s^{-1} \Delta U_{sp}. \quad (2.14)$$

The previous equation is valid for the two-dimensional charge density, however, KPFM measures the surface potential, and therefore, the relationship for capacity

$$\rho_{2D} = C_0 U_{sp} = \frac{\epsilon_r \epsilon_0}{w} V \quad (2.15)$$

was necessary to use. Here, the C_0 is unit area capacitance expressed as a local dielectric constant ϵ_r and ϵ_0 divided by a thickness w of the isolating layer (in case of commented paper 2, the 280 nm thick thermal SiO_2). Substituting the term (2.15) into the equation (2.14) results in a diffusion equation for surface potential

$$\frac{\partial U_{sp}}{\partial t} = \frac{1}{\rho_s C_0} \left(\frac{\partial^2 U_{sp}}{\partial x^2} + \frac{\partial^2 U_{sp}}{\partial y^2} \right), \quad (2.16)$$

which is measured by KPFM. It is a diffusion equation, where the surface diffusion coefficient (surface diffusivity) is

$$c_s = \frac{1}{\rho_s C_0} = \frac{w}{\rho_s \epsilon_0 \epsilon_r} \quad (2.17)$$

Today, the equation (2.16) can be quickly solved by numerical methods (by the finite difference method – FDM or, in case of a more complex geometry, also by the finite element method – FEM) and the parameters of surface diffusivity or surface resistivity can be optimized with KPFM measurement to find values describing a real experiment. This way, it is possible to obtain the surface resistivity of highly resistive materials from KPFM measured $U_{sp}(x, y, z, t)$ which is generally quite complicated using only transport measurements. An example of such a solution is depicted in Figure 2.5 (b-e) for a real graphene/ SiO_2 structure (a). The equation (2.16) can be used for description of the charge (or better surface potential propagation along the surface). We believe that presented way how to obtain from KPFM surface potential distribution in time to the average (2.11) or even local surface resistivity (2.14) is the most important, however a little bit hidden, result of a commented paper 2. It could be the cornerstone of a new SPM technique, if we realize the fact that only a conductive atomic force microscopy (cAFM) gives information about local conductivity and resistivity of the sample, respectively. However, unlike the process we introduced, cAFM is useful only in case of conductive samples.

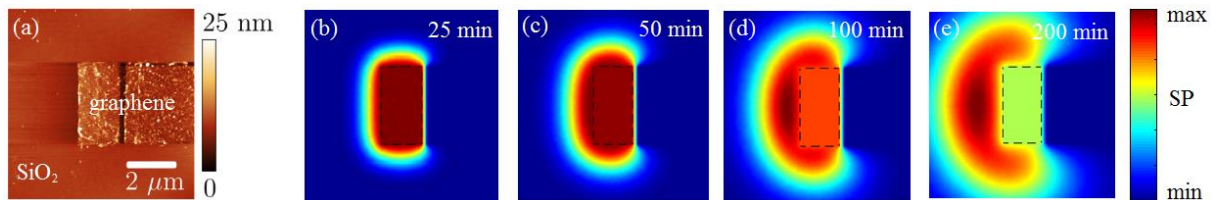


Figure 2.5: (a) AFM topography of graphene/ SiO_2 for the study of charge transport. (b-e) Surface potential distribution as a function of time simulated by a diffusion equation (2.16) corresponding to a real KPFM experiment.

In commented paper 2, we also asked the fundamental question, how the relative humidity physically influences charge transport. The answer was given by a combination of BET theory and electron hopping theory. The physisorption* BET [34] theory water molecules on a surface was designed by Brunauer, Emmett and Teller† in 1938. The theory is based on the thermodynamical equilibrium between condensation and evaporation of water molecules in first, second and higher

* It is important to emphasize that this is not a hard reversible chemisorption adhesion occurring in the early stages of hydrogen or oxide layer growth. The physisorption adhesion occurs mostly on top of the chemisorbed molecules and is easily reversible.

† Edward Teller (1908 - 2003) is known for his contribution to the development of the hydrogen bomb and is called „the father of the hydrogen bomb“.

layers without assuming completion of the previous layer. The theory enables us to calculate the coverage ratio R_c as a function of RH having an almost exponentially growing course [35]

$$R_c = \frac{k \cdot RH}{1 + (k - 1) \cdot RH}, \quad (2.18)$$

where k is a parameter characterizing the hydrophilicity of the surface. The electron hopping theory enables us to explain the changes of surface resistivity with water coverage. It is based on the assumption that electrons can quantum mechanically tunnel between the water spots, and the probability of this jump decreases with the distance between the spots formed by a “dry” SiO_2 surface. In connection with BET theory, the electron hopping theory suggests the following dependency of surface resistivity on [36] RH

$$\rho_s = \rho_s^{100\%} \exp\left(\frac{-|p|}{\hbar} b \sqrt{\frac{1 - RH}{k \cdot RH}}\right) \quad (2.19)$$

where $\rho_s^{100\%}$ is the surface resistivity at 100% RH (when the surface is completely covered by water), $|p| = \sqrt{2mV_0}$ is the modulus of the momentum in the classically forbidden region (pure SiO_2) in the potential barrier V_0 for electron of mass m , \hbar is the reduced Planck constant, and b is the width of the potential barrier (average size of the clean SiO_2 surface). Using the typical parameters for SiO_2 and fitting the data obtained in the KPFM measurement and surface resistivity calculation it was possible to estimate the $\rho_s \approx 1 \cdot 10^9 \Omega$ and $k = 2.7$. These values of surface resistivity are much lower than the surface resistivity of a standard SiO_2 in the range of $10^{10} - 10^{15} \Omega$ depending on surface treatment [34], and the k parameter corresponds the much more hydrophilic surface than standard SiO_2 whose k is [36] 0.05. This was attributed to the patterning of graphene into a required shape by mechanical lithography using AFM. Here, the tip is pushed towards the surface at a high load force 1000 nN (the tip is in strong repulsive regime, see Figure 2.2 Chapter 2), and the graphene is “scratched” away from the SiO_2 surface. The scratching causes charge traps acting as a recombination centers, leaves graphene residues on the surface (with low surface resistivity of about $10^3 \Omega$), and finally causes grooves enhancing water condensation (see Chapter 2.1). All of these influences significantly reduce the surface resistivity of the surface.

2.3 LAO and Mechanical nanolithography

In addition to surface imaging, SPM techniques are suitable to fabricate surface nanostructures, which is called SPM nanolithography. The surface is modified by physical and chemical processes running in a small region under the tip and the most famous techniques from this family are (1) manipulation of individual atoms/molecules by SPM tip, (2) Dip-pen nanolithography (DPN), (3) mechanical lithography (ML), and (4) local anodic oxidation (LAO).

The positioning of individual atoms by the SPM tip is a technique with an ultimate precision and with high demands as well. (1) The ultra-high vacuum conditions ($< 10^{-7}$ Pa), ultra-cold temperatures (< 4 K), and atomic resolution are necessary but often insufficient conditions. Although the technique of atomic manipulation is nowadays quite widely used, the pioneer of atomic manipulations is Donald Eigler, who first (in 1990) moved individual Xe atoms on a Ni surface into the famous IBM logo [37], and whose group developed this method up to the limits of possible, fabricating for example a structure enabling the observation of quantum mirage in scanning tunneling spectroscopy (STS) signal [38].

On the other hand, (2) the dip-pen nanolithography uses the SPM tip much like an ink pen is used when writing, however, the ink is replaced by a solution of molecules that are capable of adhesion

and self-assembling on the surface (self-assembled monolayer - SAM). In order to transfer the molecules from the tip to the surface, the presence of the water meniscus discussed in chapter 2.1 is necessary. The DPN is a quite easily available method working in atmospheric conditions, room temperatures and achieving a relatively high resolution [39] of 15 nm.

The simplest SPM nanolithography technique is (3) mechanical lithography (ML) using an AFM tip. Here, the tip is pushed towards the surface at a high load force to create holes or grooves. In spite of its simplicity, the technique is used in fundamental research, since there is only a purely mechanical influence on the surface. In comparison with that, electron beam lithography (EBL) using highly energetic electrons (5 – 30 keV) or reactive ion etching (RIE) using ions (0.5 keV) and following optical lithography (OL) includes more significant influence on electronic properties of the material. If a soft polymeric material is used as the substrate, the technique resolution is limited only by the tip-apex radius [40] (typically about 10 nm). The main disadvantage of this method is the mechanical damage as a consequence of direct contact between the tip and surface. ML has been used in commented paper 2 to prepare graphene nanostructures on SiO₂ surface (chapter 2.2).

The last, but certainly not least, nanolithography technique is local anodic oxidation (LAO). LAO is carried out in an ordinary atmosphere and the presence of water on the surface or under the tip in the form of water meniscus (see Chapter 2.1 and Figure 2.3) is a necessary condition. Here, a voltage is applied between the conductive AFM tip and the conductive surface causing a dissociation of water molecules into hydroxide and hydrogen ions (OH⁻, H⁺). The hydroxide ions locally oxidize the surface acting as an anode while the hydrogen atoms evaporate. The applied voltages are in order of tens of volts and, considering the short tip-surface distance in nanometer units, the intensity of electric field is quite huge approximately $E_L = 10^{10}$ V/m which is also a critical value allowing oxide growth. Such a strong field can strongly influence water behavior as will be discussed later. The technique is applicable on conductive and semiconductive materials to create local isolation barriers. It has also been used to oxidize locally the top -CH₃ groups of highly ordered SAM monolayer of OTS (n-octadecyltrichlorosilane) into -COOH groups for further selective chemical reactions [41]. Moreover, it can be utilized on a graphene [42,43], where opposite voltage was also used to hydrogenate graphene [44]. Since LAO on SiO₂ was studied in detail by the author of this work from a fundamental physical point of view in commented papers 3 and 4, and from an application point of view for selective growth of metallic nanostructures in commented paper 5, let us take a closer look at this process.

The theory of oxidation of metals was exhaustively described by Cabrera and Mott [45] and its part dealing with the formation of very thin (< 10 nm) oxide layers is suitable for LAO. Here, a propagation of oxide ions across the previously formed oxide layer (Figure 2.6) is understood as a sequence of tunneling jumps between the surface (P) and stable interstitial sites (Q₁, Q₂) through the potential barriers (S₁, S₂). Then, the general differential equation of oxide thickness h growth with time t is determined by the formula

$$\frac{dh}{dt} = u \exp\left(\frac{h_1}{h}\right) \quad (2.20)$$

where

$$u = u_0 \exp\left(-\frac{W_i + V}{k_B T}\right), \quad (2.21)$$

$$h_1 = \frac{qa'U_{\text{ext}}}{k_B T}. \quad (2.22)$$

The u_0 is the empirical constant characterizing the speed of oxidation given by the number of penetrating ions and their drift velocity. A typical value of u_0 is 10^4 cm/s. The W_i and V are the potential barriers of surface-interstitial and interstitial-interstitial sites, respectively. The k_B is the Boltzmann constant, T is the thermodynamic temperature, q is the charge of ion, a' is the half-width of the potential barrier, and U_{ext} is the externally applied voltage. Considering a certain saturation thickness of the oxide $h_L = U_{\text{ext}}/E_L$ above which the further growth is strongly reduced, the equation (2.20) can be integrated as

$$\frac{h_1}{h} = \ln\left(\frac{h_L^2}{h_1 ut}\right), \quad (2.23)$$

which is a logarithmic law of very thin oxide layer growth.

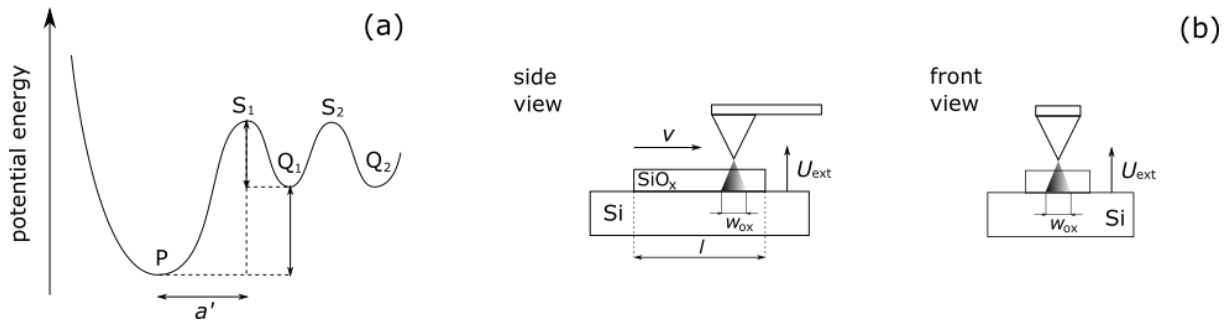


Figure 2.6: (a) The Cabrera-Mott model of very thin oxide layer potential energy as a function of ion distance from surface (point P) into the oxide potential maxima (S_1 , S_2) and stable interstitial sites (Q_1 , Q_2). (b) The scheme for explanation of Stiévenárd, Fontaine and Dubois [46] correction for local anodic oxidation.

Unlike the classical Cabrera-Mott oxidation theory where voltage is applied on a large area surface for a specific time, during the LAO the tip is being moved along the surface by the speed of v fabricating oxide with lateral width of w_{ox} . In order to estimate the time of the tip staying over a single surface point, Stiévenard, Fontaine and Dubois [46] suggested a substitution

$$t = \frac{w_{\text{ox}}}{v} \quad (2.24)$$

resulting in an indirect logarithmic dependence of the oxide thickness on the velocity

$$\frac{1}{h} = \frac{1}{h_1} \ln v + \frac{1}{h_1} \ln \frac{h_L^2}{h_1 u w_{\text{ox}}}, \quad (2.25)$$

and on applied voltage

$$h = \frac{\frac{qa'}{k_B T}}{\ln\left(\frac{h_L^2 v k T}{u w_{\text{ox}} q a'}\right) - \ln U} U. \quad (2.26)$$

The denominator in the relationship (2.26) according to experimentally reasonable values and logarithmic dependency is almost constant, and therefore the dependency on applied voltage is linear $h \approx U$.

We experimentally validated the theory of Cabrera-Mott with a substitution of Stiévenard, Fontaine, Dubois represented by equations (2.25) and (2.26) for LAO of Si(111) surface in commented

paper 3. The activation energy $W_i + V = 0.77$ eV was determined, which is between the values of activation energy of plasma oxidation (0.15 – 0.4 eV) and thermal oxidation (2 – 4 eV) [46]. Since the SiO_2 molar volume is approximately two times higher than Si, the oxidized structures protrude above the surface and its depth-height ratio is 1 – 1.4. The equations (2.25), (2.26) gives information about the oxide thickness, however, from the recent view of modern nanofabrication the lateral resolution, i. e. the width of the oxide w_{ox} is the most important. Related to this, we have proved the oxide width exhibits the similar indirect logarithmic dependency on speed and linear dependency on voltage where the smallest width (resolution) was 40 nm depending on the mentioned speed and voltage, and also on the radius of the tip (sharpness) which is given and on relative humidity (RH). Therefore, we decided to study the influence of the RH on LAO structures on GaAs in more detail in commented paper 4.

In commented paper 4, the decrease of LAO structure width with the decrease of relative humidity was experimentally proved. Too low values of RH lead to discharges in the oxidation process. Both of these effects are explained by considering the water-bridge between the AFM tip and surface (see Chapter 2.1) as the main source of hydroxide ions for LAO. Therefore, the water-bridge width as its variability with the RH is responsible for LAO structures width and its instability (Figure 2.7). In commented paper 4, the numerical finite element method (FEM) calculations of electric field distribution close to the AFM tip was performed without and with the presence of a water-bridge at different RH. It demonstrated how the water bridge (due to its high dielectric constant 81.0) pushes the equipotential lines deep into the native oxide layer (dielectric constant 3.5) increasing the intensity of the electric field as can be seen in Figure 2.7 (b), (c). As a consequence, the oxide ions are able to penetrate the oxide layer more efficiently. Therefore, the water bridge is not only a source of hydroxide ions, but works as a “lens” focusing the electric field into the native oxide under the water bridge.

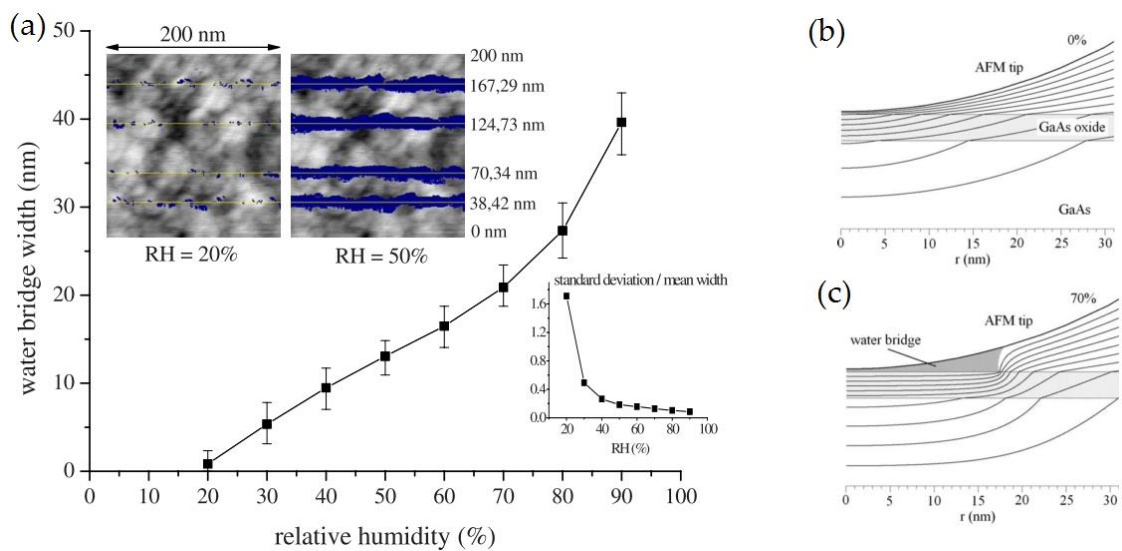


Figure 2.7: (a) The calculation of water-bridge width as a function of RH during the scanning of real GaAs surface by an AFM tip (left top insets) and the relative variability of its thickness (right bottom inset). (b, c) The influence of the water-bridge on the distribution of electric field under the AFM tip depicted in form of equipotential lines.

Finally, it is important to note that electric field also enhances the water condensation. Hans-Jürgen Butt citing [47] our commented paper 4 incorporated the influence of electrostatic energy density

$$u = \frac{\varepsilon\varepsilon_0}{2} E^2. \quad (2.27)$$

into the Gibbs energy deriving the extended Kelvin equation*

$$\ln\left(\frac{p_v^{*E}}{p_v^*}\right) = -\frac{V_m}{RT} \left[\frac{(\varepsilon - 1)\varepsilon_0 E^2}{2} - \frac{\gamma_{LV}}{r_K} \right]. \quad (2.28)$$

Here, the p_v^{*E} is the reduced saturation vapor pressure at an applied electric field E . Then it is obvious that the higher electric field can strongly enhance water condensation, or, simply said, it increases the water bridge dimensions at the same level of relative humidity.

Here, it is possible to summarize the additions to the thermodynamic description of water-bridge condensing between the AFM tip and surface in ambient conditions. The basic behavior is characterized by the Kelvin-Young-Laplace equation (2.1), however, for nanometer dimensions the corrections of surface tension should be included (2.5). In the presence of an electric field, the Kelvin equation in its extended form should be considered (2.28). This classical thermodynamic treatment can of course be overcome by the atomic calculations using molecular dynamics, or Monte-Carlo simulations, however, even these approaches are nowadays limited by the performance of computers, and also by a proper setting of inter-atomic potentials.

From an application point of view, the utilization of LAO is relatively wide. The main advantages here in comparison with the massively used electron beam lithography or photolithography is the absence of a resist, much less lithographic steps and really only a fine superficial influence on the sample. In comparison with that, the electrons in EBL and ions from reactive ion etching (RIE) following the PL influence deeper layers of surface. On the other hand, the disadvantages consist in the need of a conductive surface and impossibility to use in mass production. The LAO is seemingly useful only for preparation of oxide nanostructures, however, these structures can be easily transformed into metallic nanostructures as we have demonstrated in commented paper 5. Here, the LAO prepared oxide patterns on Si(100), and GaAs(100) were used for selective growth of gallium and cobalt, which is based on different surface functionalization and hydrogen passivation.

* Compare with the original Kelvin equation (2.1).

3 A brief overview of graphene

Graphene represents a two-dimensional (2D) one-layer thick crystalline form of carbon atoms with hexagonal “honeycomb” symmetry (Figure 3.1 a, b). It complements the family of carbon allotropes (Figure 3.1 d-g) which also includes three-dimensional (3D) forms: diamond, graphite (known from ancient times), one-dimensional (1D) carbon nanotubes, and zero-dimensional (0D) fullerenes (discovered in [48-49] 1991 and [50] 1985, respectively). Although the simplest of all allotropes, graphene was experimentally discovered and recognized as an actually existing material at the latest in [51] 2004 by Andrej K. Geim, and Konstantin S. Novoselov. Originally, graphene was not believed to exist, because of the thermodynamic prediction of Landau and Peierls, it should be immediately torn off due to thermal oscillations*. In spite of this, Geim and Novoselov prepared graphene by the most primitive method using the peeling of graphite (Figure 3.1 e) by Scotch-tape which is called mechanical exfoliation [51]. It is possible, since graphite consists of graphene layers holding together by weak van der Waals forces†.

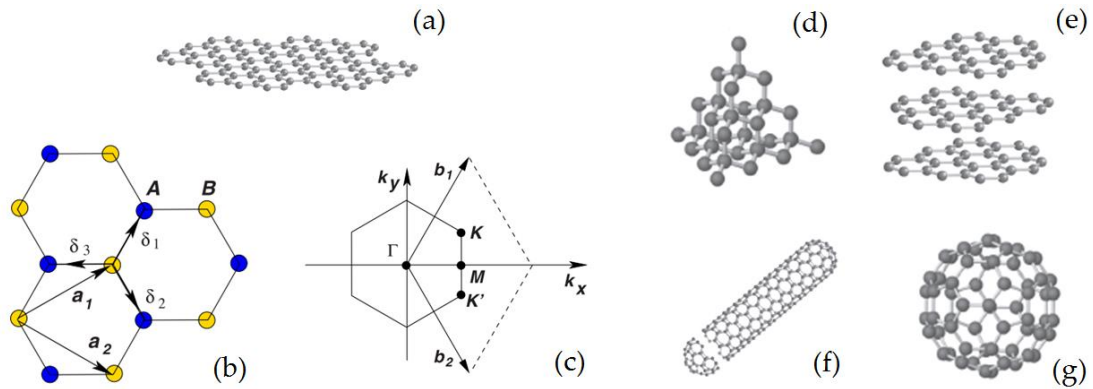


Figure 3.1: (a) Graphene, its (b) real-space and (c) reciprocal-space lattice grid [52]. Other carbon allotropes: (d) diamond, (e) graphite, (f) carbon nanotube, and (g) fullerene.

The hexagonal graphene structure can be seen as a triangular lattice with a basis of two atoms per unit cell (blue and yellow in Figure 3.1 b). The graphene lattice vectors can be written as [52]

$$\vec{a}_1 = \frac{a}{2}(3, \sqrt{3}), \quad \vec{a}_2 = \frac{a}{2}(3, -\sqrt{3}), \quad (3.1)$$

where $a = 1.42 \text{ \AA}$ is the carbon-carbon distance and the surface concentration of carbon atoms in graphene is $3.8 \times 10^{15} \text{ cm}^{-2}$. Graphene is extremely thin and its thickness can be compared with 0.335 nm which is the distance between two graphene layers in graphite, however, its experimental thickness is often hardly estimated depending on the measurement method. The reciprocal-lattice vectors \vec{b}_1, \vec{b}_2 are given by [52]

$$\vec{b}_1 = \frac{2\pi}{3a}(1, \sqrt{3}), \quad \vec{b}_2 = \frac{2\pi}{3a}(1, -\sqrt{3}). \quad (3.2)$$

* It was later proved that the stability of graphene against thermal fluctuations is ensured by its corrugations.

† The same peeling of graphite layers allowed by weak inter-layer van der Waals forces has been used since 1564 whenever we write with an ordinary pencil.

Graphene has unique and extraordinary properties. Since all the atoms are also surface atoms, graphene has the largest specific surface area (SSA) 2 630 m²/g (for comparison the carbon nanotubes SSA is 1000 m²/g). Further, the graphene is biocompatible and easily chemically functionalized [53]. No gas can penetrate the graphene membrane [54]. Graphene should be the strongest material [55-56] with an extreme Young's modulus of* 1 TPa (Young's modulus of steel 0.2 TPa) and intrinsic strength of 130 GPa which is caused by a huge covalent binding energy 7.6 eV of carbon atoms in graphene. As a monolayer, the graphene is particularly transparent, absorbing only $\pi\alpha \approx 2.3\%$ of the incident light [57] (in the infrared limit, where $\alpha = 1/137$ is a fine structure constant). The thermal conductivity of graphene is dominated by phonons and has been measured to be very high about 5000 Wm⁻¹K⁻¹ at RT [58] and 710 Wm⁻¹K⁻¹ at 500 K (for comparison the copper thermal conductivity is 401 Wm⁻¹K⁻¹) [59].

Graphene has four valence electrons. Three of them form bonds with neighboring atoms in the plane, and the fourth electron in the 2p_z state perpendicular to the plane is responsible for the conductivity of graphene (sp² hybridization)[†]. Graphene band structure was calculated theoretically by Philip R. Wallace in 1946 [61] long before its discovery as an elementary building block of graphite using tight binding[‡] model of 2p_z orbitals of the nearest and next nearest carbon atoms in a grid with the Hamiltonian [52]

$$\hat{\mathcal{H}} = -t \sum_{\langle i,j \rangle, \sigma} (\hat{a}_{\sigma,i}^\dagger \hat{b}_{\sigma,j} + \text{H. c.}) - t' \sum_{\langle\langle i,j \rangle\rangle, \sigma} (\hat{a}_{\sigma,i}^\dagger \hat{a}_{\sigma,j} + \hat{b}_{\sigma,i}^\dagger \hat{b}_{\sigma,j} + \text{H. c.}), \quad (3.3)$$

where $\hat{a}_{\sigma,i}^\dagger$ ($\hat{a}_{\sigma,j}$) are the operators annihilating (creating) an electron with spin σ ($\sigma = \uparrow, \downarrow$) on site \vec{R}_i on sublattice A (and an equivalent definition is used for sublattice B, Figure 3.1 b), $t \simeq 2.8$ eV is the nearest neighbor hopping energy (between different A and B sublattices), $t' \simeq 0.1$ eV is the next nearest-neighbor hopping energy (between the same sublattices), and H. c. is the Hermitian conjugate. Using the Hamiltonian (3.3) the energy bands can be found in a form [60]

$$E_{\pm}(\vec{k}) = \pm t \sqrt{3 + f(\vec{k})} - t' f(\vec{k}), \quad (3.4)$$

where

$$f(\vec{k}) = 2 \cos(\sqrt{3}k_y a) + 4 \cos\left(\frac{\sqrt{3}}{2}k_y a\right) \cos\left(\frac{3}{2}k_x a\right). \quad (3.5)$$

The plus sign corresponds to the conductive band and the minus sign the valence band as depicted in Figure 3.2 (a). The dispersion relation (3.4) shows the graphene is a semiconductor with zero band gap in K , K' points of Brillouin zone. The physics of charge carriers close to the K , K' points which are

* The value was estimated by pushing the AFM tip into the suspended graphene membrane similarly to force-distance spectroscopy measurement (see Chapter 2 – FDS and Figure 2.2). It was also necessary to solve the problem of strength comparison between the two-dimensional graphene when the standard strength tests are designed for three-dimensional materials.

[†] On the other hand, all four valence electrons in diamond create bonds in sp³ hybridization, and the diamond is non-conductive.

[‡] The electrons in a tight-binding model are tightly bound to the atom they belong to and the interaction with states and potentials of other atoms of crystal is limited. Therefore, the wave function of the electron is rather similar to the atomic orbital of the free atom to which it belongs.

called Dirac's points (sometimes also devil's points) is different in comparison with standard semiconductors (e. g. Si, GaAs, Ge), since there is a linear dispersion here (Figure 3.2 b)

$$E(k) \approx \pm \hbar v_F |\vec{k} - \vec{K}|, \quad (3.6)$$

where $v_F = 3ta/2 \approx 10^6$ m/s is the Fermi velocity and \vec{K} is the vector pointing to the K (Dirac's) point. The most important consequence of linear dispersion (3.6) is that the velocity of charge carriers is equal to Fermi velocity v_F and does not depend on momentum ($\vec{p} = \hbar\vec{k}$) or energy. The situation is different compared with standard semiconductors whose dispersion relation can be approximately described by a parabolic dispersion $E(k) \approx \hbar^2 k^2 / (2m)$ where the charge carrier velocity depends on momentum and energy; $v = \hbar^{-1}(dE/dk) = \hbar k/m$, where m is the charge mass. Therefore, the speed of charge carriers close to Dirac's points in graphene is constant and high even at $\vec{k} = \vec{K}$ resulting in the high mobility of graphene. It is also obvious that the charge carriers in graphene mimic the relativistic particles with zero mass, since the linear dispersion in graphene reminds the relativistic dispersion in the form of

$$E = \sqrt{(pc)^2 + (m_0c^2)^2}, \quad (3.7)$$

where p is momentum, c is the speed of light and m_0 is rest mass and for zero rest mass $m_0 = 0$ the relativistic relationship (3.7) is almost equal to linear dispersion (3.6) with effective speed of light $c = v_F$. Moreover, in graphene, the Klein paradox [62] is observed which refers to the enhanced tunneling probability of relativistic (fast moving) particles (following the Dirac's equation) approaching to unity as the height of potential barriers is in order of electron mass m_0c^2 . As a consequence, graphene is always conductive with a minimum conductivity $(4e^2/h)$ [63].

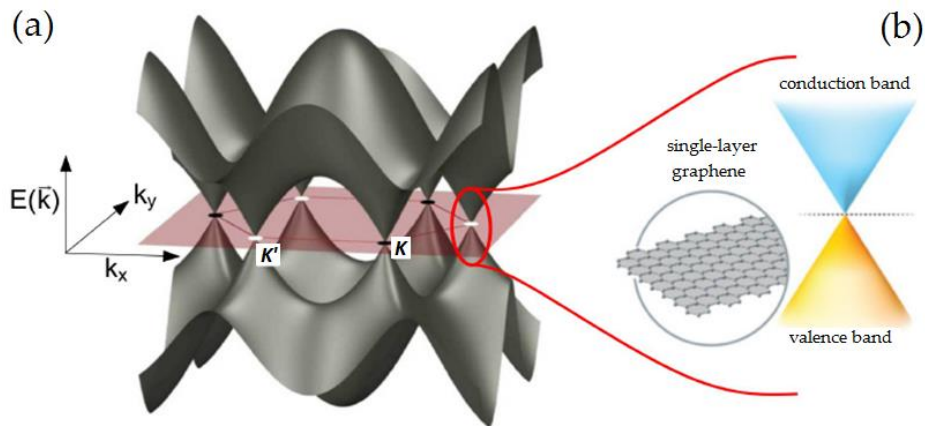


Figure 3.2: (a) Graphene electronic bands (b) and their detail close to the Dirac's point.

Graphene exhibits a strong ambipolar field effect [64] consisting in a change of charge density and consequent resistivity (Figure 3.3 - detail) as a function of gate voltage in field effect transistor multi-terminal Hall bar geometry (Figure 3.3). The Fermi level of intrinsic graphene crosses the Dirac point and there are no predominant charge carriers. Applying the positive/negative gate voltage moves the Fermi level above/below the Dirac point and the majority charge carriers will be electrons/holes. The surface charge density n_s induced by gate voltage U_G is given as

$$n_s = \frac{\epsilon_0 \epsilon}{et} U_G, \quad (3.8)$$

where ϵ_0 is the dielectric constant of vacuum, e is the elementary charge, ϵ and t is the dielectric constant and thickness of the underlying isolating layer, respectively. For the SiO_2 isolating layer with a thickness of 300 nm and dielectric constant of 3.9, it is possible to induce charge carrier surface concentrations up to 10^{13} cm^{-2} by gate voltage of 100 V resulting in a hundredfold reduction of resistivity.

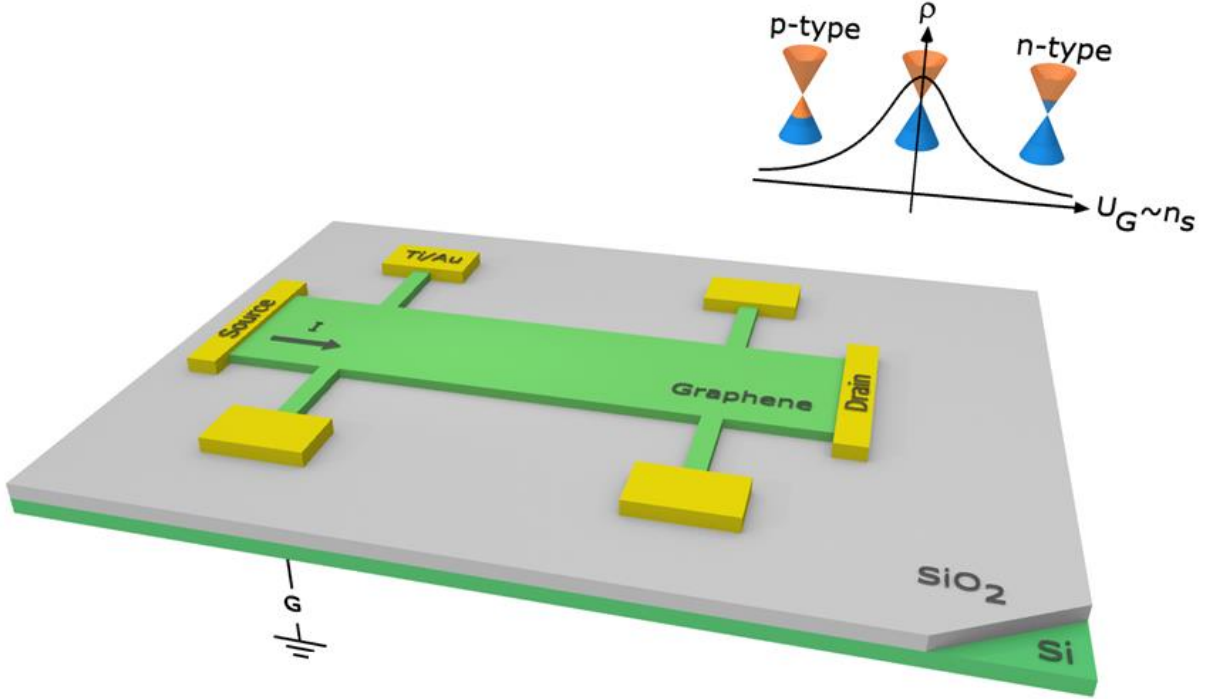


Figure 3.3: Graphene Hall bar structure and ambipolar electric field effect due to the position of Fermi level related to Dirac point.

The intrinsic mobility of graphene is theoretically limited only by scattering on acoustic phonons to $2 \times 10^5 \text{ cm}^2\text{V}^{-1}\text{s}^{-1}$ (higher than any known semiconductor), and to $4 \times 10^4 \text{ cm}^2\text{V}^{-1}\text{s}^{-1}$ by SiO_2 substrate surface phonons [65] (best InAs field effect transistors [66]). However, the experimentally measured value is lower $15 \times 10^3 \text{ cm}^2\text{V}^{-1}\text{s}^{-1}$ and above the temperature of 100 K is further reduced [67]. High mobility allowing ballistic transport makes graphene interesting for devices exhibiting quantum mechanical behavior even at room temperature [68]. In a perpendicular magnetic field B , the graphene allows undisturbed Landau levels (LL) with an energy of

$$E_n = \text{sgn}(N)v_F\sqrt{2e\hbar|N|B}, \quad (3.9)$$

where N is the electron or hole LL index. As a consequence, the half-integer quantum Hall effect and Shubnikov-de Haas oscillations occur in the measurement of transversal and longitudinal resistivity as a function of applied magnetic field (in Hall bar structure geometry shown in Figure 3.3) [66-68].

The previous properties make graphene very promising for high-frequency field effect transistors operating up to 100 GHz [70–72]. The situation is worse in integrated circuits, especially in their logic elements, since, the Klein paradox ensuring minimum conductivity prevents achieving a complete off-state, and limits the on-off ratio up to 10^3 . In order to overcome this problem, the

graphene band gap must be opened by different technological processes breaking the graphene symmetry like the patterning graphene into graphene nanoribbons [73], quantum dots [74], manufacturing related single electron transistors (SET) [75], modification by hydrogen [76], fluor [77], nitrogen [78], or by the utilization of bilayer graphene [78-79].

Due to a high sensitivity to adsorbants and biocompatibility, graphene can be used in extremely sensitive gas sensors [81] or biosensors whose principle of working is based on resistivity changes of graphene field effect transistors (GFET in Figure 3.3) [82] or changes of enhanced surface plasmon resonance (SPR) at the interface of graphene/silver, graphene/gold interface [83] caused by different biological substances adsorbing on functionalized graphene surface. As a transparent and conductive material, it is very well suitable for optoelectronic devices: solar cells [84], liquid crystal displays [85], touch screens, and ultrafast photodetectors [86]. Besides electronic and optoelectronic applications, graphene has been successfully used as a transparent support for observation in transmission electron microscopy (TEM) [87, 88] or to improve the properties of composite materials [89].

3.1 Graphene CVD fabrication on copper foil

The most serious problem for using graphene in applications is its quality on large industrial scale level. This problem was addressed by the “godfather of graphene”, A. H. Castro Neto, at the Graphene week in Barcelona in 2017 explaining the graphene properties which have been observed for layers composed from 1 to 5 monolayers perfectly arranged carbon atoms, however, the current industry produce layers composed of more than 10 poorly arranged monolayers of carbon atoms which is only a graphite.

There are about four commonly used methods to produce graphene differing in quality and costs for mass production. In terms of quality, the size of crystal grains l and charge carrier mobility μ is evaluated. The best quality is achieved by original mechanical exfoliation ($l > 1000 \mu\text{m}$, $\mu > 2 \times 10^5 \text{ cm}^2\text{V}^{-1}\text{s}^{-1}$) [90] and further deteriorates at chemical vapor deposition ($l = 1000 \mu\text{m}$, $\mu > 10^4 \text{ cm}^2\text{V}^{-1}\text{s}^{-1}$), silicon carbide (SiC) decomposition ($l = 50 \mu\text{m}$, $\mu > 10^4 \text{ cm}^2\text{V}^{-1}\text{s}^{-1}$), and chemical (or liquid phase) exfoliation ($l < 0.1 \mu\text{m}$, $\mu > 10^2 \text{ cm}^2\text{V}^{-1}\text{s}^{-1}$) [91, 92]. Moreover, both exfoliation methods produce only individual flakes, which is not suitable for planar mass technology. Therefore, chemical vapor deposition (CVD) of graphene seems to be the most suitable method in terms of quality and mass production.

CVD growth of graphene catalyzed by metallic substrate is an effective way to fabricate high-quality large-area graphene [93]. Copper is the most promising substrate in comparison with cobalt and nickel due to low carbon solubility in copper and low concentration of defects on copper grown graphene [94, 95]. Graphene CVD growth on a copper foil is based on the decomposition of methane into carbon forming graphene and hydrogen leaving the surface at high temperature, which can be realized by the procedure described by Li *et al.* [91]. Here, the Cu foil is heated up to 1000 °C in $\text{H}_{2(\text{g})}$ atmosphere (pressure 5.4 Pa, flow 2 sccm) to clean and anneal the copper, and then the $\text{CH}_{4(\text{g})}$ is introduced (67 Pa, 35 sccm) for graphene formation on the copper. Generally, to provide further analysis, the graphene must be transferred to an isolating surface (mostly SiO_2 on Si). For this purpose the PMMA-assisted wet transfer method is used as follows. First, the graphene on copper is coated with poly-methyl methacrylate (PMMA) by a spincoating method. Second, copper is dissolved by wet etching in an iron nitrate solution. Finally, the graphene with PMMA is lifted from the solution by a suitable wafer [96].

The CVD growth of graphene on a copper foil was improved in commented paper 6 by introducing a template stripping method [97] for fabrication of ultra-smooth copper foils. The foils are

prepared by ion beam assisted deposition (IBAD) from a high purity copper target in a home-built high vacuum setup based on Kaufman broad ion beam sources [97] onto Si/SiO₂ substrate (Figure 3.4 a-c). Further, the copper supporting layer is deposited by electrolysis in a mixture of sulfuric acid (H₂SO₄) and copper sulfate (CuSO₄) (Figure 3.4 d-e). The roughness of the copper surface is limited only by the smoothness of the SiO₂ template, and was below 0.6 nm, i. e. almost two orders of magnitude lower than the one observed on commercial Cu foils (Figure 3.4 f). The Cu surface also exhibits a low level of oxidation, low concentration of defects and contaminants resulting in the growth of a high quality graphene.

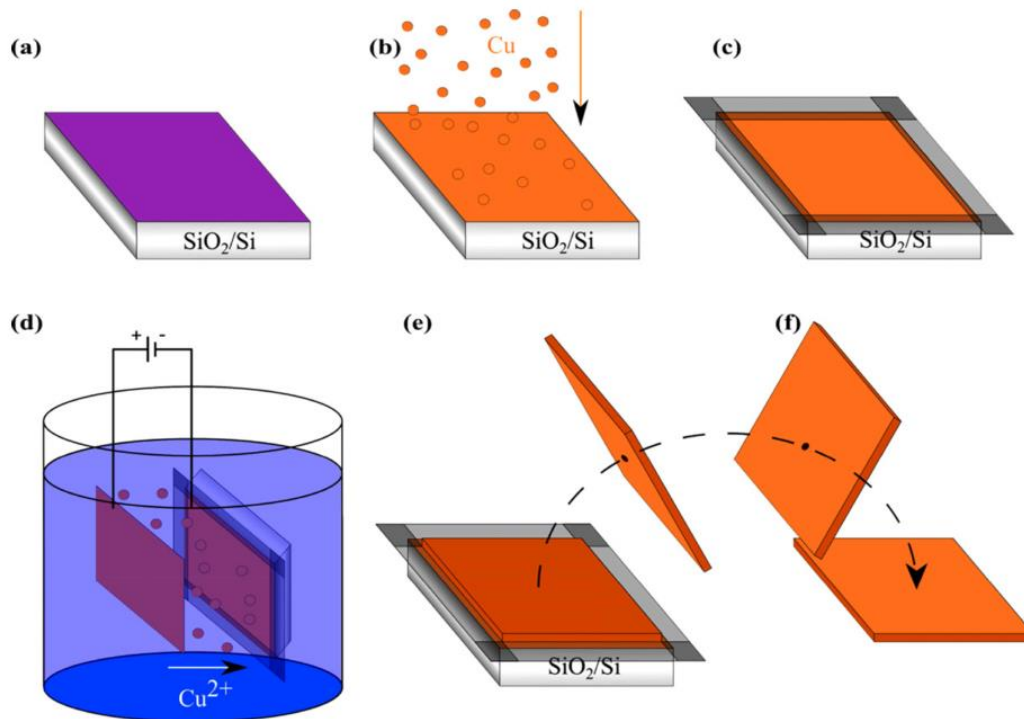


Figure 3.4: Preparation of a copper foil by template stripping: (a) Si/SiO₂ template, (b) deposition of copper, (c) protection of the edge areas, (d) electrolysis of a thick supporting Cu layer, (e) peeling-off the prepared foil, (f) top Cu surface is defined by template [98].

The mobility of graphene prepared on ultra-smooth Cu foils was quite high $3600 \text{ cm}^2\text{V}^{-1}\text{s}^{-1}$ in comparison with graphene on commercial copper foils $1200 \text{ cm}^2\text{V}^{-1}\text{s}^{-1}$ (at electron surface density of $2 \times 10^{12} \text{ cm}^{-2}$). The value is still below the state-of-the-art values beyond $10^4 \text{ cm}^2\text{V}^{-1}\text{s}^{-1}$ reported for CVD graphene when the graphene growth process (domain sizes and shapes) is optimized [99]. However, in the experiment the graphene fabrication was not been optimized, and the attention was paid only to the influence of Cu foil. On the other hand, generally, at less ideal conditions, CVD graphene exhibits a lower mobility [91] $4050 \text{ cm}^2\text{V}^{-1}\text{s}^{-1}$, and line defects at grain boundaries can the mobility fall down to the value [100] $1100 \text{ cm}^2\text{V}^{-1}\text{s}^{-1}$ which corresponds to our values. Moreover, we have measured visible Shubnikov-de Haas oscillations on the graphene prepared on ultrasmooth metallic Cu foil at low temperatures (2 K) and high magnetic fields (9T), proving well defined Landau levels [101].

3.2 Graphene and gallium

As has been mentioned, graphene itself stands out with a number of remarkable features, however, some of its properties are suitable to improve in order to achieve practical applications. One way is to combine graphene with other 2D materials into heterostructures. Here, for example, the hexagonal boron nitride (hBN) is used as an insulating substrate for conductive graphene, and materials from transition metal dichalcogenides like molybdenum disulfide (MoS_2) is used to incorporate a band gap for high enough on-off ratio in nonvolatile memory [102]. Another way is a deposition of individual atoms onto/into a graphene grid. Commented paper 7 focused on the change of electronic properties as a function of gallium (Ga) atoms deposited on a graphene surface. The motivation consists in the following facts moving graphene further to practical applications: (1) Ga nanoparticles can tune the localized surface plasmon resonance (LSPR) of graphene [103], (2) Ga enhances the reactivity and sensitivity of graphene on gas [104], (3) Ga can also be used as a catalyst for graphene synthesis [105], and (4) Ga enhances the surface-enhanced Raman scattering useful for detection of biomolecules [106].

During the experiment presented in commented paper 7, a low dose deposition of Ga (< 4 ML) on CVD graphene was performed in UHV (10^{-7} Pa) while the transport properties in FET geometry were measured in-situ. For Ga concentration up to $39.6 \times 10^{12} \text{ cm}^{-2}$ (* corresponding to 0.04 ML) graphene proved to be strongly n-doped with an efficiency of 0.64 electrons per one Ga atom. On the other hand, above this concentration, graphene started to be less n-doped (removing the electrons). Such a behavior is interesting in view of utilization of Ga for electronic and plasmonic applications. However, the sudden reversal of graphene doping is surprising. In order to understand the physics behind, density functional theory (DFT) calculation was used. It has been proved the individual Ga atoms dope graphene more than Ga layers and clusters as a consequence of utilization of electrons to bind Ga atoms themselves. To understand the argumentation in commented paper 7, the following text will briefly describe the DFT calculations and our arguments relating to this problem.

Density functional theory is a theoretical and computational approach for finding the energetic ground state of a system. DFT is based on an expression of the whole energy in the form of functional of electron density designed in agreement with best practices of quantum-mechanics and finding minimum of the functional using variational principles. Hohenberg and Kohn [107] have proved that the functional is a definite functional of electron density and acquires its minima for electron density corresponding to the quantum-mechanical ground state

$$E_0 = \min(E[n(\vec{r})]), \quad (3.10)$$

where E_0 is the ground state, $E[n(\vec{r})]$ is the functional of density, and $n(\vec{r})$ is the electron density that can be further expressed as

$$n(\vec{r}) = \sum_i^{\text{occupied}} |\psi_i(\vec{r})|^2. \quad (3.11)$$

Here, $\psi_i(\vec{r})$ are the individual electron wave-functions and the sum is performed over all the occupied states. The introduction of electron density depending only on 3 space coordinates is the main advantage in comparison with the multi-electron wave function $\psi(\vec{r}_1, \dots, \vec{r}_N)$ depending on $3N$ coordinates of all the N electrons used in the Born-Oppenheimer approximation[†]. This way, the DFT

* Here, the one Ga monolayer (1 ML) on graphene is equal to the Ga concentration of $9.815 \times 10^{14} \text{ cm}^{-2}$ calculated by density functional theory (DFT calculation – see below).

[†] In the most general case, the motion of electrons and nuclei has to be considered. The Born-Oppenheimer approximation (BOA) is based on the fact that the motion of lightweight electrons is relatively higher in

reduces the dimensionality of the problem from $3N$ to 3, significantly reducing the computational difficulty.

DFT is based on the proposal of an appropriate energy functional describing the physical reality. A suitable form is [108]

$$E[n] = -\frac{1}{2} \sum_i \int \psi_i^* \vec{\nabla}^2 \psi_i d\vec{r} + \int V_{\text{ext}}(\vec{r}) n(\vec{r}) d\vec{r} + \frac{e^2}{2} \int \frac{n(\vec{r}) n(\vec{r}')}{|\vec{r} - \vec{r}'|} d\vec{r} d\vec{r}' + E_{\text{XC}}[n], \quad (3.12)$$

where the first term describes the kinetic energy of electrons, the second term is the electron-nuclei electrostatic potential energy where the nuclei contribution is expressed as external potential, the third term is the electrostatic potential energy between electrons based on the Hartree approximation* $V_{\text{H}}[n]$ and the fourth term is the so called exchange correlation functional incorporating the energy contribution of electron spins. The proposal of the exchange correlation term can stand out in different approximations, from the most simple local density approximation [108] (LDA) that can be expressed in an analytical form to the more complicated analytically indescribable forms. In commented paper 7, the general gradient approximation [109] (GGA) was used taking, in addition to density, also its gradient. Finding the minimum of the functional described by the expression (3.12) using variational Euler-Lagrange equations results in a system of equations called the Kohn-Sham equations [108]

$$\left[-\frac{1}{2} \vec{\nabla}^2 + V_{\text{ext}}(\vec{r}) + \frac{\delta V_{\text{H}}[n]}{\delta n} + \frac{\delta E_{\text{XC}}(n)}{\delta n} \right] \psi_i(\vec{r}) = \varepsilon_i \psi_i(\vec{r}), \quad (3.13)$$

which is an eigenvalue equation for eigenstates of one-electron wave functions $\psi_i(\vec{r})$ and eigenvalues ε_i . Since the electron density n is expressed by one-electron wave functions $\psi_i(\vec{r})$ described by (3.11), the equation (3.13) needs to be solved by self-consistent iteration. The DFT numerical calculation in commented paper 7 was performed by Vienna ab-initio simulation package (VASP) which is supported also by molecular dynamics (MD) for finding relaxed atom positions [110–112]. Using this combination, the energy, energy bands and consequent arrangement of atoms can be determined.

comparison with the motion of heavyweight nuclei, therefore, BOA assumes the motion of electrons in static distribution of nuclei to answer the question of electron-dynamics.

* The Hartree approximation replaces the electrostatic interaction expressed as a sum of individual interactions between electrons by a more simple dependency of electrostatic energy on electron density expressed in the form of a functional (The Hartree approximation uses very similar concepts like the described DFT).

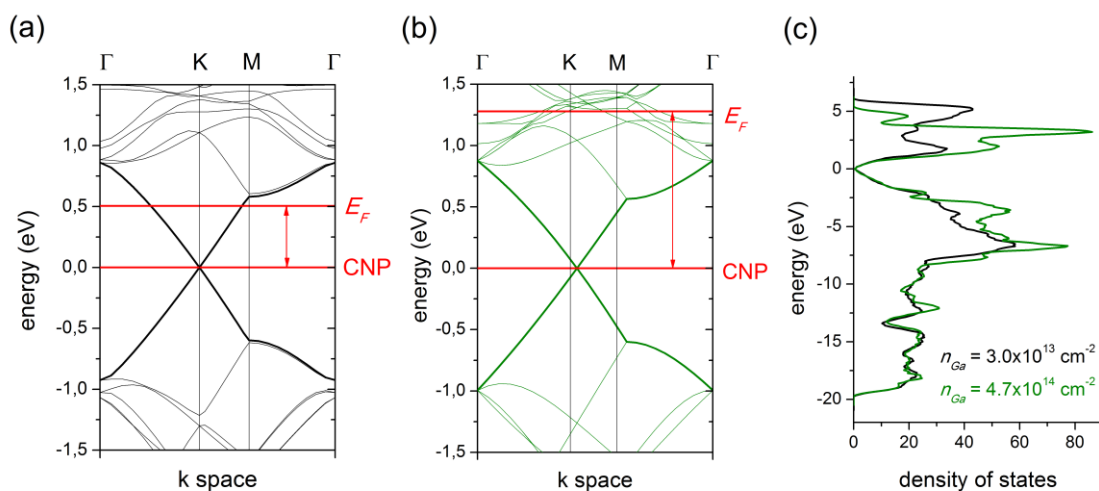


Figure 3.5: (a, b) Graphene band structure and (c) density of states at two distinct low concentrations of Ga atoms corresponding to 0.03 ML (a and black curve in c) and 0.50 ML (b and green curve in c) Ga coverage.

The DFT calculated adsorption energy of a Ga atom on a graphene surface is approximately* 1 eV and the equilibrium distance of a Ga atom from a graphene plane is 0.222 nm. The adsorbed Ga atoms do not open a band gap in graphene, and n-dope the graphene, since the Fermi level is above Dirac (charge neutrality) point (CNP) (Figure 3.5 a, b). In density of states (DOS), an increase of states close to CNP can be observed at higher Ga concentration (Figure 3.5 c). The increase of Ga concentration results in a higher n-doping of graphene until the first Ga monolayer (Ga coverage 1 ML) is formed when the doping is zero (Figure 3.5 a). Such a result of calculation can be understood as a consequence of a lower binding of Ga onto the graphene in case of a complete Ga monolayer. The adsorption energy per one individual Ga atom on graphene in a completely formed first Ga monolayer is only 8 meV (more than 100x less than for individual Ga atom) and the distance of the Ga monolayer from the graphene plane is 0.404 nm (almost two times more than for an individual Ga atom). Further, the completion of a second and third Ga monolayer does not significantly change the adhesion energy and the distance of the first Ga layer from graphene. Simply said, after a completion of the first Ga monolayer, the electrons are involved in the binding of Ga atoms together, and therefore, there are almost no electrons to create Ga-graphene bonds and dope the graphene. While the first Ga atoms strongly dope graphene by electrons, the next ones take a part of the electrons from graphene back, and at a higher coverage Ga no more dopes the graphene (Figure 3.6 b).

* In the most stable central position – above the middle of the graphene ring the adsorption energy is 987 meV, and in the least stable top position – above the graphene carbon atom the adsorption energy is 941 meV.

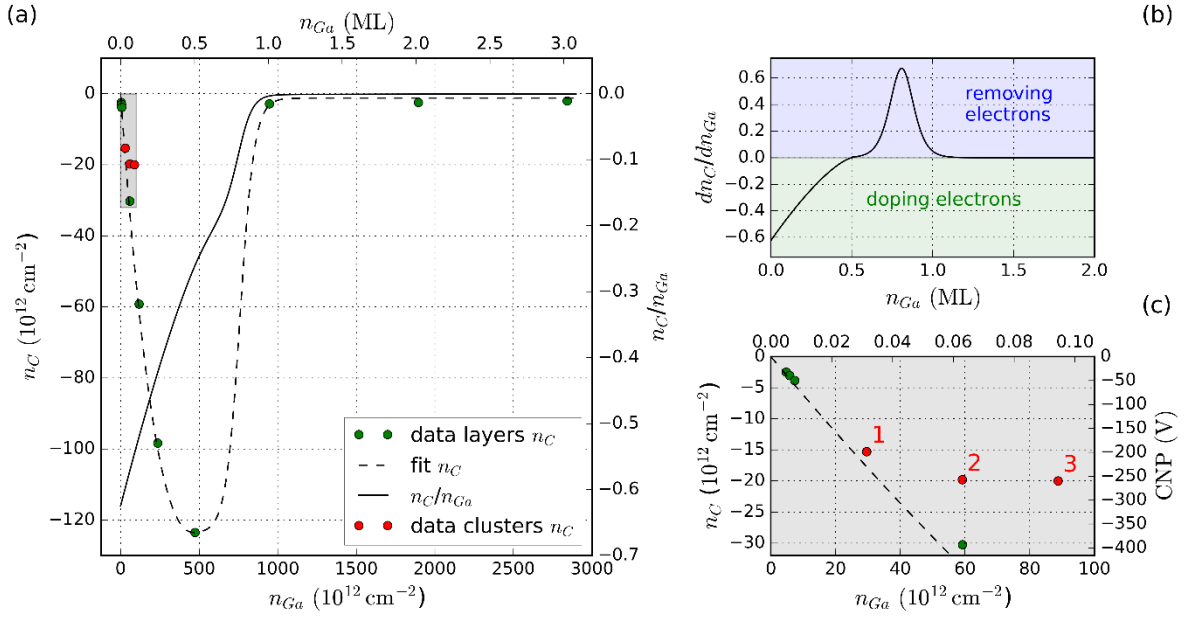


Figure 3.6: (a) Concentration of charge carriers (electrons) in graphene as a function of Ga concentration calculated by DFT for layer growth (green circles) and for clusters composed of 2 and 3 Ga atoms (red circles). (b) The change of graphene charge carrier concentration caused by adding one Ga atom as a function of Ga coverage. (c) Detail of (a) for Ga clusters composed of 2 and 3 atoms.

In DFT calculations it is possible to increase the concentration of ideally and evenly distributed Ga atoms on graphene until the completion of the first, second, third and other monolayers as has been done. However, this calculation helped us to understand the influence of Ga-Ga bonds by shortening their distances on the doping, in real room temperature conditions the Ga atoms can diffuse* along the graphene surface forming clusters and islands which has also been supported by the observation of island-like growth in commented paper 7. Due to clusters formation, the decrease of graphene doping can occur at lower Ga concentrations than in case of evenly distributed ideal layer growth that has also been supported by the DFT calculation. In Figure 3.6 (c) a significant slowdown of doping can be observed when clusters consisting of 2 and 3 Ga atoms are formed (red circles) in comparison with evenly distributed Ga atoms at the same concentration. However, it has not been published yet, recently, we have results for clusters up to 8 atoms proving a complete stop of doping after the formation of 4 or 6 atoms in clusters in case of a calculation without or with the incorporation of van der Waals corrections, respectively.

Considering the previous model of clusters formation and its influence on doping, the point of return in resistivity-back gate voltage measurement is a sign of a sufficiently large clusters formation. This phenomenon has two interesting consequences. Firstly, it is a point beyond which the additional doping is no longer relevant, and, secondly, it can help to estimate the diffusion length of Ga along the graphene surface. The second consequence was further developed in commented paper 7, where the diffusion length was estimated following the proposed theory that the return point in the experiment occurs at the formation of 3 atom clusters predicted by DFT. The estimated values incorporating only experimentally measured surface resistivity, DFT calculation or their combination ranged from approximately 1 to 2.2 nm which is a good agreement.

* The energy barrier of the Ga diffusion on a graphene surface calculated by DFT is only 106 meV.

4 Great unification – graphene, biosensors, sensors and SPM

The last but one chapter of the habilitation thesis has a character of a future vision where the author would like to aim his scientific interest in the future. Since all the aforementioned aims somehow combine graphene and scanning probe microscopy, I dared to call the chapter great unification. Hopefully, I will not offend theoreticians in the area of the grand unified theory (GUT) or even the theory of everything (TOE) by the illustrating but just playful similarity of the chapter title. The connection in this vision has a much more modest intentions, namely:

- 1) to understand how the charge flow on graphene/SiO₂ or on graphene/hydrogenated graphene influences the functionality of biosensors
- 2) to use the graphene based water molecules sensor to estimate the SPM water bridge dimensions
- 3) to use SPM or STM to observe a real arrangement of Ga clusters on graphene surface to support our indirect theory about the formation of clusters of Ga

The first intention is closely related to Chapter 2.2 where the first pioneering KPFM measurement was used to observe the charge transport on a graphene/SiO₂ system at different relative humidity. Since the recent graphene based biosensors operate in ambient conditions or in a water solution and their active graphene parts and passive isolating parts are directly exposed to environment water molecules, their functionality is influenced by charge transport across the graphene/isolating interface. In spite of this problem that is generally considered as a solved, however, that can be the cause of hysteresis and unpredictable sensor behavior, the attention is paid only to a better functionalization of graphene or increase the precision of transport response measurement. In this respect, the simultaneous measurement of biosensor resistivity sensor by a standard transport measurement and charge distribution evolution measured by KPFM in a controlled environment could help us to understand the physics behind the sensor response, to uncover the potential problems of specific types of biosensors, and finally improve their design.

The second intention is closely related to Chapter 2.1 and partly to Chapter 2.3 where the interesting problems of nano-volume water embodied by the SPM water-bridge were addressed. Since graphene itself proved to be a very sensitive sensor of water, and also the graphene based sensor utilizing the surface conductivity of SiO₂ was used to design the most sensitive water sensor that has ever been made [33], the author of this work believes that the graphene based water sensor could be used to map the real dimensions of water in an SPM water bridge better than any method used so far and give us valuable information for our understanding of water in nanovolumes.

The third intention is closely related to chapter 3.2 where the influence of gallium on graphene electronic properties was discussed. However, our theory based on clusters formation appears to be probable, the experimental part is leaning on an indirect transport properties measurement, and despite of this theory's logical simplicity and perhaps beauty, there is no direct experimental evidence, however, it might be done by UHV STM measurement. We believe such a measurement, despite of its complications (atomic resolution on not very well ordered CVD graphene on isolating SiO₂), could dispel our last doubts about the truth can sometimes be beautifully simple, which I believe is also the sense of science.

5 Conclusion

The background of the entire habilitation thesis has two fundamental questions. First, why the SPM technology and graphene material have had such a strong impact in modern surface physics, and second, what is the author contribution to this field.

The first question has been answered in introduction and in brief overviews chapters. In a short summary, both SPM and graphene have opened two big doors into research and application of surfaces. SPM has opened the wide door of studying surfaces down to individual atoms and graphene has opened the other fabrication door of really two-dimensional self-standing one-atom thick monolayers which are the very embodiment of the surface. The importance of SPM and graphene in today's surface physics is indisputable and confirmed.

The second question about the contribution of the author has been answered in the chapters following the brief introductions. Here, a transition from general SPM and graphene problems to more specific issues solved by the author has been performed. These chapters deal with the atomic force microscopy water-bridge, Kelvin probe force microscopy (KPFM) mapping of a charge transport at different RH, local anodic oxidation fundamentals and applications in selective growth, graphene fabrication and doping of graphene by gallium. In this respect, author's scientific contribution covers the topics more focused either on physical theory or on experiment (applications), but also on the borders of both. At the same time, the author has been contributing to the research field of nanotechnology for 15 years of his pedagogical activities at the Faculty of Mechanical Engineering, BUT which is briefly mentioned at the end of this conclusion.

Author's contribution to the physical theory mainly covers the following areas.

First, the complete thermodynamical model of the nano-volume AFM water-bridge explaining more precisely its shape and the forces acting on the tip in atmospheric conditions was suggested. The idea of surface tension correction has never been used in case of the SPM tip nano-volume water-bridge, however, excellent physical chemists as Josiah Willard Gibbs and Richard Chace Tolman emphasized the necessity of such a correction in case of highly-curved surfaces in their fundamental works, which is just the case of this SPM water-bridge. This approach has shown the way, how the thermodynamic approach can be extended down to the mesoscopic dimensions on the border of classical macroscopic thermodynamics and modern molecular dynamics.

Second, the author proposed a complete model enabling the calculation of surface resistivity and hydrophilicity in case of highly resistive surfaces from KPFM measurements of surface potential. The model is based on a charge diffusion equation, however, it is expanded by transitions between the charge and surface potential measured by KPFM and by transition between surface diffusivity and resistivity. Further, the knowledge of surface resistivity as a function of relative humidity enables to determine the surface hydrophilicity using the connection between the Brunauer-Emmett-Teller theory and description of surface resistivity as a sequence of multiple-charge-carrier quantum mechanical tunneling processes. The connection of all this theories has never been used in case of AFM, however, it could open the door to some new SPM techniques enabling the measurement of surface resistivity of highly resistive surfaces, or the measurement of the hydrophilicity. With expanding computing capabilities, both of the mentioned quantities (surface resistivity, hydrophilicity) could be examined locally with a resolution limited only by a resolution of KPFM (recently approximately 40 nm).

Third author's theoretical contribution shows the mechanism of interplay between the AFM-water bridge formation and corresponding electric field distribution close to the AFM-tip, which is especially important in case of nanolithography techniques like local anodic oxidation (LAO). The calculation emphasizes the fact that water, due to its high dielectric constant, pushes the electric field into the underlying oxidized layer enhancing the ion penetration. Considering the above, the water-bridge can be treated not only as a source of oxygen ions, but also as a "lens" focusing the electric field into the space of an isolating layer and thus enhancing ion penetration.

Author's contribution to the physical experiment and applications mainly addresses the following areas.

First, it has been experimentally shown how the dimensions of LAO structures (height, depth, half-width) are related to the experimental conditions such as applied voltage, scanning speed, sharpness of the tip and relative humidity. Such a knowledge is a critical in nanotechnology where the method is used to fabricate the smallest nanostructures and shows the limits of the method. Here, the limits are in order of tens of nanometer in respect to width and in order of units of nanometers in case of height and depth. This technique has been recently used mainly in surface science rather than in technology applications, however, in future, it can expand and move the resolution limits of mechanical, electrical engineering methods of mass machining.

Second, the methods have been developed to transfer the pure oxide structures prepared by LAO into a metallic form with almost the same nanometer-scale resolution using a combination of ion beam sputtering or selective growth of metals. While the transfer using ion beam sputtering is based on further ion beam milling of material masked by oxide structures, the transfer based on selective growth is based depends on different sticking coefficients of metallic particles (atoms, ions) on oxidized and non-oxidized areas. These transfer methods further expand the exploitation of SPM nanolithography into other fields related to preparation of metallic nanostructures.

Third, more applied contribution falls into the field of graphene preparation. Here, an original method for preparation of ultra-smooth copper foils for graphene growth was proposed and varified. The method is based on the deposition of a copper thin film on Si/SiO₂ template, and subsequent peeling-off of this film then offers an ultra-smooth and extra-clean copper surface for CVD graphene growth. Despite its simplicity, the method can rapidly improve the quality of graphene (e. g. mobility of charge carriers and crystallinity) grown on as prepared Cu foils. Since the utilization of graphene extraordinary properties in different fields reaching from graphene composite materials to graphene based electronics extremely depends on the quality of graphene and the CVD technique shows to be the most universal and promising method for large-scale graphene fabrication in science and industry, the mentioned method could become a necessary complement of CVD graphene growth.

The last author contribution mentioned in this thesis lies on the border of application and theory. The graphene itself is not a solution for all the problems, however, it could sometimes appear so. Its properties must often be tuned to meet the criteria of a specific applications. In case of electronic applications, it is necessary to tune the density of charge carriers, and in case of photonics, it is necessary to influence the interaction with electromagnetic waves, which can be achieved by deposition of metallic particles. Related to this, the extraordinary n-doping ability of Ga atoms has been proved experimentally by simultaneous deposition and transport response measurement. Moreover, there is a certain critical Ga concentration above which Ga does not dope the graphene. Based on the quantum mechanical density functional theory (DFT) calculation, the author was able to explain this behavior as a consequence of Ga island formation. In such Ga islands composed of several

atoms, the electrons are involved in Ga-Ga bonds, therefore, they cannot increase the number of free charge carriers in underlying graphene, which determines and limits the doping ability of Ga.

Finally, the fields of graphene and SPM technology has been completely connected to a recent three-year GAČR project granted called “In-situ Kelvin Probe Force Microscopy of a Graphene Nanosensor at Different Relative Humidity” where the author of this thesis is the principal investigator. Here, the team composed of 3 postdocs and 5 Ph.D. students carries out simultaneous KPFM and transport measurements of graphene sensors and nanosensors in ambient and vacuum conditions. Related to this project, the answer of fundamental questions dealing with the problem of graphene sensor transport response and its relation to the distribution of the electric charge measured by KPFM should be given.

The author of this thesis is a founder of the graphene group at the Institute of Physical Engineering, Faculty of Mechanical Engineering at Brno University of Technology (FME BUT). At present, the graphene group counts 3 postdocs, 5 Ph.D. students, 15 master and bachelor students. In the field of SPM and graphene, the author was a co-supervisor of 1 Ph.D. student, 10 master students and 13 bachelor students, who successfully defended their theses. Nowadays, he is a co-supervisor of 3 Ph.D. students, 2 master students and 2 bachelor students. The experience of the author’s research has been completely projected into special lectures “SPM nanolithography” and „Graphene“ organized for students of the Physical Engineering and Nanotechnology course as a part of the „Diagnostics of nanostructures“ subject. Suitable problems of SPM and graphene are also discussed during “Quantum mechanics” and “Solid state physics” exercises led by the author for the students of the 3rd year of the Physical Engineering and Nanotechnology course at FME BUT. Some simple interesting problems of nanotechnology dealing with classical mechanics, thermodynamics and electromagnetism (e. g. forces acting on SPM tip, Coulomb blockage as an extension of spherical capacitor etc.) have been regularly used as enrichment of routinely solved problems in courses of “Physics I”, “Physics II” for the students of Mechanical Engineering having been taught by the author for the last 15 years.

References

- [1] BHUSHAN, Bharat. *Handbook of Nanotechnology*. 4th vyd. B.m.: Springer-Verlag, 2017. ISBN 978-3-662-54355-9e.
- [2] BINNIG, Gerd a Heinrich ROHRER. Scanning Tunneling Microscopy - from Birth to Adolescence. In: *Nobel lecture*. 1986, s. 389–409. ISBN 978-0-7923-2065-4.
- [3] BINNIG, G., H. ROHRER, Ch GERBER a E. WEIBEL. 7×7 Reconstruction on Si(111) Resolved in Real Space. *Physical Review Letters* [online]. 1983, **50**(2), 120–123. ISSN 00319007. Dostupné z: doi:10.1103/PhysRevLett.50.120
- [4] BARO, AM, R MIRANDA, J ALAMAN, N GARCIA, G. BINNIG, H. ROHRER, C. GERBER a JL CARRASCOSA. Determination of surface topography of biological specimens at high resolution by scanning tunnelling microscopy. *Nature* [online]. 1985, **315**, 253–254. Dostupné z: <http://www.nature.com/nature/journal/v315/n6016/abs/315253a0.html>
- [5] GERBER, Ch, G. BINNIG, H. FUCHS, O. MARTI a H. ROHRER. Scanning tunneling microscope combined with a scanning electron microscope. *Review of Scientific Instruments* [online]. 1986, **57**(2), 221–224. ISSN 00346748. Dostupné z: doi:10.1063/1.1138973
- [6] LOZANNE, A. L., S. A. ELROD a C. F. QUATE. Spatial Variations in the Superconductivity of Nb₃Sn Measured by Low-Temperature Tunneling Microscopy. *Physical Review Letters*. 1985, **54**(22), 2433–2437.
- [7] MURALT, P. a D. W. POHL. Scanning tunneling potentiometry. *Applied Physics Letters* [online]. 1986, **48**(8), 514–516. ISSN 00036951. Dostupné z: doi:10.1063/1.96491
- [8] BINNIG, Gerd. US Patent: Atomic Force Microscope and method for imaging surfaces with atomic resolution. 1986.
- [9] BINNIG, G. a C. F. QUATE. Atomic Force Microscope. *Physical Review Letters* [online]. 1986, **56**(9), 930–933. ISSN 0031-9007. Dostupné z: doi:10.1103/PhysRevLett.56.930
- [10] GIESSIBL, Franz J., S. HEMBACHER, H. BIELEFELDT a J. MANNHART. Subatomic features on the silicon (111)-(7x7) surface observed by atomic force microscopy. *Science* [online]. 2000, **289**(5478), 422–425. ISSN 00368075. Dostupné z: doi:10.1126/science.289.5478.422
- [11] EMMRICH, M., F. HUBER, F. PIELMEIER, J. WELKER, T. HOFMANN, M. SCHNEIDERBAUER, D. MEUER, S. POLESYA, S. MANKOVSKY, D. KÖDDERITZSCH, H. EBERT a F. J. GIESSIBL. Subatomic resolution force microscopy reveals internal structure and adsorption sites of small iron clusters. *Scienceexpress*. 2015, **348**(6232), 1–7.
- [12] FEYNMAN, Richard P., Robert B. LEIGHTON a Matthew SANDS. *The Feynman Lectures on Physics, Volume 1: Mainly Mechanics, Radiation, and Heat*. New Millen. New York: Basic Books, 2011. ISBN 978-0-465-02414-8.
- [13] RODRIGUES, Mario S., Luca COSTA, Joël CHEVRIER a Fabio COMIN. Why do atomic force microscopy force curves still exhibit jump to contact? *Applied Physics Letters* [online]. 2012, **101**(20). ISSN 00036951. Dostupné z: doi:10.1063/1.4766172
- [14] ISRAELACHVILI, Jacob N. *Intermolecular and Surface Forces*. 3rd vyd. B.m.: Elsevier Inc., 2011. ISBN 978-0-12-375182-9.
- [15] BARTOŠÍK, Miroslav, Lukáš KORMOŠ, Lukáš FLAJŠMAN, Radek KALOUSEK, Jindřich MACH, Zuzana LIŠKOVÁ, David NEZVAL, Vojtěch ŠVARC, Tomáš ŠAMOŘIL a Tomáš ŠIKOLA.

- Nanometer-sized water bridge and pull-off force in AFM at different relative humidities: Reproducibility measurement and model based on surface tension change. *Journal of Physical Chemistry B* [online]. 2017, **121**(3), 610–619. ISSN 15205207. Dostupné z: doi:10.1021/acs.jpcc.6b11108
- [16] YANG, Seung Ho, Michael NOSONOVSKY, Huan ZHANG a Koo-Hyun CHUNG. Nanoscale water capillary bridges under deeply negative pressure. *Chem. Phys. Lett.* [online]. 2008, **451**, 88–92 [vid. 2013-08-22]. ISSN 00092614. Dostupné z: doi:10.1016/j.cplett.2007.11.068
- [17] GREENSPAN, M. a C. TSCHIEGG. No Title. *Natl. Bur. Stand. Sect. C 71*. 1967, **71**, 299.
- [18] ANGELL, C. A. Approaching the limits. *Nature* [online]. 1988, **336**, 206–207. ISSN 0028-0836. Dostupné z: doi:10.1038/332141a0
- [19] ZHENG_ET AL. Liquids at Karge Negative Presuures: Water at the Homogeneous Nucleation Limit. *Science*. 1991, **254**(18), 829–832.
- [20] WEEKS, Brandon L, Mark W VAUGHN a James J DEYOREO. Direct imaging of meniscus formation in atomic force microscopy using environmental scanning electron microscopy. *Langmuir* [online]. 2005, **21**, 8096–8098. ISSN 0743-7463. Dostupné z: doi:10.1021/la0512087
- [21] VAN HONSCHOTEN, J. W., N. R. TAS a M. ELWENSPOEK. The profile of a capillary liquid bridge between solid surfaces. *Am. J. Phys.* [online]. 2010, **78**, 277–286 [vid. 2013-08-22]. ISSN 00029505. Dostupné z: doi:10.1119/1.3273854
- [22] ROZHOK, Sergey, Peng SUN, Richard PINER, Marya LIEBERMAN a Chad a. MIRKIN. AFM Study of Water Meniscus Formation between an AFM Tip and NaCl Substrate. *Journal of Physical Chemistry B* [online]. 2004, **108**(23), 7814–7819. ISSN 1520-6106. Dostupné z: doi:10.1021/jp0401269
- [23] SHANKLAND, S. IBM's 35 atoms and the rise of nanotech. *cnet* [online]. 2009 [vid. 2018-08-06]. Dostupné z: <https://www.cnet.com/news/ibms-35-atoms-and-the-rise-of-nanotech/>
- [24] XUE, Yong-Qiang, Xin-Cheng YANG, Zi-Xiang CUI a Wei-Peng LAI. The Effect of Microdroplet Size on the Surface Tension and Tolman Length. *J. Phys. Chem. B* [online]. 2011, **115**, 109–12. ISSN 1520-5207. Dostupné z: doi:10.1021/jp1084313
- [25] JANG, Joonkyung a George C. SCHATZ. Lattice Gas Monte Carlo Simulation of Capillary Forces in Atomic Force Microscopy. *J. Adhes. Sci. Technol.* [online]. 2010, **24**, 2429–2451. ISSN 0169-4243. Dostupné z: doi:10.1163/016942410X508172
- [26] MEN, Yumei, Xianren ZHANG a Wenchuan WANG. Capillary Liquid Bridges in Atomic Force Microscopy: Formation, Rupture, and Hysteresis. *J. Chem. Phys.* [online]. 2009, **131**, 184702 1-8 [vid. 2013-08-08]. ISSN 1089-7690. Dostupné z: doi:10.1063/1.3257624
- [27] KELVIN, Lord. V. *Contact electricity of metals. Philosophical Magazine Series 5* [online]. 1898, **46**(278), 82–120. ISSN 1941-5982. Dostupné z: doi:10.1080/14786449808621172
- [28] SASCHA SADEWASSER, Thilo Glatzel. *Kelvin Probe Force Microscopy: Measuring and Compensating Electrostatic Forces* [online]. 2011. ISBN 9783642225659. Dostupné z: doi:10.1007/978-3-642-22566-6
- [29] ZISMAN, W A. A New Method Of Measuring Contact Potential Differences In Metals. *Review of Scientific Instruments* [online]. 1932, **3**, 367. ISSN 00346748. Dostupné z: doi:10.1063/1.1748947
- [30] NONNENMACHER, M., M. P. O'BOYLE a H. K. WICKRAMASINGHE. Kelvin probe force microscopy. *Applied Physics Letters* [online]. 1991, **58**(25), 2921 [vid. 2014-01-09].

ISSN 00036951. Dostupné z: doi:10.1063/1.105227

- [31] WEAVER, J. M. R. a D. W. ABRAHAM. High resolution atomic force microscopy potentiometry. *Journal of Vacuum Science & Technology B*. 1991, **9**, 1559.
- [32] MIRONOV, V. L. *Fundamentals of Scanning Probe Microscopy*. Nizhniy Novgorod: The Russian Academy of Sciences Institute for Physics of Microstructures, 2004. ISBN 9783540343141.
- [33] SONG, Seok-ho, Hyun-ho YANG, Chang-hoon HAN, Seung-deok KO a Seok-hee LEE. Metal-oxide-semiconductor field effect transistor humidity sensor using surface conductance. *Appl. Phys. Lett.* [online]. 2015, **100**(2012), 101603. Dostupné z: doi:10.1063/1.3691936
- [34] BRUNAUER, Stephen, P. H. EMMETT a Edward TELLER. Adsorption of Gases in Multimolecular Layers. *Journal of the American Chemical Society* [online]. 1938, **60**(2), 309–319. ISSN 15205126. Dostupné z: doi:10.1021/ja01269a023
- [35] INVESTIGATIONS OF T H E SURFACE CONDUCTIVITY. 1987, **187**, 201–211.
- [36] CASTAGNE, R., P. HESTO a A. VAPAILLE. Surface Conductivity of the Insulator of an MIS or MIM Device. *Thin Solid Films*. 1973, **17**, 253–264.
- [37] EIGLER, E. K. a D. K. SCHWEIZER. *Positioning single atoms with a scanning tunneling microscope* [online]. 1990. ISBN 0028-0836. Dostupné z: doi:10.1038/344524a0
- [38] MANOHARAN, H. C., C. P. LUTZ a D. M. EIGLER. Quantum mirages formed by coherent projection of electronic structure. *Nature* [online]. 2000, **403**(6769), 512–515. ISSN 00280836. Dostupné z: doi:10.1038/35000508
- [39] HONG, Seunghun, Jin ZHU a Chad A. MIRKIN. Multiple ink nanolithography: Toward a multiple-pen nano-plotter. *Science* [online]. 1999, **286**(5439), 523–525. ISSN 00368075. Dostupné z: doi:10.1126/science.286.5439.523
- [40] JO, Ara, Wonchul JOO, Won Hyeog JIN, Hyojin NAM a Jin Kon KIM. Ultrahigh-density phase-change data storage without the use of heating. *Nature Nanotechnology* [online]. 2009, **4**(11), 727–731. ISSN 17483395. Dostupné z: doi:10.1038/nnano.2009.260
- [41] LIU, Shantang, Rivka MAOZ a Jacob SAGIV. Planned nanostructures of colloidal gold via self-assembly on hierarchically assembled organic bilayer template patterns with in-situ generated terminal amino functionality. *Nano Letters* [online]. 2004, **4**(5), 845–851. ISSN 15306984. Dostupné z: doi:10.1021/nl049755k
- [42] MASUBUCHI, Satoru, Miho ARAI a Tomoki MACHIDA. Atomic force microscopy based tunable local anodic oxidation of graphene. *Nano letters* [online]. 2011, **11**(11), 4542–6. ISSN 1530-6992. Dostupné z: doi:10.1021/nl201448q
- [43] GIESBERS, a.J.M., U. ZEITLER, S. NEUBECK, F. FREITAG, K.S. NOVOSELOV a J.C. MAAN. Nanolithography and manipulation of graphene using an atomic force microscope. *Solid State Communications* [online]. 2008, **147**(9–10), 366–369 [vid. 2013-11-04]. ISSN 00381098. Dostupné z: doi:10.1016/j.ssc.2008.06.027
- [44] BYUN, Ik-Su, Duhee YOON, Jin Sik CHOI, Inrok HWANG, Duk Hyun LEE, Mi Jung LEE, Tomoji KAWAI, Young-Woo SON, Quanxi JIA, Hyeonsik CHEONG a Bae Ho PARK. Nanoscale lithography on monolayer graphene using hydrogenation and oxidation. *ACS nano* [online]. 2011, **5**(8), 6417–24. ISSN 1936-086X. Dostupné z: doi:10.1021/nn201601m
- [45] CABRERA, N. a N. F. MOTT. Theory of the oxidation of metals. *Reports on Progress in Physics* [online]. 1949, **12**(1), 163–184. ISSN 00344885. Dostupné z: doi:10.1088/0034-4885/12/1/308

- [46] STIÉVENARD, D., P. A. FONTAINE a E. DUBOIS. Nanooxidation using a scanning probe microscope: An analytical model based on field induced oxidation. *Applied Physics Letters* [online]. 1997, **70**(24), 3272–3274. ISSN 00036951. Dostupné z: doi:10.1063/1.118425
- [47] BUTT, Hans-Jürgen, Maria B UNTCH, Ali GOLRIZ, Sascha A PIHAN a Rüdiger BERGER. Electric-field-induced condensation: An extension of the Kelvin equation. *Physical Review E*. 2011, **83**(6), 61604.
- [48] LIJIMA, Sumio. Helical microtubules of graphitic carbon. *Nature* [online]. 1991, **354**, 56–58. ISSN 0028-0836. Dostupné z: doi:10.1038/354056a0
- [49] IJIMA, Sumio a Toshinari ICHIHASHI. Single-shell carbon nanotubes of 1-nm diameter. *Nature* [online]. 1993, **363**(6430), 603–605. ISSN 00280836. Dostupné z: doi:10.1038/363603a0
- [50] KROTO, H. W., J. R. HEATH, S. C. O'BRIEN, R. F. CURL a R. E. SMALLEY. C60: Buckminsterfullerene. *Nature* [online]. 1985, **318**(6042), 162–163. ISSN 00280836. Dostupné z: doi:10.1038/318162a0
- [51] K. S. NOVOSELOV, A. K. GEIM, S. V. MOROZOV, D. JIANG, Y. ZHANG, S. V. DUBONOS, I. V. GRIGORIEVA, A. A. Firsov. Electric Field Effect in Atomically Thin Carbon Films. *Science* [online]. 2004, **306**(October), 666–669. ISSN 0036-8075. Dostupné z: doi:10.1126/science.1102896
- [52] CASTRO NETO, a. H., N. M. R. PERES, K. S. NOVOSELOV a a. K. GEIM. The electronic properties of graphene. *Reviews of Modern Physics* [online]. 2009, **81**(1), 109–162 [vid. 2014-03-19]. ISSN 0034-6861. Dostupné z: doi:10.1103/RevModPhys.81.109
- [53] LOH, Kian Ping, Qiaoliang BAO, Priscilla Kailian ANG a Jiaxiang YANG. The chemistry of graphene. *Journal of Materials Chemistry* [online]. 2010, **20**(12), 2277–2289. ISSN 09599428. Dostupné z: doi:10.1039/b920539j
- [54] BUNCH, J. Scott, Scott S. VERBRIDGE, Jonathan S. ALDEN, Arend M. VAN DER ZANDE, Jeevak M. PARPIA, Harold G. CRAIGHEAD a Paul L. MCEUEN. Impermeable atomic membranes from graphene sheets. *Nano Letters* [online]. 2008, **8**(8), 2458–2462. ISSN 15306984. Dostupné z: doi:10.1021/nl801457b
- [55] LEE, Changgu, Xiaoding WEI, Jeffrey W. KYSAR, James HONE a =. Measurement of the Elastic Properties and Intrinsic Strength of Monolayer Graphene. *Science* [online]. 2008, **321**(18 July 2008), 385–388. ISSN 0036-8075. Dostupné z: doi:10.1126/science.1157996
- [56] LIU, Fang, Pingbing MING a Ju LI. Ab initio calculation of ideal strength and phonon instability of graphene under tension. *Physical Review B - Condensed Matter and Materials Physics* [online]. 2007, **76**(6), 1–7. ISSN 10980121. Dostupné z: doi:10.1103/PhysRevB.76.064120
- [57] NAIR, R. R., P. BLAKE, A. N. GRIGORENKO, K. S. NOVOSELOV, T. J. BOOTH, T. STAUBER, N. M R PERES a A. K. GEIM. Fine structure constant defines visual transparency of graphene. *Science* [online]. 2008, **320**(5881), 1308. ISSN 00368075. Dostupné z: doi:10.1126/science.1156965
- [58] BALANDIN, Alexander A, Suchismita GHOSH, Wenzhong BAO, Irene CALIZO, Desalegne TEWELDEBRHAN, Feng MIAO a Chun Ning LAU. Superior Thermal Conductivity of Single-Layer Graphene.pdf. *Nano Lett.* 2008, **8**(3), 902–907.
- [59] LEE, Jae Ung, Duhee YOON, Hakseong KIM, Sang Wook LEE a Hyeonsik CHEONG. Thermal conductivity of suspended pristine graphene measured by Raman spectroscopy. *Physical Review B - Condensed Matter and Materials Physics* [online]. 2011, **83**(8), 1–4. ISSN 10980121. Dostupné z: doi:10.1103/PhysRevB.83.081419

- [60] KADIRKO, V., K. ZIEGLER a E. KOGAN. Next-nearest-neighbor Tight-binding Model of Plasmons in Graphene [online]. 2011, **2013**(July), 97–101. ISSN 2169-3439. Dostupné z: doi:10.4236/graphene.2013.23014
- [61] WALLACE, P. R. The band theory of graphite. *Physical Review* [online]. 1947, **71**(9), 622–634. ISSN 0031899X. Dostupné z: doi:10.1103/PhysRev.71.622
- [62] YOUNG, Andrea F. a Philip KIM. Quantum interference and Klein tunnelling in graphene heterojunctions. *Nature Physics* [online]. 2009, **5**(3), 222–226. ISSN 17452473. Dostupné z: doi:10.1038/nphys1198
- [63] GEIM, a K a K S NOVOSELOV. The rise of graphene. *Nature materials* [online]. 2007, **6**(3), 183–91. ISSN 1476-1122. Dostupné z: doi:10.1038/nmat1849
- [64] NOVOSELOV, K S, a K GEIM, S V MOROZOV, D JIANG, Y ZHANG, S V DUBONOS, I V GRIGORIEVA a a a FIRSOV. Electric field effect in atomically thin carbon films. *Science (New York, N.Y.)* [online]. 2004, **306**(5696), 666–9 [vid. 2014-03-19]. ISSN 1095-9203. Dostupné z: doi:10.1126/science.1102896
- [65] CHEN, Jian-hao, Chaun JANG, Shudong XIAO, Masa ISHIGAMI a Michael S FUHRER. Intrinsic and extrinsic performance limits of graphene devices on SiO₂. *Nature nanotechnology* [online]. 2008, **3**(4), 206–9. ISSN 1748-3395. Dostupné z: doi:10.1038/nnano.2008.58
- [66] BENNETT, Brian R., Richard MAGNO, J. Brad BOOS, Walter KRUPPA a Mario G. ANCONA. Antimonide-based compound semiconductors for electronic devices: A review. *Solid-State Electronics* [online]. 2005, **49**(12), 1875–1895. ISSN 00381101. Dostupné z: doi:10.1016/j.sse.2005.09.008
- [67] NOVOSELOV, K S, a K GEIM, S V MOROZOV, D JIANG, M I KATSNELSON, I V GRIGORIEVA, S V DUBONOS a a a FIRSOV. Two-dimensional gas of massless Dirac fermions in graphene. *Nature* [online]. 2005, **438**(7065), 197–200 [vid. 2014-03-19]. ISSN 1476-4687. Dostupné z: doi:10.1038/nature04233
- [68] MAYOROV, Alexander S., Roman V. GORBACHEV, Sergey V. MOROZOV, Liam BRITNELL, Rashid JALIL, Leonid A. PONOMARENKO, Peter BLAKE, Kostya S. NOVOSELOV, Kenji WATANABE, Takashi TANIGUCHI a A. K. GEIM. Micrometer-scale ballistic transport in encapsulated graphene at room temperature. *Nano Letters* [online]. 2011, **11**(6), 2396–2399. ISSN 15306984. Dostupné z: doi:10.1021/nl200758b
- [69] ZHANG, Yuanbo, Yan Wen TAN, Horst L. STORMER a Philip KIM. Experimental observation of the quantum Hall effect and Berry's phase in graphene. *Nature* [online]. 2005, **438**(7065), 201–204. ISSN 00280836. Dostupné z: doi:10.1038/nature04235
- [70] LIN, Yu-Ming, Keith A. JENKINS, Alberto VALDES-GARCIA, Joshua P. SMALL, Damon B. FARMER a Phaeton AVOURIS. Operation of Graphene Transistors at Gigahertz Frequencies. *Nano Letters* [online]. 2009, **9**(1), 422–426. ISSN 1530-6984. Dostupné z: doi:10.1021/nl803316h
- [71] LIN, Y, C DIMITRAKOPOULOS, K a JENKINS, D B FARMER, H CHIU, a GRILL a Ph AVOURIS. 100-GHz Transistors from. *Nano* [online]. 2010, **327**(5966), 100. ISSN 10959203. Dostupné z: doi:10.1126/science.1184289
- [72] MOON, J. S., D. CURTIS, M. HU, D. WONG, C. MCGUIRE, Paul M. CAMPBELL, Glenn JERNIGAN, Joseph L. TEDESCO, Brenda VANMIL, Rachael MYERS-WARD, Chip EDDY a D. Kurt GASKILL. Epitaxial-graphene RF field-effect transistors on Si-face 6H-SiC substrates. *IEEE Electron Device Letters* [online]. 2009, **30**(6), 650–652. ISSN 07413106. Dostupné z: doi:10.1109/LED.2009.2020699

- [73] HAN, Melinda Y., Barbaros ÖZYILMAZ, Yuanbo ZHANG a Philip KIM. Energy band-gap engineering of graphene nanoribbons. *Physical Review Letters* [online]. 2007, **98**(20), 1–4. ISSN 00319007. Dostupné z: doi:10.1103/PhysRevLett.98.206805
- [74] PONOMARENKO, L. A., F. SCHEDIN, M. I. KATSNELSON, R. YANG, E. W. HILL, K. S. NOVOSELOV a A. K. GEIM. Chaotic dirac billiard in graphene quantum dots. *Science* [online]. 2008, **320**(5874), 356–358. ISSN 00368075. Dostupné z: doi:10.1126/science.1154663
- [75] STAMPFER, C., J. GÜTTINGER, F. MOLITOR, D. GRAF, T. IHN a K. ENSSLIN. Tunable Coulomb blockade in nanostructured graphene. *Applied Physics Letters* [online]. 2008, **92**(1), 1–4. ISSN 00036951. Dostupné z: doi:10.1063/1.2827188
- [76] HALL, E O, N J PETCH, K W JACOBSEN, S YIP, M a MEYERS, a MISHRA, D J BENSON, P G SANDERS, J a EASTMAN, J R WEERTMAN, C C KOCH, K M YOUSSEF, R O SCATTERGOOD, K L MURTY, Y F SHEN, L LU, Q H LU, Z H JIN, K LU, Y SHEN, X CHEN, L QIAN, J CHEN, a MISRA, X ZHANG, D HAMMON, R G HOAGLAND, K K CHAWLA, M HORTON, Upper SADDLE, N HANSEN, N TSUJI, R K MISHRA, S a Syed ASIF, O L WARREN, a M MINOR, J MIZERA, J W WYRZYKOWSKI, N R TAO, P M HAZZLEDINE, S SURESH, J LI, a SAMANTA, H G KIM, Z JIN, W PANTLEON, B RALPH a X SI. Control of Graphene's Properties by Reversible Hydrogenation: Evidence for Graphane [online]. 2009, (January), 610–613. ISSN 0036-8075. Dostupné z: doi:10.1126/science.1167130
- [77] CHENG, S. H., K. ZOU, F. OKINO, H. R. GUTIERREZ, A. GUPTA, N. SHEN, P. C. EKLUND, J. O. SOFO a J. ZHU. Reversible fluorination of graphene: Evidence of a two-dimensional wide bandgap semiconductor. *Physical Review B - Condensed Matter and Materials Physics* [online]. 2010, **81**(20), 1–5. ISSN 10980121. Dostupné z: doi:10.1103/PhysRevB.81.205435
- [78] USACHOV, D., O. VILKOV, A. GRÜNEIS, D. HABERER, A. FEDOROV, V. K. ADAMCHUK, A. B. PREOBRAJENSKI, P. DUDIN, A. BARINOV, M. OEHZELT, C. LAUBSCHAT a D. V. VYALIKH. Nitrogen-doped graphene: Efficient growth, structure, and electronic properties. *Nano Letters* [online]. 2011, **11**(12), 5401–5407. ISSN 15306984. Dostupné z: doi:10.1021/nl2031037
- [79] ZHANG, Yuanbo, Tsung Ta TANG, Caglar GIRIT, Zhao HAO, Michael C. MARTIN, Alex ZETTL, Michael F. CROMMIE, Y. Ron SHEN a Feng WANG. Direct observation of a widely tunable bandgap in bilayer graphene. *Nature* [online]. 2009, **459**(7248), 820–823. ISSN 00280836. Dostupné z: doi:10.1038/nature08105
- [80] CASTRO, Eduardo V., K. S. NOVOSELOV, S. V. MOROZOV, N. M R PERES, J. M B LOPES DOS SANTOS, Johan NILSSON, F. GUINEA, A. K. GEIM a A. H. CASTRO NETO. Electronic properties of a biased graphene bilayer. *Journal of Physics Condensed Matter* [online]. 2010, **22**(17). ISSN 09538984. Dostupné z: doi:10.1088/0953-8984/22/17/175503
- [81] SCHEDIN, F, a K GEIM, S V MOROZOV, E W HILL, P BLAKE, M I KATSNELSON a K S NOVOSELOV. Detection of individual gas molecules adsorbed on graphene. *Nature materials* [online]. 2007, **6**(9), 652–5 [vid. 2013-09-16]. ISSN 1476-1122. Dostupné z: doi:10.1038/nmat1967
- [82] HE, Qiyuan, Shixin WU, Zongyou YIN a Hua ZHANG. Graphene-based electronic sensors. *Chemical Science* [online]. 2012, **3**(6), 1764–1772. ISSN 20416520. Dostupné z: doi:10.1039/c2sc20205k
- [83] WU, L., H. S. CHU, W. S. KOH a E. P. LI. Highly sensitive graphene biosensors based on surface plasmon resonance. *Optics Express* [online]. 2010, **18**(14), 14395. ISSN 1094-4087. Dostupné z: doi:10.1364/OE.18.014395
- [84] WANG, Xuan, Linjie ZHI a Klaus MÜLLEN. Transparent, conductive graphene electrodes for dye-sensitized solar cells. *Nano Letters* [online]. 2008, **8**(1), 323–327. ISSN 15306984. Dostupné z: doi:10.1021/nl072838r

- [85] BLAKE, P, P D BRIMICOMBE, R R NAIR, T J BOOTH, D JIANG, F SCHEDIN, L A PONOMARENKO, S V MOROZOV, H F GLEESON, E W HILL, A K GEIM a K S NOVOSELOV. Graphene Based Liquid Crystal Device. *Nano letters* [online]. 2008, **8**, 1704. Dostupné z: doi:10.1021/nl080649i
- [86] XIA, Fengnian, Thomas MUELLER, Yu-Ming LIN, Alberto VALDES-GARCIA a Phaeton AVOURIS. Ultrafast graphene photodetector. *Nature nanotechnology* [online]. 2009, **4**(12), 839–43 [vid. 2013-09-24]. ISSN 1748-3395. Dostupné z: doi:10.1038/nnano.2009.292
- [87] WILSON, N R, N R WILSON, P A PANDEY, P A PANDEY, R BEANLAND, R BEANLAND, R J YOUNG, R J YOUNG, I a KINLOCH, I a KINLOCH, L GONG, L GONG, Z LIU, Z LIU, K SUENAGA, K SUENAGA, J P ROURKE, J P ROURKE, S J YORK, S J YORK, J SLOAN a J SLOAN. Graphene oxide: structural analysis and application as a highly transparent support for electron microscopy. *ACS nano* [online]. 2009, **3**(9), 2547–2556. ISSN 1936-0851. Dostupné z: doi:10.1021/nn900694t
- [88] NAIR, R. R., S. ANISSIMOVA, R. ZAN, P. BLAKE, J. R. BLAKE, A. K. GEIM, U. BANGERT, A. P. GOLOVANOV, S. V. MOROZOV, K. S. NOVOSELOV a T. LATYCHEVSKAIA. Graphene as a transparent conductive support for studying biological molecules by transmission electron microscopy. *IEEE Transactions on Information Theory* [online]. 1993, **39**(3), 1057–1064. ISSN 15579654. Dostupné z: doi:10.1109/18.256515
- [89] GONG, Lei, Ian A. KINLOCH, Robert J. YOUNG, Ibtisam RIAZ, Rashid JALIL a Konstantin S. NOVOSELOV. Interfacial stress transfer in a graphene monolayer nanocomposite. *Advanced Materials* [online]. 2010, **22**(24), 2694–2697. ISSN 09359648. Dostupné z: doi:10.1002/adma.200904264
- [90] NOVOSELOV, K S, V I FAL'KO, L COLOMBO, P R GELLERT, M G SCHWAB a K KIM. A roadmap for graphene. *Nature* [online]. 2012, **490**(7419), 192–200 [vid. 2014-03-19]. ISSN 1476-4687. Dostupné z: doi:10.1038/nature11458
- [91] LI, Xuesong, Weiwei CAI, Jjinho AN, Seyoung KIM, Junghyo NAH, Dongxing YANG, Richard PINER, Aruna VELAMAKANNI, Inhwa JUNG, Emanuel TUTUC, Sanjay K. BANERJEE, Luigi COLOMBO a Rodney S. RUOFF. Large area synthesis of high quality and uniform graphene films on copper foils. *Science (New York, N.Y.)* [online]. 2009, **324**(5932), 1312–1314. ISSN 0036-8075. Dostupné z: doi:10.1126/science.1171245
- [92] BAE, Sukang, Hyeongkeun KIM, Youngbin LEE, Xiangfan XU, Jae Sung PARK, Yi ZHENG, Jayakumar BALAKRISHNAN, Tian LEI, Hye RI KIM, Young Il SONG, Young Jin KIM, Kwang S. KIM, Barbaros ÖZYILMAZ, Jong Hyun AHN, Byung Hee HONG a Sumio IJIMA. Roll-to-roll production of 30-inch graphene films for transparent electrodes. *Nature Nanotechnology* [online]. 2010, **5**(8), 574–578. ISSN 17483387. Dostupné z: doi:10.1038/nnano.2010.132
- [93] EDWARDS, Rebecca S. a Karl S. COLEMAN. Graphene film growth on polycrystalline metals. *Accounts of Chemical Research* [online]. 2013, **46**(1), 23–30. ISSN 00014842. Dostupné z: doi:10.1021/ar3001266
- [94] AGO, Hiroki, Yui OGAWA, Masaharu TSUJI, Seigi MIZUNO a Hiroki HIBINO. Catalytic growth of graphene: Toward large-area single-crystalline graphene. *Journal of Physical Chemistry Letters* [online]. 2012, **3**(16), 2228–2236. ISSN 19487185. Dostupné z: doi:10.1021/jz3007029
- [95] WANG, Lu, Xiuyun ZHANG, Helen L.W. CHAN, Feng YAN a Feng DING. Formation and healing of vacancies in graphene chemical vapor deposition (CVD) growth. *Journal of the American Chemical Society* [online]. 2013, **135**(11), 4476–4482. ISSN 00027863. Dostupné z: doi:10.1021/ja312687a
- [96] REINA, Alfonso, Hyungbin SON, Liying JIAO, Ben FAN, Mildred S DRESSELHAUS, Zhongfan LIU a Jing KONG. Transferring and Identification of Single- and Few-Layer Graphene on Arbitrary

- Substrates Transferring and Identification of Single- and Few-Layer Graphene on Arbitrary Substrates [online]. 2008, 17741–17744. Dostupné z: doi:10.1021/jp807380s
- [97] WEISS, Emily A., George K. KAUFMAN, Jennah K. KRIEBEL, Zhefeng LI, Richard SCHALEK a George M. WHITESIDES. Si/SiO₂-templated formation of ultraflat metal surfaces on glass, polymer, and solder supports: Their use as substrates for self-assembled monolayers. *Langmuir* [online]. 2007, **23**(19), 9686–9694. ISSN 07437463. Dostupné z: doi:10.1021/la701919r
- [98] PROCHÁZKA, Pavel, Jindřich MACH, Dominik BISCHOFF, Zuzana LIŠKOVÁ, Petr DVOŘÁK, Marek VAŇATKA, Pauline SIMONET, Anastasia VARLET, Dušan HEMZAL, Martin PETRENEC, Lukáš KALINA, Miroslav BARTOŠÍK, Klaus ENSSLIN, Peter VARGA, Jan ČECHAL a Tomáš ŠIKOLA. Ultrasmooth metallic foils for growth of high quality graphene by chemical vapor deposition. *Nanotechnology* [online]. 2014, **25**(185601), 1–8. Dostupné z: doi:10.1088/0957-4484/25/18/185601
- [99] YAN, Zheng, Jian LIN, Zhiwei PENG, Zhengzong SUN, Yu ZHU, Lei LI, Changsheng XIANG, E LOI, Carter KITRELL a James M TOUR. Toward the Synthesis of Wafer-Scale. *ACS nano* [online]. 2012, **6**(10), 9110–9117. Dostupné z: doi:10.1021/nn303352k
- [100] SONG, H. S., S. L. LI, H. MIYAZAKI, S. SATO, K. HAYASHI, A. YAMADA, N. YOKOYAMA a K. TSUKAGOSHI. *Origin of the relatively low transport mobility of graphene grown through chemical vapor deposition* [online]. 2012. ISBN 2045-2322 (Electronic)n2045-2322 (Linking). Dostupné z: doi:10.1038/srep00337
- [101] PROCHÁZKA, Procházka, Miroslav BARTOŠÍK, Jindřich MACH, Zuzana LIŠKOVÁ, Jan HULVA, Martin KONEČNÝ, Bohumil DAVID a Tomáš ŠIKOLA. Shubnikov-de Haas oscillations on graphene fabricated by CVD method. *Fine mechanics and optics*. 2014, **6–7**, 195.
- [102] BERTOLAZZI, Simone, Daria KRASNOZHON a Andras KIS. Nonvolatile memory cells based on MoS₂/graphene heterostructures. *ACS Nano* [online]. 2013, **7**(4), 3246–3252. ISSN 19360851. Dostupné z: doi:10.1021/nn3059136
- [103] LOSURDO, Maria, Congwen YI, Alexandra SUVOROVA, Sergey RUBANOV, Tong Ho KIM, Maria M. GIANGREGORIO, Wenyuan JIAO, Iris BERGMAIR, Giovanni BRUNO a April S. BROWN. Demonstrating the capability of the high-performance plasmonic gallium-graphene couple. *ACS Nano* [online]. 2014, **8**(3), 3031–3041. ISSN 1936086X. Dostupné z: doi:10.1021/nn500472r
- [104] SHARMA, Sheetal a A S VERMA. A theoretical study of H₂S adsorption on graphene doped with B, Al and Ga. *Physica B: Physics of Condensed Matter* [online]. 2013, **427**, 12–16. ISSN 0921-4526. Dostupné z: doi:10.1016/j.physb.2013.05.019
- [105] FUJITA, Jun-ichi, Ryuuichi UEKI, Yousuke MIYAZAWA a Toshinari ICHIHASHI. Graphitization at interface between amorphous carbon and liquid gallium for fabricating large area graphene sheets. *Journal of Vacuum Science & Technology B: Microelectronics and Nanometer Structures* [online]. 2009, **27**(6), 3063. ISSN 10711023. Dostupné z: doi:10.1116/1.3253542
- [106] XU, Hua, Liming XIE, Haoli ZHANG a Jin ZHANG. Effect of graphene Fermi level on the Raman scattering intensity of molecules on graphene. *ACS Nano* [online]. 2011, **5**(7), 5338–5344. ISSN 19360851. Dostupné z: doi:10.1021/nn103237x
- [107] HOHENBERG, P. a Kohn W. Inhomogeneous Electron Gas. *Physical Review*. 1964, **136**(1962), 864–871.
- [108] KOHN, W. a L. J. SHAM. Self-Consistent Equations Including Exchange and Correlation Effects.

Physical Review [online]. 1965, **140**(4), 1133. Dostupné z: [doi:http://dx.doi.org/10.1103/PhysRev.140.A1133](http://dx.doi.org/10.1103/PhysRev.140.A1133)

- [109] PERDEW, John, J. CHEVARY, S. VOSKO, Koblar JACKSON, Mark PEDERSON, D. SINGH a Carlos FIOUHAIS. Atoms, molecules, solids, and surfaces: Applications of the generalized gradient approximation for exchange and correlation. *Physical Review B* [online]. 1993, **48**(7), 4978–4978. ISSN 0163-1829. Dostupné z: [doi:10.1103/PhysRevB.48.4978.2](http://dx.doi.org/10.1103/PhysRevB.48.4978.2)
- [110] KRESSE, G. a J. FURTHMÜLLER. Efficient iterative schemes for ab initio total-energy calculations using a plane-wave basis set. *Physical Review B* [online]. 1996, **54**(16), 11169–11186. ISSN 0163-1829. Dostupné z: [doi:10.1103/PhysRevB.54.11169](http://dx.doi.org/10.1103/PhysRevB.54.11169)
- [111] KRESSE, G. a HAFNER J. Ab initio molecular dynamics for liquid metals. *Physical Review B*. 1993, **47**(1), 558–561.
- [112] KRESSE, G. a J. FURTHMÜLLER. Efficient iterative schemes for ab initio total-energy calculations using a plane-wave basis set. *Physical Review B* [online]. 1996, **54**(16), 11169–11186. ISSN 0163-1829. Dostupné z: [doi:10.1103/PhysRevB.54.11169](http://dx.doi.org/10.1103/PhysRevB.54.11169)

Commented paper 1

BARTOŠÍK, Miroslav, Lukáš KORMOŠ, Lukáš FLAJŠMAN, Radek KALOUSEK, Jindřich MACH, Zuzana LIŠKOVÁ, David NEZVAL, Vojtěch ŠVARC, Tomáš ŠAMOŘIL a Tomáš ŠIKOLA.

Nanometer-sized water bridge and pull-off force in AFM at different relative humidities: Reproducibility measurement and model based on surface tension change. *Journal of Physical Chemistry B* [online]. 2017, **121**(3), 610–619. ISSN 15205207. Dostupné z: doi:10.1021/acs.jpcc.6b11108

Nanometer-Sized Water Bridge and Pull-Off Force in AFM at Different Relative Humidities: Reproducibility Measurement and Model Based on Surface Tension Change

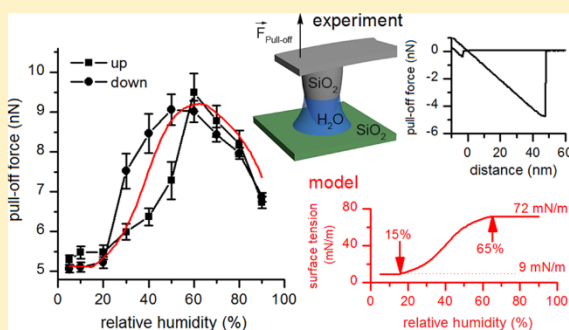
Miroslav Bartošík,^{*,†,‡,§} Lukáš Kormoš,[†] Lukáš Flajšman,[†] Radek Kalousek,^{†,‡} Jindřich Mach,^{†,‡} Zuzana Lišková,[†] David Nezval,[‡] Vojtěch Švarc,[‡] Tomáš Šamořil,[†] and Tomáš Šikola^{†,‡}

[†]Central European Institute of Technology - Brno University of Technology (CEITEC BUT), Purkyňova 123, 612 00 Brno, Czech Republic

[‡]Institute of Physical Engineering, Faculty of Mechanical Engineering, Brno University of Technology, Technická 2, 616 69 Brno, Czech Republic

Supporting Information

ABSTRACT: This article deals with the analysis of the relationship between the pull-off force measured by atomic force microscopy and the dimensions of water bridge condensed between a hydrophilic silicon oxide tip and a silicon oxide surface under ambient conditions. Our experiments have shown that the pull-off force increases linearly with the radius of the tip and nonmonotonically with the relative humidity (RH). The latter dependence generally consists of an initial constant part changing to a convex–concave-like increase of the pull-off force and finally followed by a concave-like decrease of this force. The reproducibility tests have demonstrated that the precision limits have to be taken into account for comparing these measurements carried out under atmospheric conditions. The results were fitted by a classical thermodynamic model based on water-bridge envelope calculations using the numerical solution of the Kelvin equation in the form of axisymmetric differential equations and consequent calculation of adhesive forces. To describe the measured data more precisely, a decrease of the water surface tension for low RH was incorporated into the calculation. Such a decrease can be expected as a consequence of the high surface curvature in the nanometer-sized water bridge between the tip and the surface.



INTRODUCTION

The water bridge condensed between a hydrophilic surface and tip under ambient conditions plays a very important role in measurements and applications provided by atomic force microscopes (AFMs) nowadays.¹ The presence of water can significantly affect the adhesive and frictional force interaction between the tip and the surface.^{2–5} Furthermore, the bridge size directly determines the dimensions of nanostructures fabricated by dip-pen nanolithography^{6,7} or local anodic oxidation^{8–10} and introduces one of the limitations of their resolution. Because of these reasons, the information about the amount of water condensed under the tip has a significant consequence for interpretation of force magnitudes in measurements and progress in resolution of AFM-based nanolithography techniques.

In principle, there are two ways to obtain information about the water-bridge dimensions (given by the main radii and boundary angles). The first one is a direct observation using environmental scanning electron microscopy (SEM).¹¹ The disadvantage of this method is that electrons affect the surface energy of water. Hence, the bridge appears bigger than that

without the electron beam.¹² The second one is an indirect method based on detecting pull-off forces in AFM force–distance spectroscopy. Here, a suitable theoretical model for calculating the water-bridge dimensions from the pull-off force measurement is needed. Then, the method could be straightforwardly utilized for determining the amount of water in the bridge and applied, for instance, for estimation of local hydrophilicity/hydrophobicity of the sample.

The dependence of the AFM total pull-off (or adhesive) force on relative humidity (RH) was assessed by many groups during the last years. Unfortunately, even for the most cited combination of a silicon AFM tip and silicon oxide surface, the published results are ambiguous as they comprise increasing, increasing–decreasing, or stepwise-increasing dependency of pull-off force on RH^{13,14} (see details in discussion). Tremendous effort has been made to understand the experimental results using various theoretical models and to

Received: November 4, 2016

Revised: November 29, 2016

Published: January 11, 2017

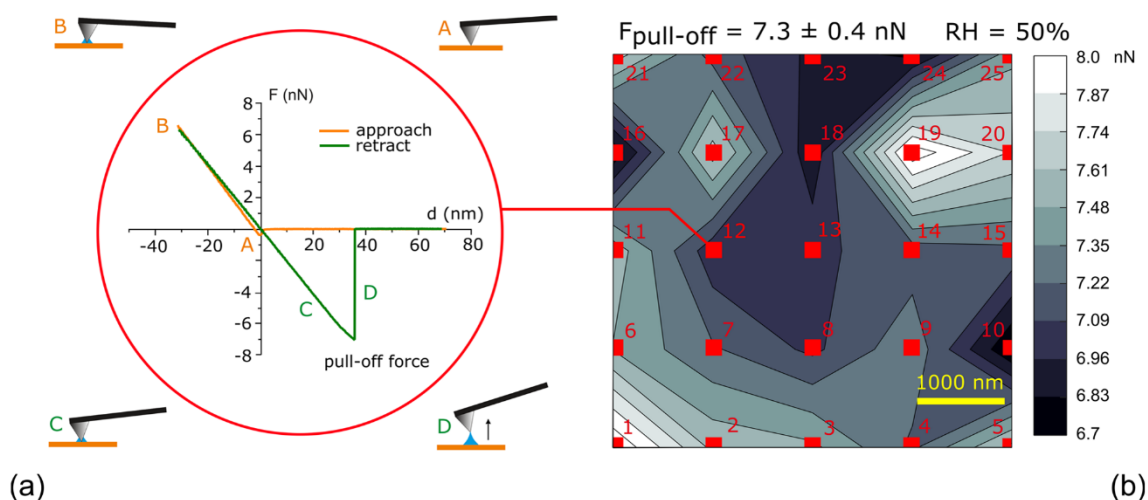


Figure 1. Force–distance curve taken during approaching/retracting the tip to/from the surface at one point (a) and the 5×5 point map of the pull-off forces (b). The red squares (b) mark the points where the individual force–distance curves (a) were measured gradually in the order of numbers.

calculate the pull-off force as a function of RH based on density functional theory,¹⁵ Monte Carlo simulations,^{16–19} and classical thermodynamic Kelvin equation calculations.^{20,21} However, the conclusions of individual authors are different, often not only quantitatively but also qualitatively, and strongly vary with small changes of the conditions or input parameters of the calculation.

This article deals with the study of water meniscus using AFM force–distance spectroscopy. Moreover, an effort was made to eliminate the ambiguity in the experiments on RH pull-off force dependence by more thorough investigation of measurement reproducibility. This part is aimed at the study of limits of the AFM force–distance spectroscopy and shows the experimental conditions and procedure providing sufficient reproducibility. Then, the results are explained by numerical calculations based on the classical Kelvin equation utilizing variable surface tension for nanometer-sized water bridges. Although the first-principles calculations were not used, the applied semiempirical classical treatment may give an insight into the behavior of water at nanometer volumes.

METHODS

The pull-off force measurements were performed with a commercial multifunctional SPM system (NTEGRA Prima, NT-MDT). The RH in the working environment of AFM was controlled during the experiments by a home-built flow box fitted to the measuring head of the microscope (the scheme of the setup is given in Figures S1 and S2). To achieve a specific RH within the range 5–90%, a variable mixture of dry and H₂O-saturated nitrogen was flown through the box. The accuracies of the commercial digital sensor (SHT15, SENSI-RION) were $\pm 2\%$ (for RH within the range 10–90%) and $\pm 4\%$ (for the other RH values). The fluctuation of the adjusted RH value displayed by the sensor during one measurement was lower than 1%.

For the experiments, the substrate with the native SiO₂ surface (thickness ~ 2 nm) on Si(100) was used. The silicon samples were treated to remove organic contaminants and to achieve a hydrophilic surface; that is, before the experiment, the

silicon samples were immersed in a piranha solution consisting of 98% H₂SO₄ and 30% H₂O₂ mixed in a H₂SO₄/H₂O₂ volume ratio of 7:3 at 80 °C for 30 min. The piranha treatment increases the thickness of oxide to ~ 2.5 nm (Figure S3). Then, the silicon samples were sequentially immersed for 2 min in acetone, isopropanol, and deionized water in an ultrasonic bath (this procedure was repeated three times). The water contact angle measured on the sample surface was $\sim 40^\circ$ (measurement details²² in Figure S4). The root-mean-square roughness determined from the measured AFM topography (Figure S5) was 0.14 nm.

The single crystal silicon tips (CSG10, NT-MDT) mounted on rectangular cantilevers were used to measure the pull-off force. The spring constant of each cantilever needed for calibration of forces was estimated from the resonant frequency and quality factor (as published by Sader et al.²³) using NT-MDT software. The measurement of each cantilever spring constant was performed many times before and many times after the force–distance mapping (whenever the cantilever was retracted from the surface). The individual cantilever spring constants mutually differed; the lowest spring constant was 0.073 ± 0.002 N/m and the highest spring constant was 0.279 ± 0.014 N/m. There was no obvious difference between the values measured before and after the force–distance mapping in the standard experiment (except for the “blunting” experiment, see further). The highest standard deviation (SD) of the spring constant occurred for the cantilever used in the “blunting” experiment (spring constant: 0.154 ± 0.051 N/m), which could be caused by the development of a mechanical stress in the cantilever during this process. This is also supported by the fact that the spring constant of the cantilever before “blunting” was in the bottom part of the range and much less fluctuating (0.130 ± 0.006 N/m). All of the measured spring constants were within a range of values claimed by the producer (0.01–0.50 N/m). According to the producer, the tip apex radius should have been typically 6 nm. However, the real apex radius of an unused tip and that of the same tip after application observed by a SEM (VEGA and LYRA systems, TESCAN) was 10 nm (except for the tips used

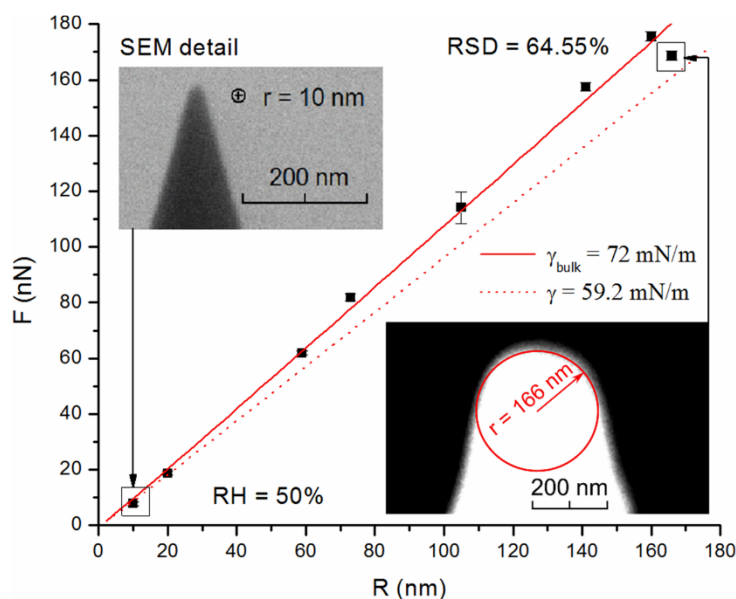


Figure 2. Measured pull-off force as a function of tip radius at a constant RH of 50% (black squares) and detailed SEM images of a new AFM tip (left inset) and blunted tip (right inset). The model based on the standard water-vapor surface tension (solid red line) and the surface tension corrected according to the improved model (dotted red line).

for the observation of the apex radius changes). The repeated measurements of tip apex angle by SEM showed the value 30° ; therefore, this value was taken for the following calculations of the water bridge shape. Before the measurement, the same hydrophilic treatment as that for the samples was accomplished for the tips. The ultrasonic bath was replaced by a mild stirring procedure so as not to damage the cantilever.

The pull-off force measured at one point was taken from the force–distance curve collected during approaching/retracting the AFM tip to/from the surface (Figure 1a). The force–distance curve is shown in a plot of the vertical cantilever deflection (calibrated to the tip–sample force) versus the lever–sample distance. The lever–sample distance was measured between the sample and the rigidly held back end of the cantilever and determined from the vertical extension of the piezo tube. During approaching, the lever bends downward the sample as the tip senses attractive forces, and further after getting into contact, the lever bends upward due to repulsive forces. The maximum repulsive force, being equal to the applied load force, was 5 nN (for the dependence on the tip radius – Figure 2) and later only 1 nN (for the dependence on RH – Figure 4) to avoid a progressive destruction of the tip. During retraction, an additional adhesive force comes into action and rapidly increases the force necessary to pull the tip off the surface. This so-called pull-off force corresponds to the point where the attractive force gradient equals the spring constant of the cantilever.²⁴ Therefore, the actual pull-off force is not precisely equal to the maximum adhesive force, but it is affected by the cantilever stiffness: the less stiff the cantilever, the lower the pull-off force obtained (theoretically, if the cantilever was infinitely stiff, the pull-off force would be equal to the maximum adhesive force). This fact has a fundamental impact on the interpretation of the pull-off force on the basis of an adhesive force model and is crucial for performing the experiment when the same cantilever (with the same stiffness)

is used for all individual comparative measurements of RH dependence in this work.

Each force–distance curve consisted of 1000 data points. The approach and withdrawal of the tip during the measurement of one force–distance curve took 2 s, and the resting of the tip on the surface at the maximum load force took 20 s. The static part was chosen considerably longer (20 s) than the 2 s lasting dynamic part (approach/withdrawal) to achieve the conditions closer to the thermodynamic equilibrium of water-bridge condensation. Wei et al.²⁵ proved that the equilibrium time was ~ 4.14 s, which was reliably met in this work.

To reduce statistical errors and the influence of surface roughness, the pull-off forces were measured in $n \times n$ points of a square matrix to get the force map of a specific region with dimensions of $5 \times 5 \mu\text{m}^2$ (Figure 1b). The total pull-off force was then evaluated as an average value across these points and the SD was calculated from all of the n^2 pull-off forces.

RESULTS

Influence of the Tip. The AFM tip is the most unknown variable in the interpretation of the measurement of the pull-off force. This results not only from different stiffness coefficients for each cantilever but also mainly from the difficulties in the determination of the tip radius (shape) and the contact angle between the tip and the water surface. The tip shape significantly influences the course of the force–RH dependency.^{26–29} Tao et al.³⁰ tried to estimate the wetting properties of the tip through the force–distance curves measured for different liquid surfaces. However, their determination was strongly dependent on the proper knowledge of the tip radius that had been estimated by deconvolution of an image from an AFM calibration grid of sharp spikes.³¹ For the small radii of the tip used in this work, this method proved to be insufficiently precise. Therefore, SEM was used for finding

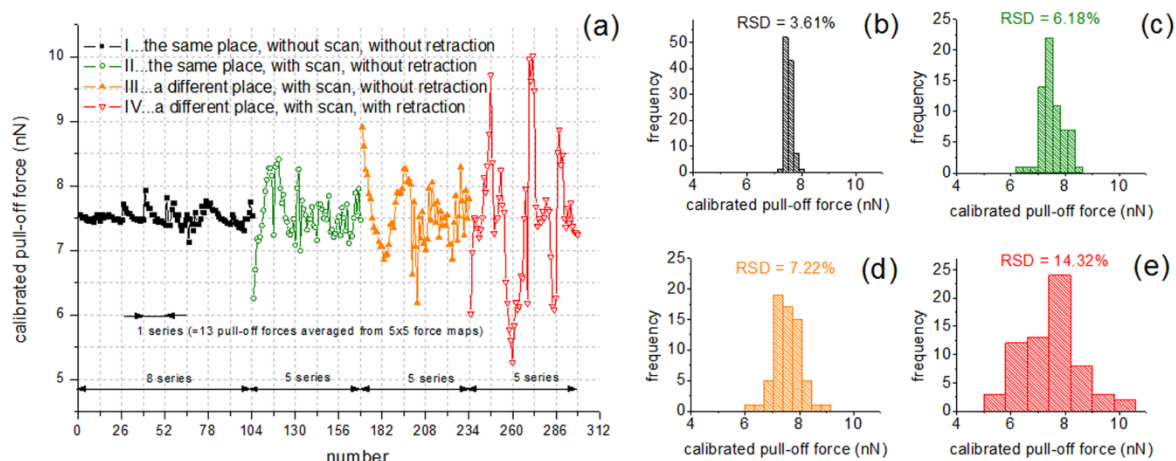


Figure 3. Reproducibility measurement: calibrated pull-off force for different procedures carried out at constant RH and tip radius (a). The corresponding histograms are in (b), (c), (d), and (e), respectively. Each calibrated pull-off force is an average of 5×5 pull-off forces taken in one force map; however, the relative standard deviation (RSD) was calculated from all forces measured in maps. The number of gradually measured force maps is marked along the x axis.

the tip radius and its impact on the pull-off force, as depicted in Figure 2.

There is a strong dependence of the pull-off force on the tip radius. The obtained experimental data can be quite well approximated by a line (Figure 2). The experiment was carried out at constant RH (50%), at which the tip was intentionally “blunted” during repeated force–distance spectroscopy (30×30 points) at a high load force of 5 nN. The pull-off force changed from 5 nN to almost 180 nN upon increasing the radius of the tip from about 10 to 170 nm. The result implicates that such a change of the radius of the tip during the pull-off force measurement can prevail the contribution of other parameters (mainly the RH *v.i.*). To eliminate the changes of the tip during the spectroscopic experiment, the decrease of the load force to 1 nN and reduction of the number of measured points to 5×5 were successfully applied.

When the tip is pushed toward the surface, the radius of the circular contact area between the tip and the surface is in the range from 1.89 nm (radius of the tip 10 nm, load force 1 nN, measurement) to 12.27 nm (radius of the tip 170 nm, load force 5 nN, blunting) according to Johnson–Kendall–Roberts²⁴ theory. However, the pull-off force is measured at a point on the force–distance curve (Figure 1) when the total adhesive force is (almost) in equilibrium with the pull-off force. At this point, the contact load force between the tip and the surface is close to zero and also the contact area is close to the point contact.

Reproducibility. Besides the control of the input parameters (e.g., RH, load force, temperature, etc.), also the methodology (procedure) of the AFM pull-off force measurement is important for keeping the sufficient reproducibility of the experiment. This is especially important when the results of pull-off force measurements on different samples are being compared.

The different testing procedures were performed as follows. The standard testing pull-off force measurement, giving its average value out of 5×5 points (map) at the load force 1 nN (Figure 1b), was repeated 13 times in one series by keeping one of four different types of measurement procedures and using one AFM tip. The AFM tips were changed only between the

series. The measurement procedures varied from each other by the number of interventions into the experiment after each map measurement. The first one (I) was performed across the same surface area, without scanning along the surface and without macroscopic retraction (more than $1 \mu\text{m}$) of the tip between each pull-off force mapping. The others sequentially added the scanning of the area (II), change of the scanning area (III), and retraction of the tip (IV). The series of procedure I was repeated eight times and that of the other ones five times, and the results are shown in Figure 3. As more cantilevers (with different real stiffness coefficients) had to be used for this purpose (to keep the radius of the tips same), the pull-off force had to be calibrated so that the results could be compared. The smaller pull-off force fluctuations during the same procedure and under the same conditions indicate better reproducibility of the specific methodology.

To quantify the rate of reproducibility, the RSD was calculated for each procedure. The RSD is defined as a ratio of SD and average force corresponding to one procedure. Theoretically, the better the reproducibility, the smaller the RSD.

The RSD was ascending from the most to the least reproducible procedure as follows: 3.61% (I), 6.18% (II), 7.22% (III), and 14.32% (IV), as can be seen from the fluctuation of calibrated pull-off forces and RSD histograms in Figure 3. It can be simply said that the higher number of measurement steps (interventions) in the used measurement methodology (procedure) results in rapid deterioration of reproducibility. This fact radically limits the interpretation of the individual experiments. For instance, the experiment depicted in Figure 2 was performed in a way being very close to procedure IV, whose reproducibility expressed in RSD was the worst one (14.32%) but sufficient to make conclusion about much stronger linear dependence of pull-off force on tip radius, whose RSD was about 4.5 times higher ($\sim 65\%$). In the case of weaker dependence, the measurement procedure plays a critical role, as will be seen in the next section.

Influence of the RH. The previous experiments have shown how important is to reduce tip radius changes and choose a proper methodology to provide sufficient reproducibility.

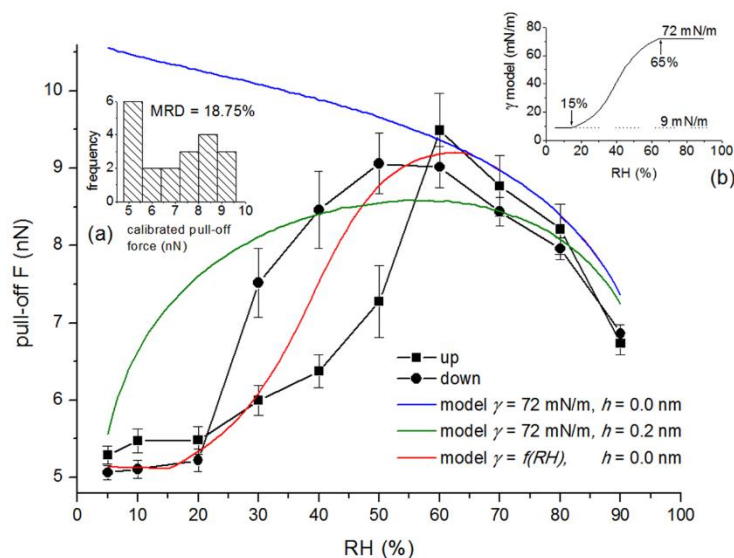


Figure 4. Measured pull-off force dependence on upward/downward changes of the RH (the error bars are the \pm SD) and the corresponding fit by a model for different surface tension of water, γ , and the shortest distance between the tip and surface, h . The left inset: corresponding histogram of the pull-off forces and calculated RSD. The right inset: model assuming the variation of surface tension for small water bridges.

bility of pull-off force measurements. Considering this fact, correct measurements of pull-off forces as a function of RH were carried out (Figure 4). To avoid the changes caused by different tip parameters, the whole dependence was measured using one tip to guarantee the constant coefficient of stiffness. Moreover, the small area pull-off force maps (5×5 points) obtained at a low load force (1 nN) (Figure 1) were the subject of investigation; thus, the changes of the tip radius were kept low and were not observable by SEM. The whole measurement was performed in the most reproducible manner (procedure I) over the same area, that is, without scanning and macroscopic retraction of the AFM tip.

The RH was being changed upward and downward in 20 steps between 5 and 90% of RH. Before measurement of each pull-off force map, the RH in the flow box had been set to the desired value and kept constant for 20 min to stabilize the conditions. There were three different regions in the pull-off force versus RH dependence curve (Figure 4). First, the force was constant for the RH below 20%. In the RH interval 20–60%, the force was increasing from 5 nN to almost 10 nN with RH. Finally, for RH above 60%, the force was decreasing with RH. Furthermore, the hysteresis between the upward and downward parts of the measuring cycle was visible, primarily in the RH interval 20–60%, which can be attributed to the rests of water trapped on hydrophilic silicon dioxide if the RH is gradually changed from higher to lower.

The changes of the pull-off forces as a function of RH are much bigger than the fluctuations of forces when the RH had been kept constant during the previous reproducibility testing; therefore, the conclusions about the influence of RH on pull-off forces are statistically valid. This is shown by much larger dispersion of calibrated pull-off force values depicted in the histogram in Figure 4 (left inset) in comparison with that in the histogram of reproducibility testing procedure I in Figure 3b. This fact has also been quantitatively proved by the calculated RSD, being almost 6 times higher in the case of RH dependence (21.3 vs 3.6%).

Model Assuming the Surface Tension Changes for Small Water Bridges. As previously mentioned, a theoretical model for indirect determination of water meniscus from pull-off force measurements is essential. The model provides the relationship between the shape of the meniscus and the pull-off force.

The computational model is based on the Kelvin equation that gives the relationship between the principal radii of meniscus curvatures, r_1 (<0), r_2 (>0) (Figure 5), and the RH

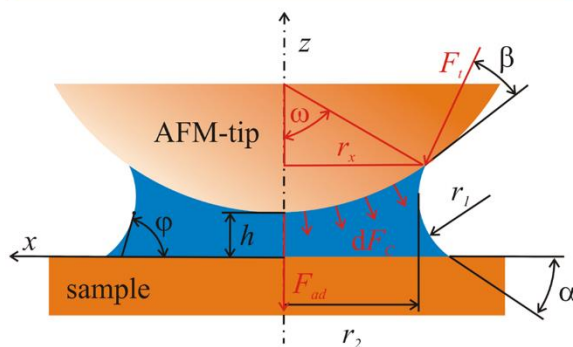


Figure 5. Geometry of the water bridge envelope (meniscus) between the AFM tip and the surface.

expressed by the ratio of partial water vapor pressure, p_v , and saturated water vapor pressure, p_v^* :³²

$$r_K = \left(\frac{1}{r_1} + \frac{1}{r_2} \right)^{-1} = - \frac{\gamma_{LV} V_m}{RT \ln \left(\frac{p_v}{p_v^*} \right)} \quad (1)$$

where γ_{LV} is the interfacial energy of liquid and vapor water, V_m is the molar volume of water, R is the molar gas constant, and T is the thermodynamic temperature. r_K is the Kelvin radius equal

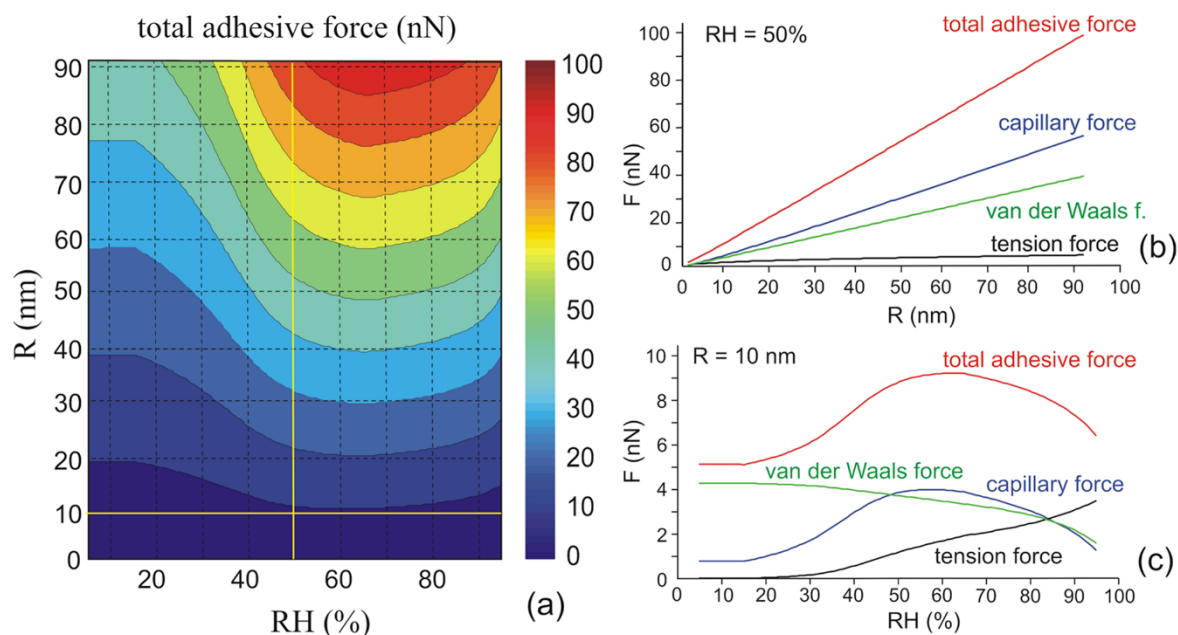


Figure 6. Calculated total adhesive force as a function of the tip radius and RH for water–surface and water–tip contact angles $\alpha = \beta = 40^\circ$ (a). Profiles of the total adhesive force and its constituents for a RH of 50% (b) and a tip radius of 10 nm (c).

to the radius of an equivalent spherical liquid droplet ($r_K > 0$) or vapor cavity ($r_K < 0$) being in equilibrium with its vapor or liquid, respectively. Considering the term $\gamma_{LV}V_m/(RT) = 0.54$ nm for the water–air interface at room temperature and RH ($< 100\%$), the water bridge under the AFM tip has a concave shape (cavity-like nature) and is thermodynamically stable. To find the shape of the meniscus envelope, the Young–Laplace equation for an axisymmetric meniscus in the form³⁵

$$\frac{dx}{d\varphi} = \frac{\cos(\varphi)}{1/r_K - \sin(\varphi)/x} \quad (2)$$

$$\frac{dz}{d\varphi} = \frac{-\sin(\varphi)}{1/r_K - \sin(\varphi)/x} \quad (3)$$

was numerically solved. Here, φ is the angle between the meniscus surface tangent and the horizontal (sample surface) plane (Figure 5). The boundary conditions are given by the contact angle of water on the sample surface, α , and on the tip surface, β .

Provided that the water bridge envelope was known, the total adhesive force, F_{ad} , acting on the tip could be calculated as a vector sum of the capillary force, \vec{F}_c , tension force, \vec{F}_t , and van der Waals force, \vec{F}_v (Figure 6)

$$\vec{F}_{ad} = \vec{F}_c + \vec{F}_t + \vec{F}_v \quad (4)$$

The chemical bonds between the tip and the sample were neglected as both the tip and the sample surface were expected to be chemically saturated. Furthermore, the electrostatic forces were put equal to zero as the tip and sample had been exposed to air for a few hours; thus, the net charges were assumed to be neutralized.

All of the three forces on the right side of eq 4 get reduced when the tip–sample distance increases. Consequently, the adhesive force achieves its maximum value at the shortest tip–

sample distance at which no tip–sample deformations occur yet.

The capillary force²⁴ is caused by the Laplace pressure decrease in the water bridge as a consequence of the negative Kelvin radius, r_K . Yang et al. have experimentally proved that the pressure inside the meniscus can be strongly negative.³⁴ The absolute value of the Laplace capillary force is given by the pressure difference ΔP and the area of the tip wet by water, A (more precisely, by its horizontal projection)

$$|\vec{F}_c| = \Delta P \cdot A = \frac{\gamma_{LV}}{|r_K|} \pi \cdot r_x^2 \quad (5)$$

where r_x is described in Figure 5.

The tension force is caused by the tension along the triple line, and its z -component can be calculated subsequently

$$|\vec{F}_t|_z = 2\pi r_x \gamma_{LV} \cos(\beta) \sin(\omega) \quad (6)$$

Assuming that the van der Waals interaction is much lower in water than in air, the total contribution of van der Waals forces acting between the sphere and the plane was approximated using the following equation

$$|\vec{F}_v| = (H_{air}(1 - \text{rel}A) + H_{water} \text{rel}A) \frac{R}{6h^2} \quad (7)$$

where $H_{air} = 10.38 \times 10^{-20}$ J and $H_{water} = 1.9 \times 10^{-20}$ J are the Hamaker constants for the interfaces $\text{SiO}_2/\text{air}/\text{SiO}_2$ and $\text{SiO}_2/\text{water}/\text{SiO}_2$, respectively. According to Israelachvili,³² the shortest distance between the tip and the surface atoms in the contact was chosen comparable with the radius of an average molecule as $h \approx 0.2$ nm. Parameter $\text{rel}A$ is the relative area of the tip surface being covered by the bridge water and can be expressed by the relationship $\text{rel}A = A(\text{RH})/A(\text{RH} = 99\%)$, where $A(\text{RH})$ is the tip area covered by condensed bridge water at specific RH and $A(\text{RH} = 99\%)$ is the tip area covered by condensed water at RH = 99%. If there are no water

vapors involved in outside environment, the total van der Waals force consists only of the air contribution and reaches a value of ~ 4.32 nN. However, for a RH of 99% and a tip radius of 10 nm, the whole van der Waals force consists only of the water contribution and is more than 5 times lower (~ 0.79 nN).

Assuming that for individual measurements the cantilever with the same stiffness was used, the dependence of the measured pull-off force on the humidity should correspond to the numerical model and thus this model can be used to explain the experimental data.

The model predicts the linear increase of the total adhesive force with the radius of the tip, which is in agreement with the experimental results presented in Figure 2 (solid red line). However, to meet the slope of the experimental curve, the cantilever stiffness had to be changed in the model from 0.15 ± 0.05 N/m (the value given by the producer) to 0.11 N/m. The linear dependence of the pull-off force on the tip radius was always observed in these experiments, which verifies the validity of the model.

To explain the dependence of the total pull-off force on the RH, the more complex consideration had to be done. First, it is essential to realize that the adhesive force in the model achieves its maximum when the tip is in touch with the surface (zero tip–sample distance h) and the measured pull-off force is approximately equal to this maximum.²⁴ The total adhesive force as a function of RH calculated for the tip touching the substrate surface ($h = 0$) is depicted in Figure 4 (blue curve). The force monotonically decreases with RH from 10.5 to 7.5 nN. There is agreement with the measured data only for the RH above 65%, whereas for the lower RH, the model does not fit to the experiment.

Second, better agreement between the model and the experimental data is achieved when a small tip–sample distance, $h = 0.2$ nm, is assumed, as was previously analytically done by Xiao et al.³⁵ Then, both increasing and decreasing tendencies of the total adhesive force, similar to those in the experiment, were obtained and its value ranges from 5.5 to 8.5 nN (Figure 4, green curve). The model data fit quite well to the measured one for the RH above 60%, and in accordance with the experiment, the adhesive force increases with RH up to RH = 40%. However, the increase follows a concave curve and does not correspond to the experimental one, which is characteristic of the transition from the concave to the convex form with the inflection point between 30 and 50% of RH. Moreover, the experimental data are almost constant below RH = 30%, whereas in the model, they rapidly fall down.

Third, the previous discrepancies between the model and the experimental data indicate the limits of the classical macroscopic Kelvin equation and its parameters, mainly the surface tension. Early in the 19th century, Gibbs had concluded that surface tension depends on the curvature when the droplet size is very small (on the order of a few nanometers). In 1949, Tolman³⁶ found that the surface tension was decreasing with the decreasing droplet size in a wide range and obtained the formula of surface tension, which proved Gibbs's conclusion and could be written in a simplified form³⁷

$$\frac{\gamma}{\gamma_{\text{bulk}}} = \frac{1}{1 + 2\delta_{\infty}/R_s} \quad (8)$$

where γ is the surface tension for a specific final radius of the droplet, R_s , γ_{bulk} and δ_{∞} are the surface tension and Tolman length, respectively, for a droplet of infinite radius. Considering

the radius of the tip to be 10 nm, RH 5%, and water surface tension 72 mN/m, the volume of water trapped in the meniscus is only 1.611 nm³, which corresponds to the radius of an equivalent water sphere, $R_s = 0.727$ nm. Hence, upon choosing the Tolman length $\delta_{\infty} = 0.096$ nm for water,³⁸ the surface tension of water calculated according to eq 8 is 57 mN/m. This implies about 20% reduction of surface tension for a bridge of nanometer dimensions. A simple direct application of Tolman's equation (eq 8) in the Kelvin formula expressed in the form of eqs 2 and 3 is not possible because the dimensions of the water bridge meniscus or equivalent sphere radius, R_s , which are necessary for surface tension calculation, are obtained only after solving the differential equations themselves (self-consistent problem). As the decrease of surface tension in eq 1 under the same boundary conditions leads to a reduction in the dimensions of the meniscus and, consequently, to a further decrease of surface tension (see eq 8), finding the correct dimensions and surface tension is a self-consistent problem. Therefore, the solution would converge to disappearance of the water bridge that does not reflect the physical reality. However, a certain reduction of surface tension, especially for the smallest water bridges, should be included in the calculations. To meet this need, the dependence of surface tension on RH was assumed so that the best fit of the theoretical model to the experimental data of the pull-off force dependence on RH could be found. Such a best fit was achieved when the surface tension was considered constant for RH below 15% (9 mN/m) and above 65% (72 mN/m). Between these constant parts, a smooth transition described by the arctangent function was chosen, as depicted in the right inset of Figure 4. Although the onset value of 9 mN/m is much smaller than 57 mN/m obtained from the Tolman equation (see above), it provides the best agreement with the measured data. The arctangent-like transition used in the middle part has no obvious physical meaning and was chosen to provide a smooth transition between the two different surface tension values of water in nano- and macro-dimensions. However, the model intuitively using such a variable surface tension and zero tip–substrate surface distance (solid red curve in Figure 4) describes the measured data of the pull-off force reasonably well. This supports our idea of necessity to implement the changes of macroscopic thermodynamic surface tension for small volumes of water. The map of the total adhesive forces calculated from the model with implemented surface tension changes as a function of the RH and radius of the tip is shown in Figure 6a. The two cross-sectional profiles for a RH of 50% and tip radius of $R = 10$ nm are depicted in detail in Figure 6b,c, respectively. In addition to the total adhesive force, the profiles of the individual force constituents are depicted here as well. All these constituents, that is, the capillary force, tension force, and van der Waals force, show up the linear dependence on the tip radius. The main contribution comes from the capillary force and then that from the van der Waals force, whereas the tension force appears to be almost negligible even for large radii of the tip. As for the profile of the total adhesive pull-off force across the RH interval, its shape is not a straight line anymore. For the smaller tip radii and low RH, the main contribution comes from the van der Waals force, whereas the capillary force is strongly reduced due to lower values of surface tension used in the model (small dimensions of the water bridge). If the decrease of surface tension was not considered, the capillary force would overweight even in this case. For the mid RH range (50–85%), the capillary force prevails over the van der Waals force as a

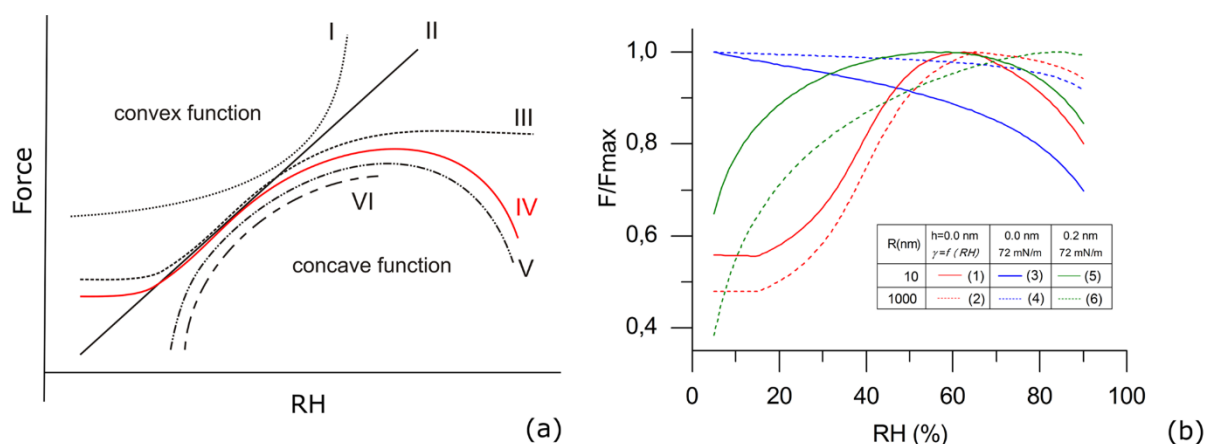


Figure 7. Qualitative comparison of the dependence of the pull-off force on RH measured by different authors (a). The increasing force RH dependence: convex (I),^{41,42} linear (II),^{45,46} convex–concave (III),^{43,44} concave (VI)^{39,40} and the increasing–decreasing dependence: convex–concave (IV)^{21,45,46,49–52} and concave (V).⁴⁸ Comparison of the models for the dependence of the relative adhesive force on RH based on the Kelvin equation (b). In the model, the different tip radii, tip–surface distance, h , and surface tension were set.

consequence of approaching the macroscopic value of the surface tension. The decrease of the van der Waals force is caused by an increasing portion of the water environment between the tip and the substrate surface. The more significant decrease of the capillary force at the highest RH compared to that of the van der Waals force is a consequence of a dominant decrease of the Laplace underpressure with the size of the water bridge. However, the tension force increases with RH in the whole RH range, which is caused by the increasing triple line length and tension force in the model, and for the values above 85%, the tension force represents the most significant contribution to the total adhesive force.

Figure 6 demonstrates the necessity of keeping the radius (shape) of the tip as constant as possible if the proper relation between the force and the amount of trapped water (proportional to RH) is to be found. A small blunting of the tip causes a rapid increase in force that has no relation to a water bridge volume change.

DISCUSSION

In principle, two types of typical behaviors of the pull-off force (or adhesive force) between the spherical tip and the flat substrate surface have been published until now depending on the RH. First, some authors have shown the increasing tendency of this force with RH (Figure 7a), and the dependence usually has the shape of a concave (VI),^{39,40} convex (I),^{41,42} convex–concave (III),^{43,44} or linear (II)^{45–47} function. Second, there have been publications where the authors present dependencies with an initial increase of the pull-off force with RH followed by its reduction for higher RH. Such dependencies have either a concave (V)⁴⁸ or convex–concave (IV)^{21,45,46,49–52} character, the latter is also the case in this work. The authors in these works mostly used silicon nitride (Si_3N_4) or silicon (Si) tips and silicon or mica substrates, both having low surface roughness and comparable water contact angles. The radii of the tips were in the range from 10 to 140 nm, except for big glass tips with a radius of 3.7 μm used by He et al.⁴⁶ and 20 μm used by Jones et al.⁴⁵ Besides the big glass sphere tips, He/Jones conducted measurements with a small Si_3N_4 (Si) tip having a radius of 10–20 (20) nm on

a silicon surface and observed a transition between the linear increase of the pull-off force with RH for big tips and a convex–concave increase–decrease for small tips. Although some authors,^{39–44} having used the tips with radii smaller than 140 nm, proved only the increasing part of the discussed dependence, this work as well as the results of the others^{21,45,46,48–52} support the final drop in force for high RH. On the other hand, the demonstrated initial convex-like growth of the force with RH^{41–46,49,50,21,52} prevails in published studies over the concave shape,^{39,40,48} which has been considered in our theoretical model.

Using the classical model with a constant surface tension value, it is possible to explain only the concave part of the initial increase both for nanotips ($R = 10$ nm) and microtips ($R = 1$ μm) (Figure 7b, curves 5 and 6). The presented model with a change of surface tension with RH can describe such a convex part of the initial growth for nanotips (curve 1). However, its application for large microtips (curve 2) is not acceptable because the volume of water trapped under the microtip is high and reaches 663 nm^3 even for the lowest RH = 5%. Therefore, using a classical model with a specific tip–surface distance ($h = 0.2$ nm) can be more suitable in case of micrometer-sized tips. On the other hand, the presented model with implemented surface tension changes is suitable only for tip radii and menisci of a few nanometer size.

Application of the Kelvin equation at a molecular scale may be speculative due to its macroscopic thermodynamic nature. To overcome this problem, Jang et al.¹⁶ performed the simulation using a grand canonical Monte Carlo method with a lattice-gas model of water. In this work, both a strongly hydrophilic tip and a weakly hydrophilic tip differing in the ratio of the water molecule–tip binding energy and the binding energy between two water molecules were used. In both cases, the radius of the spherical tips was 11 nm. The weakly hydrophilic tip resulted in an increase in the adhesive force under RH up to 40% followed by an almost constant part. On the other hand, in the simulation, the strongly hydrophilic tip led to a faster increase at low RH followed by a slow decrease at higher RH. Jang's simulations could explain the first increasing part in the experimental pull-off force dependence presented in this work. However, it cannot describe the constant and convex

dependence for low relative humidity and the stronger decrease in the adhesive force at high RH.

Another comparable molecular-scale simulation was performed by Men et al.¹⁵ using the lattice density functional theory constrained at the meniscus envelope. However, the simulation inputs were similar to those used by Jang et al.¹⁶ (tip curvature radius and hydrophilicity conditions), and they only showed either an increase of the adhesive force with RH in the case of a weakly hydrophilic tip or a decrease in the case of a strongly hydrophilic tip. Provided that no change in tip hydrophilicity occurred during the experiment presented in this work, such a result cannot explain the measured nonmonotonic dependence of the pull-off force on RH. Therefore, the model presented in our work implementing a change of surface tension with RH describes the experimental increasing–decreasing pull-off force dependence on RH for tip radii of a few nanometer size in the best way.

CONCLUSIONS

In this article, the relationship between the pull-off force and the amount of water trapped in the water bridge between a nanoscale hydrophilic AFM tip and a substrate surface at different values of RH has been investigated. Both experimental work and modeling have been done, and their results have been compared. In the experimental part, the importance and limits of the reproducibility consideration in pull-off force measurements have been demonstrated first. Next, the linear dependence of the pull-off force on the tip radius has been presented. Furthermore, it has been presented how this dependence can affect the measurement results when small changes of tip shape result in big changes in the magnitude of pull-off force. Finally, it has been shown that the dependence of the total pull-off force on RH is not monotonic and has a complex behavior consisting of an initial constant part, an intermediate section with the convex–concave-like increase of the pull-off force, and a final part having the concave-like decrease of this force.

Because such a complex behavior makes the explicit determination of the water bridge volume from the pull-off force measurement difficult, the classical thermodynamic model based on the solution of the Kelvin equation with implemented dependence of surface tension on RH has been proposed. Such a dependence assumes the transition between two states of water with low and standard surface tension values, which enables fitting the measured pull-off force data even more accurately than that using pure thermodynamic models.

Although the future theoretical strategy for description of nano-volume-water behavior will belong to the molecular computational approach, it is still necessary to adapt molecular models to real conditions. In this respect, the molecular model results for large dimensions should approach the continual model ones for small dimensions. Moreover, any more accurate measurement describing the nano-volume-bridge behavior is necessary as a feedback for any theoretical approach.

ASSOCIATED CONTENT

Supporting Information

The Supporting Information is available free of charge on the ACS Publications website at DOI: 10.1021/acs.jpcc.6b11108.

Experimental setup; thickness of oxide after piranha treatment; contact angle measurement; surface roughness (Figures S1–S5) (PDF)

AUTHOR INFORMATION

Corresponding Author

*E-mail: bartosik@fme.vutbr.cz. Phone: +420 54114 2814.

ORCID

Miroslav Bartošík: 0000-0003-4706-9112

Notes

The authors declare no competing financial interest.

ACKNOWLEDGMENTS

We acknowledge the support by Technology Agency of the Czech Republic (grant No. TE01020233), European Regional Development Fund (project No. CZ.1.05/1.1.00/02.0068), MEYS CR (project No. LQ1601 – CEITEC 2020), the Grant Agency of the Czech Republic (grant No. 17-21413S, grant No. 15-21581S), and BUT (project No. FSI-S-14-2496).

REFERENCES

- Jenkins, K.; Camacho, J.; Farina, L.; Wu, Y. Examination of Humidity Effects on Measured Thickness and Interfacial Phenomena of Exfoliated Graphene on Silicon Dioxide via Amplitude Modulation Atomic Force Microscopy. *Appl. Phys. Lett.* **2015**, *107*, 243107–4.
- Gueye, B.; Zhang, Y.; Wang, Y.; Chen, Y. Experimental and Theoretical Investigations on the Nanoscale Kinetic Friction in Ambient Environmental Conditions. *Nano Lett.* **2015**, *15*, 4704–4712.
- Yeo, C.-D.; Lee, J.; Polycarpou, A. A. Dynamic Adhesive Forces in Rough Contacting Bodies Including Normal and Sliding Conditions. *J. Adhes. Sci. Technol.* **2012**, *26*, 2709–2718.
- Yaqoob, M. A.; De Rooij, M. B.; Schipper, D. J. Relating Friction and Adhesion for Single Smooth Contact by Means of Models and Experiments. *Tribol. Int.* **2013**, *65*, 228–234.
- Shin, M. W.; Rhee, T. H.; Jang, H. Nanoscale Friction Characteristics of a Contact Junction with a Field-Induced Water Meniscus. *Tribol. Lett.* **2016**, *62*, 31.
- Rozhok, S.; Piner, R.; Mirkin, C. A. Dip-Pen Nanolithography: What Controls Ink Transport? *J. Phys. Chem. B* **2003**, *107*, 751–757.
- Nafday, O. A.; Weeks, B. L. Relative Humidity Effects in Dip-Pen Nanolithography of Alkanethiol Mixtures. *Langmuir* **2006**, *22*, 10912–10914.
- Bartošík, M.; Škoda, D.; Tomanec, O.; Kalousek, R.; Jánský, P.; Zlámal, J.; Spousta, J.; Dub, P.; Šíkola, T. Role of Humidity in Local Anodic Oxidation: A Study of Water Condensation and Electric Field Distribution. *Phys. Rev. B* **2009**, *79*, No. 195406.
- Su, M.; Pan, Z.; Dravid, V. P.; Thundat, T. Locally Enhanced Relative Humidity for Scanning Probe Nanolithography. *Langmuir* **2005**, *21*, 10902–10906.
- Kremmer, S.; Peissl, S.; Teichert, C.; Kuchar, F.; Hofer, H. Modification and Characterization of Thin Silicon Gate Oxides Using Conducting Atomic Force Microscopy. *Mater. Sci. Eng., B* **2003**, *102*, 88–93.
- Weeks, B. L.; Vaughn, M. W.; Deyoreo, J. J. Direct Imaging of Meniscus Formation in Atomic Force Microscopy Using Environmental Scanning Electron Microscopy. *Langmuir* **2005**, *21*, 8096–8098.
- van Honschoten, J. W.; Tas, N. R.; Elwenspoek, M. The Profile of a Capillary Liquid Bridge between Solid Surfaces. *Am. J. Phys.* **2010**, *78*, 277–286.
- Harrison, A. J.; Corti, D. S.; Beaudoin, S. P. Capillary Forces in Nanoparticle Adhesion: A Review of AFM Methods. *Part. Sci. Technol.* **2015**, *33*, 526–538.
- Butt, H.-J. Capillary Forces: Influence of Roughness and Heterogeneity. *Langmuir* **2008**, *24*, 4715–4721.
- Men, Y.; Zhang, X.; Wang, W. Capillary Liquid Bridges in Atomic Force Microscopy: Formation, Rupture, and Hysteresis. *J. Chem. Phys.* **2009**, *131*, No. 184702.

- (16) Jang, J.; Yang, M.; Schatz, G. Microscopic Origin of the Humidity Dependence of the Adhesion Force in Atomic Force Microscopy. *J. Chem. Phys.* **2007**, *126*, No. 174705.
- (17) Harrison, A. J.; Beaudoin, S. P.; Corti, D. S. Wang-Landau Monte Carlo Simulation of Capillary Forces at Low Relative Humidity in Atomic Force Microscopy. *J. Adhes. Sci. Technol.* **2016**, *30*, 1165–1177.
- (18) Jang, J.; Schatz, G. C. Lattice Gas Monte Carlo Simulation of Capillary Forces in Atomic Force Microscopy. *J. Adhes. Sci. Technol.* **2010**, *24*, 2429–2451.
- (19) Kim, H.; Smit, B.; Jang, J. Monte Carlo Study on the Water Meniscus Condensation and Capillary Force in Atomic Force Microscopy. *J. Phys. Chem. C* **2012**, *116*, 21923–21931.
- (20) Stifter, T.; Marti, O.; Bhushan, B. Theoretical Investigation of the Distance Dependence of Capillary and van Der Waals Forces in Scanning Force Microscopy. *Phys. Rev. B* **2000**, *62*, 13667–13673.
- (21) Xiao, X.; Qian, L. Investigation of Humidity-Dependent Capillary Force. *Langmuir* **2000**, *16*, 8153–8158.
- (22) Navrátil, Z.; Bursiková, V.; Štáhel, P.; Sira, M.; Zverna, P. On the Analysis of Surface Free Energy of DLC Coatings Deposited in Low Pressure RF Discharge. *Czech. J. Phys.* **2004**, *54*, C877–C882.
- (23) Sader, J. E.; Chon, J. W. M.; Mulvaney, P. Calibration of Rectangular Atomic Force Microscope Cantilevers. *Rev. Sci. Instrum.* **1999**, *70*, 3967–3969.
- (24) Bhushan, B. *Springer Handbook of Nanotechnology*; Bhushan, B., Ed.; Springer: Berlin, 2004; pp 564–566, 605–630.
- (25) Wei, Z.; Zhao, Y.-P. Growth of Liquid Bridge in AFM. *J. Phys. D: Appl. Phys.* **2007**, *40*, 4368–4375.
- (26) Butt, H.-J.; Kappl, M. Normal Capillary Forces. *Adv. Colloid Interface Sci.* **2009**, *146*, 48–60.
- (27) Köber, M.; Sahagún, E.; García-Mochales, P.; Briones, F.; Luna, M.; Sáenz, J. J. Nanogeometry Matters: Unexpected Decrease of Capillary Adhesion Forces with Increasing Relative Humidity. *Small* **2010**, *6*, 2725–2730.
- (28) Çolak, A.; Wormeester, H.; Zandvliet, H. J. W.; Poelsema, B. The Influence of Instrumental Parameters on the Adhesion Force in a Flat-on-Flat Contact Geometry. *Appl. Surf. Sci.* **2014**, *308*, 106–112.
- (29) Çolak, A.; Wormeester, H.; Zandvliet, H. J. W.; Poelsema, B. Surface Adhesion and Its Dependence on Surface Roughness and Humidity Measured with a Flat Tip. *Appl. Surf. Sci.* **2012**, *258*, 6938–6942.
- (30) Tao, Z.; Bhushan, B. Wetting Properties of AFM Probes by Means of Contact Angle Measurement. *J. Phys. D: A* **2006**, *39*, 3858–3862.
- (31) Villarrubia, J. S. Morphological Estimation of Tip Geometry for Scanned Probe Microscopy. *Surf. Sci.* **1994**, *321*, 287–300.
- (32) Israelachvili, J. N. *Intermolecular and Surface Forces*, 3rd ed.; Elsevier Inc., 2011.
- (33) Sirghi, L.; Szoszkiewicz, R.; Riedo, E. Volume of a Nanoscale Water Bridge. *Langmuir* **2006**, *22*, 1093–1098.
- (34) Yang, S. H.; Nosonovsky, M.; Zhang, H.; Chung, K.-H. Nanoscale Water Capillary Bridges under Deeply Negative Pressure. *Chem. Phys. Lett.* **2008**, *451*, 88–92.
- (35) Hu, J.; Xiao, X.-d.; Ogletree, D. F.; Salmeron, M. The Structure of Molecularly Thin Films of Water on Mica in Humid Environments. *Surf. Sci.* **1995**, *344*, 221–236.
- (36) Tolman, R. C. The Effect of Droplet Size on Surface Tension. *J. Chem. Phys.* **1949**, *17*, 333–337.
- (37) Xue, Y.-Q.; Yang, X.-C.; Cui, Z.-X.; Lai, W.-P. The Effect of Microdroplet Size on the Surface Tension and Tolman Length. *J. Phys. Chem. B* **2011**, *115*, 109–112.
- (38) Lu, H. M.; Jiang, Q. Length of Droplets. *Langmuir* **2005**, *21*, 779–781.
- (39) Zaghoul, U.; Bhushan, B.; Pons, P.; Papaioannou, G. J.; Coccetti, F.; Plana, R. Nanoscale Characterization of Different Stiction Mechanisms in Electrostatically Driven MEMS Devices Based on Adhesion and Friction Measurements. *J. Colloid Interface Sci.* **2011**, *358*, 1–13.
- (40) Thundat, T.; Chen, G. Y.; Warmack, R. J. Role of Relative Humidity in Atomic Force Microscopy Imaging. *Surf. Sci. Lett.* **1993**, *294*, L939–L943.
- (41) Kim, D.-L.; Jeong, Y.-K.; Kang, M.-C.; Ahn, H.-S.; Kim, K. H. Effect of Relative Vapor Pressure on Separation of Nanoscale Contact in Atomic Force Microscope. *J. Appl. Phys.* **2010**, *108*, No. 114309.
- (42) Binggeli, M.; Mate, C. M. Influence of Capillary Condensation of water on nanotribology studied by Force Microscopy. *Appl. Phys. Lett.* **1994**, *65*, 415–417.
- (43) Sedin, D. L.; Rowlen, K. L. Adhesion Forces Measured by Atomic Force Microscopy in Humid Air. *Anal. Chem.* **2000**, *72*, 2183–2189.
- (44) Thundat, T.; Zheng, X.-Y.; Chen, G. Y.; Sharp, S. L.; Warmack, R. J.; Schowalter, L. J. Characterization of Atomic Force Microscope Tips by Adhesion Force Measurements. *Appl. Phys. Lett.* **1993**, *63*, 2150–2152.
- (45) Jones, R.; Pollock, H. M.; Cleaver, J. A. S.; Hodges, C. S. Adhesion Forces between Glass and Silicon Surfaces in Air Studied by AFM: Effects of Relative Humidity, Particle Size, Roughness, and Surface Treatment. *Langmuir* **2002**, *18*, 8045–8055.
- (46) He, M.; Szuchmacher Blum, A.; Aston, D. E.; Buenviaje, C.; Overney, R. M.; Luginbühl, R. Critical Phenomena of Water Bridges in Nanoasperity Contacts. *J. Chem. Phys.* **2001**, *114*, 1355–1360.
- (47) Yoon, E. S.; Yang, S. H.; Han, H. G.; Kong, H. An Experimental Study on the Adhesion at a Nano-Contact. *Wear* **2003**, *254*, 974–980.
- (48) Asay, D. B.; Kim, S. H. Effects of Adsorbed Water Layer Structure on Adhesion Force of Silicon Oxide Nanoasperity Contact in Humid Ambient. *J. Chem. Phys.* **2006**, *124*, No. 174712.
- (49) Chen, L.; Gu, X.; Fasolka, M. J.; Martin, J. W.; Nguyen, T. Effects of Humidity and Sample Surface Free Energy on AFM Probe-Sample Interactions and Lateral Force Microscopy Image Contrast. *Langmuir* **2009**, *25*, 3494–3503.
- (50) Stukalov, O.; Murray, C. A.; Jacina, A.; Dutcher, J. R. Relative Humidity Control for Atomic Force Microscopes. *Rev. Sci. Instrum.* **2006**, *77*, No. 033704.
- (51) Farshchi-Tabrizi, M.; Kappl, M.; Cheng, Y.; Gutmann, J.; Butt, H.-J. On the Adhesion between Fine Particles and Nanocontacts: An Atomic Force Microscope Study. *Langmuir* **2006**, *22*, 2171–2184.
- (52) Xu, L.; Lio, A.; Hu, J.; Ogletree, D. F.; Salmeron, M. Wetting and Capillary Phenomena of Water on Mica. *J. Phys. Chem. B* **1998**, *102*, 540–548.

Commented paper 2

KONEČNÝ, Martin, Miroslav BARTOŠÍK, Jindřich MACH, Vojtěch ŠVARC, David NEZVAL, Jakub PIASTEK, Pavel PROCHÁZKA, Aleš CAHLÍK a Tomáš ŠIKOLA. Kelvin Probe Force Microscopy and Calculation of Charge Transport in a Graphene/Silicon Dioxide System at Different Relative Humidity. *ACS Applied Materials and Interfaces* [online]. 2018, **10**(14), 11987–11994. ISSN 19448252. Dostupné z: doi:10.1021/acsami.7b18041

Kelvin Probe Force Microscopy and Calculation of Charge Transport in a Graphene/Silicon Dioxide System at Different Relative Humidity

Martin Konečný,^{†,‡} Miroslav Bartošík,^{*,†,‡,§,||} Jindřich Mach,^{†,‡} Vojtěch Švarc,^{†,‡} David Nezval,^{†,‡} Jakub Piastek,^{†,‡} Pavel Procházka,^{†,‡} Aleš Cahlík,^{||} and Tomáš Šikola^{†,‡}

[†]Central European Institute of Technology, Brno University of Technology (CEITEC BUT), Purkyňova 123, 612 00 Brno, Czech Republic

[‡]Institute of Physical Engineering, Brno University of Technology, Technická 2, 616 69 Brno, Czech Republic

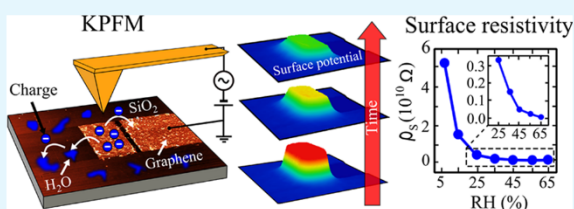
[§]Department of Physics and Materials Engineering, Faculty of Technology, Tomas Bata University in Zlín, Vavrečkova 275, 760 01 Zlín, Czech Republic

^{||}Department of Thin Films and Nanostructures, Institute of Physics, The Czech Academy of Sciences, Cukrovarnická 10/112, 162 00 Praha 6, Czech Republic

Supporting Information

ABSTRACT: The article shows how the dynamic mapping of surface potential (SP) measured by Kelvin probe force microscopy (KPFM) in combination with calculation by a diffusion-like equation and the theory based on the Brunauer–Emmett–Teller (BET) model of water condensation and electron hopping can provide the information concerning the resistivity of low conductive surfaces and their water coverage. This is enabled by a study of charge transport between isolated and grounded graphene sheets on a silicon dioxide surface at different relative humidity (RH) with regard to the use of graphene in ambient electronic circuits and especially in sensors. In the experimental part, the chemical vapor-deposited graphene is precisely patterned by the mechanical atomic force microscopy (AFM) lithography and the charge transport is studied through a surface potential evolution measured by KPFM. In the computational part, a quantitative model based on solving the diffusion-like equation for the charge transport is used to fit the experimental data and thus to find the SiO₂ surface resistivity ranging from 10⁷ to 10¹⁰ Ω and exponentially decreasing with the RH increase. Such a behavior is explained using the formation of water layers predicted by the BET adsorption theory and electron-hopping theory that for the SiO₂ surface patterned by AFM predicts a high water coverage even at low RHs.

KEYWORDS: graphene, silicon dioxide, KPFM, RH, BET, electron hopping



I. INTRODUCTION

Graphene, a single atomic layer of carbon atoms arranged in a hexagonal lattice, with its excellent electrical,^{1–4} mechanical,^{5,6} and optical properties,^{7,8} has been considered as a promising candidate to be used in the future electronic devices. Furthermore, one of the largest specific surface areas of 2630 m²·g⁻¹, the high electrocatalytic activity, and easy functionalization^{9,10} by different chemical end groups have made the graphene an ideal candidate for ultrahigh-sensitive sensors.^{11,12}

The majority of graphene-based sensors work on the principle of resistivity changes due to the adsorption of different molecules on the graphene surface where the adsorbed molecules act as electron donors or acceptors.¹³ Thanks to the linear and vanishing density of states close to the Dirac point,¹⁴ a small change in carrier concentration causes a significant change in graphene resistivity.¹⁵ A wide range of studies demonstrating the performance of graphene-based sensors for detection of gas molecules, e.g., NO,¹⁶ NO₂,^{15,17,15,17} CO₂,^{18,18} NH₃,^{15,17,19} O₂,²⁰ or water^{15,21,22} have been already published. The typical concentration sensitivity is about 100 ppb;

however, even single-molecule detection was demonstrated.¹⁵ Because of the graphene biocompatibility, the large application potential of graphene-based sensors is located in biosensing²³ where the graphene needs to be functionalized to achieve a selective reaction on different biomolecules.^{24–26}

Since most of the graphene-based sensors are required to operate in ambient atmospheric conditions, it gives rise to an important question related to the way of how the water influences the performance of graphene-based devices. For example, it has been found out that graphene field-effect transistor (FET) devices operating in ambient conditions exhibit a hysteresis in gate-voltage driven conductivity.^{27–29} The size of hysteresis depends on gate-voltage sweeping, and it was attributed to water adsorption.²⁹ Moreover, all of the individual graphene-based electronic components (e.g., FET, sensors, and capacitors) are nowadays linked to more complex

Received: November 28, 2017

Accepted: March 20, 2018

Published: March 20, 2018

electronic circuits put on one dielectric substrate. Here, the graphene sheets are often mutually placed in close proximity and the surface charge transport along the substrate enhanced by water adsorption can strongly influence the performance of the individual devices and the whole circuit as well. In addition, the dependence of SiO₂ surface conductivity on water vapors was also utilized in the design of the most sensitive relative humidity (RH) sensor by Song et al.³⁰ Therefore, the understanding of this phenomenon will play a crucial role in design of such devices and circuits. In this context, the article deals with the Kelvin probe force microscopy (KPFM) investigation and computer simulation of the charge transfer between closely separated chemical vapor-deposited (CVD) graphene sheets on insulating SiO₂ substrate as a function of RH.

It has been shown that carbon nanotubes,³¹ graphene oxide,³² and exfoliated graphene sheets³³ on an insulating substrate can be electrically charged when attached with an electrically biased conductive atomic force microscopy (AFM) tip. After the tip is retracted, these structures remain charged and this phenomenon can be monitored using the electrostatic force microscopy,³¹ KPFM,^{33,34,34} or scanning polarization force microscopy.^{35,36} Verdaguer et al.³³ studied the discharging of charged exfoliated sheets by KPFM surface potential (SP) measurements and showed that the discharging rate depends on RH and that the charge spreads from the charged sheet along the surrounding insulating substrate. Further, Shen et al.³² have found that the charge spreading from the charged sheet can be collected on the adjacent uncharged one separated by a gap.

Contrary to these studies, in this work, the charging and discharging experiments will be carried out using the CVD graphene transferred on a SiO₂ substrate and subsequently patterned by mechanical AFM lithography. The main advantage of this approach is the reproducible fabrication of isolated graphene sheets with well-defined geometries, which is also suitable for computer simulations. Moreover, the experimental data obtained from KPFM monitoring of charge transfer as a function of RH and gap size between separated graphene sheets are used in computer simulations based on a diffusion-like equation³⁷ to calculate the surface resistivity of SiO₂ substrate. To our best knowledge, the procedure enabling the finding of the precise resistivity value of poor-conductive surfaces from a time-dependent KPFM measurement has not been published yet. Finally, the dependence of surface resistivity on RH is then explained by a thermodynamic Brunauer–Emmett–Teller (BET) theory and quantum-mechanical electron-hopping theory.³⁸ It enables to utilize KPFM measurements in estimation of local small-area surface hydrophilicity/hydrophobicity (presented by an empirical parameter *k* in BET).

II. METHODS

The polycrystalline graphene layer was grown by a standard CVD method³⁹ and subsequently transferred on a p-doped silicon substrate (resistivity of (0.1–1.5) × 10⁻³ Ω·cm) with 280 nm of thermally grown SiO₂ using the conventional poly(methyl methacrylate) (PMMA)-assisted wet transfer method.^{40,41}

All of the scanning probe microscope (SPM) measurements and modifications of the graphene layer were performed by a commercial multifunctional SPM system (NTEGRA Prima, NT-MDT). The microscope head was placed in a home-built environmental chamber, enabling us to control the RH within the range from 2% up to 90%, with an accuracy ±1%.

During the mechanical lithography step, the diamond-coated AFM tip (DCP20, NT-MDT) is pushed toward the graphene surface at a high load force of 1000 nN and then the graphene is scratched away in the direction of the tip movement to pattern the graphene into a required lateral shape. The mechanical lithography was performed successfully in the contact AFM mode on the CVD graphene covering the entire area of the sample.⁴² However, the AFM lithography can also be used in the tapping mode-dynamic plowing lithography.⁴³ Further, the AFM topography measurements and Raman spectroscopy were utilized to confirm that graphene was removed from a particular area of interest (Figure S1, Supporting Information, AFM and Raman spectroscopy). The AFM topography and KPFM measurement on prefabricated structures were performed in tapping mode using conventional two-pass technique (1st AFM, 2nd KPFM). The scanning speed was 5 μm/s and the vertical distance of the second KPFM pass was 10 nm to enhance the effect of electric force. Both AFM and KPFM measurements were done by a gold-coated tip with an apex radius of the curvature of 35 nm and the resonance frequency of 240 kHz (NSG10/Au NT-MDT).

The study of charging and charge transfer process were mainly focused on two types of isolated graphene sheets geometries shown in Figure 1 (a) the single rectangular isolated graphene sheet and (b) the isolated graphene sheet separated by a gap from the graphene grounded through wire.

III. EXPERIMENTAL RESULTS

Charging of isolated graphene sheets was performed by the AFM tip, as reported previously.⁴⁴ First, the image of an isolated graphene sheet was taken in the tapping mode with the grounded tip. Then, the tip was placed above the center of the graphene sheet, brought into contact with it, and a bias voltage in the range from -8 to 8 V was applied to the tip. After 2 min, the tip was retracted keeping the tip biased. As soon as the tip was retracted from the graphene sheet, the biased voltage was switched off and the surface potential image was taken by two-pass KPFM. Schematic diagram of the KPFM second pass setup is shown in Figure 1c. Figure 1a,d shows the AFM topography and the SP image, respectively, related to the isolated graphene sheet before charging. After charging, a negative or positive change of the graphene SP according to the bias voltage polarity occurred (see Figure 1d–f). Here, the measurements were carried out at low RH (<5%) to minimize the discharging through the water adsorbed on the SiO₂ surface during the charge injection and the KPFM measurement. The observed change of the SP before and after charging (Δ SP) exhibits a linear dependence on the tip bias during the charging (see Figure 1f), which is in agreement with previous experiments done on an exfoliated graphene.⁴⁴ On the other hand, the observed Δ SP/voltage ratio 1:3 was approximately 2 times higher than in the case of the exfoliated graphene.

The main part of the experiment was concentrated on an estimation of charge transfer on SiO₂ surface between isolated and grounded graphene sheets. The central charged graphene sheet was separated by a gap from the grounded graphene defining a zero potential level in the experiment and in subsequent simulations (Figure 1c). The experiments were done for four different widths of gaps (40, 300, 1000, and 2000 nm) and within the RH range from 5 up to 65%. The graphene was charged similarly, as described in the previous experiment for isolated graphene sheet. The isolated graphene sheet was charged at very low RH (<5%) applying 6 V for 2 min. Thereafter, the RH was quickly (in less than 1 min) changed to a required value and continual KPFM imaging was being performed for 200 min. Between each charging experiment, the sample was left at least for 1 day either on air or for few hours at RH around 70% to completely discharge the graphene sheet and recover initial conditions. Figure 2a shows the SP time evolution of the charged graphene sheet and grounded graphene separated by 300 nm wide gap at 25% RH. The borders of graphene sheets are marked in the SP images by white dotted lines. Figure 2b shows the time evolution of SP profiles along the charged and grounded graphene sheet depicted in Figure 2a by the white dashed line. As evident from Figure 2b, the value of the SP of the grounded

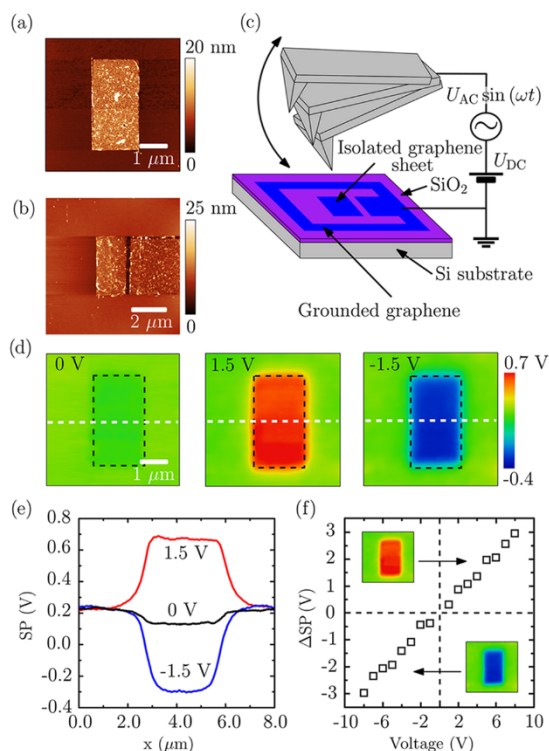


Figure 1. AFM topography image of the isolated graphene sheets on the SiO₂/Si substrate: (a) the single rectangular isolated graphene sheet and (b) an isolated graphene sheet separated by the gap from grounded graphene. (c) The schematic of KPFM setup during the charge transport mapping experiment. (d) KPFM image of a single isolated graphene sheet before charging (0 V), after charging by the voltage of ± 1.5 V applied for 2 min (black dashed lines highlight the edges of the charged graphene sheet), and (e) corresponding SP profiles (marked by the white dashed lines in d). (f) The linear relationship between the surface potential difference and the applied bias voltage during the charging. The charge injection and the KPFM measurements were done at low RH (<5%).

graphene remains constant; meanwhile, the SP on SiO₂ surface is increasing (see the arrow in Figure 2b) because of charge outflow from the charged sheet and because of the diffusion along the SiO₂. This can also be seen in Figure 2a as the spread of the light blue “halo” around the charged sheet. Figure 2c–f shows the time evolution of the Δ SP between the charged and grounded sheet in dependence on RH and on the gap width. It is remarkable that the discharging rate increases as a function of RH and decreases as a function of the gap width. In the case of 40 and 300 nm gap at RH 35 and 45%, respectively, the discharging was too quick to observe the surface potential changes by KPFM.

IV. COMPUTATIONAL RESULTS

To estimate the charge surface diffusion coefficient and the surface resistivity of SiO₂, graphene surfaces, and their dependence on RH, the experimental data were fitted by solving a two-dimensional diffusion equation (Supporting Information, diffusion equation, detailed description)

$$\frac{\partial U_{SP}}{\partial t} = c_s \left(\frac{\partial^2 U_{SP}}{\partial x^2} + \frac{\partial^2 U_{SP}}{\partial y^2} \right) \quad (1)$$

where U_{SP} is the surface potential and c_s is the charge surface diffusion coefficient of SiO₂ and graphene. Equation 1 was solved numerically using finite difference method (FDM) with the Dirichlet’s boundary condition ($U_{SP} = 0$ V) and with the requirement of the continuity of values and the first derivations at the interface of SiO₂ and graphene. The parameters of the surface diffusion coefficient of SiO₂ and graphene were optimized so that the sum of square deviations of the calculated surface potentials from the experimental values measured by KPFM would be minimal. The corresponding surface resistivity ρ_s could be then derived from the relation (Supporting Information, diffusion equation)

$$c_s = \left(\frac{1}{\rho_s C_0} \right) = \left(\frac{w}{\rho_s \epsilon_0 \epsilon_r} \right) \quad (2)$$

where C_0 is the capacitance per unit area, w is the thickness of SiO₂ dielectric layer, and ϵ_0 and ϵ_r are the vacuum and SiO₂ relative permittivity, respectively. The well-controlled fabrication of regular graphene nanostructures enables to perform the computations with the simulated sample geometry similar to that in the experiment. The simulated geometry is shown in Figure 3a, and it corresponds to the experimental one in Figure 2. The diffusion coefficient and subsequently the surface resistivity for each RH was estimated by fitting the corresponding SP profiles measured within 200 min after the charging. For this purpose, the SP profiles were taken at the same location as profiles shown in Figure 2 and were fitted by the surface diffusion coefficient of SiO₂ and graphene. The example of the fit is illustrated in Figure 3b.

Further, the utilization of diffusion eq 1 enables us to simulate the time evolution of the SP in 2D and the results correspond well with SP images obtained by KPFM measurements. Figure 3c,d shows the simulated SP time evolution for the case of graphene sheet separated from grounded sheet by 300 nm gap during the discharging at 25% RH. Finally, Figure 4 shows the RH dependence of the calculated diffusion coefficient and surface resistivity. It is evident that the diffusion coefficient increases and the surface resistivity decreases with higher RH. The estimated diffusion coefficient and surface resistivity of SiO₂ was in the range of 15×10^{-8} to 7×10^{-4} m²·s⁻¹ and 5.4×10^{10} to 1.2×10^7 Ω , respectively, within the range of RH from 5 to 65%. The graphene diffusion coefficient was 1.9 m²·s⁻¹ corresponding to the surface resistivity 4.2×10^3 Ω , supporting a much faster motion of charge across the graphene than the motion of charge on a SiO₂ layer. As expected, the charge transport is limited primarily by SiO₂; therefore, the main attention is subsequently paid to this surface. Surprisingly, both the diffusion coefficient and surface resistivity of SiO₂ exhibit also the dependence on the width of the gap between the charged and grounded sheet, although one would expect both of these properties to be independent from the sample geometry because of their infinitesimal nature. In addition, as it can be seen, the diffusion coefficient decreases and the surface resistivity increases with a wider gap. This phenomenon might be explained by a different surface resistivity in the vicinity of graphene sheet borders (step between the graphene sheet and SiO₂) where the conductivity of SiO₂ substrate could be increased due to an enhanced water adsorption at the borders and on the surface impurities in the form of graphene remaining on the SiO₂ substrate after nanostructuring the graphene using the mechanical AFM lithography. With growing width of the gap, the effect of increased conductivity near the

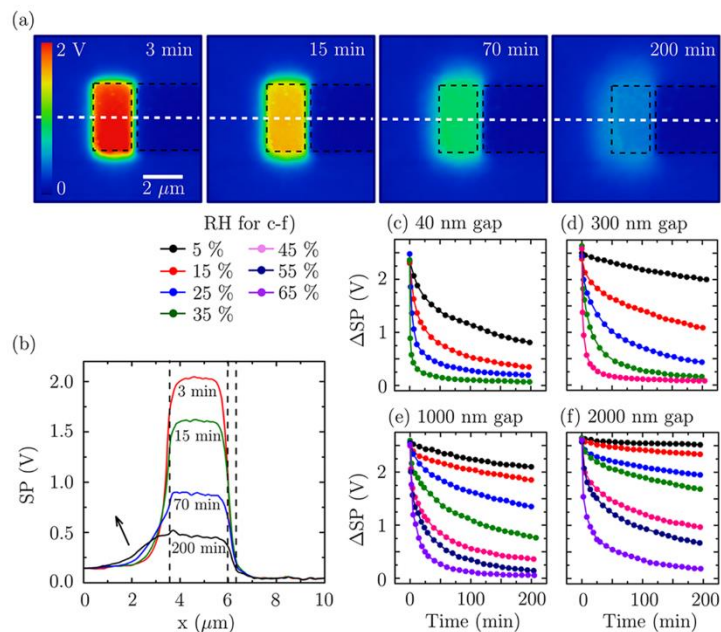


Figure 2. (a) KPFM images showing the time evolution of the surface potential measured at 25% RH and on a graphene sheet separated from the grounded one by the 300 nm gap after the isolated sheet was charged using 6 V voltage applied for 2 min. The black dashed lines in the images represent the borders of charged and grounded graphene sheets. (b) The cross-section profiles along the white dashed lines shown in the surface potential images (a). (c–f) The time evolution of the surface potential difference in the center of the charged sheet was measured within the range of the RH from 5 to 65% for the separation gaps 40, 300, 1000, and 2000 nm, respectively.

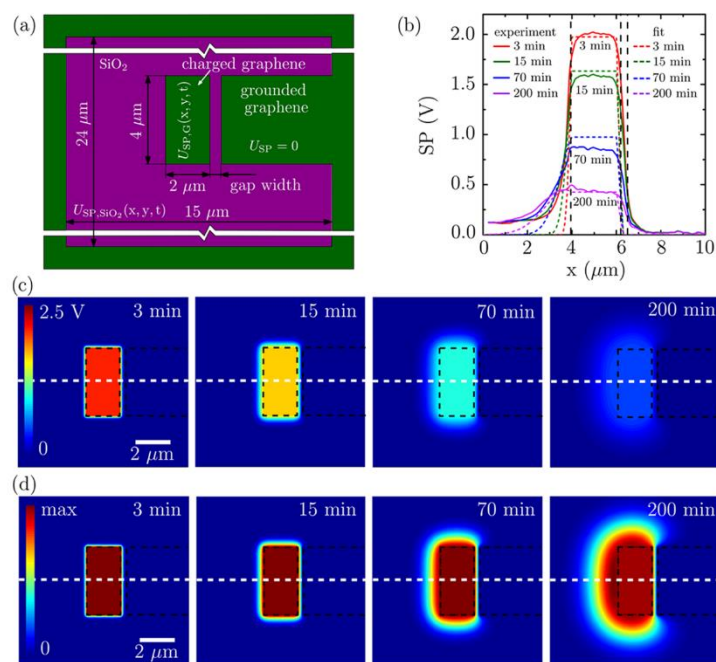


Figure 3. (a) Schematic illustration of simulated sample geometry, (b) the measured SP profiles (solid line) fitted by solving the two-dimensional diffusion eq 1 with FDM (dashed line). The example of the fit is shown for SP profiles taken at 3, 15, 70, and 200 min at 25% RH after the charging graphene sheet has been separated from the grounded sheet by 300 nm wide gap. (c, d) The corresponding simulated SP time evolution for the same sample geometry. The vertical black dashed lines in (b), (c), and (d) indicate the borders of graphene sheet.

graphene borders on the overall surface resistivity of SiO₂ vanishes, resulting in a decrease of the calculated surface

resistivity that is in the calculations assumed to be constant for the specific RH over the whole SiO₂ substrate. From this point

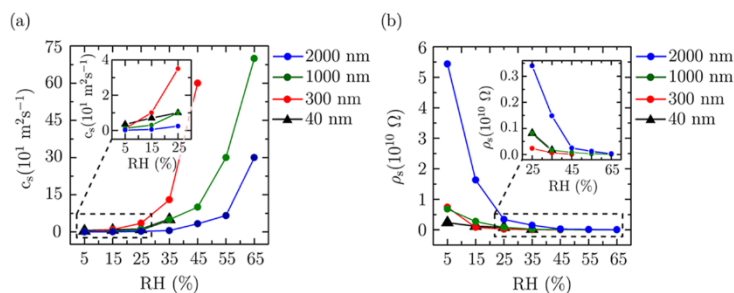


Figure 4. (a) Charge surface diffusion coefficient c_s and (b) surface resistivity ρ_s estimated for four different widths of gap between the grounded and the isolated (charged) graphene sheet. Inset graphs show the detail of the regions depicted by the dashed black line.

of view, the most precise values of the diffusion coefficient and corresponding surface resistivity typical for SiO_2 are the ones for the widest gap of 2000 nm (where the influence of borders is the smallest one). Therefore, these values are further considered in more detail.

V. DISCUSSION

The calculated values of the silicon dioxide surface resistivity in the range of 1.2×10^7 (RH 65%) to $5.4 \times 10^{10} \Omega$ (RH 5%) enables a comparison with typical values for the silicon dioxide in the literature. Voorthuyzen et al.³⁷ estimated the surface resistivity (from macroscopic transport measurement) of silicon dioxide at 96% RH for the untreated surface as $10^{10} \Omega$ and for the surface treated with the hexamethyldisilane (HDMS) as $10^{15} \Omega$. The bath in HDMS converts the hydrophilic Si–OH end groups to hydrophobic Si–O–Si–(CH₃)₃ groups so that the SiO_2 surface adsorbs less water molecules. Even from these results, the importance of adsorbed water on the surface resistivity is obvious.

Further, the previous comparison shows that the calculated values of surface resistivity are significantly lower than the values published elsewhere for higher RH. This fact may be caused by carbon residues, surface roughness, and a higher amount of surface charge traps produced during AFM mechanical lithography on the SiO_2 surface. Although the presence of a complete graphene layer in scraped places has not been proven by AFM and Raman spectroscopy (Supporting Information, AFM and Raman spectroscopy), there still might be residual carbon fragments that decrease the surface resistivity. After all, the typical graphene resistivity is approximately $10^3 \Omega$.^{45–47} Therefore, the silicon dioxide surface with carbon fragments can exhibit a much lower resistivity than the clean silicon dioxide surface. Moreover, the rougher and more curved surface after mechanical scratching will enhance water condensation,^{48–50} lowering again the surface resistivity. Finally, the resist-free mechanical lithography may be a source of higher amount of surface charge traps,⁵¹ enhancing the propagation of charge on silicon dioxide⁵² in comparison with standard optical lithography using reactive ion etching processes.^{53,54}

A deeper look into the role of water on the surface of SiO_2 enhancing the surface conductivity enables the combination of BET theory and electron-hopping theory.³⁸ According to this theory, the electrons move along the surface through quantum-mechanical tunneling, whereas the areas of clean SiO_2 and water-covered surface represent higher and lower potential barrier, respectively (Figure 5). More specifically, BET theory based on the thermodynamic equilibrium between the

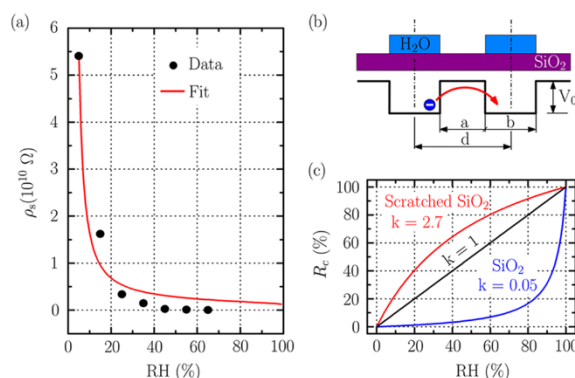


Figure 5. (a) Surface resistivity of SiO_2 as a function of relative humidity. The experimentally measured data was fitted by a model combining the BET theory and the electron-hopping model theory (eq 4) following (b) the depicted geometry and the corresponding electrostatic potential distribution. (c) The BET theory-predicted (eq 3) coverage ratio R_c as a function of relative humidity for the experimentally measured SiO_2 surface (the red solid line), for the linear growth (the black solid line), and for the typical SiO_2 surface.

condensation and evaporation of physisorbed water predicts the ratio of surface covered by water R_c as a function of RH³⁸

$$R_c = \frac{k \cdot \text{RH}}{1 + (k - 1) \cdot \text{RH}} \quad (3)$$

where k is the empirical material parameter (for SiO_2 typically³⁷ 0.05; see Figure 5c). The electron-hopping model then describes the motion of charge along the surface through quantum tunneling between the nearby water-covered SiO_2 spots across the potential barrier created by a pure SiO_2 surface (Figure 5b). In connection with BET theory, the electron-hopping theory suggests the following dependency of surface resistivity on RH³⁸

$$\rho_s = \rho_s^{100\%} \exp\left(\frac{-|p| a}{\hbar}\right) = \rho_s^{100\%} \exp\left(\frac{-|p| b \sqrt{1 - \text{RH}}}{\hbar k \cdot \text{RH}}\right) \quad (4)$$

where $\rho_s^{100\%}$ is the surface resistivity at 100% RH (when the surface is completely covered by water), $|p| = \sqrt{2mV_0}$ is the modulus of the momentum in the classically forbidden region (pure SiO_2), a is the width of the potential barrier (average size of the clean SiO_2 surface), \hbar is the reduced Planck constant, b is the average width of the water-covered SiO_2 surface, m is the electron mass, and V_0 is the height of the potential barrier (the

difference of the highest-occupied surface electron energy level on pure SiO₂ and on water-covered SiO₂ surface). Considering the typical values for SiO₂/water system,³⁸ the height of the potential barrier $V_0 = 2$ eV and the average width of pure SiO₂ spot $b = 2$ Å; the data of surface resistivity as a function of relative humidity (for the gap width $2 \mu\text{m}$) can be well fitted by eq 4, which is shown in Figure 5a, as the red curve. The fitted parameter $\rho_s^{100\%} \approx 1 \times 10^9 \Omega$ is 1 order of magnitude lower in comparison with the surface conductivity of the untreated silicon dioxide published in the literature ($10^{10} \Omega$ at 96% RH).³⁸ This can be attributed to the mentioned carbon residues and charge traps on the surface enhancing the surface conductivity. Both residues and charge traps are still present on the surface, even if the surface is completely covered by water. The fitted parameter $k = 2.7$ that characterizes the course of the surface covered by water as a function of relative humidity is many times higher than the published parameter for water/SiO₂ system,³⁷ 0.05. Therefore, the silicon dioxide surface used in this work captures the water much more, already at lower RH, as obvious from the chart of the coverage ratio in Figure 5c. This fact supports the idea of higher surface roughness as a consequence of AFM scratching and carbon residues, which enhance the condensation of water at a lower RH (Figure S3, Supporting Information, comparison of surface roughness of SiO₂ and scratched graphene on SiO₂). Moreover, the empirical parameter k used in BET theory gives the information about the vaporization heat of the first water monolayer E_1 and higher layers E_L (2nd, 3rd, etc.) since³⁸

$$k \approx \exp\left(\frac{E_1 - E_L}{RT}\right) \quad (5)$$

where R is the molar gas constant and T thermodynamic temperature. It is obvious that for the fitted value $k = 2.7$, the vaporization heat of the first layer must be higher than that for the following layers, indicating the strong hydrophilicity of the measured mechanically scratched SiO₂ surface in comparison with the standard SiO₂ surface. As already mentioned, such a hydrophilicity is the consequence of higher surface roughness helping water to condensate even at lower RH.^{48–50} This has also been confirmed by our experiments (Figure S4, Supporting Information, charge transport and surface scratch) when the charge was flowing much faster through a strong scratch along the SiO₂ surface enhancing the water condensation and increasing the charge transport, as predicted by the electron-hopping theory.

Finally, the experiment and simulation highlight an important practical fact that charge trapped in silicon dioxide is quite difficult to divert. This can be seen in the experimental Figure 2b (black arrow) and in the simulation Figure 3d, 200 min, where on the left, beside the charged graphene sheet, the charge is still kept in silicon dioxide; however, the charge on the graphene sheet is flowing away across the gap to the grounded graphene. Such an accumulation of charge outside the graphene parts is a source of additional electrical field that can influence the charge flow inside the graphene devices on SiO₂ surface, limiting their electronic width. Such an accumulation is dependent on the working time of the device so that it can exhibit a different electrical behavior, e.g., resistivity, under otherwise the same conditions, as well as it might provoke the hysteresis in resistive response of graphene/SiO₂-based devices. Therefore, the in situ observation of the surface potential

evolution close to the graphene device using KPFM enables the finding of such problematic areas to improve their design.

VI. CONCLUSIONS

The experimental part of this work has researched the charge propagation along the silicon dioxide surface between nearby CVD graphene as a function of RH studied by a measurement of surface potential using KPFM. The graphene patterning was done by mechanical AFM lithography, allowing a precise shaping and a minimal contamination in comparison with standard lithography techniques utilizing PMMA resists. The KPFM measurement proves the diffusion of charge from the charged sheet into the neighboring silicon dioxide and the nearby sheet exponentially growing with RH. The calculation using the diffusion-like equation solved by the FDM enables the estimation of the surface diffusion coefficient and especially the surface resistivity of studied mechanically “scratched” silicon dioxide in the range of $1.2 \times 10^7 \Omega$ (RH 65%) to $5.4 \times 10^{10} \Omega$ (RH 5%), which is much lower than the values listed in the literature $\approx 10^{10} \Omega$. This fact may be caused by carbon residues, roughness of the surface, and by a higher amount of surface charge traps produced during AFM mechanical lithography on a SiO₂ surface. The influence of charge traps is worth of a further study comparing distinct lithography techniques introducing different concentration of charge traps into a SiO₂ surface (such as optical lithography, electron beam lithography, and mechanical AFM lithography). Related to water condensation, the BET theory and electron hopping model-based fit of experimental data predict a much higher adhesion of water molecules onto the studied surface (the BET parameter of water adhesion $k = 2.75$) in comparison to that of the standard silicon dioxide surface ($k = 0.05$), even at lower RHs.

Therefore, the lower resistivity is attributed to the higher coverage of the surface by water molecules enhanced by surface roughness, charge traps, and also the conductive carbon residues after the mechanical lithography of graphene.

The results of the study have shown how the dynamic local mapping of surface potential using KPFM can be preferably combined with the solving of the differential diffusion-like equation to get the surface resistivity of low conductive surfaces. Moreover, the results also highlight the influence of a charge trapped on SiO₂ close to the graphene on the functionality of electronic devices based on graphene/SiO₂ interfaces, e.g., sensors; when the surrounding charge trapped in silicon dioxide can limit the electronic width of graphene channels, narrowing the electronic width of channels and causing hysteresis effects progressively evolving over time. Only the in situ observation of working graphene/SiO₂ devices by the KPFM themselves can significantly contribute to detecting the problematic charge captures.

■ ASSOCIATED CONTENT

📄 Supporting Information

The Supporting Information is available free of charge on the ACS Publications website at DOI: 10.1021/acsami.7b18041.

AFM and Raman spectroscopy of measured nanostructure, diffusion equation-detailed description, charge transport and surface scratch detail imaged by AFM and KPFM (PDF)

AUTHOR INFORMATION

Corresponding Author

*E-mail: bartosik@fme.vutbr.cz.

ORCID

Miroslav Bartošík: 0000-0003-4706-9112

Notes

The authors declare no competing financial interest.

ACKNOWLEDGMENTS

We acknowledge the support of this work by the Grant Agency of the Czech Republic (grant No. 17-21413S). We also acknowledge the Technology Agency of the Czech Republic (grant No. TE01020233) and MEYS CR (grant No. LQ1601-CEITEC 2020) for providing the background. Part of the work was carried out with the support of CEITEC Nano Research Infrastructure (LM2015041, MEYS CR, 2016–2019).

REFERENCES

- (1) Du, X.; Skachko, I.; Barker, A.; Andrei, E. Y. Approaching Ballistic Transport in Suspended Graphene. *Nat. Nanotechnol.* **2008**, *3*, 491–495.
- (2) Bolotin, K. I.; Sikes, K. J.; Jiang, Z.; Klima, M.; Fudenberg, G.; Hone, J.; Kim, P.; Stormer, H. L. Ultrahigh Electron Mobility in Suspended Graphene. *Solid State Commun.* **2008**, *146*, 351–355.
- (3) Castro Neto, A. H.; Peres, N. M. R.; Novoselov, K. S.; Geim, A. K.; et al. The Electronic Properties of Graphene. *Rev. Mod. Phys.* **2009**, *81*, 109–162.
- (4) Goerbig, M. O. Electronic Properties of Graphene in a Strong Magnetic Field. *Rev. Mod. Phys.* **2011**, *83*, No. 1193.
- (5) Frank, I. W.; Tanenbaum, D. M.; van der Zande, A. M.; McEuen, P. L. Mechanical Properties of Suspended Graphene Sheets. *J. Vac. Sci. Technol., B: Microelectron. Nanometer Struct.-Process., Meas., Phenom.* **2007**, *25*, No. 2558.
- (6) Lee, C.; Wei, X.; Kysar, J. W.; Hone, J. Measurement of the Elastic Properties and Intrinsic Strength of Monolayer Graphene. *Science* **2008**, *321*, 385–388.
- (7) Bonaccorso, F.; Sun, Z.; Hasan, T.; Ferrari, A. C. Graphene Photonics and Optoelectronics. *Nat. Photonics* **2010**, *4*, 611–622.
- (8) Avouris, P.; Freitag, M. Graphene Photonics, Plasmonics, and Optoelectronics. *IEEE J. Sel. Top. Quantum Electron.* **2014**, *20*, 72–83.
- (9) Chen, D.; Feng, H.; Li, J. Graphene Oxide: Preparation, Functionalization, and Electrochemical Applications. *Chem. Rev.* **2012**, *112*, 6027–6053.
- (10) Georgakilas, V.; Otyepka, M.; Bourlinos, A. B.; Chandra, V.; Kim, N.; Kemp, K. C.; Hobza, P.; Zboril, R.; Kim, K. S. Functionalization of Graphene: Covalent and Non-Covalent Approaches, Derivatives and Applications. *Chem. Rev.* **2012**, *112*, 6156–6214.
- (11) Yavari, F.; Koratkar, N. Graphene-Based Chemical Sensors. *J. Phys. Chem. Lett.* **2012**, *3*, 1746–1753.
- (12) Toda, K.; Furue, R.; Hayami, S. Recent Progress in Applications of Graphene Oxide for Gas Sensing: A Review. *Anal. Chim. Acta* **2015**, *878*, 43–53.
- (13) Wehling, T. O.; Novoselov, K. S.; Morozov, S. V.; Vdovin, E. E.; Katsnelson, M. I.; Geim, A. K.; Lichtenstein, A. L. Molecular Doping of Graphene. *Nano Lett.* **2008**, *8*, 173–177.
- (14) Novoselov, K. S.; Geim, A. K.; Morozov, S. V.; Jiang, D.; Katsnelson, M. I.; Grigorieva, I. V.; Dubonos, S. V.; Firsov, A. A. Two-Dimensional Gas of Massless Dirac Fermions in Graphene. *Nature* **2005**, *438*, 197–200.
- (15) Schedin, F.; Geim, A. K.; Morozov, S. V.; Hill, E. W.; Blake, P.; Katsnelson, M. I.; Novoselov, K. S. Detection of Individual Gas Molecules Adsorbed on Graphene. *Nat. Mater.* **2007**, *6*, 652–655.
- (16) Li, W.; Geng, X.; Guo, Y.; Rong, J.; Gong, Y.; Wu, L.; Zhang, X.; Li, P.; Xu, J.; Cheng, G.; Sun, M.; Liu, L. Reduced Graphene Oxide Electrically Contacted Graphene Sensor for Highly Sensitive Nitric Oxide Detection. *ACS Nano* **2011**, *5*, 6955–6961.
- (17) Lu, G.; Ocola, L. E.; Chen, J. Reduced Graphene Oxide for Room-Temperature Gas Sensors. *Nanotechnology* **2009**, *20*, No. 445502.
- (18) Yoon, H. J.; Jun, D. H.; Yang, J. H.; Zhou, Z.; Yang, S. S.; Cheng, M. M.-C. Carbon Dioxide Gas Sensor Using a Graphene Sheet. *Sens. Actuators, B* **2011**, *157*, 310–313.
- (19) Iezhokin, I.; Offermans, P.; Brongersma, S. H.; Giesbers, A. J. M.; Flipse, C. F. J. High Sensitive Quasi Freestanding Epitaxial Graphene Gas Sensor on 6H-SiC. *Appl. Phys. Lett.* **2013**, *103*, No. 053514.
- (20) Chen, C. W.; Hung, S. C.; Yang, M. D.; Yeh, C. W.; Wu, C. H.; Chi, G. C.; Ren, F.; et al. Oxygen Sensors Made by Monolayer Graphene under Room Temperature. *Appl. Phys. Lett.* **2011**, *99*, No. 243502.
- (21) Dan, Y.; Lu, Y.; Kybert, N. J.; Luo, Z.; Johnson, A. T. C. Intrinsic Response of Graphene Vapor Sensors. *Nano Lett.* **2009**, *9*, 1472–1475.
- (22) Borini, S.; White, R.; Wei, D.; Astley, M.; Haque, S.; Spigone, E.; Harris, N.; et al. Ultrafast Graphene Oxide Humidity Sensors. *ACS Nano* **2013**, *7*, 11166–11173.
- (23) Song, Y.; Luo, Y.; Zhu, C.; Li, H.; Du, D.; Lin, Y. Recent Advances in Electrochemical Biosensors Based on Graphene Two-Dimensional Nanomaterials. *Biosens. Bioelectron.* **2016**, *76*, 195–212.
- (24) Lu, Y.; Goldsmith, B. R.; Kybert, N. J.; Johnson, A. T. C. DNA-Decorated Graphene Chemical Sensors. *Appl. Phys. Lett.* **2010**, *97*, No. 083107.
- (25) Saltzgeber, G.; Wojcik, P.; Sharf, T.; Leyden, M. R.; Wardini, J. L.; Heist, C. A.; Adenuga, A. A.; Remcho, V. T.; Minot, E. D. Scalable Graphene Field-Effect Sensors for Specific Protein Detection. *Nanotechnology* **2013**, *24*, No. 355502.
- (26) Khatayevich, D.; Page, T.; Gresswell, C.; Hayamizu, Y.; Grady, W.; Sarikaya, M. Selective Detection of Target Proteins by Peptide-Enabled Graphene Biosensor. *Small* **2014**, *10*, 1505–1513.
- (27) Jung, I.; Dikin, D.; Park, S.; Cai, W.; Mielke, S. L.; Ruoff, R. S. Effect of Water Vapor on Electrical Properties of Individual Reduced Graphene Oxide Sheets Effect of Water Vapor on Electrical Properties of Individual Reduced Graphene Oxide Sheets. *J. Phys. Chem. C* **2008**, *112*, 20264–20268.
- (28) Lafkioti, M.; Krauss, B.; Lohmann, T.; Zschieschang, U.; Klauk, H.; Klitzing, K. V.; Smet, J. H. Graphene on a Hydrophobic Substrate: Doping Reduction and Hysteresis Suppression under Ambient Conditions. *Nano Lett.* **2010**, *10*, 1149–1153.
- (29) Wang, H.; Wu, Y.; Cong, C.; Shang, J.; Yu, T. Hysteresis of Electronic Transport in Graphene Transistors. *ACS Nano* **2010**, *4*, 7221–7228.
- (30) Song, S.; Yang, H.; Han, C.; Ko, S.; Lee, S. Metal-Oxide-Semiconductor Field Effect Transistor Humidity Sensor Using Surface Conductance. *Appl. Phys. Lett.* **2015**, *100*, No. 101603.
- (31) Zdrojek, M.; Mélin, T.; Diesinger, H.; Stievenard, D.; Gebicki, W.; Adamowicz, L. Charging and Discharging Processes of Carbon Nanotubes Probed by Electrostatic Force Microscopy Charging and Discharging Processes of Carbon Nanotubes Probed by Electrostatic Force Microscopy. *J. Appl. Phys.* **2006**, *100*, No. 114326.
- (32) Shen, Y.; Zhang, X.; Wang, Y.; Zhou, X.; Hu, J.; Hu, J.; Guo, S. Charge Transfer between Reduced Graphene Oxide Sheets on Insulating Substrates Charge Transfer between Reduced Graphene Oxide Sheets on Insulating Substrates. *Appl. Phys. Lett.* **2013**, *103*, No. 053107.
- (33) Verdager, A.; Cardellach, M.; Segura, J. J.; Sacha, G. M.; Moser, J.; et al. Charging and Discharging of Graphene in Ambient Conditions Studied with Scanning Probe Microscopy. *Appl. Phys. Lett.* **2009**, *94*, No. 233105.
- (34) Kondratenko, S. V.; Lysenko, V. S.; Kozyrev, Y. N.; Kratzer, M.; Storozhuk, D. P.; Iliash, S. A.; Czibula, C.; Teichert, C. Applied Surface Science Local Charge Trapping in Ge Nanoclusters detected by Kelvin Probe Force Microscopy. *Appl. Surf. Sci.* **2016**, *389*, 783–789.

- (35) Wang, Y.; Shen, Y.; Zhang, X.; Zhang, Y.; Hu, J.; Wang, Y.; Shen, Y.; Zhang, X.; Zhang, Y.; Hu, J. Humidity Induced Charge Migration on Single Layer Graphene Oxide Sheets Humidity Induced Charge Migration on Single Layer Graphene Oxide Sheets. *Appl. Phys. Lett.* **2014**, *105*, No. 233107.
- (36) Shen, Y.; Wang, Y.; Zhang, J.; Hai, C.; Zhou, Y.; Hu, J.; Zhang, Y.; Shen, Y.; Wang, Y.; Zhang, J.; Hai, C.; Zhou, Y.; Hu, J. Sample-Charged Mode Scanning Polarization Force Microscopy for Characterizing Reduced Graphene Oxide Sheets. *J. Appl. Phys.* **2014**, *115*, No. 244302.
- (37) Voorthuyzen, J. A.; Keskin, K.; Bergveld, P. Investigations of the Surface Conductivity of Silicon Dioxide and Methods to Reduce It. *Surf. Sci.* **1987**, *187*, 201–211.
- (38) Castagne, R.; Hesto, P.; Vapaille, A. Surface Conductivity of the Insulator of an MIS or MIM Device. *Thin Solid Films* **1973**, *17*, 253–264.
- (39) Li, X.; Cai, W.; An, J.; Kim, S.; Nah, J.; Yang, D.; Piner, R.; Velamakanni, A.; Jung, I.; Tutuc, E.; Banerjee, S. K.; Colombo, L.; Ruoff, R. S. Large Area Synthesis of High Quality and Uniform Graphene Films on Copper Foils. *Science* **2009**, *324*, 1312–1314.
- (40) Li, X.; Zhu, Y.; Cai, W.; Borysiak, M.; Han, B.; Chen, D.; Piner, R. D.; Colombo, L.; Ruoff, R. S. Transfer of Large-Area Graphene Films for High-Performance Transparent Conductive Electrodes. *Nano Lett.* **2009**, *9*, 4359–4363.
- (41) Suk, J. W.; Kitt, A.; Magnuson, C. W.; Hao, Y.; Ahmed, S.; An, J.; Swan, A. K.; Goldberg, B. B.; Ruoff, R. S. Transfer of CVD-Grown Monolayer Graphene onto Arbitrary Substrates. *ACS Nano* **2011**, *5*, 6916–6924.
- (42) Giesbers, A. J. M.; Zeitler, U.; Neubeck, S.; Freitag, F.; Novoselov, K. S.; Maan, J. C. Nanolithography and Manipulation of Graphene Using an Atomic Force Microscope. *Solid State Commun.* **2008**, *147*, 366–369.
- (43) Vasić, B.; Kratzer, M.; Matković, A.; Nevošad, A.; Ralević, U.; Jovanović, D.; Ganser, C.; Teichert, C.; Gajić, R. Atomic Force Microscopy Based Manipulation of Graphene Using Dynamic Plowing Lithography. *Nanotechnology* **2013**, *24*, No. 015303.
- (44) Verdaguier, A.; Cardellach, M.; Segura, J. J.; Sacha, G. M.; Moser, J.; Zdrojek, M.; Bachtold, A.; Fraxedas, J. Charging and Discharging of Graphene in Ambient Conditions Studied with Scanning Probe Microscopy. *Appl. Phys. Lett.* **2009**, *94*, No. 233105.
- (45) Song, H. S.; Li, S. L.; Miyazaki, H.; Sato, S.; Hayashi, K.; Yamada, A.; Yokoyama, N.; Tsukagoshi, K. Origin of the Relatively Low Transport Mobility of Graphene Grown through Chemical Vapor Deposition. **2012**, *2*, 337, 1–6. DOI: [10.1038/srep00337](https://doi.org/10.1038/srep00337).
- (46) Tan, Y.; Zhang, Y.; Stormer, H. L.; Kim, P. Temperature Dependent Electron Transport in Graphene. *Eur. Phys. J.: Spec. Top.* **2007**, *148*, 15–18.
- (47) Procházka, P.; Mach, J.; Bischoff, D.; Lišková, Z.; Dvořák, P.; Vaňatka, M.; Simonet, P.; Varlet, A.; Hemzal, D.; Petrevec, M.; Kalina, L.; Bartošík, M.; Ensslin, K.; Varga, P.; Čechal, J.; Šíkola, T. Ultrasoft Metallic Foils for Growth of High Quality Graphene by Chemical Vapor Deposition. *Nanotechnology* **2014**, *25*, No. 185601.
- (48) Israelachvili, J. N. *Intermolecular and Surface Forces*, 3rd ed.; Elsevier Inc., 2011.
- (49) Bartošík, M.; Kormoš, L.; Flajšman, L.; Kalousek, R.; Mach, J.; Lišková, Z.; Nezval, D.; Švarc, V.; Šamořil, T.; Šíkola, T. Nanometer-Sized Water Bridge and Pull-Off Force in AFM at Different Relative Humidities: Reproducibility Measurement and Model Based on Surface Tension Change. *J. Phys. Chem. B* **2017**, *121*, 610–619.
- (50) Bartošík, M.; Škoda, D.; Tomanec, O.; Kalousek, R.; Janský, P.; Zlámal, J.; Spousta, J.; Dub, P.; Šíkola, T. Role of Humidity in Local Anodic Oxidation: A Study of Water Condensation and Electric Field Distribution. *Phys. Rev. B* **2009**, *79*, No. 195406.
- (51) Neamen, D. A. *Semiconductor Physics and Devices: Basic Principles*, 4th ed.; McGraw-Hill, 2012.
- (52) Tarrach, F.; Ch'hayder, A.; Guermazi, S. Charge Trapping and Ac Conductivity in Amorphous Silicon Oxide. *Phys. Procedia* **2009**, *2*, 941–945.
- (53) Aitken, J. M.; Young, D. R.; Pan, K. Electron Trapping in Electron-Beam Irradiated SiO₂. *J. Appl. Phys.* **1978**, *49*, 3386–3391.
- (54) DiMaria, D. J.; Cartier, E.; Arnold, D. Impact Ionization, Trap Creation, Degradation, and Breakdown in Silicon Dioxide Films on Silicon. *J. Appl. Phys.* **1993**, *73*, 3367–3384.

Commented paper 3

ČERVENKA, Jiří, Radek KALOUSEK, Miroslav BARTOŠÍK, David ŠKODA, Ondřej TOMANEC a Tomáš ŠIKOLA. Fabrication of nanostructures on Si(1 0 0) and GaAs(1 0 0) by local anodic oxidation. *Applied Surface Science* [online]. 2006, **253**(5), 2373–2378. ISSN 01694332. Dostupné z: doi:10.1016/j.apsusc.2006.03.095

Fabrication of nanostructures on Si(1 0 0) and GaAs(1 0 0) by local anodic oxidation

Jiří Červenka, Radek Kalousek, Miroslav Bartošík, David Škoda, Ondřej Tomanec, Tomáš Šíkola*

Institute of Physical Engineering, Brno University of Technology, Technická 2, 616 69 Brno, Czech Republic

Received 25 May 2006; accepted 20 March 2006

Available online 19 June 2006

Abstract

Atomic force microscopes have become useful tools not only for observing surface morphology and nanostructure topography but also for fabrication of various nanostructures itself. In this paper, the application of AFM for fabrication of nanostructures by local anodic oxidation (LAO) of Si(1 0 0) and GaAs(1 0 0) surfaces is presented. A special attention is paid to finding relations between the size of oxide nanolines (height and half-width) and operational parameters as tip-sample voltage and tip writing speed. It was demonstrated that the formation of silicon oxide lines obeys the Cabrera–Mott theory, i.e. the height of the lines grow, linearly with tip-sample voltage and is inversely proportional to logarithm of tip writing speed. As for GaAs substrates, the oxide line height grows linearly with tip-sample voltage as well but LAO exhibits a certain deviation from this theory. It is shown that the selective chemical etching of Si or GaAs ultrathin films processed by LAO makes it possible to use these films as nanolithographic masks for further nanotechnologies, e.g. fabrication of metallic nanostructures by ion-beam bombardment. The ability to control LAO and tip motion can be utilized in fabrication of complex nanostructures finding their applications in nanoelectronic devices, nanophotonics and other high-tech areas.

© 2006 Elsevier B.V. All rights reserved.

PACS: 81.16.Nd; 81.16.Pr

Keywords: Nanotechnology; Nanostructure fabrication; Local anodic oxidation; AFM

1. Introduction

Nanotechnologies have become one of the promising research areas which might bring a significant progress into material and device development [1]. At present, there is a wide spectrum of technological approaches capable of producing nanoparticles and simple nanostructures, however, none of them can be considered as an ideal and generally acceptable tool [2]. To get specific nanoobjects and their properties, particular techniques should be selected. In addition to surface microscopy, scanning probe microscopes (SPM) find their application in fabrication of nanostructures and nanodevices as well [3]. As they represent a technique for the serial processing of surfaces, they have been exclusively used for applications in

laboratory-scale experiments on building the nanostructures and verification of their fundamental properties.

In this paper, the fabrication of nanostructures by a commercial atomic force microscope (Autoprobe, Veeco) is presented. The attention is aimed at a local anodic oxidation technique (LAO) [4] of non-noble material surfaces as Si(1 0 0) and GaAs(1 1 0). Similarly to our previous studies on Ti local oxidation [5], the influence of operational parameters such as tip-sample voltage and tip writing speed on the dimensions of nanostructures is demonstrated in particular.

2. Principles and experimental

Nanostructures have been fabricated by a commercial SPM microscope AutoProbe CP-R produced by Veeco company. The microscope is equipped with a nanotechnology software package providing the control of tip-sample voltage and tip motion according to a pre-designed pattern. In addition to this

* Corresponding author. Tel.: +420 5 4114 2707; fax: +420 5 4114 2842.
E-mail address: sikola@fme.vutbr.cz (T. Šíkola).

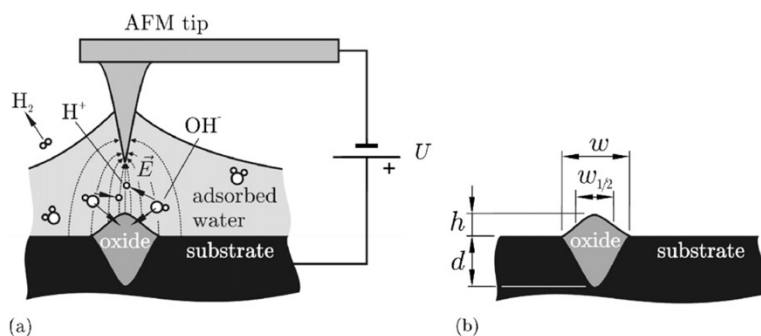


Fig. 1. (a) Schematic view of local anodic-oxidation process induced by AFM tip and (b) important parameters characterizing quality of the nanostructure lines: w , width; $w_{1/2}$, half-width; h , height; d , depth.

mode, the microscope works in standard SPM modes as in the STM mode, contact, non-contact and tapping AFM mode, magnetic mode (MFM), and lateral force mode (LFM). This makes a more detailed study of substrates and fabricated nanostructures possible.

The local-anodic-oxidation process performed by AFM is schematically shown in Fig. 1a. In this technique, oxides grow on a chemically reactive substrate by the application of a voltage between a conductive AFM tip and a substrate surface which acts as an anode. There is a threshold voltage at which the anodic oxidation starts [6]. Water molecules adsorbed on a substrate dissociates due to a high electric field ($E > 10^7$ V/m) into fragments (e.g. H^+ , OH^- , and O^{2-}) and acts as an electrolyte. Oxygen containing radicals then contribute to the formation of surface oxides and, due to an electric field-enhanced diffusion through the oxide layer, also to the growth of the oxide underneath. This field induced oxidation mechanism for very thin oxide films was first described by Cabrera and Mott [7] and adapted to LAO by Stievenard [6]. The stoichiometry of the oxide is generally not homogeneous. Owing to their lower density, the oxide protrudes above the surface and hence oxide patterns are detectable by AFM without any additional etching. Detailed chemical analysis of the local anodic oxidation process on titanium substrate is given for instance in ref. [8].

The SPM software is extended with a program package for the well-defined movement of the tip over a sample. This facility associated with the control of other tip-sample parameters gives us possibilities to accomplish pre-defined patterns at various tip-sample voltages, contact forces and speeds of the tip over a sample in the contact or non-contact mode of AFM. This enables us to control important size parameters of nanostructure objects, e.g. width (w) or half-width ($w_{1/2}$), height (h), and depth (d) (see Fig. 1b).

The local anodic oxidation was carried out in the contact AFM mode and in the regime of the contact force using silicon cantilevers with conical conductive tips coated by W_2C (MicroMasch CSC11/ W_2C). The tip radius was below 35 nm and its specific resistivity less than $50 \mu\Omega$ cm. In some cases specified below, cantilevers with conical silicon tips covered by doped diamond-like layer (Veeco, ULCT-DCBO) were applied

as well. The tips had a radius of about 100 nm and specific resistivity less than 0.1Ω cm. Nanostructures were prepared at room temperature under specific but uncontrolled relative humidity.

To imagine the already fabricated nanostructures silicon cantilevers with ultrasharp conical tips (Veeco, ULCT-AUMT) in the contact mode were used, since they gave better resolution than those applied for LAO. To find nanostructures after the tip exchange guiding scratches had been made by a diamond knife into a substrate before local oxidation.

Two substrates were used for nanostructure fabrication: Si(1 0 0) with the specific resistivity 6–9 Ω cm and GaAs(1 0 0) doped by Si (concentration, 7×10^{17} atoms/cm³). The Si(1 0 0) surface was cleared of the native oxide and passivated by hydrogen in a 2% solution of HF (etching time = 2 min). The GaAs(1 0 0) surface was not treated before oxidation.

3. Results and discussion

Fabrication and application of nanostructures for a study of their unique quantum properties and for building new nanodevices requires a reliable control of individual technological steps. To be able to prepare nanostructures of required dimensions and properties, the relations between the operation parameters of the fabrication and the resultant product parameters should be fairly well-known and understood.

Generally, the LAO process is controlled by several major parameters as follows: tip radius, air humidity, tip-sample voltage, and writing speed of a tip. As in our case, the variability of the first two parameters have been limited, we have exclusively concentrated on a study of the influence of tip-sample voltage and tip writing speed on nanostructure fabrication.

To quantify these dependences experimentally, testing arrays of nanolines were fabricated.

In Fig. 2, such an array of Si lines fabricated under a relative humidity of 46% and temperature of 23 °C is depicted. Going from left to right, in this picture, one can see the lines prepared at progressively increasing writing speeds. On the other hand, going from bottom to top, the lines made at progressively higher tip-sample voltages are present. It is obvious that the line prepared at the highest tip-sample voltage and the lowest

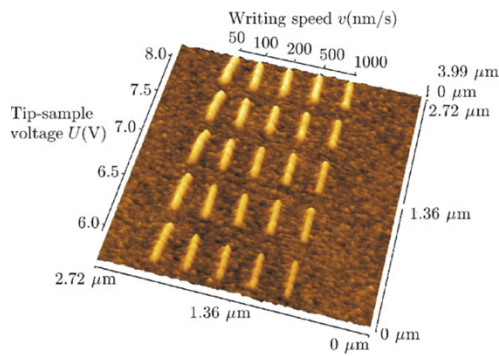


Fig. 2. A testing array of Si nanolines prepared at different tip-sample voltages and writing speeds on a Si(1 0 0) substrate (relative humidity = 46%; $T = 23\text{ }^{\circ}\text{C}$).

writing speed (top-left) is the best developed one in height and width. On the other hand, the line fabricated at the lowest tip-sample voltage and highest writing speed (bottom-right) is less developed. Such a testing line structure makes it possible to find the relations between the size of nanostructures and operational parameters as shown in Figs. 3–5.

The height of Si oxide lines showed a linear dependence on tip-sample voltage which is in agreement with the Cabrera–Mott theory. This behaviour together with linear fits to experimental data for two different writing speeds (50 and 500 nm/s) are shown in Fig. 3. The theoretical threshold voltages calculated from both fits were 2.3 and 2.5 V, respectively. However, the experimental threshold values were found for all writing speeds between 3 and 4 V which indicates the oxidation does not run linearly with voltage in the vicinity of the threshold values. The smallest height (1.5 nm) was achieved at a tip-sample voltage of 6 V and a tip writing speed of 500 nm/s.

In Fig. 4, the half-width of Si oxide lines as a function of tip-sample voltage for two distinct writing speeds is depicted. The width of nanostructures is an important parameter determining properties of quantum nanodevices. Similarly, to the height of oxide lines, their half-width grew linearly with tip-sample voltage and was the smallest one (46 nm) for the tip-sample

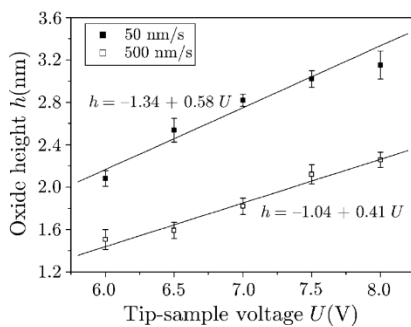


Fig. 3. The height of Si oxide lines as a function of tip-sample voltage for two tip writing speeds (relative humidity = 46%; $T = 23\text{ }^{\circ}\text{C}$).

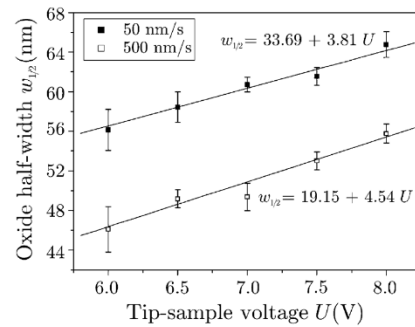


Fig. 4. The half-width of Si oxide lines as a function of tip-sample voltage for two tip writing speeds (relative humidity = 46%; $T = 23\text{ }^{\circ}\text{C}$).

voltage and writing speed corresponding to the smallest height of lines.

The Si oxide height was inversely proportional to the logarithm of tip writing speed v as demonstrated in Fig. 5. This is in agreement with the Cabrera–Mott theory [7] and in contradiction with Vullers et al. [9] who found deviations in their LAO experiments from this theory, probably due to local stresses built in oxidized Si films.

Similar dependence as in Fig. 5 has been found for the oxide line width as well.

The behaviour in accordance with the Cabrera–Mott theory makes it possible to calculate the activation energy of the oxidation process using a method described in [6]. Here, the theoretical curve corresponding to the formula derived from the Cabrera–Mott theory was fitted to the experimental one. From this fit, the parameters of the theoretical curve were found and by means of them the activation energy calculated.

Applying this procedure to our experimental data using the Origin 6.0 software, we got activation energies of 0.05 and 0.02 eV for 6 and 8 V tip-sample voltages, respectively. The dispersion in the activation energy was caused by errors in experimental data and consequent ambiguities in fitting procedure. Despite this dispersion, both activation energy values are reasonably lower than that found for local anodic oxidation of a highly reactive titanium (0.1 eV) by Vullers [10].

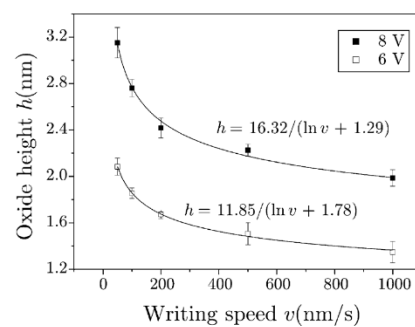


Fig. 5. The height of Si oxide lines as a function of tip writing speed for two tip-sample voltages (relative humidity = 46%; $T = 23\text{ }^{\circ}\text{C}$).

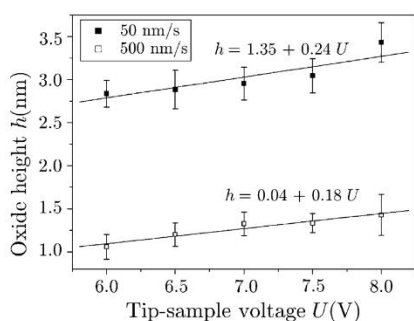


Fig. 6. The height of GaAs oxide lines as a function of tip-sample voltage for two tip writing speeds (relative humidity = 52%; $T = 22^\circ\text{C}$).

Oxide lines fabricated on GaAs substrates were generally less developed. This is demonstrated in Figs. 6–8 where analogous plots to Figs. 3–5 are presented. The oxide lines were fabricated under almost identical temperature (22°C) and a bit higher relative humidity (52%). The smallest height of an oxide line was achieved again at a tip-sample voltage of 6 V and a writing speed of 500 nm/s and was 1.1 nm (Fig. 6). The half-width of the same line was the smallest one and reached 28 nm (Fig. 7). Both height and half-width of the lines possessed a linear dependence on tip-sample voltage. Approximately, both parameters were inversely proportional to the logarithm of writing speed v , however, the fits of expected theoretical curves given by the Cabrera–Mott theory to experimental data have not been successful (Fig. 8). Hence, local anodic oxidation of GaAs was governed by similar process as in case of Si, however, cannot be fully described by the Cabrera–Mott theory.

The fact that the width of oxide lines fabricated by LAO is in one order of magnitude bigger than their height indicates that the tip apex radius is a critical parameter determining the smallest width of the lines. This was proved by LAO experiments carried out with tips coated by diamond-like protective layers (Veeco, ULCT-DCBO) which possessed a bigger apex radius ($\sim 100\text{ nm}$). The smallest half-width of oxide lines made by these tips was not smaller than 100 nm both for Si and GaAs. Correspondingly, their height was also bigger (up to 10 nm).

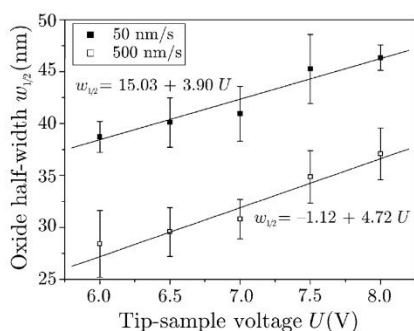


Fig. 7. The half-width of GaAs oxide lines as a function of tip-sample voltage for two tip writing speeds (relative humidity = 52%; $T = 22^\circ\text{C}$).

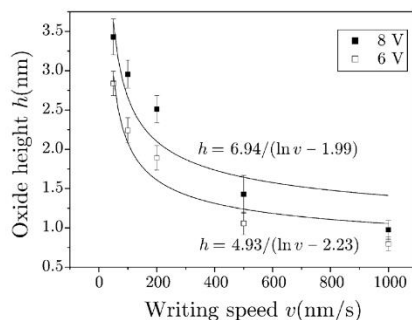


Fig. 8. The height of GaAs oxide lines as a function of tip writing speed for two tip-sample voltages (relative humidity = 52%; $T = 22^\circ\text{C}$).

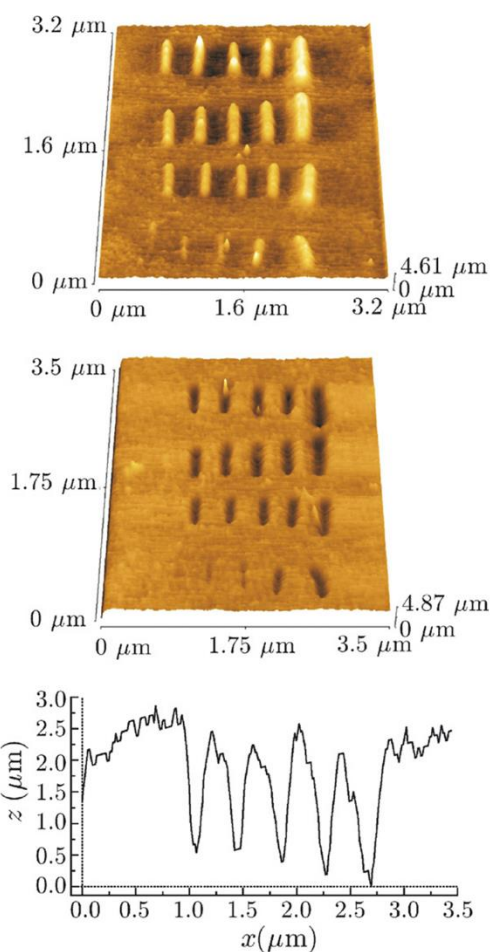


Fig. 9. Si oxide nanolines prepared by LAO (top) on a Si(1 0 0) substrate, and nanotrenches obtained by selective etching of these lines in 2% HF (middle and bottom), a ULCT-DCBO tip.

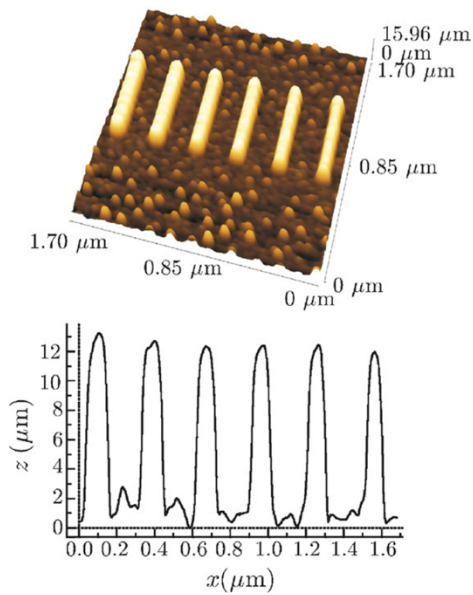


Fig. 10. Enhancement of the profile of Si oxide lines by selective etching of Si in 40% TMAH (ULCT-DCBO tip).

Another essential parameter decisive for the oxide line size is air humidity. Higher humidity resulted in bigger lines, both in height and width. This is in agreement with the results obtained for Ti oxide nanostructures in our earlier studies.

LAO can be used not only for fabrication of insulating barriers in nanoelectronic devices but also for the patterning of substrates and thin films. This is demonstrated in Figs. 9 and 10 where a Si(1 0 0) substrate surface was patterned by LAO using the ULCT-DCBO tips and after that selectively chemically etched. In Fig. 9, the Si oxide nanolines (top) and nanotrenches (middle) obtained by selective etching of these lines in 2% HF are shown. In this way, the subsurface profile of the trenches (bottom) and thus the volume of the oxide can be checked and, consequently, its chemical composition according to the method described in ref. [9] estimated. If a Si ultrathin film (<10 nm), instead of a Si bulk substrate is patterned in this way (e.g. a:Si-H ultrathin film), it can be used as a proper nanolithographic mask (positive inorganic resist). On the other hand, if we use a selective etching agent of Si (e.g. 40% TMAH), we can enhance the profile of oxide lines as shown in Fig. 10. The Si ultrathin film patterned in this way can be applied as a negative inorganic resist. Similarly to ref. [11] we utilized the mask of an amorphous silicon (a:Si-H) ultrathin film deposited by PECVD in fabrication of metallic (Ti) nanostructures by ion beam etching [12].

By choosing proper etching agents also GaAs ultrathin films patterned by LAO may find their application as nanolithographic masks. In our lab, the selective etching of oxide patterns in GaAs by a 5% HCl solution resulted in fabrication of nanotrenches similar to those in Fig. 9.

The knowledge how to control the LAO process and the availability of a proper software make us possible to prepare

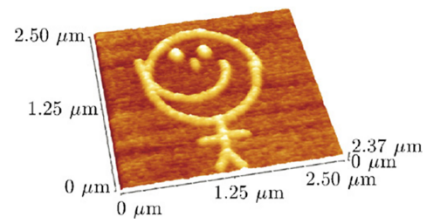


Fig. 11. A nanobot drawn by LAO on a Si substrate (ULCT-DCBO tip).

more complex nanostructures than just oxide lines. They can be used in the fabrication of nanoelectronic devices (e.g. single electron transistors, quantum rings) [13,14], nanostructures for photonics and simply in building of various miniaturized logos and protective marks. As an example of a nanostructure of more complex nature, the picture of a nanobot drawn by LAO is shown in Fig. 11. The picture was made on a silicon substrate using a ULCT-DCBO tip and, hence, the half-width of the lines was over 100 nm. On the other hand, these diamond-coated tips exhibit higher resistivity against the wear and damage compared to the sharper tips coated by W_2C and, thus, larger sample areas might be processed.

4. Conclusions

In the paper, the application of AFM for fabrication of nanostructures by local anodic oxidation is presented. In principle, the LAO process is controlled by several major operation parameters as a tip radius, air humidity, tip-sample voltage, and writing speed of a tip. Here, the role of the latter two parameters was discussed in detail. By this nanolithography technique, testing arrays of nanolines on surfaces of Si(1 0 0) and GaAs(1 0 0) substrates were prepared at different tip-sample voltages and writing speeds. In such a way, the influence of these parameters on the size (height and half-width) of the lines has been quantified. Formation of silicon oxide lines proved to obey the Cabrera–Mott theory, i.e. the height of the lines grew linearly with tip-sample voltage and was inversely proportional to logarithm of tip writing speed. GaAs local oxidation exhibited a certain deviation from this theory, but the oxide line height grew linearly with tip-sample voltage as well.

Selective chemical etching of Si or GaAs ultrathin films processed by LAO makes it possible to use these films as nanolithographic masks for further nanotechnologies, e.g. fabrication of metallic nanostructures by ion-beam bombardment. The ability to control LAO and tip motion can be utilized in fabrication of complex nanostructures finding their applications in nanoelectronic devices, nanophotonics and other high-tech areas.

Acknowledgements

This work was supported by the GAAV project IAA1010413, Ministry of Education CR (MSM0021630508) and the Austrian–Czech project Kontakt (No. 2004-15).

References

- [1] G. Timp (Ed.), *Nanotechnology*, Springer–Verlag, New York, 1999.
- [2] Nanotech, *Scientific American* September 2001 (special issue).
- [3] E.M. Ford, H. Ahmed, *Appl. Phys. Lett.* 75 (1999) 421.
- [4] J.A. Dagata, J. Schneir, H.H. Harary, C.J. Evans, M.T. Postek, J. Bennet, *Appl. Phys. Lett.* 56 (1990) 2001.
- [5] F. Lopour, R. Kalousek, D. Škoda, J. Spousta, F. Matějka, T. Šíkola, *Surf. Interface Anal.* 34 (2002) 352.
- [6] D. Stievenard, P.A. Fontaine, E. Dubois, *Appl. Phys. Lett.* 70 (1997) 3272.
- [7] N. Cabrera, N.F. Mott, *Rep. Prog. Phys.* 12 (1948) 163.
- [8] R. Held, T. Heinzel, P. Studerus, K. Ensslin, *Physica E* 2 (1998) 748.
- [9] R.J.M. Vullers, M. Ahlskog, M. Cannaearts, C. van Haesendonck, *J. Vac. Sci. Technol., B* 17 (1999) 2417.
- [10] R.J.M. Vullers, *Oxidation of Titanium Films with an Atomic Force Microscope*, PhD Thesis, Katholieke Universiteit Leuven, 2000.
- [11] N. Kramer, J. Jorritsma, H. Birk, C. Schonenberger, *Microelectron. Eng.* 27 (1995) 47.
- [12] J. Červenka, *Application of Scanning Probe Microscopy in Nanotechnology*, Diploma Thesis, Brno University of Technology, Brno, 2004.
- [13] K. Matsumoto, M. Ishii, K. Segawa, Y. Oka, *Appl. Phys. Lett.* 68 (1996) 34.
- [14] T. Ihn, *Electronic Quantum Transport*, Springer–Verlag, 2004.

Commented paper 4

BARTOŠÍK, Miroslav, David ŠKODA, Ondřej TOMANEC, Radek KALOUSEK, Pavel JÁNSKÝ, Jakub ZLÁMAL, Jiří SPOUSTA, Petr DUB a Tomáš ŠIKOLA. Role of humidity in local anodic oxidation: A study of water condensation and electric field distribution. *Phys. Rev. B* [online]. 2009, **79**, 195406 1-6 [vid. 2013-09-23]. ISSN 1098-0121. Dostupné z: doi:10.1103/PhysRevB.79.195406

Role of humidity in local anodic oxidation: A study of water condensation and electric field distribution

Miroslav Bartošík, David Škoda, Ondřej Tomanec, Radek Kalousek, Pavel Jánský, Jakub Zlámal, Jiří Spousta, Petr Dub, and Tomáš Šíkola

Faculty of Mechanical Engineering, Institute of Physical Engineering, Brno University of Technology, Technická 2, 616 69 Brno, Czech Republic

(Received 21 October 2008; published 7 May 2009)

This paper deals with the analysis of the influence of humidity on the process of local anodic oxidation carried out by atomic force microscope (AFM) on GaAs (100) surfaces. Recent experiments have shown that the height and half width of oxide nanolines do not increase monotonously with relative humidity, but for lower relative humidities (<50%) the lines comparable in size to those prepared at 90% were obtained. However, their height and width along the lines revealed significant variations. To better understand these phenomena, the AFM force-distance spectroscopy measurements together with computer simulations of an electric-field distribution and water bridge formation between the tip and the substrate at different relative humidities were carried out. Our experiments on AFM force-distance spectroscopy have not proved an enhanced water condensation between the tip and the surface at lower humidities. However, the simulations of the electric field in the vicinity of the tip at the early stages of the oxidation process at low relative humidities showed an increase in the average intensity in the oxide layer promoting the diffusion of oxidizing species toward the substrate and, hence, the formation of oxide lines under these conditions. Finally, our simulations on water bridge variations along the tip track showed that at lower humidities there are higher relative standard deviations in the size of the water bridge while the tip is being moved along the surface. This indicates why the oxide lines showed a bigger variability in size.

DOI: [10.1103/PhysRevB.79.195406](https://doi.org/10.1103/PhysRevB.79.195406)

PACS number(s): 81.16.Pr, 81.16.Nd

I. INTRODUCTION

Local formation of oxides on solid surfaces in the close vicinity of the tip of an AFM probe has become a favorite inexpensive nanotechnology method used in many laboratories worldwide. Despite the relative experimental simplicity of this technique called generally local anodic oxidation (LAO), its principles have not been understood in detail yet. The LAO is generally described by the Cabrera-Mott¹ mechanism of oxidation adapted to the configuration with an electric field between the tip and the sample² providing enhanced diffusion of charged particles in the sample.^{3,4} Most of the papers on LAO deals with empirical or semiempirical data related to particular materials. For instance, the influence of operational parameters on local oxidation, such as tip-sample voltage, tip writing speed, and tip load force, has been already studied using contact and noncontact modes of atomic force microscope (AFM).^{5,6}

LAO depends on an ionic current between the tip and the sample surface going through a water bridge between the tip and the surface. The size and shape of this bridge depends on the amount of the water condensed both on the surface and between the tip and the surface. Generally, the amount of this water increases with humidity and, hence, it has been widely accepted that the dimensions of oxide elements produced by LAO should grow with humidity as well. This presumption has been reported by several research teams for various distinct surfaces but just few exact and detailed humidity dependences have been published yet; e.g., for *n*-Si(100),⁷ *p*-Si(001),⁸ and *p*-GaAs(100) substrates for relative humidity from 50–80 %.⁹

In our previous work,¹⁰ the role of humidity in fabrication of oxide nanostructures at GaAs (100) surfaces by LAO was

investigated for a wider relative humidity interval (35–90 %). Contrary to the expectations, the height and the half width of oxide nanolines grew monotonously with relative humidity just in the relative humidity interval starting from 60% up. However, for lower relative humidities (<50%), the lines were surprisingly comparable in size to those prepared at 90%. Nevertheless, unlikely to the lines at higher humidities their height and width along the lines revealed a significant variability indicating unstable conditions for the oxidation process at lower humidity.

A similar nonstandard behavior-independence of oxide height for low relative humidities under 50% and linear dependence for higher humidities has been observed by another group as well.¹¹ This paper deals with such a phenomenon, in a more detail, and looks for some possible key factors (e.g., water condensation, surface roughness, and electric-field distribution) responsible for this more complex behavior.

II. EXPERIMENTAL DETAILS AND PRINCIPLES

An atomic force microscope (AutoProbe CP-R, Veeco) operated in the contact mode was used both in nanolithography, microscopic, and spectroscopic experiments. The probes for nanolithography were triangular silicon cantilevers (MicroMasch) with a W₂C coated tip having the average force constant 0.35 N/m and tip apex radius 35 nm, according to the producer. The real tip apex radii found by scanning electron microscope (SEM) (FEI) were in the range from 50 to 108 nm. The surface imaging and force-distance measurements were performed using rectangular phosphorus-doped silicon cantilevers (Veeco) with the average force constant

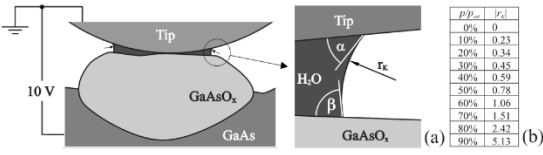


FIG. 1. Local anodic oxidation by AFM. A water bridge between the tip and the surface with the (a) meniscus detail and the values of the Kelvin radius (in nm) for (b) different relative humidity.

0.9 N/m and radius below 12.5 nm (data provided by the producer).

To carry out the oxidation, a software for nanolithography (NANOLITHOGRAPHY 1.7, Veeco) was used to control the tip trajectory, tip-surface voltage, and speed and load force of the tip. The relative humidity in the working environment of AFM was controlled during the experiments by a home-built miniflow box fitted to the measuring head of the microscope. To achieve a specific relative humidity with an accuracy of 1% within the range from 20–90 %, the variable mixture of dry and H₂O-saturated nitrogen was flown through the box. The value of humidity was controlled every 10 s by a logger with an external resistive probe.

The LAO and force-distance measurements were performed on GaAs (100) substrates doped by Si (7×10^{17} atoms/cm³) and having a specific *n*-type resistivity of 10 Ω cm. Their surface had not been treated before oxidation and spectroscopy experiments and was relatively smooth; its root-mean-square (RMS) surface roughness and average surface roughness (Ra) were 1.04 nm and 1.34 nm, respectively.

The local anodic oxidation carried out by AFM is a technique where oxides locally grow on a substrate by the application of a voltage between the conductive tip and the substrate surface acting as an anode [Fig. 1(a)]. The main process being responsible for this growth is an electric-field enhanced diffusion of oxyanions (OH⁻ and O²⁻) from the condensed water to the surface. This field-induced oxidation mechanism for very thin oxide films was first described by Cabrera and Mott¹ and adapted to LAO by Stiévenard *et al.*¹² In the case of LAO on *n*-type GaAs, a depletion layer is created in the semiconductor close to its surface. Such a barrier prevents minority holes from transfer and this process stops oxidation reaction¹³ unless sufficient external voltage is applied.

Except tip-sample voltage and oxidation time, the LAO process strongly depends on the amount of water adsorbed on the surface and especially on the water bridge created between the tip and the surface.^{6,14} Both of these factors are influenced by relative humidity because water on hydrophilic surfaces spontaneously condenses from vapor into pores and cracks on the surface and also under the tip. At equilibrium, the water meniscus curvatures at the condensation sites are linked to the relative vapor pressure p/p_{sat} (i.e., relative humidity for water) by the Kelvin equation,¹⁵

$$r_K = \left(\frac{1}{r_1} + \frac{1}{r_2} \right)^{-1} = \frac{\gamma V}{RT \ln(p/p_{\text{sat}})},$$

where r_K is the Kelvin radius representing an effective radius of meniscus, r_1 and r_2 are the two principal radii of the

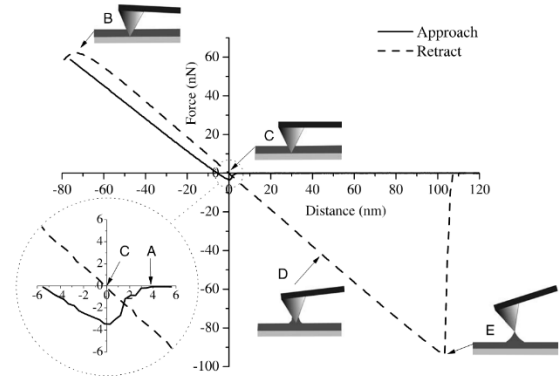


FIG. 2. Force versus distance spectroscopy (RH=91%).

meniscus in the horizontal and vertical cross-section planes of the meniscus, and γ and V are the surface tension and the molar volume, respectively.

The equation shows that with decreasing relative humidity the Kelvin radius becomes smaller. The dependence of the Kelvin radius on the relative humidity for water at 20 °C ($\gamma V/RT=0.54$ nm) is shown in table of Fig. 1(b).

In practice it means that at lower humidities the condensation occurs preferentially only at surface imperfections (e.g., cracks and pits) and features of higher curvatures (with the radii equal or smaller than the Kelvin radius). Concerning the condensation between the tip and the surface, the higher Kelvin radius given by higher humidities and defining the meniscus result in an increase in the neck width of the water bridge [see Fig. 1(a)]. The growth of the neck width and, hence, of the amount of condensed water results in changes in capillary forces between the tip and the surface¹⁶ and also in the modification of an electric field in the tip-substrate area during LAO, as will be demonstrated below.

To monitor the amount of water condensed on the surface and forming the water bridge, the force-distance AFM spectroscopy was used. This method is based on measuring the dependencies of the normal force acting on the AFM tip versus the tip-sample separation during approaching/retracting the sample to/from the tip (Fig. 2). The tip first starts to experience an attractive force at the sample approach (Fig. 2: point A) which can be interpreted as the combination of van der Waals interaction and capillary forces related to the onset of the water bridge formation. As the sample further approaches the tip, the normal force eventually turns repulsive and reaches its maximum at the point B (Fig. 2: point B). When the sample is being retracted the force becomes zero in the point C and the attractive force gradually increases (Fig. 2; point D) to its maximum value (Fig. 2: point E). The distance between the tip positions corresponding to the maximum and zero capillary force (C-E distance) called the break-free length is a measure of the size of the water bridge that is formed between the tip and the sample during the contact.¹⁷ The force-distance curves recorded in our experiments were averaged using the values from 15 approaches and retractions.

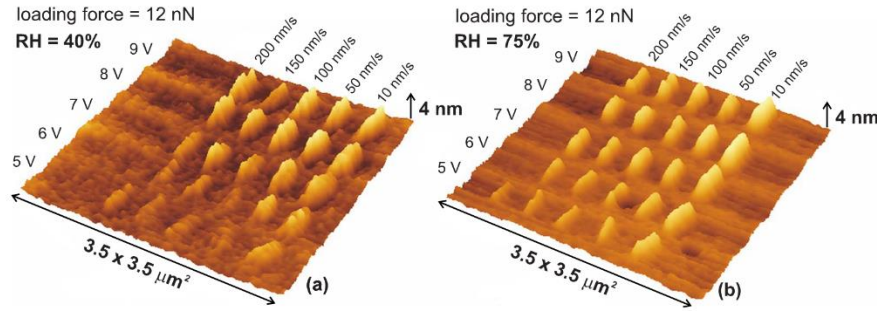


FIG. 3. (Color online) Test arrays of oxide nanolines on GaAs(100) fabricated as a function of the tip-surface voltage and tip speed at the relative humidity (a) 40% and (b) 75%. The nanolines prepared at lower humidity show up a bigger variability in height and width.

III. RESULTS AND DISCUSSION

A. Humidity effect on LAO fabricated nanostructures

Our experimental results on the role of humidity in the LAO process at GaAs(100) surfaces were presented in Ref. 9. In that work, test arrays of oxide nanolines were fabricated by LAO at various tip-sample voltages and under different relative humidities in the range 35–90 %.

The experiments showed that the lines fabricated at lower humidities (<50%) were unexpectedly comparable in size (height, depth, and half width) to those prepared at the highest once (90%); however, their height and width along the lines revealed significant variability. The size of oxide lines became stabilized at relative humidities higher than 50%. This fact is clearly observable in Fig. 3, where the AFM images of test oxide lines for relative humidities of 45% and 75%, are presented. To better understand an enhanced oxidation and size variability of lines, the force-distance spectroscopy measurements by AFM together with computer simulations of an electric-field distribution between the tip and the surface and of water condensation were performed. The results of these approaches will be discussed below.

B. Force-distance AFM spectroscopy

Figure 4 shows a plot of the maximum capillary force at five distinct surface sites of a GaAs(100) sample as a function of relative humidity. The sample had been kept for 20 min under specific humidity atmosphere and then the spectroscopy measurements were carried out at these selected sites inside the area $200 \times 200 \text{ nm}^2$. In the figure inset, there is a plot of the force values averaged over the test sites and provided with the calculated standard deviations. The corresponding break-free length determined by the conversion of the average capillary force shown in the inset of Fig. 4 is presented in Fig. 5.

A maximum possible effort was made to keep the identical test sites for measurements at different relative humidities. Despite that fact the obtained values are loaded with big errors, nevertheless, they give us useful information on the curve development. As mentioned above, the break-free length is a measure of the size of the water bridge between the tip and the sample.

The break-free length (and force values) is low for relative humidities around 20% and 60%. When the relative humidity exceeds 60%, it starts quickly to grow. It represents the growth of the width of the water bridge which has also been confirmed by our simulations (see below). There is a local maximum of the capillary force and break-free length around the relative humidity 40%. However, the standard deviations of the break-free length are big and so the local maximum might not be a true one. Further, the values of the Kelvin radius for lower humidities are smaller than 1 nm (see Sec. II and table in Fig. 1) and the RMS surface roughness is about 1 nm, which means that the size of surface corrugations and imperfections is even bigger. It means that there is no coincidence of the Kelvin radius at this humidity with the size of these features which should have resulted in an enhanced water condensation and so in a more efficient oxidation process induced by the tip. Hence, the force-distance spectroscopy has not confirmed this effect and, therefore, other processes should be responsible for the development of bigger oxide lines at lower humidities.

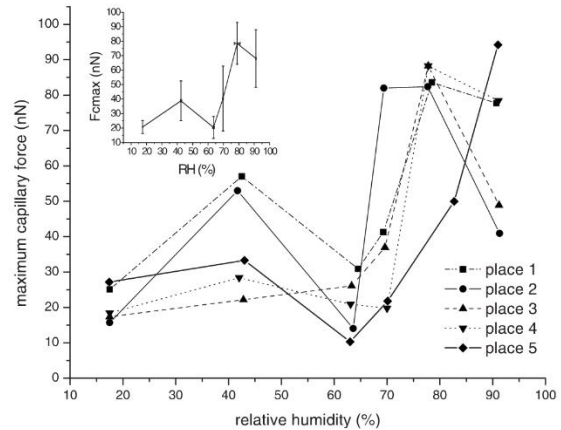


FIG. 4. Maximum capillary force between the tip and the surface during the sample retraction as a function of relative water humidity. In the inset, the force values averaged over the test sites and provided with the corresponding standard deviations.

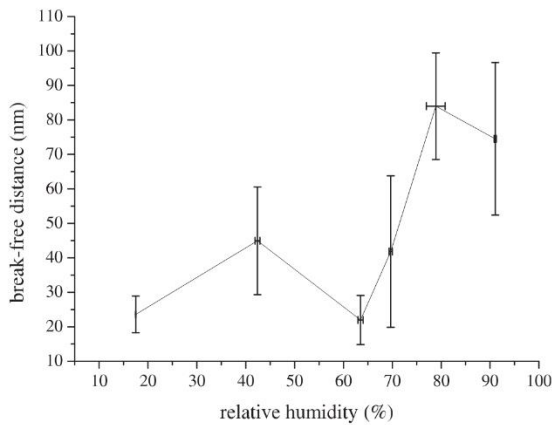


FIG. 5. The break-free length as a function of relative humidity corresponding to the capillary force experiments in Fig. 4

C. Simulation of water condensation under the tip moving over a surface

To better understand the formation of the water bridge between the tip and the surface under different humidities, the computer simulation was carried out using a code written in the VISUAL BASIC. The code simulates water bridge profiles in four cross-sectional vertical planes of the bridge above the specific site. Each plane is rotated from the neighboring one by 45° (Fig. 6). The boundary conditions of the meniscus were defined by water contact angles [Fig. 1(a)] at the sample surface ($\beta=76^\circ$ determined in a separate experiment for the GaAs substrate covered with a native oxide by optical microscopy) and at the silicon tip surface ($\alpha=38^\circ$ measured on a phosphorus-doped silicon substrate by optical microscopy), as well as by the Kelvin radius calculated from the Kelvin equation for a given humidity [Fig. 1(b)]. The tip apex radius was approximated in the simulations by a sphere with a radius of 65 nm (determined by the SEM measurements of the real tips).

To find how the size of the water bridge changes from one to another surface site (and thus to explain the variations in line height and width along the oxide lines), the tip was moved in simulations over the surface in the x direction along four different lines and floated at the distance 0.3 nm from the nearest point of the surface (constant height mode). The simulation utilized experimental-surface-morphology data provided by AFM on the GaAs (100) surface over an

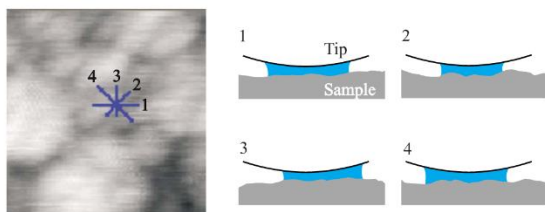


FIG. 6. (Color online) Simulation of water meniscus in four different planes at one surface site.

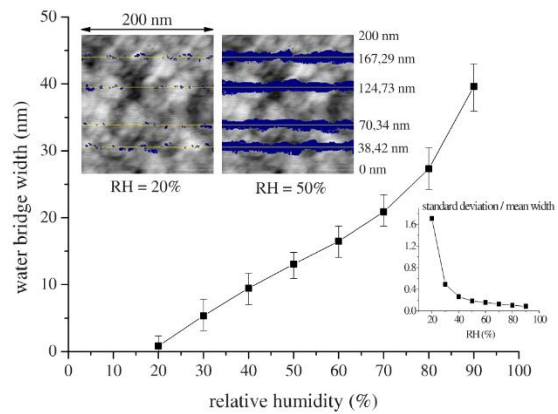


FIG. 7. (Color online) The width of the water bridge between the tip and the surface as a function of relative humidity; ratios of the standard deviation to the mean width (bottom right inset); development of an area given by the projection of a simulated water bridge into the surface during the tip movement from the left to the right for two different humidities (top left inset).

area of $200 \times 200 \text{ nm}^2$. In the LAO experiment, the writing speed was just 10 nm/s. Hence, the tip passed particular sites for the relatively long time which justifies the application of the equilibrium Kelvin radius theory in our simulations.

In each test point, the diameters of the water bridge at the contact point with the substrate surface were calculated in all the four cross-sectional planes. The track made of the water surface areas defined by these diameters (projection of the water bridges) at different test points along the scanned lines is drawn in blue in Fig. 7 (top left inset). Further, in this figure the average track width (i.e., the water bridge diameter in the y direction over the whole track) along with its standard deviation as a function of relative humidity is plotted as well. As expected, the size of the water bridge and so the track width increases monotonously with humidity because the Kelvin radius grows with this parameter as well – the growing Kelvin radius increases the probability that the envelope of the bridge represented by the meniscus will form the required contact angle to the local surface features at higher radial distances from the center of the water bridge than in case of low humidities (small Kelvin radii). As the standard deviation grows with the humidity much more slowly the relative deviation of the track width expressed by the ratio of the standard deviation to the mean width goes up with decreasing humidity (Fig. 7, bottom right inset). This explains bigger variations in cross-sectional dimensions (height and width) of oxide lines being observed mostly at lower values of relative humidity.

Supposing the main source of oxyanions is water, the water bridge size is important in the determination of the width of oxide lines. In accordance with that a reduction in lateral dimensions of dots fabricated by LAO with a decrease in the water bridge width controlled by the tip-surface distance was observed.¹² On the other hand, the width of simulated water bridges in Fig. 7 does not correspond to that of the real oxide lines, which were several times broader.⁹ However, the width

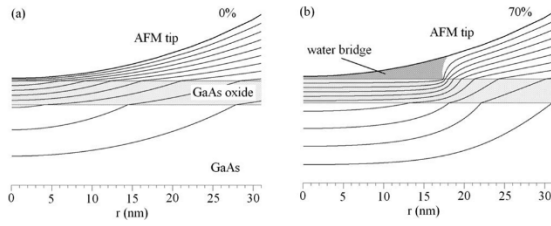


FIG. 8. The equipotential lines in the vicinity of an AFM tip and the model sample consisting of a native GaAs oxide layer and GaAs substrate. Without the water bridge at the (a) relative humidity 0% and with the water bridge at the (b) relative humidity 70%. The thickness of the tip-sample gap, GaAs oxide layer, and GaAs substrate chosen for the simulations was 0.3 nm, 2.5 nm, and 10 nm, respectively.

of oxide lines is an interplay of more factors and besides the size of the reservoir of oxyions (water bridge) it also depends on an electric-field distribution between the tip and the surface. This will be discussed in the next section.

D. Simulation of the electric field in the tip vicinity

To imagine the forces governing the diffusion of ions in the early stage of the LAO process, the simulation of an electric field in the nearest neighborhood of the AFM tip was performed using the EOD (electron optical design) code¹⁸ based on the finite element method (FEM). Particularly, the influence of the water bridge (the size of which depends on relative humidity) on the electric-field distribution between the tip and the surface was studied. The distribution of equipotential lines between the tip and the sample surface shows that the occurrence of the water bridge results in “pushing” the equipotential lines out of the tip-sample space into the native oxide layer of the GaAs sample beneath, as demonstrated in Fig. 8. This is a direct consequence of significant differences in relative permittivities of water ($\epsilon_r=81$), GaAs oxide ($\epsilon_r=3.5$), and GaAs ($\epsilon_r=13.9$). In this sense the water meniscus can be considered as a lens concentrating the electric field into the layer of GaAs oxide. This enhances the electric field in the whole oxide layer and, hence, a diffusion of ions through it.

Figure 9 shows a radial distribution (taken from the tip apex center) of the magnitude of electric-field intensity in the GaAs oxide layer in a depth of 0.25 nm under its surface for different humidities. Under dry conditions (relative humidity 0%), the equipotential lines are not pushed out of the tip-sample space into the oxide layer and the electric field in the oxide layer is smaller and falls down from the center according to a Gaussian-type function. Under the total wet conditions (relative humidity 100%) the surface is fully covered with water; therefore no significant “pushing” of the lines into the oxide layer occurs and thus only a slight increase in the electric-field intensity is observed here. The field is almost constant over relatively large radial distances from the tip (falling down just due to the finite curvature of the tip). The electric-field profiles for humidities between these two extremes (dry and fully wet) differ substantially from the

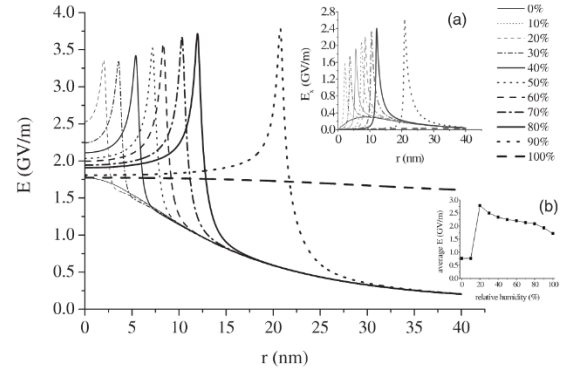


FIG. 9. The radial profiles of the magnitude of electric intensity in the GaAs oxide layer 0.25 nm deep below its surface for different relative humidities; the radial \bar{x} component of electric-field intensity [inset (a)]; the average value of the magnitude of electric intensity in the oxide layer under the water bridge [inset (b)].

previous ones. In the central part of the investigated tip area, the electric-field intensity is the highest for the lowest humidities and, generally, its radial profiles have a peaklike character at radial distances corresponding to the edge of the water bridge. As a consequence of it the average value of the magnitude of electric-field intensity in the oxide layer under the water bridge is higher for lower relative humidities (Fig. 9 inset). This effect contributes to a lower humidities to the formation of the oxide structures of a similar size such as in the case of higher humidities, as demonstrated in Fig. 3. However, to quantify it, additional simulations have to be done yet.

Further, pushing the equipotential lines into the substrate by the water bridge causes a rise of the radial component of the electric-field intensity at radial distances closer to the edge of the water bridge (Fig. 9). This effect can contribute to an additional lateral enlargement of the oxide area far beyond the space defined by the water meniscus.

IV. CONCLUSION

To better understand an enhanced oxidation and size variability of oxide lines at lower humidities reported in our previous paper, the force-distance spectroscopy measurements by AFM together with computer simulations of an electric-field distribution between the tip and substrate and of water condensation, respectively, were performed. Our experiments on AFM force-distance spectroscopy have not proved an enhanced water condensation between the tip and the surface at lower humidities. Hence, more intensive growth of oxide lines under low humidities reported in our previous work cannot be explained by this effect. The AFM-force-distance spectroscopy confirmed enhanced water condensation only at higher humidities which was in line with our simulations.

On the other hand, the simulations of the electric field in the vicinity of the tip at the early stages of the oxidation process showed an increase in the average intensity in the

oxide layer for lower humidities. This contributes to an enhanced diffusion of reactive ions and thus certainly to the more intense development of oxide lines under these conditions. The enhanced radial component of the electric intensity at radial distances closer to the edge of the water bridge at all relative humidities could be one of the reasons for an additional lateral enlargement of the oxide area beyond the space defined by the water bridge

The profound size variations in oxide lines observed at low humidities indicate variability in the oxidation process when the tip is moved over the surface under these conditions. This occurs as a result of the less probable water con-

densation between the tip and the surface at low humidities resulting from the smaller Kelvin radius of the meniscus. Our simulations showing variations in the water bridge size along the tip track at different relative humidities support this idea.

ACKNOWLEDGMENTS

This work was supported by the research programs of the Ministry of Education of the Czech Republic (Projects No. MSM0021630508 and No. LC04060), GAAV (Projects No. IAA1010413 and No. KAN400100701), and GACR (Project No. FON/06/E001).

-
- ¹N. Cabrera and N. F. Mott, *Rep. Prog. Phys.* **12**, 163 (1949).
²D. Stiévenard, P. A. Fontaine, and E. Dubois, *Appl. Phys. Lett.* **70**, 3272 (1997).
³H. Kuramochi, F. Pérez-Murano, J. A. Dagata, and H. Yokoyama, *Nanotechnology* **15**, 297 (2004).
⁴S. F. Lyuksyutov, P. B. Paramonov, I. Dolog, and R. M. Kalich, *Nanotechnology* **14**, 716 (2003).
⁵P. A. Fontaine, E. Dubois, and D. Stiévenard, *J. Appl. Phys.* **84**, 1776 (1998).
⁶J. Cervenka, R. Kalousek, M. Bartosik, D. Skoda, O. Tomanec, and T. Sikola, *Appl. Surf. Sci.* **253**, 2373 (2006).
⁷P. Avouris, T. Hertel, and R. Martel, *Appl. Phys. Lett.* **71**, 285 (1997).
⁸H. Kuramochi, K. Ando, and H. Yokoyama, *Surf. Sci.* **542**, 56 (2003).
⁹S.-R. Jian, T.-H. Fang, and D.-S. Chuu, *J. Phys. D* **38**, 2424 (2005).
¹⁰M. Bartosik, D. Skoda, O. Tomanec, R. Kalousek, P. Jansky, J. Zlamal, J. Spousta, and T. Sikola, *J. Phys.: Conf. Ser.* **61**, 75 (2007).
¹¹C. Albonetti, J. Martinez, Nuria S. Losilla, Pierpaolo Greco, Massimiliano Cavallini, Francesco Borgatti, Monica Montecchi, Luca Pasquali, Ricardo Garcia, and Fabio Biscarini, *Nanotechnology* **19**, 435303 (2008).
¹²D. Stiévenard, P. A. Fontaine, and E. Dubois, *Appl. Phys. Lett.* **70**, 3272 (1997).
¹³S. K. Ghandhi, *VLSI Fabrication Principle*, 2nd ed. (Wiley, New York, 1994).
¹⁴R. Garcia, M. Calleja, and H. Rohrer, *J. Appl. Phys.* **86**, 1898 (1999).
¹⁵J. Israelachvili, *Intermolecular and Surface Forces*, 2nd ed. (Academic Press, San Diego, 1992).
¹⁶T. Stifter, O. Marti, and B. Bhushan, *Phys. Rev. B* **62**, 13667 (2000).
¹⁷M. Binggeli and C. M. Mate, *Appl. Phys. Lett.* **65**, 415 (1994).
¹⁸B. Lencova and J. Zlamal, *Microsc. Microanal.* **13**, 2 (2007).

Commented paper 5

BARTOŠÍK, Miroslav, Miroslav KOLÍBAL, Jan ČECHAL, Jindřich MACH a Tomáš ŠIKOLA.
Selective Growth of Metallic Nanostructures on Surfaces Patterned by AFM Local Anodic
Oxidation. *Journal of nanoscience and nanotechnology* [online]. 2009, **9**(10), 5887–5890.
ISSN 1533-4880. Dostupné z: doi:10.1166/jnn.2009.1251



Selective Growth of Metallic Nanostructures on Surfaces Patterned by AFM Local Anodic Oxidation

Miroslav Bartošík, Miroslav Kolíbal*, Jan Čechal, Jindřich Mach, and Tomáš Šíkola

Institute of Physical Engineering, Brno University of Technology, Technická 2, 616 69Brno, Czech Republic

We report on an alternative approach for the fabrication of metallic nanostructures: a selective growth on silicon substrates patterned by local anodic oxidation using atomic force microscopy. Our method represents a maskless, four-step process which combines a top-down and bottom-up approach. The dimensions of both the oxide lines and metallic elements can be controlled during the technological process. In this paper we demonstrate the preparation of gallium and cobalt structures on silicon substrates but this method can be extended to other combinations of metals and substrates enabling thus the fabrication of ordered nanostructures of various compositions and properties on locally oxidized surfaces.

Keywords: Selective Growth, Local Anodic Oxidation, Gallium Droplets, Cobalt Islands, Metallic Nanostructures, Patterning.

1. INTRODUCTION

In the recent years, various methods for the controlled fabrication of functional nanostructures, devices and systems in the nanometre size range¹ have been developed and applied in microelectronics,² magnetic data storage,³ plasmonics as well as biological and bio-medical applications.

Two basic approaches to the formation of nanostructures and devices in a controlled and repeatable manner are the 'top-down' and 'bottom-up' techniques.⁴ In addition to these distinct groups of methods there are special hybrid techniques combining both approaches¹ and, hence, bridging the top-down and bottom-up strategies. For example, micromolding or optical lithography is applied for fabrication of patterns to guide a bottom up assembly of inorganic sol-gel species⁵ or colloidal particles⁶ from solutions. Further, a selective growth of atoms by molecular beam epitaxy (MBE) techniques on substrate surfaces patterned by copolymer self-assembly,⁷ electron beam,⁸ interferometric⁹ and holographic¹⁰ lithographies have been published. Here, we report on the fabrication of metallic structures by the selective growth on substrates patterned by a scanning probe lithographic method called local anodic oxidation (LAO).¹¹ In this method silicon oxide lines – barriers are made on a silicon substrate by an AFM tip, creating thus the frames of silicon windows. The effect of the selective

growth can be achieved by an interplay of the following mechanisms:

- different sticking coefficients of the evaporated metal on Si windows and silicon oxide barriers;
- preferential desorption from either the silicon oxide or the Si windows during annealing the substrate;
- different diffusion lengths of metal adatoms on the Si windows and silicon oxide barriers.

Gallium and cobalt were chosen for the demonstration of this technique because of a practical use of both metals (cobalt as a magnetic material and gallium as a constituent of group III–V semiconductors and wide-band gap semiconductors) and due to their distinct growth behaviour on silicon substrates. While cobalt is associated with the layer-by-layer growth and tends to form silicides (CoSi₂) at elevated temperatures (up to 10 ML of Co),^{12,13} gallium forms droplets on the surface even at temperatures slightly above room temperature (liquid metal).¹⁴ Even though the growth modes of both metals are different, they are appropriate for the selective growth since the sticking coefficient and the diffusion length on the bare and oxidized silicon surfaces vary significantly.

2. EXPERIMENTAL DETAILS

The applicability of gallium for the selective growth is illustrated in Figure 1 where a temperature dependence of the relative sticking coefficient of Ga on both the bare Si

* Author to whom correspondence should be addressed.

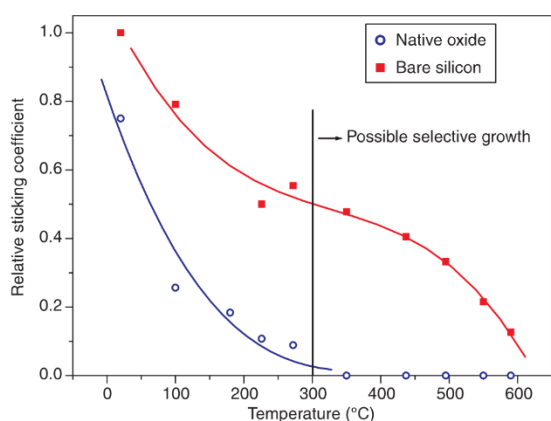


Fig. 1. The relative sticking coefficient of Ga (normalized to the Ga sticking coefficient on the bare Si(111) at room temperature) measured by low energy ion scattering, on both the bare Si(111) surface (open circles) and the native silicon oxide substrate surface (filled squares) after deposition of 1 ML of Ga at different substrate temperatures.

surface and the Si surface covered with the native oxide is shown. The data were collected from low energy ion scattering measurements on the flash-annealed (i.e., oxygen free)¹⁴ and thermally cleaned (maintaining the native oxide)¹³ silicon samples after deposition of 1 ML of Ga. The selective growth of Ga is possible above 300 °C where the sticking coefficient of Ga to the native silicon oxide is reduced to zero, while on the bare Si surface its value is still reasonably high.

The whole fabrication process is schematically described in Figure 2. The first step is the etching of a silicon substrate to prepare hydrogen-terminated silicon surface resistant against the oxidation in ambient atmosphere for at least several hours. The etching procedure consists of pre-etching in a buffered hydrofluoric acid solution (1:5, 40% HF and 40% NH₄F, 2 minutes) and of final etching in 40% NH₄F (30 seconds, 70 °C).¹⁵ The substrate prepared in this way is patterned by local anodic oxidation (LAO) afterwards. This method utilizes diffusion of ionized fragments of water molecules adsorbed on the substrate surface enhanced by a strong electric field between

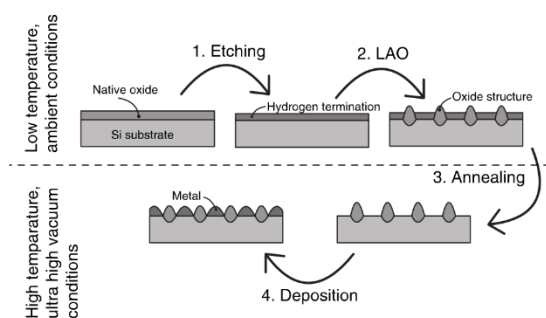


Fig. 2. A schematic diagram of the fabrication process.

the AFM tip and the sample acting as an anode. The OH⁻ and O²⁻ anions are driven by this field and penetrate into deeper layers of the substrate, forming local oxide features.¹¹ The dimensions of oxide structures fabricated by LAO can be controlled by tip-sample voltage, oxidation time (tip speed), relative humidity, sharpness and material of the tip¹⁶ (typical parameters in our experiments were as follows: tip-sample voltage 9 V, tip speed 10–50 nm/s, relative humidity 48–55% and the Si tip coated by a TiN or Au thin film). Moving the tip according to a prescribed recipe, various nanostructure patterns can be created. Afterwards, the patterned sample is inserted into an ultrahigh vacuum chamber and before the metal deposition it is annealed according to a two-step process: First, slow heating up to 350 °C is followed by a 10 minute annealing at this temperature. This step ensures that most of species adsorbed on the substrate except hydrogen (hydrogen desorption temperature ~400 °C)¹⁷ are desorbed. Next, the sample is annealed at 550 °C for 20 minutes to desorb hydrogen atoms from hydrogen-terminated silicon windows and remaining contaminants from the whole sample surface. A single-step annealing to 550 °C was found inappropriate since in this case voids are probably formed in the terminating hydrogen layer covered with adsorbents (e.g., water, oxygen, carbon) and, hence, the post-oxidation/contamination of the corresponding unprotected silicon surface areas occurs (observed by X-ray photoelectron spectroscopy). The annealing temperature should not exceed 650 °C since this would lead to the destruction of the LAO patterns. Annealing at lower temperatures does not affect the LAO structure. During the thermal treatment the pressure did not exceed $2 \cdot 10^{-6}$ Pa.

In the final step, metal was deposited from an e-beam evaporator onto the sample held at a specific temperature under ultrahigh vacuum conditions ($p \sim 5 \cdot 10^{-7}$ Pa). The effective coverages of metal layers (in ML) at specific temperatures were determined from the knowledge of the fluxes generated by the calibrated effusion cells and the dependences of the sticking coefficients on temperature (see Fig. 1).

AFM images of the structures were taken *ex situ* under ambient conditions. If not specified in the text below, the noncontact mode was used.

3. RESULTS AND DISCUSSION

In Figures 3(a, b) *ex situ* AFM images of the Si(111) substrate patterned by LAO and consequently covered by 8 monolayers (ML) of Ga at 300 °C are shown. The height of the oxide lines ranged from 2 to 5 nm. The island growth mode of Ga is obvious, moreover, Ga droplets are of a nearly uniform size, which is due to a droplet coarsening on the surface.¹⁸ The growth on the patterned oxide regions is significantly reduced, however, as apparent from the inset, not completely. It is clear that the deposition at

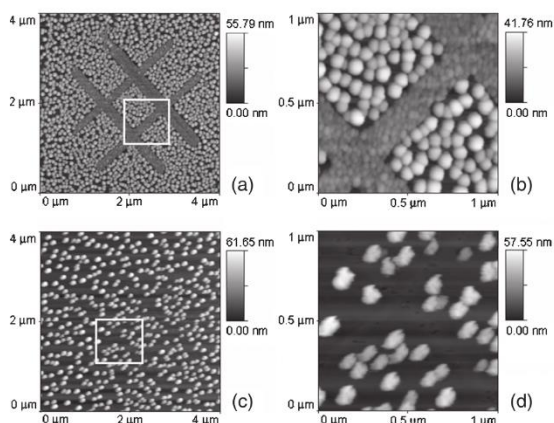


Fig. 3. AFM images of LAO patterns on Si(111) surface after selective growth. (a) After deposition of 8 ML of Ga at 300 °C, (b) a detailed scan of the pattern. (c) after deposition of 4 ML of Ga at 350 °C, (d) a detailed scan of the pattern.

a higher temperature is necessary to promote the selective growth. Figures 3(c, d) shows *ex situ* AFM images of another Si(111) sample patterned by LAO and covered by 4 ML of Ga at 350 °C. The growth on the oxide structures is suppressed and the Ga droplets are formed only in the windows on the bare silicon surface. Note that the size of the droplets increases with temperature.

In order to investigate the behaviour of Ga droplets in the bare Si surface windows, an asklepian rod-like zig-zag structure consisting of several Si windows of different sizes was prepared by LAO (Fig. 4(a)). Consequently, 8 ML of Ga was deposited onto the patterned sample at 350 °C. The AFM image taken after the deposition is shown in Figure 4(b). Obviously, the larger windows the more droplets are formed. The droplets are uniform in size, similar to that one possessed by droplets surrounding the pattern. As proved in our previous experiments and shown above (see Figs. 3(a, c)) this is caused by the fact that the size of the droplets is controlled by deposition substrate temperature. As the windows get smaller, the number of droplets decreases, since the amount of material available in these windows for building the droplets goes down. When the window becomes so small that there is not enough material even for building one droplet of the size

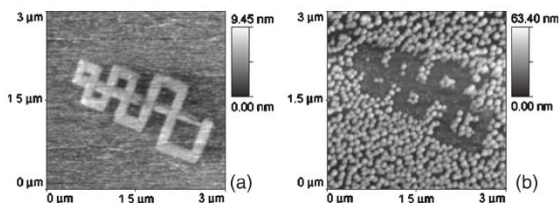


Fig. 4. (a) AFM image (contact mode) of a zig-zag structure made by LAO consisting of several Si windows of different sizes, (b) the same after deposition of 8 ML of Ga at 350 °C.

defined by the temperature, a smaller droplet is formed. Hence, reducing the size of windows leads to decreasing the dimensions of droplets.

To demonstrate the ability of the method in nanotechnology, a grid of silicon oxide lines creating small and uniform windows of bare silicon was prepared by LAO on the Si(111) surface and after that Ga was deposited under conditions satisfying the selective growth (8 ML, 350 °C). In Figure 5 an AFM image of the resulting structure is shown. The surface windows are filled with Ga droplets separated from each other by oxide barriers with an original height of (2.8 ± 0.2) nm. The metallic droplets and oxide lines are (104 ± 5) nm and (164 ± 12) nm wide, respectively. The average height of the droplets is (32 ± 2) nm. Note this is not the limit of the method since the width of the oxide lines can be reduced by optimizing the operational conditions.¹⁶ For instance, in our previous experiments we fabricated silicon oxide lines with a thickness below 40 nm,¹⁶ additionally, oxide lines down to 10 nm in width were reported for cantilever tips made of carbon nanotubes.^{19, 20}

As mentioned above, cobalt growth behaviour on silicon substrates is quite different from the gallium one. Below the critical thickness cobalt disilicide (CoSi_2) is formed and the growth itself proceeds in the layer-by-layer mode. Since the silicide formation is limited by diffusion of atoms through this layer, once the amount of cobalt on the surface is sufficient, silicide formation is stopped and the growth of magnetic cobalt layers follows. The selective

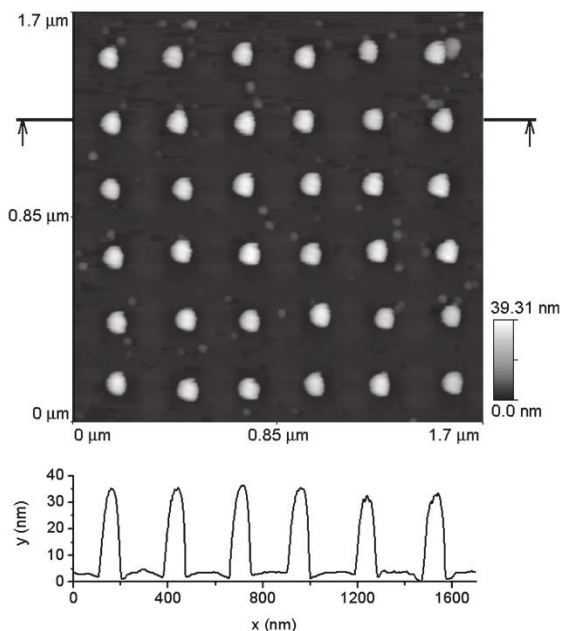


Fig. 5. An AFM scan and a profile of an array of Ga droplets separated from each other by silicon oxide barriers (8 ML of Ga, 350 °C).

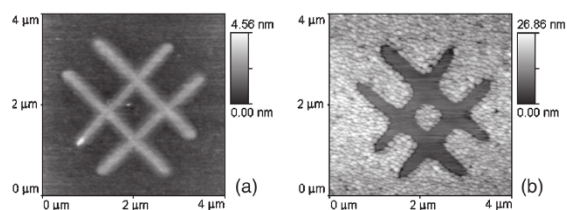


Fig. 6. AFM images of the patterned Si(111) substrate, (a) after patterning, (b) after deposition of 20 ML of Co at 400 °C.

growth of Co can be expected for deposition temperatures above 400 °C since at these values the growth mode of Co on oxidized silicon surfaces changes from the layer-by-layer to the island one while the Co diffusion length considerably increases and Co atoms tend to migrate off the oxide surface. Moreover, above 500 °C the sticking coefficient of cobalt on the native silicon oxide dramatically decreases, while at a bare Si(111) surface remains reasonably high up to ~600 °C.^{12,13} The Si(111) substrate was patterned by LAO in a usual way and afterwards 20 ML of cobalt was deposited at 400 °C. The results of the experiment are shown in Figure 6. As follows from the figure, the selective growth was successfully achieved. The height of the cobalt island inside the cross was 10 nm.

4. CONCLUSION

In conclusion, we have presented the selective growth as an alternative approach for fabrication of metallic nanostructures on silicon surfaces patterned via local anodic oxidation by AFM. In principle, the process of the selective growth can be applied for any metals having significantly different sticking coefficients or diffusion lengths on bare and oxidized surfaces as having been demonstrated for the selective growth of gallium and cobalt. The method can be extended to the surfaces where the oxide is selectively prepared or removed and material contrast (oxide vs. bare surface) achieved. The critical parameter for the selective growth of a given metal is the deposition substrate temperature controlling changes in the growth mode and kinetic growth parameters (e.g., sticking coefficient, diffusion lengths). Although this paper deals with silicon

substrates only, patterning by LAO can be applied also to other substrates (e.g., GaAs). Thus, in principle the selective growth studies can be easily extended to these surfaces as well.

Acknowledgment: This work was supported by the research programmes of the Ministry of Education of the Czech Republic (Projects No. MSM0021630508, and LC06040), GAAV (Projects No. IAA1010413 and KAN400100701) and the EUROCORES – GACR project (FON/06/E001).

References and Notes

1. J.V.Barth, G.Constantini, and K.Kern, *Nature* 43, 671 (2005).
2. M.T.Bohr, *IEEE Trans. Nanotechnol.* 1, 56 (2002).
3. D.A.Thomson and J.S.Best, *IBM J. Res. Dev.* 44, 311 (2000).
4. B.D.Gates, Q.Xu, M.Stewart, D.Ryan, C.G.Willson, and G.M. Whitesides, *Chem. Rev.* 105, 1171 (2005).
5. P.Yang, T.Deng, D.Zhao, P.Feng, D.Pine, B.F.Chmelka, G.M. Whitesides, and G.D.Stucky, *Science* 282, 2244 (1998).
6. Y.Yin, Y.Lu, B.Gates, and Y.Xia, *J. Am. Chem. Soc.* 123, 8718 (2001).
7. S.Yoon, Z.Zhao, J.Liu, Y.H.Xie, D.Y.Ryu, T.P.Russel, H.-M. Kim, and K.-B. Kim, *Appl. Phys. Lett.* 89, 063107 (2006).
8. M.Shibata, S.S.Stoyanov, and M.Ichikawa, *Phys. Rev. B* 59, 10289 (1999).
9. S.C.Lee, K.J.Malloy, L.R.Dawson, and S.R.J.Brueck, *J. Appl. Phys.* 92, 6567 (2002).
10. Z.Zhong, A.Halilovic, H.Lichtenberger, F.Schäffler, and G.Bauer, *Physica E* 23, 243 (2004).
11. P.A.Fontaine, E.Dubois, and D.Stiévenard, *J. Appl. Phys.* 84, 1776 (1998).
12. W.Weiss, U.Starke, K.Heinz, G.Rangelov, Th.Fauster, and G.R. Castro, *Surf. Sci.* 347, 117 (1996).
13. J. Čechal, J.Luksch, K.Koňáková, M.Urbánek, E.Brandejsová, and T.Šíkola, *Surf. Sci.* 602, 2693 (2008).
14. M.Kolřbal, O.Tomanec, S.Průša, M.Plojhar, S.N.Markin, L.Dittrichová, J.Spousta, P.Bauer, and T.Šíkola, *Nucl. Instr. and Meth. in Phys. Res. B* 265, 569 (2007).
15. H.Sakaue, S.Fujiwara, S.Shingubara, and T.Takahagi, *Appl. Phys. Lett.* 78, 309 (2001).
16. J.Cervenka, R.Kalousek, M.Bartošík, D.Škoda, O.Tomanec, and T.Šíkola, *Appl. Surf. Sci.* 253, 2373 (2006).
17. J.Mach, J. Čechal, M.Kolřbal, M.Potoček, and T.Šíkola, *Surf. Sci.* 602, 1898 (2008).
18. A.Lo and R.T.Skodje, *J. Chem. Phys.* 112, 1966 (2000).
19. H.Dai, N.Franklin, and J.Han, *Appl. Phys. Lett.* 73, 1508 (1998).
20. R.García, M.Calleja, and H.Rohrer, *J. Appl. Phys.* 86, 1898 (1999).

Received: 13 June 2008. Accepted: 11 November 2008.

Commented paper 6

PROCHÁZKA, Pavel, Jindřich MACH, Dominik BISCHOFF, Zuzana LIŠKOVÁ, Petr DVOŘÁK, Marek VAŇATKA, Pauline SIMONET, Anastasia VARLET, Dušan HEMZAL, Martin PETRENEC, Lukáš KALINA, Miroslav BARTOŠÍK, Klaus ENSSLIN, Peter VARGA, Jan ČECHAL a Tomáš ŠIKOLA. Ultrasmooth metallic foils for growth of high quality graphene by chemical vapor deposition. *Nanotechnology* [online]. 2014, **25**(185601), 1–8. Dostupné z: doi:10.1088/0957-4484/25/18/185601

Ultrasmooth metallic foils for growth of high quality graphene by chemical vapor deposition

This content has been downloaded from IOPscience. Please scroll down to see the full text.

2014 Nanotechnology 25 185601

(<http://iopscience.iop.org/0957-4484/25/18/185601>)

View [the table of contents for this issue](#), or go to the [journal homepage](#) for more

Download details:

IP Address: 134.129.115.40

This content was downloaded on 26/05/2014 at 17:01

Please note that [terms and conditions apply](#).

Ultrasmooth metallic foils for growth of high quality graphene by chemical vapor deposition

Pavel Procházka^{1,2}, Jindřich Mach^{1,2}, Dominik Bischoff³,
Zuzana Lišková^{1,2}, Petr Dvořák^{1,2}, Marek Vaňatka², Pauline Simonet³,
Anastasia Varlet³, Dušan Hemzal⁴, Martin Petrevec⁵, Lukáš Kalina⁶,
Miroslav Bartošík^{1,2}, Klaus Ensslin³, Peter Varga¹, Jan Čechal^{1,2} and
Tomáš Šíkola^{1,2}

¹CEITEC—Central European Institute of Technology, Brno University of Technology, Technická 3058/10, 616 00 Brno, Czech Republic

²Institute of Physical Engineering, Brno University of Technology, Technická 2896/2, 616 69 Brno, Czech Republic

³Solid State Physics Laboratory, ETH Zurich, Schafmattstrasse 16, CH-8093 Zurich, Switzerland

⁴CEITEC—Central European Institute of Technology, Masaryk University, Kamenice 753/5, 625 00 BRNO, Czech Republic

⁵Tescan Orsay Holding, a.s., Libušina Třída 21, 623 00 Brno, Czech Republic

⁶Brno University of Technology, Faculty of Chemistry, Centre for Materials Research, Purkyňova 464/118, Brno, 612 00, Czech Republic

E-mail: cechal@fme.vutbr.cz


Received 27 January 2014, revised 7 March 2014

Accepted for publication 13 March 2014

Published 16 April 2014

Abstract

Synthesis of graphene by chemical vapor deposition is a promising route for manufacturing large-scale high-quality graphene for electronic applications. The quality of the employed substrates plays a crucial role, since the surface roughness and defects alter the graphene growth and cause difficulties in the subsequent graphene transfer. Here, we report on ultrasmooth high-purity copper foils prepared by sputter deposition of Cu thin film on a SiO₂/Si template, and the subsequent peeling off of the metallic layer from the template. The surface displays a low level of oxidation and contamination, and the roughness of the foil surface is generally defined by the template, and was below 0.6 nm even on a large scale. The roughness and grain size increase occurred during both the annealing of the foils, and catalytic growth of graphene from methane (≈ 1000 °C), but on the large scale still remained far below the roughness typical for commercial foils. The micro-Raman spectroscopy and transport measurements proved the high quality of graphene grown on such foils, and the room temperature mobility of the graphene grown on the template stripped foil was three times higher compared to that of one grown on the commercial copper foil. The presented high-quality copper foils are expected to provide large-area substrates for the production of graphene suitable for electronic applications.

 Online supplementary data available from stacks.iop.org/NANO/25/185601/mmedia

Keywords: graphene, CVD growth, metallic foils

(Some figures may appear in colour only in the online journal)

Introduction

Graphene has attracted enormous attention for its unique mechanical, optical and electronic properties [1–3]. Synthesis by means of chemical vapor deposition (CVD) catalyzed by metallic substrates is a promising route for fabrication of high-quality large-area monolayer graphene sheets [4, 5]. Here, the copper foils are among the most promising substrates for the CVD growth of graphene thanks to low carbon solubility in Cu [4], and low concentration of defects formed in graphene compared to Co and Ni substrates [6–8]. Since domain boundaries have a deleterious effect on the electronic properties of graphene [9–11], intense research is being carried out on the CVD growth of large-area single-domain graphene [7, 12–15]. The single domain growth has been achieved by synthesis at high temperatures and the presence of hydrogen [13, 16, 17] when nucleation of carbon atoms on surface defect sites is restricted [13, 17–19], or by oxygen passivation of potential nucleation sites [14, 15]. The quality of the employed metallic foils, therefore, plays a crucial role in the growth process [17, 18, 20]. In addition, the surface morphology of the foils is critical for the formation of wrinkles on graphene during its transfer to insulating substrates [21, 22]. Commercially available foils generally possess high surface roughness, mainly due to the metal rolling process during their production [7]. Therefore, the metal foils are usually electropolished and annealed at high temperatures (>1000 °C) under vacuum or hydrogen atmosphere for several hours [12, 13, 18, 20, 23, 24], or the copper is melted and resolidified on a tungsten foil support [25] to clean and smoothen the surface before the graphene growth. However, after this process, the surface roughness over larger areas remains relatively high and has a significant influence on the growth and transfer processes. Another issue is the purity of the copper foil since the impurity atoms often segregate on the surface in the form of clusters [26], causing an increase in the nucleation center density.

Here, we introduce a template stripping method [27–29] for the fabrication of ultrasmooth copper metallic foils, whose surface roughness is defined by the employed templates, i.e. silicon substrates, which display one of the smoothest commercially available surfaces. The resulting large-area roughness of the prepared foils (typically over $50 \times 50 \mu\text{m}^2$) is below 0.6 nm, i.e. almost two orders of magnitude lower than the one observed on commercial Cu foils.

The template-stripping method brings an additional advantage of very low surface contamination and oxidation because the surface of the foil is freshly exposed to ambient atmosphere after its stripping. Hence, the electropolishing and high temperature cleaning of the Cu foil before the graphene growth can be avoided. The size of the foils prepared by this method is practically limited only by the available template-size, which presents an advantage for the production of graphene on a large scale, and ensures the compatibility of the method with the semiconductor industry.

Methods

Graphene films were primarily grown on template stripped (TS) copper foils and, for comparison, also on 25 μm -thick polycrystalline copper foils from the MTI Corporation (purity >99.99%). The commercial copper foils were cleaned in an ultrasonic bath for 15 min in acetone and 15 min in isopropanol, then inserted into the home-built CVD system and annealed at 1000 °C under a hydrogen flow of 4 sccm at 10 Pa before the graphene growth.

The TS copper foils were prepared by ion beam sputter deposition from a high purity copper target (Mateck, 99.999%) in a home-built high vacuum ($<10^{-5}$ Pa) setup based on Kaufman broad ion beam sources [30]. The energy of argon ions was 600 eV and the deposition rate of copper on the template formed by a P-doped Si (100) substrate (resistivity of 0.0010–0.0015 Ωcm) covered with a 280–285 nm-thick thermal SiO₂ layer was 2.3 \AA s^{-1} . Next, the copper supporting layer was deposited by electrolysis in a mixture of 0.0012 M sulfuric acid (H₂SO₄) and 1.38 M solution of Copper Sulfate (CuSO₄, 33 g, 150 ml). The current and time of electrodeposition were controlled during the whole process in order to achieve the required thickness of the supporting layer (24 μm). The stripping of the foils was carried out just prior to their insertion into the reactor to reduce the contamination and oxidation from the ambient atmosphere.

Graphene synthesis was carried out in a home-built reactor (see supporting information for details, available at stacks.iop.org/NANO/25/185601/mmedia). Before the growth, hydrogen gas was introduced to the reactor (4 sccm, 10 Pa) and the system had been heated up to a graphene growth temperature. Graphene growth was performed under a methane atmosphere (flow of 40 sccm) for 30 min at a pressure of 70 Pa. Afterwards, the system was cooled down to room temperature in four hours. Graphene from the back-side of the copper foil was removed by oxygen plasma etching (25% O₂/75% Ar, two minutes).

To provide further analysis, the graphene layer from the front side of the foil was transferred to a SiO₂/Si substrate (the same type of substrate as that used for the template of the TS copper foils) by the PMMA-assisted wet transfer method.

Atomic force microscopy (AFM) was carried out by a commercial ambient scanning probe microscope (NT-MDT Ntegra Prima) in contact mode using commercial silicon cantilevers CSG-10 (NT-MDT). The image resolution was set to a standard of 256 × 256 points. A conventional confocal Raman microscope WITec CRM 200 with a green laser (532.2 nm, 0.8 mW) and spot diameter of 450 nm, and Renishaw inVia with a He-Ne excitation laser (632.8 nm, 50 mW) and a focused spot diameter of 2 μm were used for the room temperature measurement of the Raman spectra and spatial maps. X-ray photoelectron spectroscopy was performed in a Kratos Axis-Ultra DLD system using monochromatic Al-K α radiation. Transport properties were measured at room temperature or at 4 K in a liquid He cooled cryostat. Electron backscatter diffraction (EBSD) measurements were carried out in a Tescan FERA 3 microscope equipped by NordlysMax [2] EBSD detector from Oxford

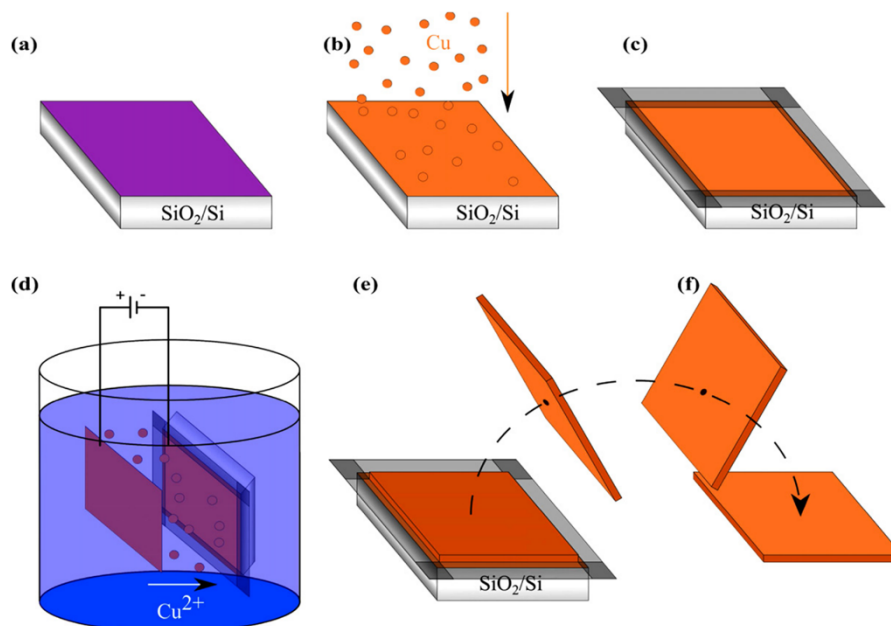


Figure 1. Preparation of a copper foil by template stripping. (a) SiO₂/Si substrate as a template. (b) Sputter-deposition of Cu. (c) Protection of edge areas of the substrate surface. (d) Electrodeposition of a thick Cu supporting layer. (e) Peeling-off the prepared foil. (f) The top layer of the foil is defined by the SiO₂/Si template surface.

Instruments, using 8 and 15 keV primary electron beams focused to the spot with a diameter of 15 nm at a sample inclined by 70 degrees relative to the incoming electron beam. The assignments of crystallographic directions were performed directly in the Aztec EBSD control software, and EBSD Post-processing was completed by HKL CHANNEL5.

Results and discussion

Figure 1 illustrates the preparation of the copper foils by template stripping using a silicon-based substrate as a template. In the first step, a 800 nm-Cu thin film is sputter deposited in a broad ion-beam setup [30] on the Si(100) substrate with a 280 nm-thick thermally grown SiO₂ layer on top of it. This is followed by the electrodeposition of a 24 μm-thick supporting Cu layer from the CuSO₄ solution. A key step here is to cover the edges of the sample by a resist layer (PMMA) or scotch tape to prevent penetration of the electrolyte to the Cu/Si interface from the side of the sample. After completing the electrodeposition, the sample is rinsed in demineralized water and dried out under ambient conditions for at least 24 h. The free-standing copper foil is then obtained by mechanically peeling-off the copper layer from the substrate. This step is enabled by the low adhesion of the Cu layer to the SiO₂ surface (see supporting information for a

more detailed discussion, available at stacks.iop.org/NANO/25/185601/mmedia).

The surface of the foils prepared in this way has very low roughness and their material composition is primarily defined by the composition of a target used for sputter deposition. In our case we have used a Cu target with 99.999% purity, and x-ray photoelectron spectroscopy (XPS) revealed no traces of contamination, except for impurities from the ambient atmosphere (see supporting information, available at stacks.iop.org/NANO/25/185601/mmedia). Compared to standard Cu-foils, which are usually stored under ambient conditions, the freshly stripped TS foils show a very low level of contamination and oxidation because their surface is protected from ambient conditions while attached to the template.

Figure 2(a) shows the in-scale comparison of the large-area surface morphology of the TS foils and non-treated commercial polycrystalline copper foils (99.99%, MTI Corporation) which are frequently used for CVD graphene growth. The surface of the commercial foil presented in the bottom part of figure 2(a) displays large corrugation (arithmetic-averaged roughness $R_a=70$ nm and root-mean-squared roughness (RMS) $R_{RMS}=90$ nm) over a large area ($50 \times 50 \mu\text{m}^2$), which is typical for the foils prepared by cold rolling. On the local scale (measured area of $1 \times 1 \mu\text{m}^2$), the roughness of the commercial foils is correspondingly lower (typically $R_a=8.6$ nm and $R_{RMS}=11$ nm). A detailed inspection of the surface of the foils prepared by template stripping, illustrated

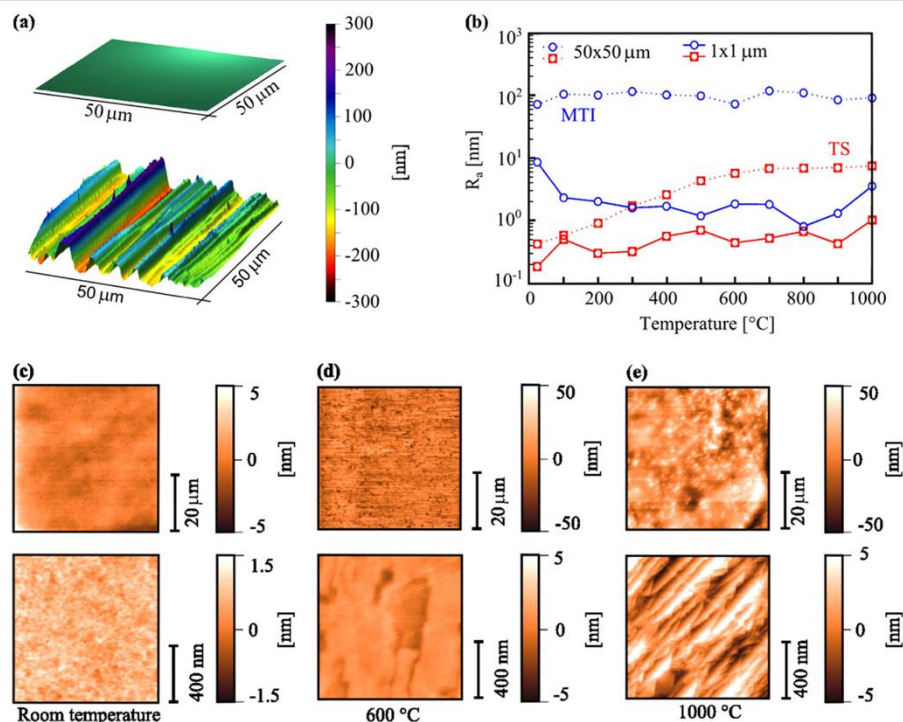


Figure 2. (a) AFM topography ($50 \times 50 \mu\text{m}^2$) of copper foils prepared by template stripping (top) and commercial copper foils (bottom). (b) Surface roughness (in logarithmic scale) of the copper foils after 30 min annealing under a low-pressure hydrogen atmosphere at different temperatures and measured over $50 \times 50 \mu\text{m}^2$ and $1 \times 1 \mu\text{m}^2$ surface areas (red: TS copper foil, blue: commercial copper foil). AFM images of TS copper foils: (c) as prepared, (d) vacuum annealed at 600 °C, and (e) 1000 °C, (top row $50 \times 50 \mu\text{m}^2$; bottom row $1 \times 1 \mu\text{m}^2$).

in figure 2(c), reveals very small surface roughness on a large scale ($R_a=0.42$ nm and $R_{\text{RMS}}=0.53$ nm, top image) and appropriately lower on a local scale ($R_a=0.18$ nm and $R_{\text{RMS}}=0.23$ nm, bottom image); no morphological features were found at both size-scales. On both foils, the large area measurements are taken to cover a sufficient area to make statistical conclusions on surface roughness.

To reveal the changes in surface morphology of the foils with increasing process temperature, we have carried out two series of experiments in a CVD apparatus: (1) annealing of the foils at 100–1000 °C in a vacuum (10^{-3} Pa), and (2) annealing of the foils in the same way and their subsequent exposure to a methane at 300–1000 °C (CVD process).

The annealing in a vacuum/hydrogen atmosphere is a typical step used for cleaning commercial copper foils prior to graphene synthesis itself [12, 13, 18, 20, 23, 24]. The dependence of surface roughness for this type of annealing is depicted in figure 2(b). In each experiment, a freshly prepared TS copper foil was used and the annealing was carried out simultaneously with the commercial foil in order to provide a direct comparison. With an increasing annealing temperature, the morphology of the TS foils (figures 2(d) and (e)) changes. The most prominent change is the formation of depressions

and pits on the substrate (600 °C) and micro-faceting observed after high temperature annealing (1000 °C). The original size of the grains after deposition is very small since the sputter deposition technique was used and no post-annealing treatment applied. This method generally results in the formation of small crystallites in an amorphous matrix [31]. To confirm this, we have performed EBSD analysis of the TS foils (see supporting information for a detailed description of results, available at stacks.iop.org/NANO/25/185601/mmedia). Indeed, the average grain size amounts to 60 nm, and a relatively large portion of the surface area could not be assigned and, hence, it is amorphous or contains clusters smaller than ~ 20 nm.

EBSD performed after annealing at 1000 °C reveals that the size of near surface grains increases: the average grain size increases to 320 nm. Further, there is a dramatic change in the grain orientation. Whereas on the pristine TS foil the majority of grains possesses the (111) surface orientation, the annealed foil displays multiple grain orientations with a minor preference for the (111) and (100) planes and orientations close to these two planes.

During annealing, the grains in the foil grow which leads to an increase of surface roughness. Since the surface of the

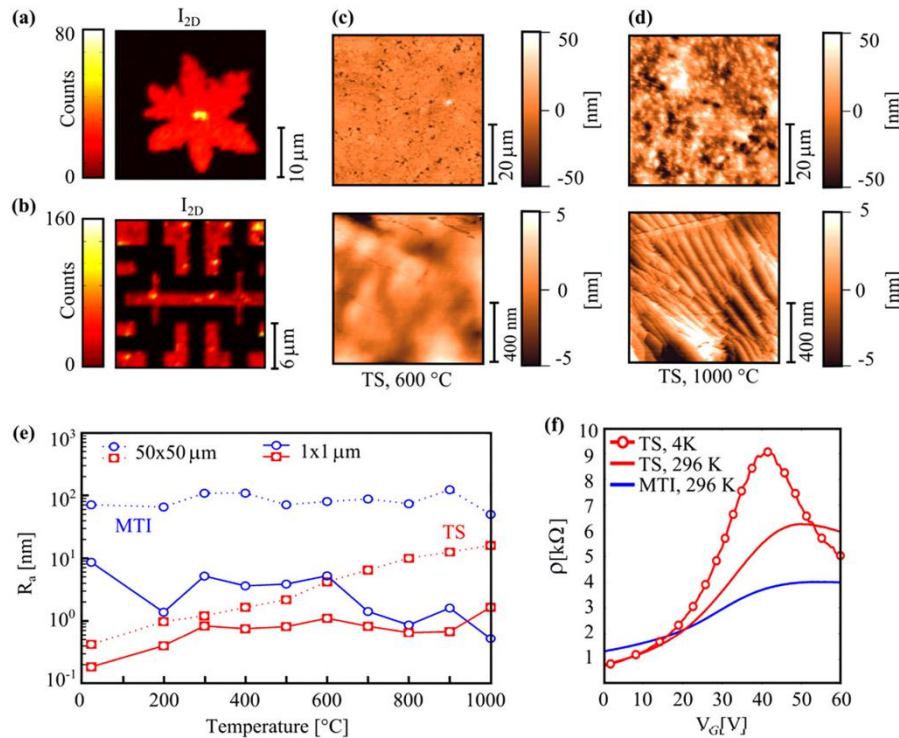


Figure 3. (a, b) Maps of the 2D-Raman peak intensity over (a) a single graphene domain grown on the TS foil and (b) polycrystalline graphene grown on the commercial copper foil with prepared contacts. Both graphene layers were grown at 1000 °C and transferred onto the SiO₂/Si substrate. (c, d) AFM images of the TS copper foils annealed in hydrogen atmosphere and then exposed to methane at 600 °C (c), and 1000 °C (d) (top row 50 × 50 μm^2 ; bottom row 1 × 1 μm^2). (e) Surface roughness (in logarithmic scale) of copper foils after their annealing in a hydrogen atmosphere and consequent exposure to methane at various process temperatures obtained from 50 × 50 μm^2 and 1 × 1 μm^2 scans (red: TS copper foil, blue: commercial copper foil). (f) Graphene resistivity as a function of applied back-gate voltage for graphene grown on the commercial copper foil (blue: room temperature) and TS foil (red: room temperature, black: 4 K).

foil is no longer covered by the Si template, and the freshly exposed areas are not necessarily of the lowest surface free energy, the grains tend to reach their equilibrium shapes and protrude out of the original surface. The material forming these grains is taken from the surrounding areas and grain boundary grooves (pits) are formed [18]. The other source of roughening is the evaporation and sublimation of copper atoms [32] which results in the overall increase of the surface roughness. Both these effects have no direct influence on the measured roughness of commercial copper foils, because their roughness is determined mainly by rolling stripes. Even though the roughness of the TS foils increases with temperature, it is still on a large scale—ten times lower than that one of the commercial foils.

In the second series of experiments, we have examined the morphology of copper foils after their annealing in a hydrogen atmosphere (10 Pa, 4 sccm) and subsequent exposure to a methane atmosphere (70 Pa, 40 sccm) at various process temperatures. The evolution of the surface roughness with process temperature is presented in figure 3(e). From the

AFM images taken after the 600 °C (figure 3(c)) and 1000 °C (figure 3(d)) experiments, it is evident that the combination of annealing and CVD process leads to similar morphological changes, as observed during annealing in hydrogen (i.e. the formation of pits and microfaceting). However, the increase in roughness is higher (up to 2 times), especially at high temperatures (≈ 1000 °C) when graphene growth was obtained (see below). The low surface roughness can be maintained by low temperature graphene synthesis. This, however, did lead to graphene of medium quality (see supporting information for details, available at stacks.iop.org/NANO/25/185601/mmedia). So we will further focus on graphene growth from the methane precursor.

To evaluate the quality of the grown graphene layers, we performed transport measurements and micro-Raman spectroscopy. The minimum temperature for the graphene growth deduced from the appearance of the 2D-peak is 900 °C. However, the graphene quality further improves with increasing growth temperature. In figures 3(a) and (b), the areal distribution (map) of the 2D-Raman peak intensities of

the graphene grown at 1000 °C on both foils and transferred onto the SiO₂/Si substrate is shown. The maps of both individual peak (2D and G) intensities and associated Raman spectra are presented in the supporting information, available at stacks.iop.org/NANO/25/185601/mmedia. The intensity ratio of the 2D and G peaks in the graphene domains and absence of D-peak proves that the single-layer graphene has a very low amount of defects. The uniform distribution of the 2D-peak intensity over the domains indicates a high homogeneity of the graphene. The best quality graphene samples were grown at 1000 °C, which is in agreement with the recently published results on CVD graphene grown on commercial copper foils [4, 7, 11, 13]. However, the large scale roughness of our TS foils is lower compared to commercial ones and, consequently, that of the graphene as well.

The regularly used copper foils prepared by cold rolling display rolling stripes as a main morphological feature. These can be smoothed by high temperature annealing but cannot be removed completely [13, 18]. Moreover, the pre-annealing can result in the formation of a 'crust' layer which can easily peel off from the surface [33]. Another way to smooth the surface is by electropolishing and etching. Electropolishing can reduce the surface roughness to about 3 nm, but the observed pit formation can result in large defects in graphene [18]. In other studies on electropolishing of graphene, the reduction of RMS roughness from 219 nm to only 64 nm [24], or even less [13], was observed. The main advantage of electropolishing is thus the removal of surface oxides [24]. Moreover, the contamination of the foil surface by the electrolyte or segregation of impurities at the surface during high temperature annealing can take place. The etching (e.g. using Fe(NO₃)₃) also does not lead to satisfactory results, since etch quarries and residues are left on the surface, even after subsequent foil annealing [33].

In comparison, the TS foils possess no rolling stripes, their surface is inherently ultra-clean and oxide-free, and hence both cleaning steps can be omitted. The main drawback of the TS foils might be that of a small grain size, and hence a high number of substrate grain boundaries which generally cause an increase in roughness of the foils during annealing, and may also act as additional nucleation centers for graphene domains. Concerning the graphene growth, substrate grain boundaries do not present significant restriction since graphene domains easily extend their growth over several substrate grains [34]. Additionally, the higher density of atomic steps on microfacets formed after annealing could help with healing point defects in the graphene layer [35]. Further, the high purity of these foils implies that the amount of impurities segregating on the surface is very low. These impurities present significant issues since the nucleation on these cannot be easily suppressed by the increase of growth temperature [17]. Hence, by further optimization of the method, we expect that the TS foil will make it possible to grow graphene layers of superior quality compared to those recently prepared on standard copper foils.

Due to the distinct nature of the surfaces of TS- and commercial-Cu foils, the growth of graphene under the same conditions differs. In the case of commercial foils, the whole

surface is covered by polycrystalline single layer graphene, whereas on the TS foil the graphene grows in separated larger crystals. This difference can be explained by the lower concentration of defects on the TS foil and, hence, a lower concentration of nucleation sites, so it takes longer to fill the entire surface.

To evaluate graphene transport properties, we transferred the graphene grown on both types of the copper foil on a highly doped silicon substrate acting as a back gate, covered with a 285 nm-thick oxide barrier. We then performed two-point measurements of charge carrier mobility. It should be noted that after the graphene transfer, no annealing steps to improve graphene quality have been carried out in order to accurately distinguish the quality of the samples. We contacted the polycrystalline graphene layer (commercial foil) with Au/Ti contacts in a Hall bar geometry (figure 3(b)) and the separate graphene areas grown on the TS foil (figure 3(a)) with two contacts. Resistivity ρ shown in figure 3(f) and measured resistance R are related via the structure length L and width W by the formula $\rho = RW/L$ (in case of the Hall bar structure $W = 19 \mu\text{m}$ and $L = 2 \mu\text{m}$, in case of the single crystal domain $W = 12 \mu\text{m}$ and $L = 12 \mu\text{m}$). Carrier mobility was deduced according to Drude's model of diffusive transport $\mu = (ne\rho)^{-1}$ for the electron surface concentration $n = 2 \cdot 10^{12} \text{ cm}^{-2}$. The measured room temperature mobility of the graphene grown on the commercial copper foil was around $1200 \text{ cm}^2 \text{ V}^{-1} \text{ s}^{-1}$ with an extracted saturation density [36] of $n_{\text{sat}} \sim 9 \cdot 10^{11} \text{ cm}^{-2}$, whereas the mobility of the graphene grown on the TS foil was, at the same conditions, 3 times higher, i.e. around $3600 \text{ cm}^2 \text{ V}^{-1} \text{ s}^{-1}$ ($n_{\text{sat}} \sim 8 \cdot 10^{11} \text{ cm}^{-2}$). The low temperature (4 K) transport measurements gave us the mobility around $4400 \text{ cm}^2 \text{ V}^{-1} \text{ s}^{-1}$ ($n_{\text{sat}} \sim 8 \cdot 10^{11} \text{ cm}^{-2}$) for TS-foil grown graphene; in this case the Dirac point is shifted to a lower value of about 42 V. This difference in mobility of graphene fabricated on two distinct types of copper foils can be explained by the higher concentration of domain boundaries present on the graphene prepared on the standard copper foil. The domain boundaries have been identified as the primary cause of the mobility decrease in CVD grown graphene [11]. It should be noted that the strong shift of the charge neutrality point to high back-gate voltages (>40 V) indicates strong p-doping. This is usually caused by the presence of water and organic residues from the transfer process. It was reduced by thermal annealing of the sample at 130 °C for 48 h in a vacuum, and led to the shift of the charge neutrality point to 18 V while the room temperature mobility retained the same level [11].

We would like to note that the obtained mobilities of $3600 \text{ cm}^2 \text{ V}^{-1} \text{ s}^{-1}$ do not present the state-of-the-art values beyond the 10 000 reported for CVD graphene [13, 37]. This is caused mainly by the fact that we did not make any attempts for improving the graphene quality (e.g. by etching, annealing) in order to make a fair comparison of both types of graphene samples. We infer that by further optimization of the transfer process and cleaning, the higher mobility values will be obtained. However, the main advantages of the TS foils (e.g. absence of detrimental morphological features, high

purity of the near-surface layer and their clean surface) make them superior over the commercial ones.

Recently, other high quality substrates employed for the CVD graphene synthesis have been reported, e.g. metal single crystals [38] and thin epitaxial layers of transition metals prepared on sapphire substrates [39–43]. In principle, our method can also be applied to sapphire substrates which may lead to foils with a large grain size and single grain orientation (see supporting information S1 for details, available at stacks.iop.org/NANO/25/185601/mmedia).

Conclusions

In conclusion, we have introduced a template stripping method for the preparation of Cu foils using SiO₂/Si substrates as a template. The ‘as prepared’ TS foils display a roughness below 0.6 nm even on a large scale, and their purity is primarily determined by the Cu target (>99.999%). However, the annealing of these foils in a low-pressure hydrogen atmosphere and during the CVD graphene synthesis, especially at temperatures around 1000 °C, leads to an increase of foil surface roughness. It is caused, presumably, by copper recrystallization and evaporation and sublimation of copper atoms. Nevertheless, the large scale roughness still remains nearly in one order of magnitude below that of typical commercial foils.

The small amount of roughness and low concentration of defects and impurities result in a low number of nucleation sites, which is an important condition for the preparation of graphene with a large domain size and thus improved transport properties. Even without any extensive attempts to improve the preparation procedure, the foils remain very smooth over a large area, which is the necessary condition for a transfer of wrinkle-free graphene. The room temperature mobility of the graphene grown on the TS foil was 3 times higher ($\approx 3600 \text{ cm}^2 \text{ V}^{-1} \text{ s}^{-1}$) compared to that one grown on the commercial copper foil, and should be further improved. We expect that by employing the presented well-defined substrates, it would be much easier to control all necessary processes required for obtaining the high quality graphene.

Acknowledgments

This work was supported by the project ‘CEITEC—Central European Institute of Technology’ (CZ.1.05/1.1.00/02.0068) from European Regional Development Fund, the Grant Agency of the Czech Republic (project No. P102/12/1881), the Technology Agency of the Czech Republic (project No. TE01020233), and the EU 7th Framework Programme (projects SYLICA, No. 286154, and UnivSEM, No. 280566). P P was supported by Sciex fellowship. L K acknowledges the support by the project ‘Centre for Materials Research at FCH BUT’ (CZ.1.05/2.1.00/01.0012) from ERDF Z L was supported by Brno PhD Talent Scholarship Holder—Funded by the Brno City Municipality. Authors thank FEI Company for providing access to plasma ripper.

References

- [1] Geim A K 2009 Graphene: status and prospects *Science* **324** 1530–4
- [2] Rao C N R, Sood A K, Subrahmanyam K S and Govindaraj A 2009 Graphene: the new two-dimensional nanomaterial *Angew. Chem. Int. Ed.* **48** 7752–7
- [3] Novoselov K S, Falco V I, Colombo L, Gellert P R, Schwab M G and Kim K A 2012 Roadmap for graphene *Nature* **490** 192–200
- [4] Li X *et al* 2009 Large-area synthesis of high-quality and uniform graphene films on copper foils *Science* **324** 1312–4
- [5] Edwards R S and Coleman K S 2013 Graphene film growth on polycrystalline metals *Acc. Chem. Res.* **46** 23–30
- [6] Iwasaki T, Park H J, Konuma M, Lee D S, Smet J H and Starke U 2011 Long-range ordered single-crystal graphene on high-quality heteroepitaxial ni thin films grown on MgO (111) *Nano. Lett.* **11** 79–84
- [7] Ago H, Ogawa Y, Masaharu T, Tsuji M, Mizuno S and Hibino H 2012 Catalytic growth of graphene: toward large-area single-crystalline graphene *J. Phys. Chem. Lett.* **3** 2228–36
- [8] Wang L, Zhang X, Chan H L W, Yan F and Ding F 2013 Formation and healing of vacancies in graphene chemical vapor deposition (CVD) growth *J. Am. Chem. Soc.* **135** 4476–82
- [9] Yu Q *et al* 2011 Control and characterization of individual grains and grain boundaries in graphene grown by chemical vapour deposition *Nat. Mater.* **10** 443–9
- [10] Koepeke J C, Wood J D, Estrada D, Ong Z-Y, He K T, Pop E and Lyding J W 2013 Atomic-scale evidence for potential barriers and strong carrier scattering at graphene grain boundaries: a scanning tunneling microscopy study *ACS Nano*. **7** 75–86
- [11] Song H S, Li S L, Miyazaki H, Sato S, Hayashi K, Yamada A, Yokoyama N and Tsukagoshi K 2012 Origin of the relatively low transport mobility of graphene grown through chemical vapor deposition *Sci. Rep.* **2** 337
- [12] Li X *et al* 2010 Graphene films with large domain size by a two-step chemical vapor deposition process *Nano. Lett.* **10** 4328–34
- [13] Yan Z, Lin J, Peng Z, Sun Z, Zhu Y, Li L, Xiang C, Samuel E L, Kittrell C and Tour J M 2012 Toward the synthesis of wafer-scale single-crystal graphene on copper foils *ACS Nano*. **6** 9110–7
- [14] Zhou H, Yu W J, Liu L, Cheng R, Chen Y, Huang X, Liu Y, Wang Y, Huang Y and Duan X 2013 Chemical vapour deposition growth of large single crystals of monolayer and bilayer graphene *Nat. Commun.* **4** 2096
- [15] Hao Y *et al* 2013 The role of surface oxygen in the growth of large single-crystal graphene on copper *Science* **342** 720–3
- [16] Li X, Magnuson C W, Venugopal A, Tromp R M, Hannon J B, Vogel E M, Colombo L and Ruoff R S 2011 Large-area graphene single crystals grown by low-pressure chemical vapor deposition of methane on copper *J. Am. Chem. Soc.* **133** 2816–9
- [17] Wang H, Wang G, Bao P, Yang S, Zhu W, Xie X and Zhang W-J 2012 Controllable synthesis of submillimeter single-crystal monolayer graphene domains on copper foils by suppressing nucleation *J. Am. Chem. Soc.* **134** 3627–30
- [18] Kim H, Mattevi C, Reyes Calvo M, Oberg J C, Artiglia L, Agnoli S, Hirjibehedin C F, Chhowalla M and Saiz E 2012 Activation energy paths for graphene nucleation and growth on Cu *ACS Nano*. **6** 3614–23
- [19] Mehdipour H and Ostrikov K 2012 Kinetics of low-pressure, low-temperature graphene growth: toward single-layer, single-crystalline structure *ACS Nano*. **6** 10276–86

- [20] Wofford J M, Nie S, McCarty K F, Bartelt N C and Dubon O D 2010 Graphene islands on Cu foils: the interplay between shape, orientation, and defects *Nano. Lett.* **10** 4890–6
- [21] Li X, Zhu Y, Cai W, Borysiak M, Han B, Chen D, Piner R D, Colombo L and Ruoff R S 2009 Transfer of large-area graphene films for high-performance transparent conductive electrodes *Nano. Lett.* **9** 4359–63
- [22] Liu N, Pan Z, Fu L, Zhang C, Dai B and Liu Z 2011 The origin of wrinkles on transferred graphene *Nano. Res.* **4** 996–1004
- [23] Murdock A T, Koos A, Britton T B, Houben L, Batten T, Zhang T, Wilkinson A J, Dunin-Borkowski R E, Lekka C E and Gobert N 2013 Controlling the orientation, edge geometry, and thickness of chemical vapor deposition graphene *ACS Nano.* **7** 1351–9
- [24] Zhang B, Lee W H, Piner R, Kholmanov I, Wu Y, Li H, Ji H and Ruoff R S 2012 Low-temperature chemical vapor deposition growth of graphene from toluene on electroplished copper foils *ACS Nano.* **6** 2471–6
- [25] Mohsin A et al 2013 Synthesis of millimeter-size hexagon-shaped graphene single crystals on resolidified copper *ACS Nano.* **7** 8924–31
- [26] Kim S M, Hsu A, Lee Y-H, Dresselhaus M, Palacios T, Kim K K and Kong J 2013 The effect of copper pre-cleaning on graphene synthesis *Nanotechnology* **24** 365602
- [27] Diebel J, Hove H and Rabe J P 2001 Fabrication of large-scale ultra-smooth metal surfaces by replica technique *Appl. Phys. A* **73** 273–9
- [28] Ragan R, Ohlberg D, Blackstock J J, Kim S and Williams R S 2004 Atomic surface structure of UHV-prepared template-stripped platinum and single-crystal platinum(111) *J. Phys. Chem. B* **108** 20187–92
- [29] Weiss E A, Kaufman G K, Kriebel J K, Li Z, Schalek R and Whitesides G M 2007 Si/SiO₂-templated formation of ultraflat metal surfaces on glass, polymer and solder supports: their use as substrates for self-assembled monolayers *Langmuir* **23** 9686–94
- [30] Šikola T et al 1999 Deposition of magnetic thin films by IBAD *Nucl. Instrum. Methods Phys. Res. Sect. B* **148** 907–11
- [31] Rafaja D, Valvoda V, Šikola T and Spousta J 1998 *Ab initio* study of thin metallic and ceramic films *Thin Solid Films* **324** 198–208
- [32] Celebi K, Cole M T, Choi J W, Wyczyszkowski F, Legagneux P, Rupasinghe N, Robertson J, Teo K B K and Park H G 2013 Evolutionary kinetics of graphene formation on copper *Nano. Lett.* **13** 967–74
- [33] Sarajlic O I and Mani R G 2013 Mesoscale scanning electron and tunneling microscopy study of the surface morphology of thermally annealed copper foils for graphene growth *Chem. Mater.* **25** 1643–8
- [34] Zhang X, Xu Z, Hui L, Xin J and Ding F 2013 How the orientation of graphene is determined during chemical vapor deposition growth *J. Phys. Chem. Lett.* **3** 2822–2827
- [35] Meng L, Wang Z, Jiang J, Yang Y and Wang J 2013 Defect healing of chemical vapor deposition graphene growth by metal substrate step *J. Phys. Chem. C* **117** 15260
- [36] Du X, Skachko I, Barker A and Andrei E Y 2008 Approaching ballistic transport in suspended graphene *Nature Nanotechnol.* **3** 491–5
- [37] Piner R et al 2013 Graphene synthesis via magnetic inductive heating of copper substrates *ACS Nano.* **7** 7495–9
- [38] Batzill M 2012 The surface science of graphene: metal interfaces, CVD synthesis, nanoribbons, chemical modifications, and defects *Surf. Sci. Rep.* **67** 83–115
- [39] Ago H, Ito Y, Mizuta N, Yoshida K, Hu B, Orofeo C M, Tsuji M, Ikeda K and Mizuno S 2010 Epitaxial chemical vapor deposition growth of single layer graphene over cobalt film crystallized on sapphire *ACS Nano.* **4** 7407–14
- [40] Sutter P W, Albrecht P M and Sutter E A 2010 Graphene growth on epitaxial Ru thin films on sapphire *Appl. Phys. Lett.* **97** 213101
- [41] Vo-Van C, Kimouche A, Reserbat-Plantey A, Fluchart O, Bayle-Guillemaud P, Bendiab N and Coraux J 2011 Epitaxial graphene prepared by chemical vapor deposition on single crystal thin iridium films on sapphire *Appl. Phys. Lett.* **98** 181903
- [42] Hu B, Ago H, Ito Y, Kawahara K, Tsuji M, Magome E, Sumitani K, Mizuta N, Ikeda K and Mizuno S 2012 Epitaxial growth of large-area single-layer graphene over Cu (111)/sapphire by atmospheric pressure CVD *Carbon* **50** 57–65
- [43] Jacobberger R M and Arnold M S 2013 Graphene growth dynamics on epitaxial copper thin films *Chem. Mater.* **25** 871–7

Commented paper 7

MACH, Jindřich, Pavel PROCHÁZKA, M BARTOŠÍK, David NEZVAL, Jakub PIASTEK, Jan HULVA, Vojtěch ŠVARC, Martin KONEČNÝ, Lukáš KORMOŠ a Tomáš ŠIKOLA. Electronic transport properties of graphene doped by gallium. *NANOTECHNOLOGY* [online]. 2017, **28**(41). ISSN 0957-4484. Dostupné z: doi:10.1088/1361-6528/aa86a4

Electronic transport properties of graphene doped by gallium

J Mach^{1,2} , P Procházka^{1,2}, M Bartošík^{1,2} , D Nezval², J Piastek², J Hulva², V Švarc², M Konečný², L Kormoš¹  and T Šikola^{1,2}

¹ Central European Institute of Technology—Brno University of Technology (CEITEC BUT) Purkyňova 123, 612 00 Brno, Czechia

² Institute of Physical Engineering, Brno University of Technology, Technická 2, 616 69 Brno, Czechia

E-mail: bartosik@fme.vutbr.cz

Received 26 June 2017, revised 1 August 2017

Accepted for publication 16 August 2017

Published 14 September 2017



CrossMark

Abstract

In this work we present the effect of low dose gallium (Ga) deposition (<4 ML) performed in UHV (10^{-7} Pa) on the electronic doping and charge carrier scattering in graphene grown by chemical vapor deposition. *In situ* graphene transport measurements performed with a graphene field-effect transistor structure show that at low Ga coverages a graphene layer tends to be strongly n-doped with an efficiency of 0.64 electrons per one Ga atom, while the further deposition and Ga cluster formation results in removing electrons from graphene (less n-doping). The experimental results are supported by the density functional theory calculations and explained as a consequence of distinct interaction between graphene and Ga atoms in case of individual atoms, layers, or clusters.

Keywords: graphene, gallium, CVD, DFT, transport, doping

(Some figures may appear in colour only in the online journal)

1. Introduction

Graphene, a single atomic layer of carbon atoms arranged in a hexagonal lattice, with its excellent electrical [1–4] mechanical [5, 6], and optical properties [7, 8], surface to volume ratio, and chemical reactivity [9], has been considered as a promising candidate for the future devices. Its unique electronic structure results from the zero band gap and the conical dispersion close to the *K* points in the Brillouin zone where the conduction and valence bands touch each other in the charge neutrality point (CNP). In the real devices, however, the interaction of graphene layer with surrounding atoms can strongly affect delocalized electrons, change the CNP, Fermi level position, and the corresponding doping type [10–14].

One of the most common factors influencing transport properties of graphene is related to the bonds between the substrates which are often used as a supporting layer for graphene e.g. SiO₂ [15, 16], BN [17], MoS₂ [18], SiC [19] and metals for graphene grown by chemical vapor deposition (CVD) [20–23]. Other important sources of electronic disruption in graphene are its structural defects [24, 25] i.e. disclinations, dislocations and grain boundaries [26]. These

imperfections are determined mainly by a graphene fabrication process. In addition, graphene transport properties can be also strongly affected by atoms and molecules adsorbed on the graphene surface.

Since the investigation of graphene transport properties necessarily involves the conductive interface between graphene and metal electrodes, a considerable effort has been also devoted to the experimental [27–32] and theoretical [33–40] studies of a graphene–metal (G–M) junction. Using the density functional theory (DFT) Giovannetti *et al* [33] have shown that G–M interfaces can be divided into two classes of interfacial bonding, the first one with weaker bonds and a larger equilibrium separation between graphene and metal atoms (Ag, Al, Cu, Cd, Ir, Pt, Au) and the second one with stronger bonds and a smaller equilibrium separation (Ni, Co, Ru, Pd, Ti) which are characteristic for the physisorption and chemisorption, respectively.

In the case of physisorption, the influence of Ga and Al atoms differs from the other atoms because of the interaction of their valence p-electrons with π -electrons of graphene [41, 42]. However, all metals in this group do not form chemical bonds with graphene and, hence, the doping type

and shift of CNP can be deduced from the G–M work function (WF) difference. Another important factor which has to be considered, is a potential step, which is related to the presence of an interfacial dipole [33]. For metals bonded to a graphene layer by chemisorption the band structure becomes more complicated because of a strong hybridization between the graphene pz orbitals and the valence electrons of metals.

As Wu *et al* [43] experimentally and theoretically showed for the G–Au interface, the chemical bonds and related interfacial WF difference can be tuned by the amount of deposited Au, and also by morphology: isolated Au nanoparticles n-dopes the graphene, while continuous Au film results in graphene p-doping. A similar behavior was observed also for the G–Pt interface [27].

A thorough study and understanding of changes in graphene electric properties caused by the interaction between graphene and adsorbed Ga atoms is very important, especially for development of electric devices using Ga semiconductors (GaAs, GaN, ...). However, such a thorough study probing the influence of different coverages of Ga atoms has not been performed so far, except that one for a fixed coverage of 200 ML Ga atoms [41]. Nevertheless, this study was provided under atmospheric conditions and thus the influence of molecules from the surrounding atmosphere could not be limited and controlled.

In this article, we study the graphene–gallium interface in detail with regard to its experimentally measured transport properties, and corresponding changes of electronic properties calculated by *ab initio* DFT.

2. Methods

In order to achieve a large area coverage, a polycrystalline graphene layer was prepared by the standard low pressure CVD method [20]. As a substrate an ultrasmooth copper foil with no additional mechanical or chemical pretreatment was used for graphene growth [44]. First, the copper foil was annealed in a flow of hydrogen (4 sccm, 10 Pa, 1000 °C, 30 min) to remove air adsorbates. Subsequently, methane was introduced (40 sccm, 70 Pa, 1000 °C, 30 min) and graphene grown in a H₂/CH₄ mixture. Finally, the graphene from the bottom side of the copper substrate was removed in an oxygen–argon plasma (20% O₂, 80% Ar, 2 min), while that one from the top side was protected from etching by a spin-coated PMMA layer.

Using a PMMA-assisted wet transfer method, graphene was transferred on a p-doped silicon substrate (resistivity of $(0.1\text{--}1.5) \times 10^{-3} \Omega \text{ cm}$) with 280 nm SiO₂ and prefabricated Au (45 nm)/Ti (3 nm) electrodes. The area between these electrodes, covered with graphene, then define a geometry of the measured graphene channel with the length $L = 50 \mu\text{m}$ and width $W = 400 \mu\text{m}$.

By applying a back-gate voltage (V_{BG}) to a silicon substrate, one is able to locally control a charge carrier density $n = (\varepsilon_0 \varepsilon_r / ed) V_{\text{BG}}$, where ε_0 is the vacuum permittivity, ε_r is the relative permittivity of SiO₂ (3.9), e is the elementary charge and d is the thickness of the SiO₂ layer. Then, the

graphene resistivity $\rho = RW/L$ as a function of V_{BG} defines a doping type and charge carrier mobility.

Resistance R of the graphene layer between the Au electrodes was measured using a lock-in amplifier SR830 (Stanford Research Systems) with a frequency of 1333 Hz, fixed current of 100 nA, and back-gate voltage being changed with a sweeping rate 0.6 V s^{-1} in a range of $\pm 80 \text{ V}$.

Ga atoms with thermal energy were evaporated by an e-beam effusion cell (Omicron EMF 3) from a PBN crucible inserted into a Mo cover. *In situ* transport measurements were carried out without breaking ultrahigh vacuum ($p_{\text{base}} = 4 \times 10^{-7} \text{ Pa}$).

The DFT study was performed by the Vienna *ab initio* Simulation Package (VASP) [45–47]. All our DFT calculations were carried out using the projected augmented wave method [48, 49] and an energy cut-off of 600 eV. The generalized gradient approximation proposed by Perdew *et al* [50] was adapted to treat the electronic exchange and correlation. A vacuum spacer of 17 Å was used to eliminate the interaction between the layers in the neighboring supercells. A Γ -centered $3 \times 3 \times 1$ Monkhorst–Pack mesh [51] was used for structure optimizations. For the calculation of the density of states (DOS) a $9 \times 9 \times 1$ mesh was used. All structures were relaxed with a tolerance of residual forces of 0.01 eV \AA^{-1} .

3. Experimental results

The influence of Ga deposition on graphene transport properties is shown in figure 1(a). The CNP of as-prepared graphene is positioned at positive values of the back-gate voltage, indicating an effect of pre-existing adsorbates which positively dope a graphene layer [52–54]. The sample annealing under vacuum at $T = 120 \text{ °C}$ promoted their desorption, and in 24 h resulted in shifting the graphene CNP to only $V_{\text{BG}} = 3 \text{ V}$, which was a starting point for Ga deposition. During the first seconds of the deposition, when the Ga coverage is much less than one monolayer, Ga atoms strongly n-dope the graphene layer (indicated by arrow 1). The CNP was shifted outside the measured range of $V_{\text{BG}} < -80 \text{ V}$ at a Ga surface concentration of about $9.7 \times 10^{12} \text{ cm}^{-2}$ ($\sim 0.01 \text{ ML}$ coverage).

During the subsequent deposition the CNP was removed left outside the measurement back-gate voltage range and then only the decrease or increase of the resistivity curve was observed. It can be assumed, that the resistivity decrease or increase corresponds to the shift of CNP into the left or right, respectively. The decrease of resistivity indicating the n-doping of graphene continued up to a Ga surface concentration of $\sim 40 \times 10^{12} \text{ cm}^{-2}$ (\sim coverage 0.04 ML), and then the reversal increase of the resistivity was observed (indicated by arrow 2). After this return point, graphene starts to be less n-doped (removing electrons from graphene).

The charge carrier density n_c and related experimental CNP position for low Ga surface concentrations of up to $\sim 9.1 \times 10^{12} \text{ cm}^{-2}$ is plotted in figure 1(b) as a function of this Ga surface concentration. The red line in the graph represents

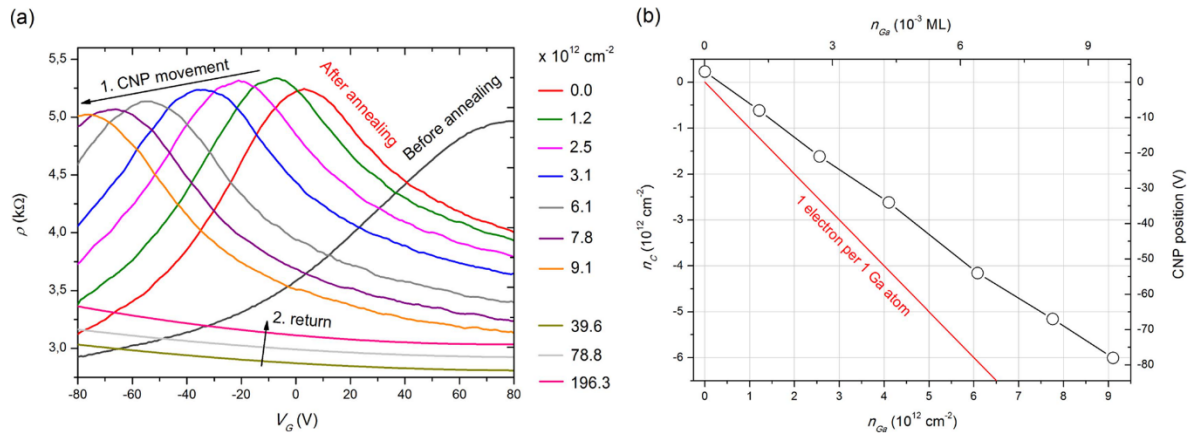


Figure 1. (a) Resistivity as a function of back-gate voltage of a graphene sample and its development with the growing surface concentration of deposited Ga atoms. Before annealing (black), and after 24 h of vacuum annealing at 120 °C (red). The arrow 1 indicates an evolution of CNP position during the Ga deposition corresponding to n-doping. The arrow 2 indicates a reversal resistivity evolution for CNP shifts less than $V_{BG} < -80$ V related to a decrease of n-doping. (b) Charge carrier density and relevant CNP position during the Ga deposition (negative values corresponds to electrons). The n-doping is caused by an electron transfer from Ga to graphene. The theoretical red line depicts charge carrier densities related to a transfer of one electron from one Ga atom.

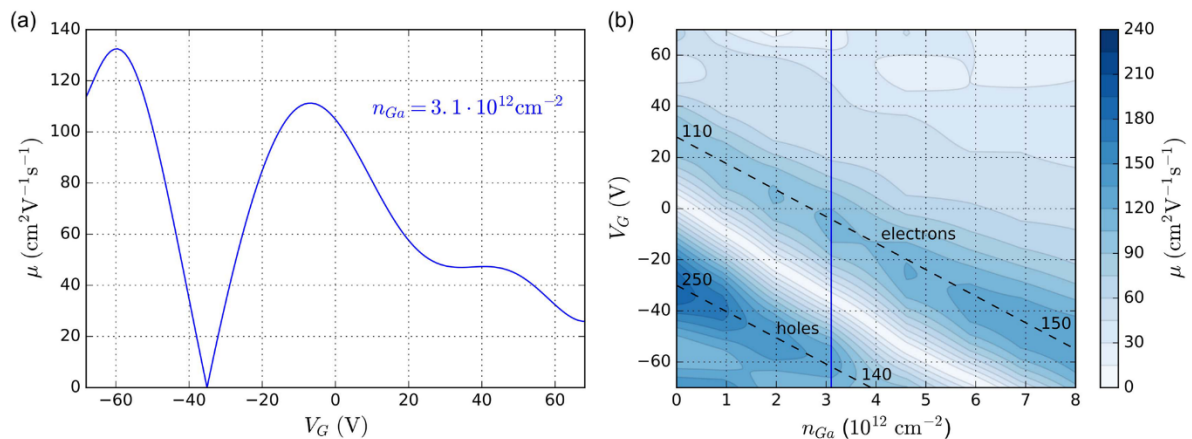


Figure 2. (a) Charge carrier mobility as a function of back gate voltage calculated according to Drude's model using the curve in figure 1(a) for a Ga concentration of $3.1 \times 10^{12} \text{ cm}^{-2}$. (b) Evolution of charge carrier mobility as a function of back gate voltage during deposition of the Ga atoms on graphene.

the theoretical charge carrier density related to the case when one Ga atom supplies one electron into the graphene layer. The experimentally measured positions of CNP and related charge carrier density decrease more slowly, the calculated doping efficiency is only about 0.64 electrons per Ga atom.

The data of charge carrier mobility plotted in figure 2(a) were calculated from the curve corresponding to the Ga surface concentration $3.1 \times 10^{12} \text{ cm}^{-2}$ (figure 1(a)—blue curve) as a function of back gate voltage according to Drude's model of diffusive transport $\mu = (ne\rho)^{-1}$. Decreasing graphene mobility with the increasing charge carrier density results from a nonlinear dependence of graphene resistivity on carrier concentration due to the long and short range scatterers [17, 55–57]. A minimum value of graphene mobility at $V_{BG} = -37$ V then define a CNP position and therefore a number of dopant carriers.

Figure 2(b) shows an evolution of charge carrier mobility during the Ga deposition calculated from the curves in figure 1(a) valid for Ga concentrations $(0-1) \times 10^{13} \text{ atoms cm}^{-2}$. The electron–hole asymmetry of the annealed sample with respect to CNP (zero mobility) is often caused by Au/Ti contacts [58, 59], charged impurities and strained grapheme [60]. The CNP shift to negative values of back gate voltage during the Ga deposition indicates an electron transfer from Ga to graphene. The electron transfer is accompanied by a remarkable decrease of the hole-mobility due to creation of new scattering centers. A slight increase of electron mobility can be explained by neutralization of charged defects, which scatter electrons more strongly than holes [60].

The electron and hole mobilities achieve their maxima at voltages distant in both directions from the CNP by about 30 V (the highest mobility value in figure 2), the maximums

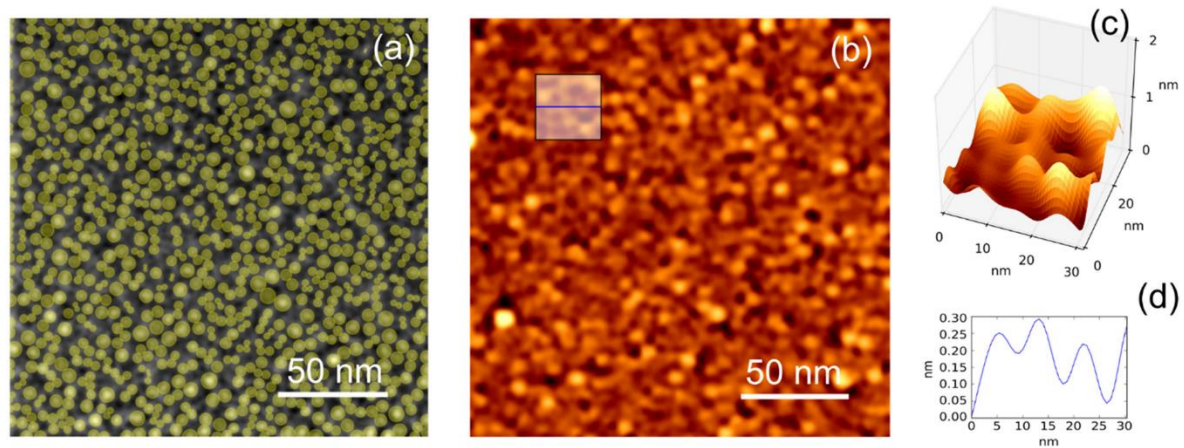


Figure 3. (a) SEM image of a surface with a high Ga concentration of $37.6 \times 10^{14} \text{ cm}^{-2}$ (~ 4 ML) provided with yellow circles constructed with respect to the nearest Ga islands, (b) AFM topography of this surface, (c) detailed AFM 3D topography (marked by the grey square in b), and (d) the corresponding profile of Ga islands (marked by the blue line in b).

of the electron-mobility reaches $110\text{--}150 \text{ cm}^2 \text{ V}^{-1} \text{ s}^{-1}$, and the hole-mobility $140\text{--}250 \text{ cm}^2 \text{ V}^{-1} \text{ s}^{-1}$. Such a small value can be hardly compared $2 \times 10^5 \text{ cm}^2 \text{ V}^{-1} \text{ s}^{-1}$ for suspended graphene at cryogenic temperatures [1, 2] or even with $4 \times 10^4 \text{ cm}^2 \text{ V}^{-1} \text{ s}^{-1}$ obtained for high quality exfoliated graphene on SiO_2 at room temperature [15]. Generally, the CVD graphene exhibits the lower mobility which is ideally about [20] $4050 \text{ cm}^2 \text{ V}^{-1} \text{ s}^{-1}$. Under less ideal growth conditions, due to line defects at grain boundaries, the mobility can fall down to the value [61] $1100 \text{ cm}^2 \text{ V}^{-1} \text{ s}^{-1}$, which is still quite high in comparison with our mobilities. Therefore, the lower hole and electron mobilities in our experiment can be probably attributed to higher density of grain boundaries [24]. A certain role can also play impurities disturbing the crystal order, and also a long-range Coulomb scattering caused by induction of electrons by Ga adsorbed atoms.

The scanning electron microscopy (SEM) image (figure 3(a)), and atomic force microscopy (AFM) topography (figure 3(b)) were taken *ex situ* after the deposition of quite huge Ga concentration of $37.6 \times 10^{14} \text{ cm}^{-2}$ (~ 4 ML). Such a huge concentration (exceeding the maximum concentration 0.5 ML in transport experiments) was necessary to observe the gallium on a surface due to the SEM and AFM resolution. It is obvious the gallium forms islands at such a high concentration. The yellow circles in the SEM image (figure 3(a)) mark the areas of gallium islands with respect to the nearest neighbor. The average radius of these circle areas corresponding the average lateral diffusion radius of Ga atoms is $2.2 \pm 0.6 \text{ nm}$. The view on individual Ga islands can be observed in detailed 3D AFM topography (figure 3(c)), and corresponding profile (figure 3(d)).

When Ga coverages were increased to values of 140–300 ML the CNP returned into the measurable range ($V_{\text{BG}} > -80 \text{ V}$). However, the electron and hole-mobilities were reduced approximately by one order of magnitude. At these high coverages the huge droplets of diameters about 400 nm were formed. Therefore, one can assume that

transport properties might be affected by stress between Ga droplets and the graphene layer [62], and by the surface conductivity of metallic gallium. Hence, these high coverages are not addressed in the following analysis.

4. Computational results

First, a hexagonal free-standing graphene structure was relaxed and the lattice constant estimated to a value of 2.47 \AA . The calculated free-standing graphene had no initial doping—the Fermi energy precisely crossed the CNP.

Three possible sites were considered for the adsorption of gallium atoms on graphene (figure 4(a))—on top of a carbon atom (T), at the center of a carbon hexagon (C) and above a carbon–carbon bond (B). Comparison of the adsorption energies at these sites has shown the site C is the most stable position of Ga atoms with an adsorption energy of 987 meV and a distance of 2.22 \AA from the graphene layer (figure 4(a) bottom).

Furthermore, the influence of different Ga concentrations in the range of $4.7 \times 10^{12} - 2.8 \times 10^{15} \text{ cm}^{-2}$ on the graphene electronic properties was studied. The calculations were mostly performed using a 8×8 graphene superstructure, and only for the lowest concentrations larger superstructures were used (16×16 for $7.4 \times 10^{12} \text{ cm}^{-2}$, 18×18 for $5.8 \times 10^{12} \text{ cm}^{-2}$, 20×20 for $4.7 \times 10^{12} \text{ cm}^{-2}$). First, the Ga atoms were relaxed on the graphene surface, then the electronic band structure and DOS were calculated for all the concentrations. The concentration of charge carriers in graphene was determined from the site-projected DOS.

The examples of band structures and DOS calculations for two different Ga concentrations ($3.0 \times 10^{13} \text{ cm}^{-2}$ and $4.7 \times 10^{14} \text{ cm}^{-2}$) are shown in figure 5. The energy band diagrams (figures 5(a), (b)) prove the n-doping of graphene by gallium, since the Fermi level is above the CNP. The higher concentration of Ga atoms moves the Fermi level more above

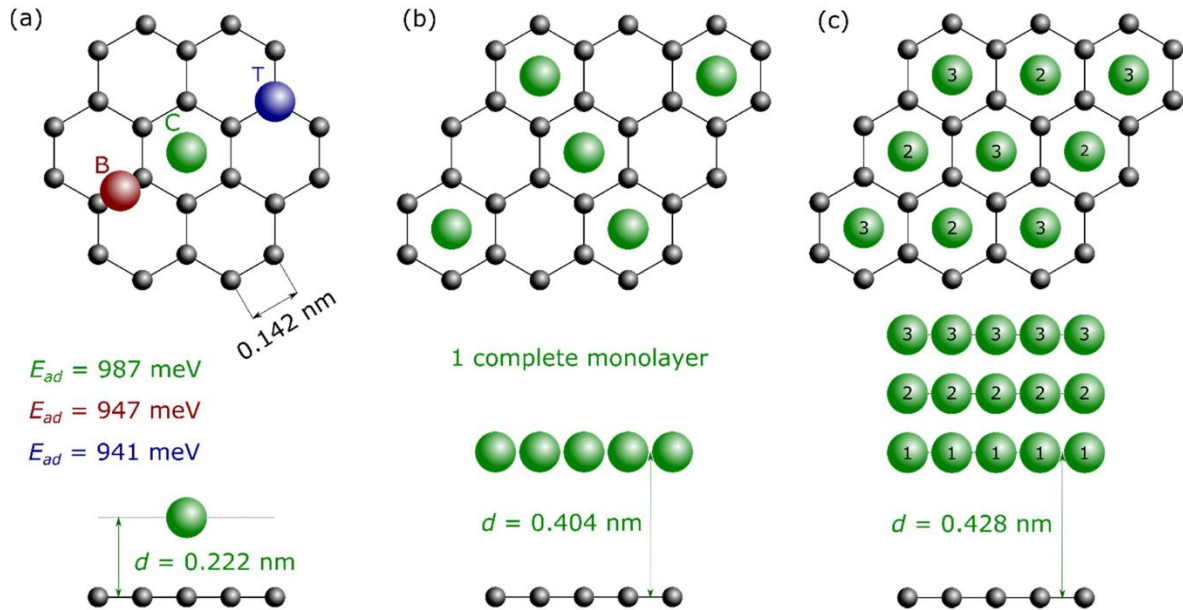


Figure 4. Space arrangement of Ga atoms on a graphene hexagonal lattice in DFT calculations in case of layer-by-layer growth. (a) Three different adsorption sites of Ga atoms—top view, corresponding adsorption energies, and a side view of an individual Ga atom in the central position. (b) The first complete monolayer of gallium atoms in the central positions on graphene—top view, and the distance between Ga and graphene monolayers—side view. (c) The first three gallium monolayers—top view, and their distance from graphene—side view (corresponding layers are labeled by numbers).

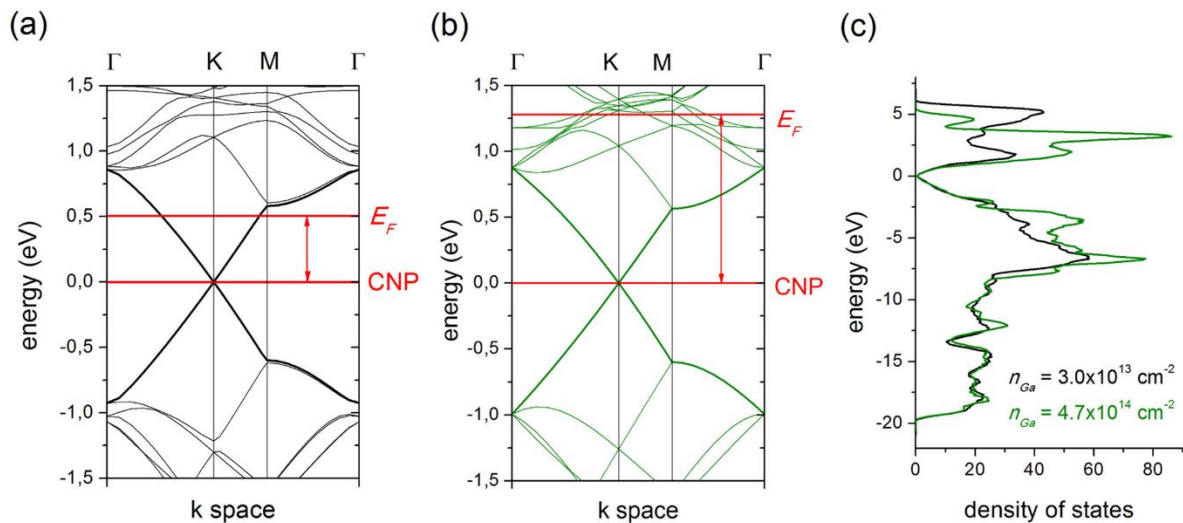


Figure 5. DFT calculated band structures of graphene for Ga concentrations (a) $3.0 \times 10^{13} \text{ cm}^{-2}$ and (b) $4.7 \times 10^{14} \text{ cm}^{-2}$, (c) the corresponding DOS.

the CNP, however, the band gap in graphene is not opened. The DOS values (figure 5(c)) close to the CNP are higher for the higher Ga concentration which is caused by formation of new states associated with additional Ga atoms.

The density of charge carriers n_C in the graphene layer (doping) as a function of deposited Ga concentration n_{Ga} calculated by DFT is shown in figure 6(a)—green dots. There

are two doping regions. When the concentration of Ga atoms is below $4.7 \times 10^{14} \text{ cm}^{-2}$ ($<0.5 \text{ ML}$) that corresponds to a Fermi level shift of 1282 meV (see figure 5(b)), the graphene electron concentration is increasing, above this Ga concentration value the electron concentration is rapidly decreasing. The DFT calculated charge carrier concentration was fitted by a reasonably smooth curve (black dashed line in

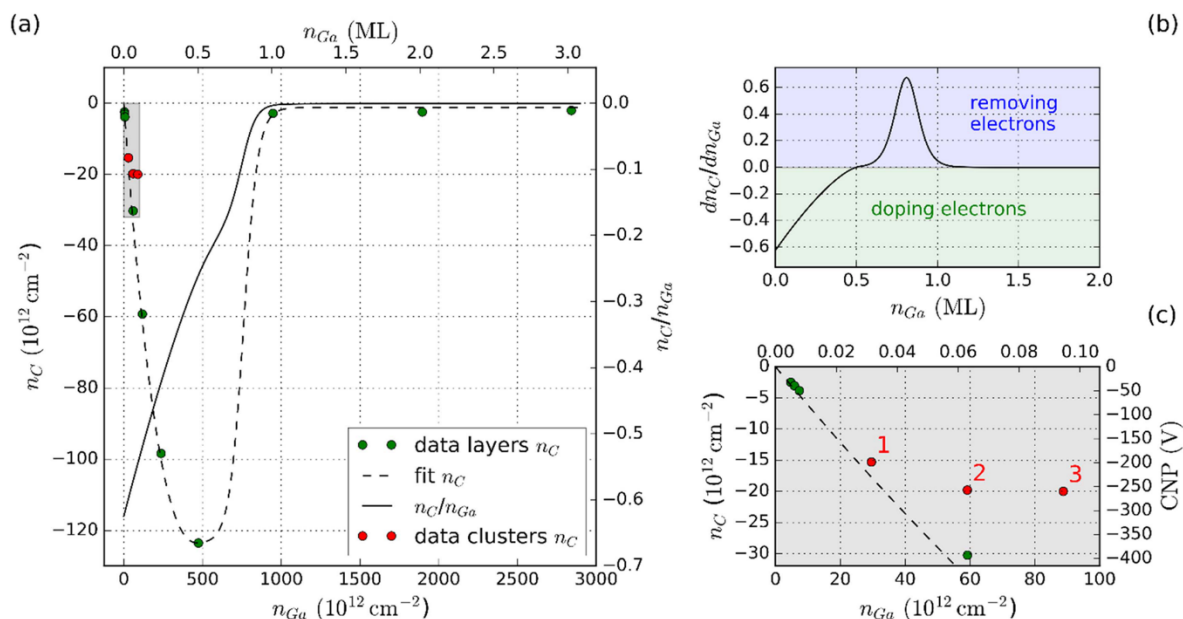


Figure 6. (a) Calculated density of charge carriers (electrons) in graphene as a function of Ga concentration. The green dots are the results of DFT calculation that were fitted by the black dashed curve. The average number of charge carriers per one Ga atom is expressed by the black solid curve. (b) The change of the number of charge carriers per every additional Ga atom was obtained by differentiation of the fitting black dashed curve, and the green and blue areas separate the doping by electrons and removing electrons, respectively. (c) The detail of the chart in (a) (marked by the grey rectangle) where the red dots are the results of DFT calculation for an individual atom (1), and clusters consisting of two (2), and three (3) Ga atoms as depicted in figures 7(a)–(c).

figure 6(a) which was used for the calculation of an average number of electrons supplied by one Ga atom (n_C/n_{Ga} —black solid line in figure 6(a)), and the change of the electrons inside graphene caused by one additional Ga atom (dn_C/dn_{Ga} —black solid line in figure 6(b)). At the lowest Ga coverage (0.005 ML) the average number of electrons brought by one Ga atom is about 0.6, however, this number rapidly goes down when the Ga concentration increases. At the higher Ga concentration $4.7 \times 10^{14} \text{ cm}^{-2}$ (~ 0.5 ML) it is equal only to 0.26 electrons per one Ga atom and then goes to zero (figure 6(a)—black solid curve). The DFT calculation for layer-by-layer growth shows the gallium effectively n-dopes graphene only up to the coverages corresponding to the 0.5 ML where the charge carrier density is the most negative (peak in figure 6(a)). Adding more Ga atoms above the coverage of the 0.5 ML the charge carrier density rapidly goes to zero which is caused by the extraction of electrons from graphene (figure 6(b)).

The decrease of electron-doping with higher Ga concentration is a direct result of our DFT calculations. Considering all the DFT results, it can be better understood via the distancing of Ga atoms from the graphene surface (figure 4). The equilibrium distance between the layer of Ga atoms and graphene is approximately 2.2 \AA for low Ga coverages (< 0.5 ML), 2.3 \AA for the 0.5 ML coverage and more than 4 \AA for higher coverages (> 0.5 ML). In other words, the further the Ga atom from graphene is, the less graphene is doped. In this context, the significant decrease of graphene doping by Ga at concentrations corresponding to the

0.5–1.0 ML coverages can be explained by a profound (almost double) increase of the distance between Ga and graphene (from 2.2 to 4.0 \AA). Although the distance between Ga and graphene gradually increases with the concentration, the step change in the distance is associated with the creation of much stronger chemical bonds between gallium atoms when the complete first monolayer is formed. Consequently, the creation of chemical bonds between Ga atoms weakens the interaction between the Ga atoms and graphene that results in this step increase of the distance between the Ga monolayer and the graphene. A further smaller increase of the Ga-graphene distance can be observed when the second, and third complete Ga layer is formed (Ga-graphene distance for two layers of Ga is 4.13 \AA and for three layers of Ga is 4.28 \AA —figure 4(c)). However, the effect is not as significant as in case of the first monolayer completion.

This fact is supported by the comparison of the adsorption energy of the individual Ga atom, and a monolayer of Ga atoms on a graphene surface, which is 987 meV , and 8 meV (per one Ga atom), respectively. It means the attractive interaction of individual Ga atoms onto the graphene is much weaker (more than hundred times) when the complete monolayer is formed.

The effect of strong chemical bonds between neighboring Ga atoms at short distances is especially important if we assume the gallium prefers the clusters (islands) growth before layer-by-layer growth. In this case the withdrawal of the Ga atoms from the surface as a consequence of strong Ga–Ga chemical bonds begins at much lower concentrations as can be seen in figures 7(a)–(c). Here, the DFT calculated

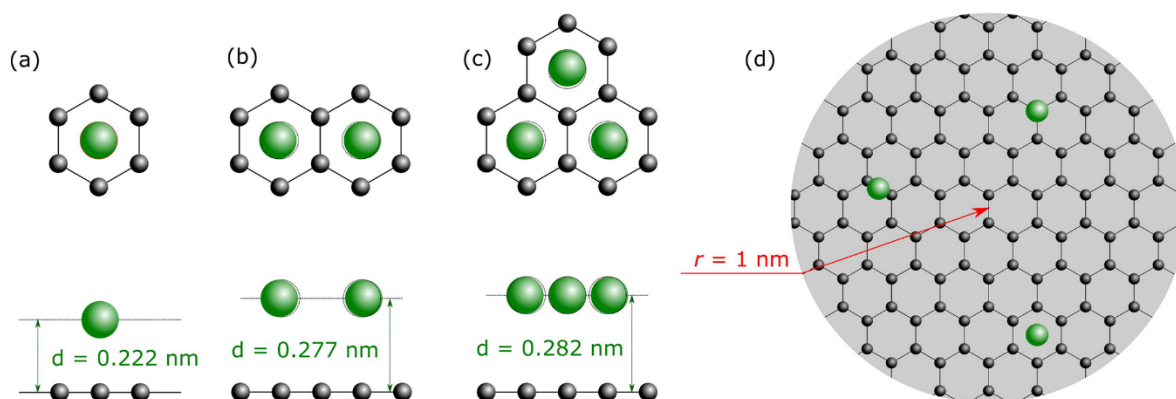


Figure 7. Space arrangement of Ga atoms on the graphene hexagonal lattice obtained from DFT calculations for small Ga clusters: (a) individual Ga atom, (b) two-atom cluster, (c) three-atom cluster. Top: top view, bottom: side view. (d) Estimation of the Ga diffusion length on a circle area.

arrangement of small clusters consisting of two and three Ga atoms in C sites is depicted. Adding Ga atoms into a cluster causes their lateral displacement mutually from each other and also relatively with respect to the original C site, and a noticeable lift of Ga atoms from the surface. In case of the two- and three-Ga atom cluster the equilibrium distance of Ga atoms from the graphene surface is 2.78 \AA , and 2.88 \AA , respectively. This is a quite significant increase (more than 24%) in comparison with the original distance of the individual Ga atom from graphene (2.2 \AA)—see figure 7(a).

The DFT calculated charge density of electrons in graphene for doping from Ga clusters is depicted as red points in figure 6(c). It can be seen that two- (point 2), and three- (point 3) Ga atom clusters dope the graphene significantly less than layer-by-layer grown Ga atoms at the same concentration (red points are above the green points and fitting dashed black curve). Moreover, the charge carrier density of two- and three-Ga atom clusters is almost the same, approximately $-20 \times 10^{12} \text{ cm}^{-2}$, so that the saturation of doping occurs in case of the island (cluster) growth at much lower Ga concentrations than in case of the layer-by-layer growth.

5. Discussion

During the real experiments (part III), Ga was deposited on graphene, and the change of transport properties was measured at room temperature. Therefore, temperature activated surface diffusion of Ga atoms along the graphene surface occurs which might lead to cluster formation. On the other hand, the DFT calculation was performed for static arrangement of atoms, which corresponds to conditions at absolute zero temperature.

Furthermore, the DFT software VASP enables the calculation of large system only if they can be combined from smaller periodic structures. Thus, the numerical processing of individual Ga atoms or layers of periodically arranged Ga atoms with graphene is a standard feasible calculation. On the other hand, the calculation of Ga cluster interaction with

graphene is much harder, because the individual building blocks (clusters) are bigger structures and cannot be easily made periodic. Therefore, this was the reason why only small clusters consisting of maximally three Ga atoms have been calculated. Hence, there is a question how the results of the experimental and computational part can be compared.

First, as for qualitative comparison, both the experimental and computational results are in good agreement. They show the Ga atoms n-dope graphene, and that there is a certain critical Ga concentration at which graphene is not more n-doped, and even the electrons start to be removed from graphene (return point in figure 1(a)—experiment, and figures 6(a), (c)—computation).

Second, in order to compare the computational and experimental results quantitatively, it is necessary to make a simple estimation of the Ga diffusion length. In case of the DFT calculation for two- and three-Ga atom clusters, the n-doping saturation appears already for three Ga atoms in a cluster which for our choice of computational cell corresponds to the Ga concentration $n_{\text{Ga}} = 89 \times 10^{12} \text{ cm}^{-2}$. It can be assumed that three Ga atoms diffusing along the graphene surface at room temperature can form one uniform cluster only if they are inside of a circle area having a radius r comparable with the diffusion length (figure 7(d)). Then the radius can be easily estimated using the simple formula

$$r = \sqrt{3/(\pi \cdot n_{\text{Ga}})} \cong 1 \text{ nm}. \quad (1)$$

In case of the experimental results, the average radius of Ga islands $r \cong 2.2 \pm 0.6 \text{ nm}$ (figure 3) with respect to the nearest neighbors is proportional to the surface diffusion length, and is only about two times higher than predicted in DFT calculations. However, both the SEM and AFM images of clusters in figure 3 were taken at much higher Ga concentration $n_{\text{Ga}} = 37.6 \times 10^{14} \text{ cm}^{-2}$ ($\sim 4 \text{ ML}$) to be able to see them on the surface at a given resolution. Therefore, the islands consist of a large number of Ga atoms and cannot be precisely compared with three Ga-atom clusters used in the DFT calculation.

The last way how to find the surface diffusion length is a combination of both, computational and experimental results. The calculation has proved the n-doping saturation starts at three Ga atoms in the cluster, and from the experimentally found return point in transport properties we know the Ga critical concentration is $n_{\text{Ga}} \cong 40 \times 10^{12} \text{ cm}^{-2}$ (figure 1(a)). Using the formula (1) the diffusion radius is $r \cong 1.5 \text{ nm}$, which is in a good agreement with the calculated value of 1 nm. Moreover, the DFT calculation gives the answer to the question why the return of CNP was not observed in figure 1(a) at $n_{\text{Ga}} 40 \times 10^{12} \text{ cm}^{-2}$. It is because the high level of n-doping and corresponding position of CNP equals to -250 V (figure 6(c)—right CNP axis) is still far outside the measurement range ($\pm 80 \text{ V}$).

The resolution of microscopic methods (AFM, SEM) we used for the mapping of initial stages of Ga growth on graphene was not sufficient to observe clusters smaller than about 1 nm and is not at all sufficient to observe the three-Ga atom clusters formation and give the direct evidence linking the DFT results for three atoms clusters with the AFM, SEM observation. On the other hand, in connection with the DFT results, especially with the conclusion that even formation of smaller Ga clusters can significantly reduce the level of n-doping, an indirect experimental proof in change of doping (return point in figure 1(a)) was introduced. From this point of view, the measurement of change in doping using transport measurement could be an interesting method for estimation of diffusion length.

Finally, let us summarize and compare our results with the results of other groups. The performed experiments and calculations prove Ga n-dopes graphene which is similar to n-doping caused by other metallic adsorbates such as Al, Ag, Cu [33, 35], and opposite to p-dopants like Au [29], Pt, water vapours [7] or to p-doping by a SiO_2 substrate. Moreover, the presented results show the n-doping saturation at a certain Ga concentration the exceeding of which leads to removal of electrons from graphene. Such an ambiguous effect was described in case of Au by Wu *et al* [43] who showed that gold in form of a continuous film p-doped the graphene while gold in form of isolated nanoparticles n-doped the graphene.

Many authors support their arguments on the type of doping by a simple comparison of the WFs of relevant metallic adsorbates and graphene, instead of DFT calculation. They directly assume the material with the lower WF with respect to graphene will n-dope graphene, or they incorporate a certain minimal WF difference that causes the electron transport (e.g. 0.9 eV) [33]. Such an approach can offer excellent results in case of large bulk volumes of materials, however, at small scales the significant discrepancies can appear due to material morphology, and inhomogeneity (effect of clusters). The bulk Ga WF being 4.2 eV [41, 63] is slightly lower than that one of graphene being reported in the interval 4.20–5.16 eV [64, 65]. It could explain the n-doping of graphene, but not the existence of the saturation point and removal of electrons in case of high Ga concentrations. These

effects cannot be clarified without the DFT simulations similar to those in our paper.

The DFT calculations performed by different groups distinguish the weak and strong binding [33, 35] between graphene and adsorbed metals like Al, Ag, Au, Cu, Pt, and Co, Ni, Pd, respectively. In this works the minimum distance 3.41 Å from graphene for weakly bonded adsorbates, and the maximum distance 2.3 Å for the strong bonds were reported. These values are in agreement with our calculations when the strong bonds between individual Ga atoms and graphene result in the 2.2 Å distance between these atoms and graphene, the weaker bonds between small clusters and graphene in the 2.82 Å mutual distance, and the weakest ones in case of complete Ga layers to the 4.04 Å distance.

The surface diffusion and formation of small clusters is beside our SEM, AFM results and return point in the measurement of resistivity versus back-gate voltage dependency also supported by a low migration energy 0.03 eV estimated by Nishi *et al* [37], however, they used the DFT based on local density approximation. They also calculated the distance of the individual Ga atom from graphene 2.11 Å which is very close to the value of 2.2 Å obtained in our calculation.

Our work contributes to the explanation of fundamental principles of electronic properties of a Ga-graphene system which is essential for increasing the application potential of this system. Besides the simple tuning of the charge carrier density by Ga doping, important in electronics, our results are useful for other applications as well. For instance, gallium, being insoluble in graphene, is a suitable catalyst for graphene synthesis at the liquid–solid interface between Ga and amorphous carbon. It also enhances the graphene sensitivity and reactivity to different gases, e.g. neurotoxic hydrogen sulfide (H_2S) [66] and, finally, localized surface plasmon resonances in Ga nanoparticles can be tuned to increase almost 100 times surface-enhanced Raman scattering [41] from graphene.

6. Conclusion

The experiments and DFT calculations performed in this work prove that Ga atoms at low concentrations negatively dope the underlying CVD graphene. Simultaneously, it has been shown that n-doping level (i.e. electron concentration) grows with the gallium coverage until its maximum value is obtained at a specific value of gallium atom surface concentration. Exceeding such a surface concentration by the ongoing Ga deposition leads to a decrease in n-doping. The whole effect has been explained by means of DFT calculations showing the return point in doping is a direct consequence of weakening the graphene–Ga bonds (and strengthening the Ga–Ga bonds) during the formation of Ga clusters related to an exchange of electrons. We hypothesize the return point is a sign of formation of larger Ga clusters caused in the room temperature experiment by surface diffusion. The estimation of surface diffusion 1.5 nm from

transport measurement, 2.2 ± 0.6 nm from experimentally measured AFM, SEM data, and 1 nm from DFT calculations for small three-atom clusters are very comparable, supporting thus the proposed model of the real experimental behavior.

Acknowledgments

We acknowledge the support by the Grant Agency of the Czech Republic (grant No. 17-21413S and grant No. 15-21581S), Technology Agency of the Czech Republic (grant No. TE01020233 and grant No. TH01011284), European Regional Development Fund (project No. CZ. 1.05/1.1.00/02.0068), MEYS CR (project No. LQ1601—CEITEC 2020), and BUT (project No. FSI-S-14-2469). This work was also supported by The Ministry of Education, Youth and Sports from the Large Infrastructures for Research, Experimental Development and Innovations project ‘IT4Innovations National Supercomputing Center—LM2015070’.

ORCID iDs

J Mach  <https://orcid.org/0000-0003-1896-0715>

M Bartošík  <https://orcid.org/0000-0003-4706-9112>

L Kormoš  <https://orcid.org/0000-0001-9099-4595>

References

- [1] Du X, Skachko I, Barker A and Andrei E Y 2008 *Nat. Nanotechnol.* **3** 491–5
- [2] Bolotin K I, Sikes K J, Jiang Z, Klima M, Fudenberg G, Hone J, Kim P and Stormer H L 2008 *Solid State Commun.* **146** 351–5
- [3] Castro Neto A H, Peres N M R, Novoselov K S and Geim A K 2009 *Rev. Mod. Phys.* **81** 109–62
- [4] Goerbig M O 2011 *Rev. Mod. Phys.* **83** 1193–243
- [5] Frank I W, Tanenbaum D M, van der Zande A M and McEuen P L 2007 *J. Vac. Sci. Technol. B* **25** 2558
- [6] Lee C, Wei X, Kysar J W and Hone J 2008 *Science* **321** 385–8
- [7] Bonaccorso F, Sun Z, Hasan T and Ferrari A C 2010 *Nat. Photon.* **4** 611–22
- [8] Avouris P and Freitag M 2014 *IEEE J. Sel. Top. Quantum Electron.* **20** 72–83
- [9] Liu H, Liu Y and Zhu D 2011 *J. Mater. Chem.* **21** 3335
- [10] Chen S, Cai W, Chen D, Ren Y, Li X, Zhu Y, Kang J and Ruoff R S 2010 *New J. Phys.* **12** 125011
- [11] Lee B, Chen Y, Duerr F, Mastrogianni D, Garfunkel E, Andrei E Y and Podzorov V 2010 *Nano Lett.* **10** 2427–32
- [12] Kong X-K, Chen C-L and Chen Q-W 2014 *Chem. Soc. Rev.* **43** 2841–57
- [13] Nouchi R and Tanigaki K 2015 *Appl. Phys. Lett.* **106** 083107
- [14] Strasser C, Ludbrook B M, Levy G, Macdonald A J, Burke S A, Wehling T O, Kern K, Damascelli A and Ast C R 2015 *Nano Lett.* **15** 2825–9
- [15] Chen J, Jang C, Xiao S, Ishigami M and Fuhrer M S 2008 *Nat. Nanotechnol.* **3** 206–9
- [16] Nagashio K, Yamashita T, Nishimura T, Kita K and Toriumi A 2011 *J. Appl. Phys.* **110** 024513
- [17] Dean C R et al 2010 *Nat. Nanotechnol.* **5** 722–6
- [18] Yu L et al 2014 *Nano Lett.* **14** 3055–63
- [19] Emtsev K V, Speck F, Seyller T, Ley L and Riley J D 2008 *Phys. Rev. B* **77** 1–10
- [20] Li X et al 2009 *Science* **324** 1312–4
- [21] Mattevi C, Kim H and Chhowalla M 2011 *J. Mater. Chem.* **21** 3324–34
- [22] Batzill M 2012 *Surf. Sci. Rep.* **67** 83–115
- [23] Zhang Y, Zhang L and Zhou C 2013 *Acc. Chem. Res.* **46** 2329–39
- [24] Jauregui L A, Cao H, Wu W, Yu Q and Chen Y P 2011 *Solid State Commun.* **151** 1100–4
- [25] Lherbier A, Dubois S M-M, Declerck X, Niquet Y-M, Roche S and Charlier J-C 2012 *Phys. Rev. B* **86** 75402
- [26] Yazzev O V and Chen Y P 2014 *Nat. Nanotechnol.* **9** 755–67
- [27] Pi K, McCreary K M, Bao W, Han W, Chiang Y F, Li Y, Tsai S W, Lau C N and Kawakami R K 2009 *Phys. Rev. B* **80** 1–5
- [28] Blake P, Yang R, Morozov S V, Schedin F, Ponomarenko L A, Zhukov A A, Nair R R, Grigorieva I V, Novoselov K S and Geim A K 2009 *Solid State Commun.* **149** 1068–71
- [29] Ren Y, Chen S, Cai W, Zhu Y, Zhu C and Ruoff R S 2010 *Appl. Phys. Lett.* **97** 053107
- [30] Liu W, Wei J, Sun X and Yu H 2013 *Crystals* **3** 257–74
- [31] Chen W, Qin S, Zhang X A, Zhang S, Fang J, Wang G, Wang C, Wang L and Chang S 2014 *Appl. Phys. Lett.* **104** 2012–6
- [32] Bangert U and Zan R 2015 *Int. Mater. Rev.* **60** 133–49
- [33] Giovannetti G, Khomyakov P A, Brocks G, Karpan V M, Van Den Brink J and Kelly P J 2008 *Phys. Rev. Lett.* **101** 26803
- [34] Vanin M, Mortensen J J, Kelkkanen A K A, Garcia-Lastra J M J, Thygesen K S K and Jacobsen K W 2010 *Phys. Rev. B* **81** 81408
- [35] Gong C, Lee G, Shan B, Vogel E M, Wallace R M and Cho K 2010 *J. Appl. Phys.* **108** 123711
- [36] Xu Z and Buehler M J 2010 *J. Phys.: Condens. Matter* **22** 485301
- [37] Nakada K and Ishii A 2011 *Solid State Commun.* **151** 13–6
- [38] Xia F, Perebeinos V, Lin Y, Wu Y and Avouris P 2011 *Nat. Nanotechnol.* **6** 179–84
- [39] Gong C, Hinojos D, Wang W, Nijem N, Shan B, Wallace R M, Cho K and Chabal Y J 2012 *ACS Nano* **6** 5381–7
- [40] Silvestrelli P L and Ambrosetti A 2015 *Phys. Rev. B* **91** 1–9
- [41] Losurdo M, Yi C, Suvorova A, Rubanov S, Kim T, Giangregorio M M, Jiao W, Bergmair I, Bruno G and Brown A S 2014 *ACS Nano* **8** 3031–41
- [42] Giangregorio M M, Jiao W, Bianco G V, Capezzuto P, Brown A S, Bruno G and Losurdo M 2015 *Nanoscale* **7** 12868–77
- [43] Wu Y et al 2012 *Small* **8** 3129–36
- [44] Procházka P et al 2014 *Nanotechnology* **25** 185601
- [45] Kresse G and Furthmüller J 1996 *Phys. Rev. B* **54** 11169–86
- [46] Kresse G and Furthmüller J 1996 *Comput. Mater. Sci.* **6** 15–50
- [47] Kresse G and Hafner J 1993 *Phys. Rev. B* **47** 558–61
- [48] Blöchl P E 1994 *Phys. Rev. B* **50** 17953–79
- [49] Kresse G 1999 *Phys. Rev. B* **59** 1758–75
- [50] Perdew J P, Burke K and Ernzerhof M 1996 *Phys. Rev. Lett.* **77** 3865–8
- [51] Monkhorst H J and Pack J D 1976 *Phys. Rev. B* **13** 5188–92
- [52] Lafkioti M, Krauss B, Lohmann T, Zscheschang U, Klauk H, Klitzing K V and Smet J H 2010 *Nano Lett.* **10** 1149–53
- [53] Ni Z H, Wang H M, Luo Z Q, Wang Y Y, Yu T, Wu Y H and Shen Z X 2010 *J. Raman Spectrosc.* **41** 479–83
- [54] Pirkle A, Chan J, Venugopal A, Hinojos D, Magnuson C W, McDonnell S, Colombo L, Vogel E M, Ruoff R S and Wallace R M 2011 *Appl. Phys. Lett.* **99** 2–5
- [55] Nomura K and MacDonald A H 2007 *Phys. Rev. Lett.* **98** 1–4
- [56] Morozov S V, Novoselov K S, Katsnelson M I, Schedin F, Elias D C, Jaszczak J A and Geim A K 2008 *Phys. Rev. Lett.* **100** 11–4
- [57] Hong X, Zou K and Zhu J 2009 *Phys. Rev. B* **80** 241415

- [58] Huard B, Stander N, Sulpizio J A and Goldhaber-Gordon D 2008 *Phys. Rev. B* **78** 121402
- [59] Barraza-Lopez S, Vanević M, Kindermann M and Chou M Y 2010 *Phys. Rev. Lett.* **104** 1–4
- [60] Bai K K, Wei Y C, Qiao J, Bin, Li S Y, Yin L J, Yan W, Nie J C and He L 2015 *Phys. Rev. B* **92** 121405
- [61] Song H S, Li S L, Miyazaki H, Sato S, Hayashi K, Yamada A, Yokoyama N and Tsukagoshi K 2012 *Sci. Rep.* **2** 337
- [62] Mohiuddin T M G *et al* 2009 *Phys. Rev. B* **79** 205433
- [63] Michaelson H B and Michaelson H B 2013 *J. Appl. Phys.* **48** 4729–33
- [64] Song S M, Park J K, Sul O J and Cho B J 2012 *Nanolett.* **12** 3887–92
- [65] Liang S and Ang L K 2015 *Phys. Rev. Appl.* **12** 014002
- [66] Sharma S and Verma A S 2013 *Physica B* **427** 12–6